
Spectral characterisation of Half-Wave Plates for Cosmic Microwave Background *B*-mode studies

by

Charlotte Braithwaite



A Thesis submitted to Cardiff University
for the degree of Doctor of Philosophy

December 2023

ABSTRACT

Cosmic Microwave Background (CMB) experiments are pushing to measure the elusive signal within the polarised CMB, the primordial B -mode signal which, if detected, would prove cosmic inflation occurred in the early Universe, therefore, dedicated studies have been deployed to measure this signal. Polarisation modulators are typically used in these instruments to modulate the linear polarised CMB signals away from $1/f$ noises sources in the experiment, one commonly used is a Half Wave Plate (HWP). However, these devices introduce non-idealities into the scientific results, therefore it is imperative to measure their level of systematic errors before deploying the devices into the instrument. The research presented in this thesis is aimed at developing and comparing techniques used to characterise HWPs designed for Cosmic Microwave Background (CMB) experiments and propagate these results through to calculate scientific results; with a focus on the tensor-to-scalar ratio, r .

The method and results for spectrally characterising an embedded metal mesh (EMM) HWP using a Vector Network Analyser (VNA) and a Fourier Transform Spectrometer (FTS) are compared and found to show that the use of both a FTS and VNA are critical to understanding the performance of a HWP over a large range of frequencies commonly used for CMB studies. It is also concluded that the performance of the EMM HWP shows these devices are useable for B -mode studies with their spectral transmission values and Mueller matrix components comparable to ones produced by Pancharatnam HWPs, while EMM HWPs are also shown to demonstrate a number of advantages compared to their Pancharatnam counterparts.

CONTENTS

Abstract	i
List of Tables	iv
List of Figures	vii
Acknowledgements	xix
1 Introduction	1
1.1 The Cosmic Microwave Background	1
1.1.1 The search for the primordial <i>B</i> -mode signal	5
1.2 <i>B</i> -mode experiments	8
1.3 The Simons Observatory	11
1.3.1 Large Aperture Telescope	12
1.3.2 Small Telescope Telescope	14
2 Half-Wave Plate Background Theory	19
2.1 Half Wave Plates (HWPs)	19
2.1.1 Pancharatnam HWPs	21
2.1.2 Embedded Metal Mesh HWPs	24
2.1.3 Mueller Matrices	28
2.1.4 HWP non-idealities	30
3 Extracting HWP performance from data analysis	33
3.1 Modelling experimental data for full characterisation of HWPs	34
3.1.1 Modelling optical measurements	34
3.1.2 Estimating the Mueller Matrix coefficient values from laboratory data	37
4 Spectral characterisation of a Half Wave Plate, using a Vector Network Analyser	39
4.1 Spectral characterisation using a Vector Network Analyser	40
4.1.1 Setting up the VNA optical bench	41
4.1.2 Optical configuration	43
4.1.3 Performing realignment of test bench	56
4.1.4 Results from VNA optical bench realignment	73
5 Spectral characterisation of a Half Wave Plate, using a Fourier Transform Spectrometer	83
5.1 The polarising Martin-Puplett FTS	83
5.1.1 Optical configuration	84

5.1.2	Measurement strategy and resulting spectra	88
5.2	Results	94
6	Discussion	101
6.1	Comparison of the VNA and FTS systems	101
6.1.1	Dynamic range	101
6.1.2	Spectral resolution and scan time	102
6.1.3	Test benches and alignments	103
6.1.4	HWP rotating mechanism	104
6.1.5	Frequency range required for characterisation	105
6.2	Comparison of the measured HWP performance	106
6.2.1	Transmission spectra of the NIKA2 HWP	106
6.2.2	Mueller matrices of the NIKA2 HWP	108
6.2.3	Modulation, optical and polarisation efficiencies	113
6.3	Summary of the comparison between the spectral systems	114
6.4	Injecting Mueller matrix coefficients into analysis pipelines to generate scientific results	114
6.5	Embedded Metal Mesh vs. Sapphire	119
7	Conclusion	121

LIST OF TABLES

4.1	NIKA2 band definitions and corresponding bandwidths (Pisano et al., 2022).	44
4.2	VNA measurements and the horn extenders required. See Table 4.3 for clarification on co-polarisation and cross-polarisation measurements.	44
4.3	Orientation of antenna horns for co-pol and cross-pol measurements at given rotation angles for the HWP, as well as the HWP rotation position.	46
4.4	Height measurements of each antenna horn from the top of the optical bench to the centre of the waveguide. This is done in both vertical and horizontal positions and the difference between the optical axis is calculated.	59
4.5	Height measurements for the collimator (closest to the transmitter) and condenser (closest to the receiver) mirror centres and compared to the height of the optical axis.	60
4.6	Measurements of the centre point between the dowel pins for both X and Y plane on the mounting stage and distance between corner of mounting stage to each centre point.	61
4.7	Measurements of the height of the centre of each lens and the height of the laser dot on each lens.	68
4.8	Measurements of the height of the laser dot on each lens at the front and back of the lens arm. Left and right positions denote the lens being flush to that side of the lens arm as you look at the antenna mounting structure head on.	71
4.9	Mean values for the Mueller matrix parameters generated using the VNA co- and cross-pol data cubes shown in Figures 4.6 and 4.24. Also included are the errors associated with these means and the theoretical values each parameter should be.	80
5.1	Band averaged matrix parameters for the NIKA2 HWP measured using a pFTS with their associated errors and expected theoretical values.	98
6.1	The spectral resolution of the FTS and VNA systems used in Chapters 4 and 5 presented in GHz units. The spectral resolution of each antenna head set used in the VNA system is provided in this Table, with the 110-170 GHz range having the highest spectral resolution of the entire set. The spectral resolution of the FTS was set by the optical path difference used in the experiment which was 10 cm^{-1}	102
6.2	NIKA2 band definitions and corresponding bandwidths (Pisano et al., 2022).	105
6.3	Mean values for the Mueller matrix parameters generated using the VNA co- and cross-pol data cubes shown in Figures 4.6 and 4.24. Also included are the errors associated with these means and the theoretical values each parameter should be.	109

6.4 The modulation, optical and polarisation efficiencies for the NIKA2 HWP calculated from the results produced using the FTS and VNA systems. From these results it is observed that each system calculates approximately the same values for each parameter. The modulation efficiency which is calculated using equation (4.6) uses the spectral transmission measured at the same rotation angles from the co-pol and cross-pol data sets, the result describes how well the HWP rotates the polarised signals and therefore how well it modulates the linear polarised light. Whilst the optical and polarisation efficiencies were calculated using equations (2.12) and (2.11) respectively using the Mueller matrix values presented in Figure 6.5 and describes the HWPs ability to transmit the total light and the total polarised light. For all of these values it is expected that they would be equal to 1. 113

LIST OF FIGURES

1.2	Examples of simplistic <i>E</i> - and <i>B</i> -mode patterns that can be observed in polarisation maps of the CMB (Incardona, 2020). The <i>E</i> -mode patterns are even parity resulting in the patterns being symmetrical, while the <i>B</i> -mode patterns are odd parity which results in the patterns being unsymmetrical.	4
1.3	Planck 2018 full sky temperature map (Collaboration et al., 2020). Red areas correspond to areas of higher density while the blue areas correspond to areas of lower density. The grey lines represents the mask of the Galactic plane, which was applied and inpainted.	5
1.4	Power spectra for the fluctuations in the temperature and polarisation signals in the CMB. Within both the temperature and polarisation signals of the CMB there are small fluctuations in their values, known as anisotropies. The anisotropies arise from scalar and tensor perturbations in the early Universe and from scattering during the reionisation epoch and gravitational lensing. The temperature anisotropies are at a level of $\sim 10^{-5}$ K (Hu & Dodelson, 2002), the <i>E</i> -mode anisotropies are at a level of $\sim 10^{-6}$ K (Durrer, 2015) and the <i>B</i> -mode anisotropies are at a level of $\sim 10^{-7}$ K (Durrer, 2015). Measurements of the anisotropies' statistical properties provide many insights into the early Universe, the contents of the Universe from the cosmological parameters and the large-scale structure. Image credit: Calabrese (2020)	6
1.5	Several CMB <i>B</i> -mode polarisation experiments with their corresponding measurements, producing either upper limits or detections. Included on this plot is the theoretical model for <i>B</i> -mode lensing (solid red line) and the theoretical model for gravitational wave <i>B</i> -modes (dashed red lines) for two values of r (BICEP/Keck Collaboration et al., 2021)	7
1.6	Simulated atmospheric transmission windows for the South Pole (black line), the Atacama plateau (blue line) and Hanoi Vietnam (red line). The least transmission through the atmosphere is simulated at Hanoi which is only 20 m above sea level. Both the Atacama plateau and the South Pole have similar transmission profiles with both being roughly 2500 m above sea level. There are three windows within the blue and black transmission profiles where transmission through the atmosphere is completely blocked. These frequencies can therefore not be measured at these locations (Kovac & Barkats, 2007).	10

1.7	Maps of the proposed sky surveys for both the small aperture telescopes and large aperture telescope being launched by SO. The SATs will observe 10% of the sky whilst the LAT will observe over 40% of the sky. Included are other surveys which probe similar patches in the sky and have similar scientific goals, such as BICEP/Keck and SPIDER whose sky patches overlap the SATs very well and also targeted the primordial B -mode signal (Ade et al., 2019).	12
1.8	Cross-sectional view of the LAT (Galitzki et al., 2018). Right hand panel shows the first mirror (M1) which will be parabolic and the secondary mirror (M2) which will be a large concave. The first mirror is off-axis meaning the incoming light won't be interfered with by the reflected light off the secondary mirror. The mirrors are also under illuminated and at millimetre and sub-infrared wavelengths this greatly reduces the systematic affects due to diffraction.	13
1.9	Cross sectional view of the LATR (Galitzki et al., 2018). A more detailed view of an optics tube has also been presented showing the three silicon lens positions which diverge the beam towards the focal plane array.	13
1.10	Schematics of the SAT design (Ali et al., 2020). The SAT is a three lens refractive system which focuses the light onto a focal plane array which operates at 100 mK. There are five cryogenic stages in total with the SAT, 300 K, 40 K, 4 K, 1 K and 100 mK. These stages are cooled using a pulse tube cooler and a dilution refrigerator. Each SAT being deployed will also include a continuously rotating HWP which will be held in the 40K stage and acts as a polarisation modulator. This HWP is based on the design deployed in the POLARBEAR-2 instrument (Hill et al., 2020).	15
1.11	The brightness rms of the Galactic foregrounds, synchrotron (green line) and thermal dust (red line) radiation, along with the polarised CMB radiation (cyan line) as a function of frequency, as observed by Planck (Collaboration et al., 2020).	16
2.1	Schematic of the HWP for the QUaD experiment (Savini et al., 2006). This is a 5-plate Pancharatnam-designed HWP (denoted by α , β and γ which represent the angle each plate is rotated by with respect to the extraordinary axis of the previous plate) and has a 3-layer anti-reflection coating (ARC), each layer is represented by the numbers 1, 2 and 3 in the diagram. This ARC was decided on to minimise the reflections caused by the large refractive index of sapphire.	22
2.2	Schematic of a uniaxial material. In a 3D setup, two axes have the same refractive index (denoted by n_1) whilst one axis has a different refractive index (denoted by n_3).	23
2.3	Example of a wave plate with three conductive layers and three inductive layers, denoted by C and L respectively. The distance between the conductive layers and inductive layers is set differently to the distance between the consecutive layers for each mesh design, denoted by d and d_C or d_L . (Pisano et al., 2008).	25
2.4	Example of a transmission line model for an EMM HWP. This shows two different transmission line models for six capacitive grids and six inductive grids, which are embedded in polypropylene. To ensure that the thickness of the models were the same as the thickness of each set of six grids and their spacers, additional sections of polypropylene was added which are depicted in the diagram as the rectangle boxes. (Zhang et al., 2011)	26

2.5	CAD drawing of an embedded metal mesh HWP. The capacitive (blue dashed lines) and inductive (red lines) grids can be observed being embedded in polypropylene layers. An anti-reflecting coating of porous PTFE is applied to reduce the level of reflection as incident light propagates between refractive indices of materials (Pisano et al., 2022).	27
2.6	a) A birefringent HWP with its extraordinary and ordinary axes shown, b) an EMM HWP with its inductive and capacitive axes. From these sketches it is shown that the inductive and capacitive axes replace the extraordinary and ordinary axes respectively for an EMM HWP. The optical axis is denoted by the large red and blue arrow, with its x and y axes shown (Pisano et al., 2022).	27
4.1	Schematic diagram of a 2-port VNA system, the terms a and b denote the input and output respectively in the system. A device under test (DUT) modifies a signal that is transmitted or reflected in the forward or reverse direction. The S_{ij} , where i and j are either numbers 1 or 2, denote the S-parameters of the system and their arrows correspond to the direction in which they refer to.	41
4.2	Schematic diagram of the optical test bench for transmission measurements for the NIKA2 HWP. An antenna horn set is used (one transmitter and one receiver) where one antenna horn transmits a signal towards a planar-convex lens (located at its focal length, which for this experiment was 200 mm), the signal is reflected off a mirror, through the HWP mounted in a rotator. Once it has been transmitted through the HWP the beam is reflected off another mirror, through a planar-convex lens (again located at its focal length) where it is then detected by the receiver.	45
4.3	VNA optical bench setup in vertical polarisation orientation and co-pol setup. This setup generates a Gaussian beam and, in this configuration, would generate a vertical polarisation background for co-pol. This photo is complimentary to the schematic given in Figure 4.2.	47
4.4	VNA optical bench setup in vertical polarisation orientation with the NIKA2 HWP placed in the beam path. The HWP position is marked to ensure repeat placement. This photo is complimentary to the schematic given in Figure 4.2.	48
4.5	Mean background spectra (black lines) as a function of frequency. These were calculated by averaging all the background spectrum measured during the experiment. The error bars, denoted by the blue, orange and green coloured regions, are quantified as the statistical error on the mean and to be able to observe the error it has been multiplied by 10.	49
4.6	Co-polarisation data cube showing all three frequency ranges (blue is 110-170 GHz, orange is 160-260 GHz and green is 220-330 GHz) and how the HWP performance varies over them. Plotted are the spectra as a function of rotation angle and frequency. In this plot all 87 spectra measured in the co-polarisation configuration are presented.	50

4.7	Cross-polarisation data cube showing all three frequency ranges (blue is 110-170 GHz, orange is 160-260 GHz and green is 220-330 GHz) which presents how the HWP performance varies over them. Plotted are the spectra as a function of rotation angle and frequency. In this plot only 8 spectra in the cross-polarisation configuration are presented, these being the angles around the maximum and minimum plots in the HWPs rotation. Through plotting these values the limits of the HWPs performance can be observed as it rotates through 360°	51
4.8	Co-pol maximum and minimum transmission spectra, which represent the HWP rotation positions where the maximum and minimum signals were detected. The yellow curves denote the background x-pol measurement, which is the signal detected with polarisers P1 and P2 orthogonal to each other and the HWP not in the optical path.	52
4.9	Maximum and minimum transmission spectra produced by the NIKA2 HWP in the cross-pol configuration using a VNA test bench. The x-pol levels are presented as the yellow curves. From this Figure a disconnect across the frequency bands is noted in the maximum spectra with approximately a 2.5 dB difference in their amplitude. This is believed to be due to misalignment in the optical setup.	53
4.10	Modulation efficiency of the NIKA2 HWP as measured on the VNA system at Cardiff University. It is important to note here that it has been obtained using the results seen in Figures 4.8 and 4.9. Using equation (4.6) produces the black curve producing an average modulation efficiency of 0.993 and 0.991 over the 150 GHz and 260 GHz bands respectively. However, this is calculated from a maximum spectrum from the co-pol data set and a minimum spectrum from the cross-pol dataset. As it was assumed that the cross-pol configuration was misaligned I have included the modulation efficiency measured at the "45°" rotation angle which is presented as the cyan curve in this Figure. The modulation efficiency measured using these spectra is 0.812 and 0.618 for the 150 GHz and 260 GHz bands respectively, indicating a much worse efficiency than previously expected. The shaded green areas indicate the working bands of the NIKA2 experiment.	54
4.11	Mueller matrix coefficients (black line) for a given angle (θ°) generated using the MCMC pipeline developed from the method described in Chapter 3 and injecting 'misaligned' cross-pol data. This only uses the maximum and minimum spectra from both the co-pol and cross-pol data sets. The error bars are shown in red and are the standard deviation in the calculated Mueller matrix coefficients. The working bands of the HWP have been included as the green shaded regions.	55
4.12	Optical (blue curve) and polarisation (magenta curve) efficiency of the NIKA2 HWP as measured on the VNA system at Cardiff University. It is important to note here that is has been obtained using the results seen in Figures 4.8 and 4.9. The shaded green areas indicate the working bands of the NIKA2 experiment. The average optical efficiency across the two bands was calculated to be 0.953 and 0.964 for 150 GHz and 260 GHz respectively. The average polarisation efficiency across the two bands was 0.884 and 0.821 for 150 GHz and 260 GHz respectively.	57

4.13	Measuring the optical height from the centre of the horn to the top of the optical bench in left) X-axis and right) Y-axis planes. It is important to note that the structure shown is held on mounting stages and therefore is further from the bench than denoted in the diagram.	60
4.14	Schematic of the measurements performed to find the position of the centre of rotation the antenna horns should be rotating about when moving from a co-pol configuration to a cross-pol configuration. Left) Finding the centre point between the dowel pins in both X (horizontal) and Y (vertical) planes. Right) Measuring the distance from the centre point, found in the left image, of the X and Y plane to the edge of the mounting plate.	61
4.15	Antenna mounting structure with a 2 mm shim added to the X-axis to correct the centre of rotation position. A centre mark for the X-plane has also been marked.	62
4.16	Antenna mounting structure in the Y-axis with the centre mark visible.	63
4.17	Aligning the laser to the optical axis of the system using the centre marks on the mounting structure and from this target was added at the end of the bench and an aperture between the laser and target. The target and aperture remained on the bench whilst the alignment of each horn was carried out.	64
4.18	Cross hair laser checking the adjustments to VNA antenna head were centred on the rotation point in the vertical polarisation orientation (X-axis).	66
4.19	Cross hair laser checking the adjustments to VNA antenna head were centred on the rotation point in the horizontal polarisation orientation (Y-axis).	67
4.20	Laser aligned to aperture and target with lens inserted to measure position of laser dot with respect to the centre of the lens. On the lens the centre is marked by a black dot. The lens is at the front of the lens mounting structure here.	69
4.21	Lens moved to the back of the lens mounting structure. Measurements of laser dot position is repeated and any change in its position denotes lateral changes as the lens moves from the front of the structure to the back.	70
4.22	Position of receiver lens on the structure.	72
4.23	Position of the transmitter lens on the structure. The lens has a 70 mm aperture in it to reduce the size of the beam.	73
4.24	Cross-polarisation data cube showing all three frequency ranges (blue is 110-170 GHz, orange is 160-260 GHz and green is 220-330 GHz) which presents how the HWP performance varies over the ranges with the corrected optical alignment. Plotted are the spectra as a function of rotation angle and frequency. In this plot all 87 spectra in the cross-polarisation configuration are presented, through plotting these values the limits of the HWPs performance can be observed as it rotates through 360°.	74
4.25	The new maxima and minima cross-pol measurements for the cross-pol measurements of the NIKA2 HWP using the VNA optical setup. The maxima spectra sit above 10^{-1} across the frequencies, whilst the minima spectra all sit below 10^{-1} across the frequencies. However, this excludes the yellow line which is background x-pol, the signal detected when the polarisers P1 and P2 are orthogonal to each other and the HWP is not present in the optical path. The shaded green areas denote the working bands of the NIKA2 experiment.	75

4.26 Modulation efficiency of the NIKA2 HWP obtained using equation (4.6) and the data cubes from the VNA experiment. In particular, this modulation efficiency arises from injecting the cross-pol measured after the realignment of the system. Included in this Figure are the modulation efficiencies calculated with the HWP rotation to "0°" and "45°", both of which should produce values equal to 1. When the HWP is at "0°" the calculated efficiency was 0.992 and 0.997 for the 150 GHz and 260 GHz bands respectively, "45°" the values calculated were 0.95 and 0.94 for the 150 GHz and 260 GHz bands respectively. While the "45°" values are 3-4% lower than when the HWP is rotated to "0°" when compared to Figure 4.10 it is shown that after the realignment these "45°" values have increased by 0.14 and 0.33 respectively. The shaded green areas correspond to the bandwidths of the NIKA2 experiment. . . . 77

4.27 Mueller matrices of the NIKA2 HWP produced using eight transmission spectra measured before (black lines) and after (cyan lines) the realignment procedure described earlier in this Chapter. Before the realignment of the optical system the three frequency ranges measured on the VNA do not overlap with each other in the M_{II} and M_{UU} terms. The amplitude of the M_{UU} term in the 110-170 and 220-330 GHz ranges were measured at ~ -0.5 or higher, in particular at the higher frequencies the amplitudes were calculated to be closer to 0. All other matrix parameters calculated overlap with each other, but the realignment data shows less spread between values over the frequency ranges. The data sets used to generate this plot are presented in Figures 4.8, 4.9 and 4.25. The shaded green areas correspond to the working bands of the NIKA2 experiment. Errors for each Muller matrix parameter value has been excluded from this plot to ensure viewing the values was easier. 78

4.28 Mueller matrix of the NIKA2 HWP (at a given angle of $\theta = 0^\circ$) measured using the VNA setup at Cardiff University. Errors are included in red and represent the standard deviation in the parameter values. The green shaded regions represent the NIKA2 bandwidths and show the frequencies over which the HWP should be performing over. 79

4.29 The optical (blue line) and polarisation (magenta line) efficiencies measured from using the Mueller matrix parameters calculated in Figure 4.28 for the NIKA2 HWP. The polarisation efficiency has a disconnect between the 160-260 GHz and 220-330 GHz ranges which follows from the spectral transmission data presented earlier. The dip at 200 GHz has more spread across the values and is due to the spread in transmission observed in the VNA transmission spectra. The shaded green areas represent the bandwidths of the NIKA2 experiment. 81

5.1	Schematic of a Martin-Puplett interferometer showing the path the light takes within the module towards the detector. A source emits radiation which is subsequently polarised by a polariser. This polarised light is split at a beamsplitter (held at 45°), half is reflected down one arm and half is transmitted down the other arm. A rooftop mirror is located at the end of each arm where the polarised light's electric vector is rotated by 90°, changing the phase of the waves. The two waves interfere at the output of beamsplitter and it is this signal which is detected. One rooftop mirror is moveable and through moving it in increments the interference signals detected create an interferogram which is Fourier transformed (FT) to obtain the systems transmission spectrum.	85
5.2	A schematic of the open air optical configuration section of the FTS used for the NIKA2 HWP characterisation. The pFTS produces diverging waves which traverse through a planar-convex lens which refracts the waves into a collimated beam. The second planar-convex lens is placed such to converge the collimated beam towards the detector. Two wire grid polarisers are placed in the collimated beam to ensure polarisation is maintained throughout the system and each is placed at slight angles to minimise standing waves which would occur. The HWP is placed in a rotator between the two polarisers on a platform which is fixed to the bench. The detector in the system is a bolometer which runs at 1.5 K.	86
5.3	Optical setup outside of the pFTS module. The setup includes two wire grid polarisers (P1 and P2), two planar-convex polyethylene lenses and a HWP platform which the rotator holding the HWP will be placed on. The white disc in front of the cryostat window is the 12 cm ⁻¹ LPE which prevents frequencies of 360GHz and higher from entering the cryostat and subsequently being detected.	86
5.4	Background spectra for co-pol (black curve) and cross-pol (green curve) with their respective errors associated (blue and orange regions). The blue and orange regions represent ten times the standard error for the background spectra measured in order for the values to be visible. The cross-pol background (green curve) has been moved by an arbitrary constant as these backgrounds overlap with the co-pol backgrounds otherwise.	89
5.5	Measured co-pol transmission spectra of a NIKA2 anti-reflection coated embedded metal mesh HWP. Spectra shown are at rotation angles close to the expected maxima and minima, the intermediate angles are omitted here but are shown in Figure 5.8. The angles denoted in the legend are arbitrary values used to reference the angle on the rotation mechanism used to rotate the HWP, allowing for repeat measurements to occur. The 'zero' values also might not occur exactly at the zero angle which is why transmission spectra are taken around the expected value. The x-pol spectrum is included as the yellow curve and the shaded green regions denote the NIKA2 frequency bands.	90
5.6	Measured cross-pol transmission spectra of the NIKA2 anti-reflection coated embedded metal mesh HWP. Spectra shown are at rotation angles close to the expected maxima and minima, the intermediate angles are omitted but are shown in Figure 5.9. The angles denoted here are arbitrary and are used to reference the angles on the rotation mechanism. The x-pol spectrum is included as the yellow curve and the shaded green regions denote the NIKA2 frequency bands.	91

5.7	Modulation efficiency of the NIKA2 HWP from the FTS experiment and was calculated using spectra in Figures 5.5 and 5.6 in equation (4.6). The modulation efficiency of the NIKA2 HWP was calculated to be greater than 0.98 across all frequencies, with its value approximating to 0.992 across the 150GHz band and 0.996 across the 260GHz band when the HWP was rotating to "0°". When the HWP was at a rotation of "45°" the modulation efficiency calculated was 0.973 and 0.969 for the 150GHz and 260GHz bands respectively. The shaded green areas represent the working bands of the NIKA2 experiment.	92
5.8	Data cube for the co-pol spectral transmissions of the HWP at rotation angles between 0° and 359°. Measurements of the spectral transmission were taken every 5° and the increments were changed to 2° close to maxima and minima angles. .	93
5.9	Data cube for cross-pol spectral transmissions of the HWP at different rotation angles. Measurements of the spectral transmission were taken every 5° and the increments were changed to 2° close to maxima and minima angles. Comparing to Figure 5.8 it is shown that these results are in counterphase to each other.	94
5.10	Measured co-polarisation transmission spectra of a NIKA2 anti-coated embedded metal mesh HWP presented in Figure 5.5 but in linear format. The angles denoted in the legend are arbitrary values used to reference the angle on the rotation mechanism used to rotate the HWP, allowing for repeat measurements to occur and are just for reference for repeat measurements in the setup. The 'zero' values also might not occur exactly at the zero angle which is why transmission spectra are taken around the expected value.	95
5.11	Measured cross-polarisation transmission spectra of a NIKA2 anti-coated embedded metal mesh HWP presented in Figure 5.6 but in linear format. The angles denoted in the legend are arbitrary values used to reference the angle on the rotation mechanism used to rotate the HWP, allowing for repeat measurements to occur and are just for reference for repeat measurements in the setup. The 'zero' values also might not occur exactly at the zero angle which is why transmission spectra are taken around the expected value.	96
5.12	Mueller matrix of the NIKA2 HWP (at a given angle of $\theta = 0^\circ$) using a pFTS at Cardiff University with errors (1σ , red shaded area) and working bands (shaded green area) included.	97
5.13	The optical (blue line) and polarisation (magenta line) efficiency measured by using the Mueller matrix parameters calculated in Figure 5.12 for the NIKA2 HWP. The average optical efficiency was 0.96 and 0.97 for the 150 GHz and 260 GHz bands respectively. The average polarisation efficiency was calculated to be 0.96 and 0.95 for the 150 GHz and 260 GHz bands respectively. The shaded green areas represent the bandwidths of the NIKA2 experiment and indicate the frequencies the HWP should be performing perfectly over.	99
6.1	Maxima and minima spectra from co-polarisation measurements using the VNA, plotted in a linear format. Structure in the system can be observed in the 160-260 GHz range by the ripples in the minima spectra. The x-pol measured level of the VNA system is plotted as the yellow curve. The angles denoted in the legend as arbitrary to the system and are noted for repeatability. Shaded green areas correspond to the working bands of the NIKA2 experiment.	107

6.2	Maxima and minima spectra produced from the co-polarisation measurements using the FTS setup, plotting in a linear format. The maxima data sets (blue, green, purple and pink curves) overlap well with each other and therefore agree well. The minima data sets (orange, red, brown and grey curves) overlap each other and therefore the measurements agree with each other. Shaded green areas correspond to the working bands of the NIKA2 experiment and the yellow curve denoted the x-pol of the FTS system which describes the polarisation mixing caused by the FTS instrument itself.	108
6.3	Modelling behaviour of the NIKA2 HWP and measurements that were taken of it in 2015 at Cardiff using an FTS. The black dashed lines indicate the bandpass of the NIKA2 experiment. The labels of C-axis and L-axis indicate the orientation of the axes of the HWP, these means that the C-axis or L-axis was parallel with the optical axis (Pisano et al., 2022).	109
6.4	Overlaying the Mueller matrix components calculated from both the FTS (black curves) and VNA (blue curves) first presented in Chapters 5 and 4 respectively. The working bands are shown at the green shaded regions centred on 150 GHz and 260 GHz. The ideal matrix parameter values are also plotted at a red shaded area. Error bars have been excluded from this plot to avoid confusion with overlapping values, the errors can be seen in Figures 4.28 and 5.12 for the VNA and FTS results respectively.	110
6.5	Mueller matrix parameters produced from the VNA (blue line) and FTS (black line) spectra with the corrected matrix parameter equations to account for the FTS polarisation orientation. Matrix parameter values for an ideal HWP is included (red lines) in the plot. The working bands for NIKA2 is included as the shaded green areas to indicate the frequencies the HWP has been designed to work for. Error bars have been excluded from the Figure but are seen in Figures 4.28 and 5.12 for the VNA and FTS respectively.	111
6.6	Flow diagram to visualise the structure for the 's4cmb' analysis pipeline (Fabbian & Peloton, 2021). The dashed box represents the analysis pipeline of s4cmb that can be edited. This pipeline inputs data generated from CMB experiments scanning the sky and injects instrumental systematic effects into the timestream to generate real data and inform future designs for CMB experiments. The Mueller matrix coefficients were stored in the Input Telescope section of the pipeline to then be called in the TOD section within its map making module 'map2tod' where the matrix coefficients are injected into the TODs.	115
6.7	Sky patch maps generated using the 's4cmb' pipeline. Left column shows the input sky maps in the I (top), Q (middle) and U (bottom) parameters. The middle column shows the maps after demodulation and the right column shows the difference between the left and middle columns. For this particular plot the Mueller matrix for an ideal HWP was injected into the TOD timestream, see equation (3.1). All difference maps, I , Q and U , produce no variation between the 'Input' and 'Demodulation' plots because the ideal HWP Mueller matrix is injected, incorporating no systematics into the system and therefore not altering the input maps.	116

6.8	Sky patch maps generated using the ' <i>s4cmb</i> ' pipeline. Left column shows the input sky maps in the I (top), Q (middle) and U (bottom) parameters. The middle column shows the maps after demodulation and the right column shows the difference between the left and middle columns. For this particular plot the Mueller matrix for a non-ideal HWP was injected into the TOD timestream. The 150 GHz averaged Mueller matrix parameters obtained from the FTS experiment, provided in Table 6.3, were used to produce these output sky maps. The difference maps for I , Q and U produce variation between the 'Input' and 'Demodulation' plots due to the HWP systematics caused by the non-ideal parameters injected.	117
6.9	BB power spectra for both the ideal (magenta curve) and non-ideal (green curve) HWP cases. Included in the plot is the input BB power spectrum (black curve) used in <i>s4cmb</i> . Comparing the two BB power spectra it is clear that the non-ideal HWP case affects the power spectrum at multipoles >250 by changing the amplitude of the spectrum.	118

*To the grumpiest dog, Henry.
You were the best thesis buddy.*

ACKNOWLEDGEMENTS

I would like to say thank you to the Science and Technology Facilities Council (STFC) for funding my PhD and acknowledge my supervisors, Carole Tucker and Erminia Calabrese, for their continuous support. Carole, for all your invaluable guidance throughout this process and pushing me to achieve my best - thank you. One pandemic later and we finally made it! Erminia, thank you for always having an open door, allowing me to wrack your brain when mine had lost all sense of reason over MCMCs and proof reading my work (even if I left some deadlines to the last moment). Thank you both for being steadfast and welcoming throughout my PhD journey and for all of your encouragement over the years.

To Ben Westbrook, thank you for mentoring me over the past year. Your constant support, whether that be proof reading my CVs and personal statements, career advice, helping with presentations or just the overall encouragement you provided, really spurred me on to believe I was capable of achieving whatever I set out to do.

To the Astronomy and Instrumentation Group at Cardiff, I've never known a more welcoming or encouraging research group (and it's not just because I've never left!). From all the help in the lab to just chatting about life in general you have truly shaped my experience over the last four years. To my old office mates, Gethin, Luke, Matt and Patrick, you helped me at through my low points and provided a safe haven to turn to and always listened to me to provide unrivalled support. You supplied endless laughs and uplifting conversations - I've never learnt so much about 3D printing in my life. And to my new office mates, Ian, Chris, Chris and Harry, thank you for helping me navigate the jump from PhD student to postdoc and for providing a wealth of knowledge on so many subjects to further my understanding. Again, I'm learning so much about 3D printing! Hopefully, my baking makes up for the endless questions I have to help fuel you through them!

When starting this PhD I remember Richard Lewis saying in his induction talk, "make sure you build a community around you as there will inevitably be hard moments, whether that be with your fellow PhD students or your friends and family." Well, my fellow PhD students at Cardiff you have been my life jacket. Helena Faustino Vieira, Andy Cook, Jacob Elford, Eva Durán Camacho Holly Davies, Hidde Jense, Luke Booth, Gethin Robson, Matt Lyons, Patrick Ashworth, Carys Evans, Hannah Ambrose, Terri Pearce, the honorary PhD student George Brown, literally everyone. Every word in the English language comes to mind, yet I can't begin to describe the moments we have all shared and how they have enriched my time over these last four years. From every trip to Bute Park, the Flute, charity shop find, cinema trips, pub quizzes, one Shrek rave too far with one too many onions, to every single belly-aching, tear inducing, cake slice shared moment - thank you. You are all incredible human beings, capable of anything and who only deserve the best life has to offer. I promise you, you will all get through this.

Lena, thank you for always being up for Waterloo Tea trips, for baking me treats when I needed a sugary pick me up, for always providing Wallace and Gromit entertainment and for

always allowing me to vent my frustrations to you. You were the best flatmate a girl could ask for, even if we did end up homeless for a little bit...what an experience! You are such an incredible astronomer - you are going to achieve incredible feats, I have every faith in you. You're a woman in STEM, Bunsen burner, ON!

But it's not just the community I've created in Cardiff that has seen me through these four years, my Bognor crew has been along for the ride too. Kish, to your unwavering support over the last four years and your incredible stories that made my days, I will forever be grateful. You celebrated my highs and you helped me get through my lows and you provided a place I could touch base with everyday. You probably ended up reading my thesis more than I did! But as you reminded me, we were in this together. Your friendship over the years has been one of a kind and I wouldn't trade it for all the riches in the Universe. And to Rue, Timothy, Clementine, Inara and River, all of your antics, grumpy (and in Tim's case, posed) photos and most importantly your bean pics, thank you for providing each of my days (and camera roll) with so much sass and laughter.

However, it has to be said that my biggest supporters have been my family. Mom and Dad, you have been my rocks throughout this process and throughout my life. From coming up on weekends to cheer me up and to constantly reminding me of my worth, you have pulled me over this finish line, thank you. Mum you are my best friend, I can always turn to you for anything and know you are only a phone call away. To have that unwavering love throughout my entire life has helped me overcome every obstacle life has thrown at me because I know I have somewhere to come back to. Dad, without you I don't think I would be as in love with science as I am today. You helping with my timetables on the way to primary school such that I was an unstoppable machine when competing with my classmates made me fall in love with the subject, which ultimately helped grow my love of the sciences. You were always on hand to transport me to any sporting fixture or commitment I had and taught me how to tie a Windsor knot properly. You've always been available at the drop of a hat and been one, if not, joint biggest supporter (joint with Mum of course) who has always and will always be in my corner. Everything you've ever done for me is appreciated so much and I promise to only raid your wine cellar every once in a while. To my uncle David, your support, hugs and help over the years meant everything to me, thank you. Grandma and Grandad, you always supported me (and put me to work gardening) with your words and amazing hugs. Your endless supply of tea, Blue Ribbons and love were a source of happiness for me growing up. I love you and miss you more than words can describe. I wish you could have been here to see this.

Lastly, but by no means least, Thomas Braithwaite and Josephine Amos, my London crew. Jo, you are one of the most put together people I know, you are the woman I aspired to be when I was younger and who I aspire to be even now. Thank you for your support along the way, from allowing me to invade your home on weekends to the last minute proof reading. And finally, Thomas, my big brother, all throughout my childhood to now you have been my role model - you may not realise it but you have shaped me into the person I am today (how else would I have realised my insane sense of dodging footballs). You achieve everything you set your mind to with such ease and grace but it is your kindness and humour I truly strive to emulate. You are always on hand when I need you, even if it's just with words of encouragement. You are truly the smartest, kindest person I know and words can not describe how proud I am of you. If by the time I can finally retire I am half the person you are, I'll have truly made it. Thank you for everything.

INTRODUCTION

"To the people who look at the stars and wish,"

Sarah J Maas, *A Court of Mist and Fury*

As Cosmic Microwave Background (CMB) experiments increase their sensitivity requirements to detect even the faintest signals and extract cosmological information, such as that regarding cosmic inflation, it is important to fully understand the level of systemically induced signals which arise from optical devices in the telescope. This thesis will discuss the implementation of a device previously used within CMB studies known as a Half Wave Plate (HWP). This device is used in experiments to detect linear polarisation and it does this by modulating linear polarisation to four times its rotation speed. This modulation allows the temperature and polarisation signals of CMB experiments to be independently measured using demodulation analysis pipelines. It moves the desired signals away from unpolarised background signals and $1/f$ noise, defined as signals with power spectra that have large amounts of signal at low frequencies, however this significantly decreases as the frequency increases. This thesis discusses the background theory of how HWPs work, two laboratory methods used to calculate the characterisation parameters of HWP and how to inject the parameters into a full analysis working pipeline to calculate the tensor-to-scalar ratio, r (the parameter used to quantify primordial gravitational waves).

1.1 THE COSMIC MICROWAVE BACKGROUND

At the beginning of the 20th century the accepted theory which explained the state of the Universe was the Steady State Model ([Burbidge \(2001\)](#), [O’Raifeartaigh et al. \(2014\)](#)). This described the Universe as being the same at any point in time with new matter being created from galaxies moving away from one another. In 1948 Georges Lemaitre theorised that the Universe originated from a finite point, coined the Big Bang ([Luminet, 2015](#)). However, if this was the case

then we would expect to find embedded in the Universe a remnant signal (Gamow (1948), Alpher & Herman (1948), Alpher & Herman (1949)), produced due to photons freely traversing after the rapid expansion in the early Universe. It was not until 1965 when Penzias and Wilson (Penzias & Wilson (1965), Mather (2010), Durrer (2015)) accidentally measured the remnant signal (the CMB) that the Big Bang theory was universally regarded as the leading theory to explain the origin of the Universe.

Our current understanding of the Universe assumes that just after the Big Bang the whole Universe was in an ionised plasma state with an extremely high temperature and density, akin to a ‘hot soup’ made up of fundamental particles like protons, neutrons, electrons, neutrinos, and photons reaching temperatures of $\sim 10^9\text{K}$ (Jepsen (2013), Fraknoi et al. (2017)). It was completely opaque to light as atoms had not yet formed and photons were constantly scattering off unbound electrons. This state changed approximately 380,000 years after the Big Bang in an event termed recombination (Hadzhiyska & Spergel, 2019). As the Universe expanded and cooled down, particles were able to bond and form neutral atoms which in turn allowed photons to freely propagate. These photons are the CMB radiation that continued to travel through the Universe from the time of last scattering to today and the CMB photons’ propagation through the Universe caused their temperature to decrease and stretch its frequency to the microwave region of the electromagnetic spectrum (Joseph, 2017).

The CMB is an electromagnetic signal, observable in all directions in the sky. The temperature of the CMB is 2.73 K almost everywhere in the sky, which was first measured by COBE (Kogut et al. (1993), Fixsen et al. (1996)) and produced an almost perfect blackbody curve to describe the signal measured, seen in Figure 1.1. The tiny fluctuations in the temperature of the CMB arise from differences in densities of structure right after the Universe formed.

In addition to its temperature, the CMB also has a polarisation signal. Roughly 10% of the CMB is linearly polarised due to Thomson scattering (Seshadri, 1999). This scattering is where the photons scatter off free electrons during the time of last scattering and later epochs, such as during the reionisation epoch which occurred approximately a billion years after the Big Bang (Zaroubi, 2013). The polarisation of the CMB is further split into two components; *E*- and *B*-modes, examples of their patterns are seen in Figure 1.2.

Both the temperature and polarisation signals mainly arise from scalar and tensor perturbations in the early Universe, however, other factors contribute to the over amplitudes of their signals, such as gravitational lensing of *E*-modes into *B*-modes.

Scalar perturbations arise from density and gravity fluctuations which were present prior to the inflation in the early Universe occurring. Inflation is the leading theory to describe the evolution of the early Universe, it describes a brief period of exponential rapid expansion at a time of $\sim 10^{-36}$ seconds after the Big Bang. In this period the scale of the Universe grew by ~ 50 *e*-folds (Remmen & Carroll, 2014), with an *e*-fold being the time it takes for space to increase by *e* times its original

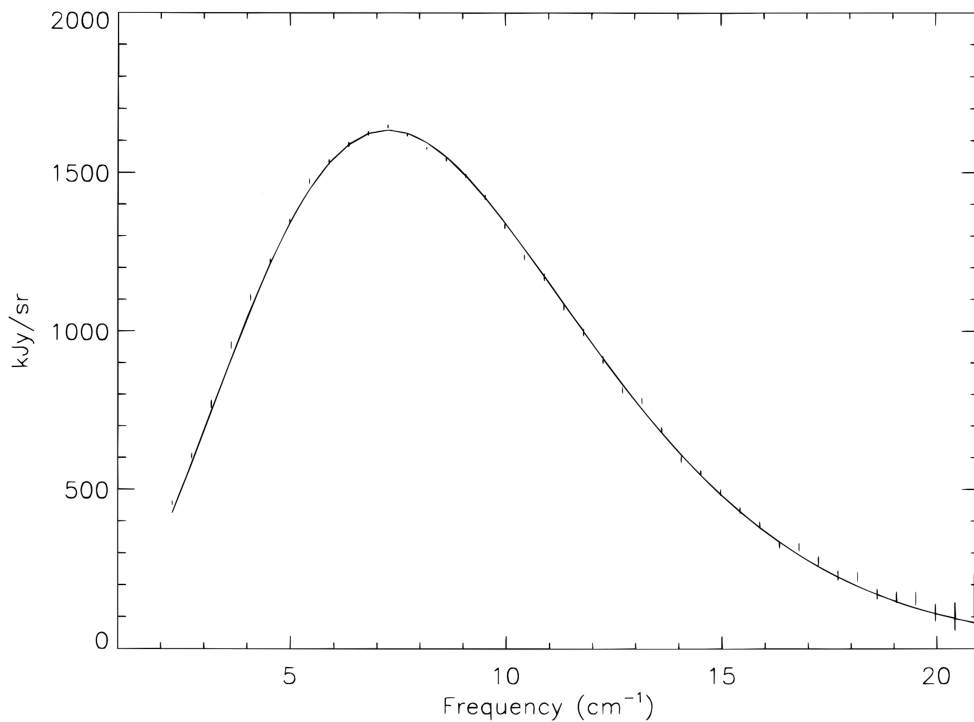


Figure 1.1 – CMB intensity measured by COBE (black dots with associated error bars) and a blackbody function (solid black line) which was generated with 2.73 K as its temperature. From the almost perfect overlap between the blackbody function and experimental data, it revealed the CMB produces a nearly perfect blackbody spectrum with a temperature of $2.725 \text{ K} \pm 0.002 \text{ K}$ (Fixsen et al., 1996).

size. As inflation occurred these fluctuations were imprinted onto the Universe and stretched with the exponential expansion. After this expansion, regions in the Universe had differing density values, causing areas of higher and lower density to occur which started the process of forming the structure observed throughout the Universe (Coil, 2013). Regions of varying density can be observed from sky maps produced from experiments like the map shown in Figure 1.3, with the red regions corresponding to areas of higher density compared to the blue regions which show lower density. The predicted scalar perturbations have been successfully measured by experiments such as WMAP (Hinshaw et al., 2009), Planck (Collaboration et al., 2020), ACT (Qu et al., 2023) and SPT (Pan et al., 2023).

In the early Universe, vacuum quantum fluctuations arose as inflation occurred, causing fluctuations in the gravity which in turn gave rise to tensor perturbations (Bonga et al., 2017). *B*-mode components only arise from tensor perturbations in the early Universe and from gravitational lensing caused by the gravitational potential deflecting *E*-mode components into *B*-mode components. *B*-modes in general are characteristically different in form and substantially weaker than *E*-modes in the CMB polarisation, which are in turn even smaller than the temperature amplitude, see Figure 1.4.

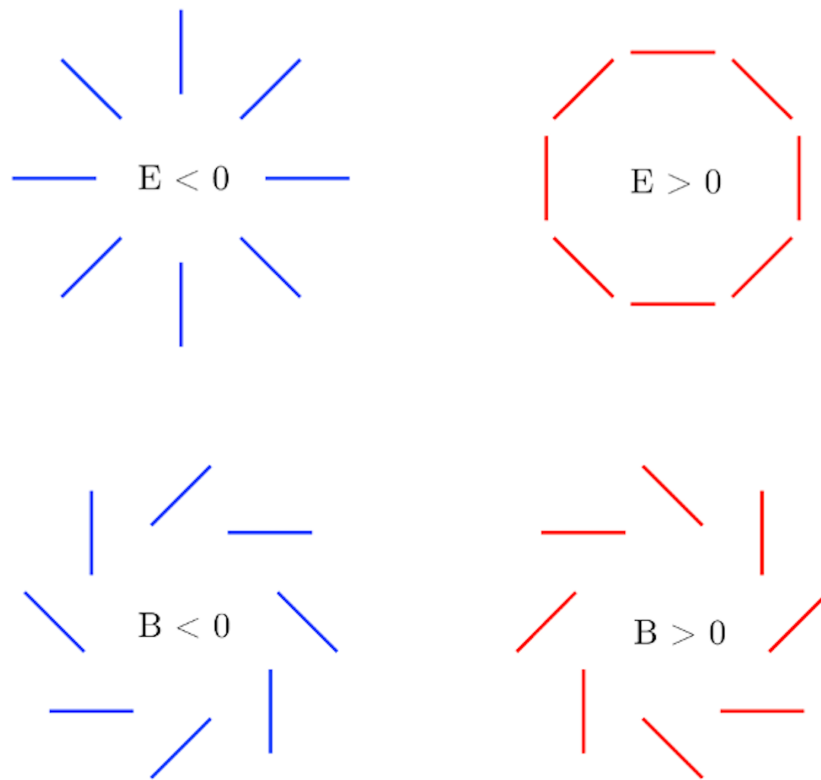


Figure 1.2 – Examples of simplistic E - and B -mode patterns that can be observed in polarisation maps of the CMB (Incardona, 2020). The E -mode patterns are even parity resulting in the patterns being symmetrical, while the B -mode patterns are odd parity which results in the patterns being unsymmetrical.

Over the decades of CMB measurements, many temperature and E -mode measurements have been conducted which have enabled precise measurements of their amplitudes. However, there is currently a strong focus on pushing down the upper limits of the B -mode signals and measuring the primordial B -mode signal. This latter signal is the subject of such attention because it is widely considered the ‘smoking gun’ that will prove inflation (Bahr-Kalus et al., 2023).

Inflation also provides solutions to problems associated with the hot Big Bang expansion model, such as the horizon, flatness and monopole problems. The horizon problem arises from the CMB radiation being isotropic, however, this indicates that points in the sky were casually connected in the past before the Last Scattering Surface (LSS) (Clesse, 2015). Inflation offers a solution to this by introducing a burst of exponential expansion meaning regions were closer together prior to the expansion and in casual contact, thus, able to obtain a uniform temperature. The flatness problem describes the curvature of space. It posits that measurements indicate that the Universe is flat (Stuart, 2022), however, with the standard Big Bang model the Universe should not have expanded enough for measurements to indicate the Universe is flat. Again, inflation

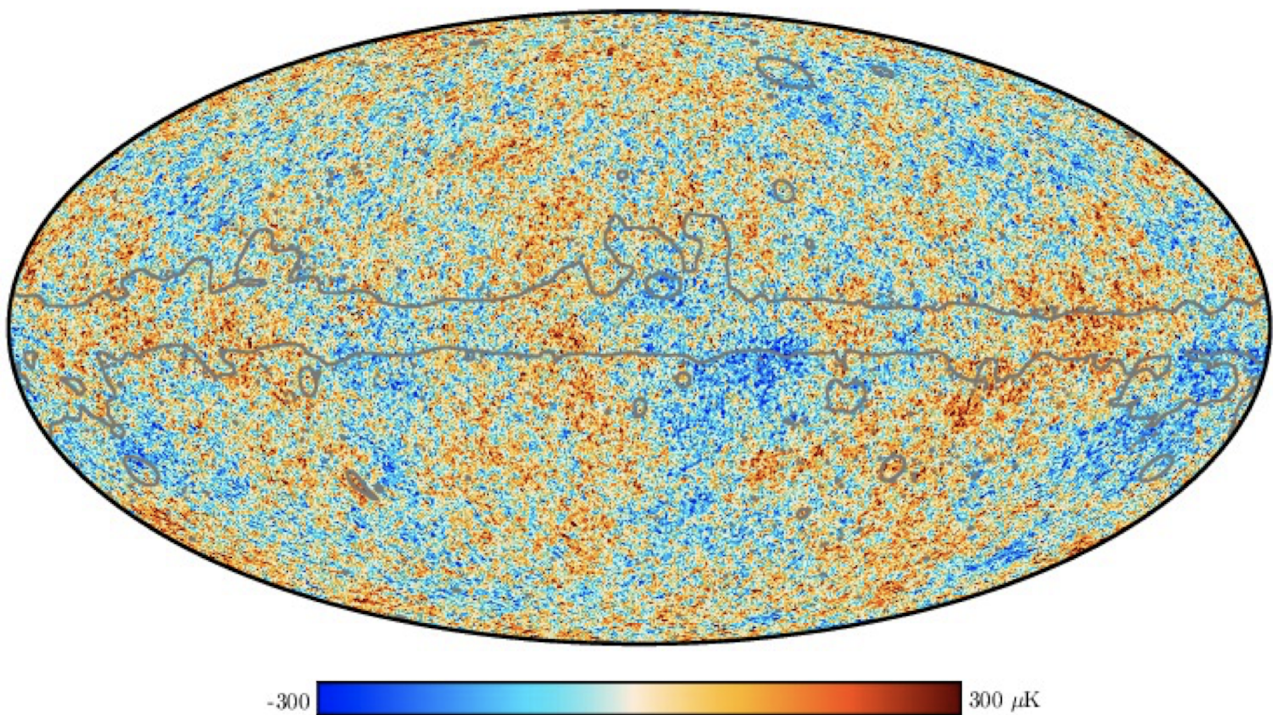


Figure 1.3 – Planck 2018 full sky temperature map (Collaboration et al., 2020). Red areas correspond to areas of higher density while the blue areas correspond to areas of lower density. The grey lines represents the mask of the Galactic plane, which was applied and inpainted.

resolves this by assuming that it would stretch any initial curvature to near flatness (Stuart, 2022). Finally, the monopole problem assumes that, if the Big Bang theory is correct, there should be an abundant amount of magnetic monopoles present in the Universe. However, these have never been detected. Once again, inflation offers a solution here by allowing these magnetic monopoles to exist prior to the rapid expansion before inflation forced them to move away from each other. This, in turn, would cause the number in observable regions to be very low and explain the difficulty in detection.

1.1.1 The search for the primordial B -mode signal

Inflation predicts the existence of a background of primordial gravitational waves (PGWs), the magnitude of which is used to measure the tensor-to-scalar ratio, r (Tristram et al., 2022). Depending on the inflation model the predicted value of r varies and therefore measuring this value can rule out certain inflation models. If the PGWs existed they would have left a signal in the B -mode pattern, known as primordial B -modes (Sheere et al., 2017). Therefore, through searching for the B -mode signal it can also serve as a probe for PGWs. However, these primordial B -modes, as of yet, have still not been measured. Experiments, such as the BICEP/Keck Array (BICEP/Keck Collaboration et al., 2021), have been able to place upper limits on the amplitude of

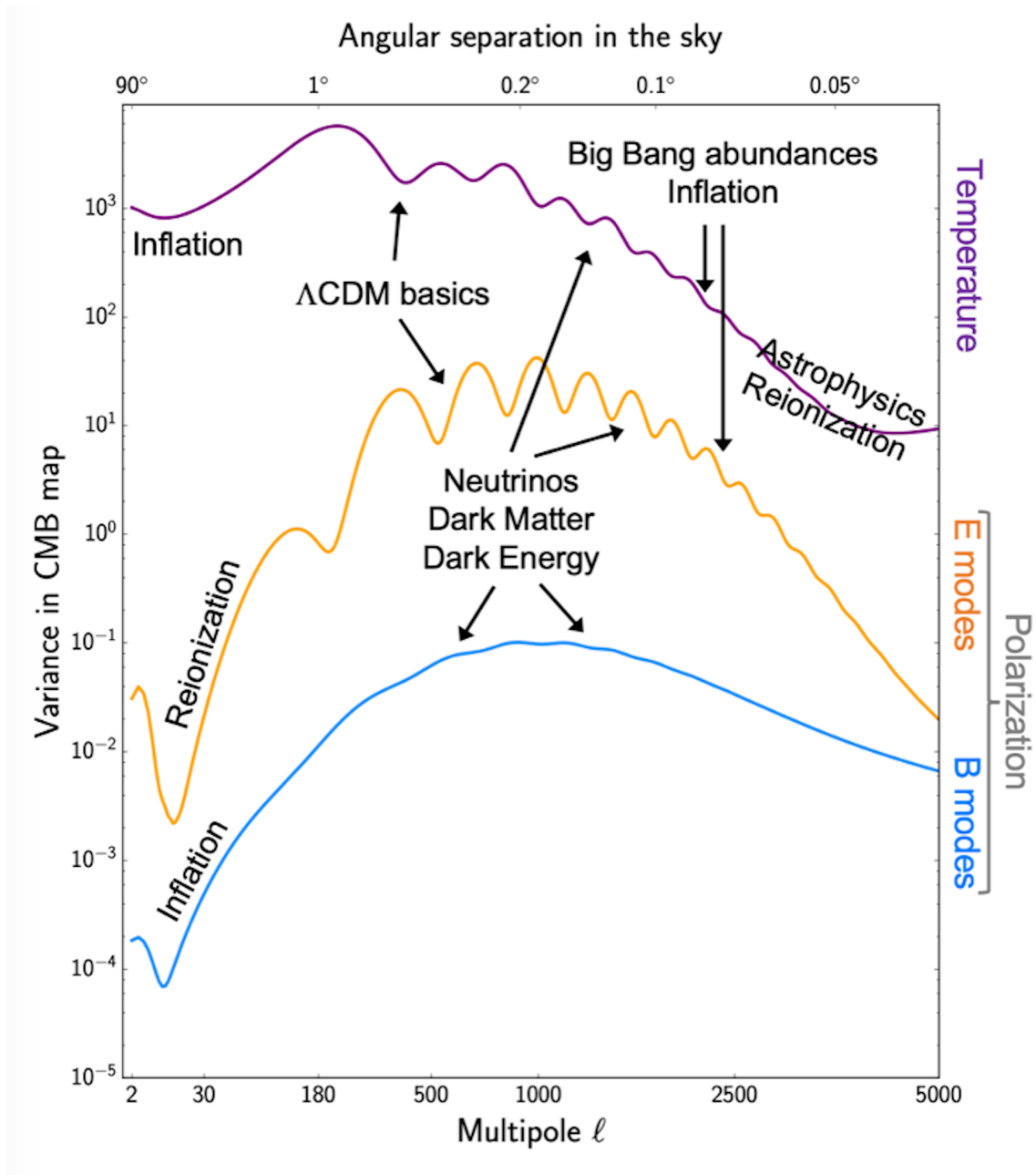


Figure 1.4 – Power spectra for the fluctuations in the temperature and polarisation signals in the CMB. Within both the temperature and polarisation signals of the CMB there are small fluctuations in their values, known as anisotropies. The anisotropies arise from scalar and tensor perturbations in the early Universe and from scattering during the reionisation epoch and gravitational lensing. The temperature anisotropies are at a level of $\sim 10^{-5}$ K (Hu & Dodelson, 2002), the *E*-mode anisotropies are at a level of $\sim 10^{-6}$ K (Durrer, 2015) and the *B*-mode anisotropies are at a level of $\sim 10^{-7}$ K (Durrer, 2015). Measurements of the anisotropies' statistical properties provide many insights into the early Universe, the contents of the Universe from the cosmological parameters and the large-scale structure. Image credit: Calabrese (2020).

the primordial B -mode signal and their results are presented in Figure 1.5.

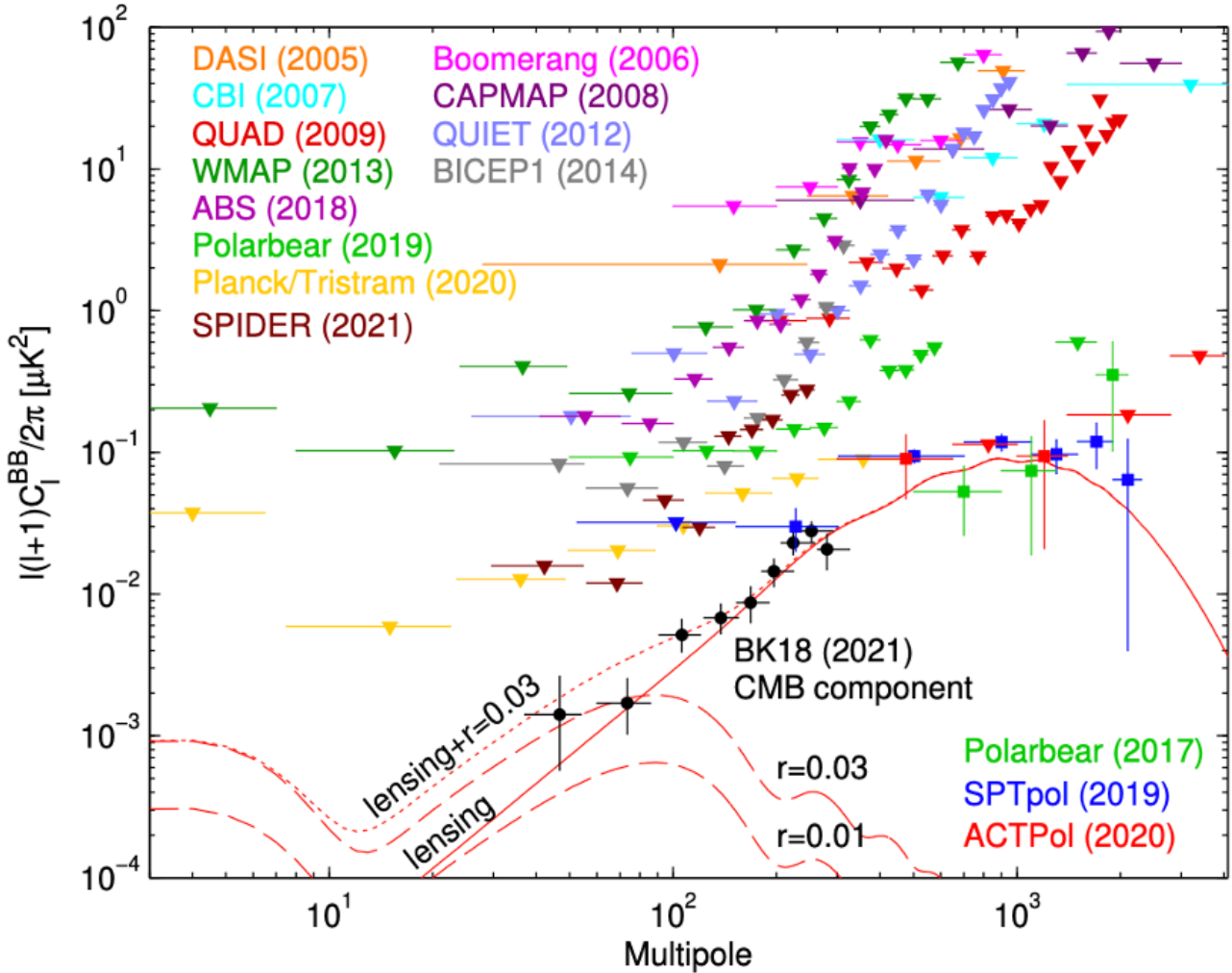


Figure 1.5 – Several CMB B -mode polarisation experiments with their corresponding measurements, producing either upper limits or detections. Included on this plot is the theoretical model for B -mode lensing (solid red line) and the theoretical model for gravitational wave B -modes (dashed red lines) for two values of r (BICEP/Keck Collaboration et al., 2021)

Galactic foregrounds can obscure the detection of primordial B -modes (Hervías-Caimapo et al., 2022). From the published results using the data from the BICEP2 (Ogburn Iv et al., 2010) (a telescope located in the South Pole) analysis, and Planck (Collaboration et al., 2020) (a space-based telescope) data in 2014 (Ade et al., 2014), it showed that at high microwave frequencies the thermal emission from dust in our galaxy dominates the B -mode signals. Galactic polarised synchrotron radiation has also been shown, from previous studies (La Porta et al., 2008), to dominate the B -mode signals at low frequencies. Therefore, in order to measure the primordial B -mode signal multi-frequency measurements are necessary to account for the foreground contribution.

Two theoretical models for the primordial B -mode component are presented in Figure 1.5.

These indicate that we would expect the signal to produce a bump in its power spectrum at a multipole of ~ 3 and ~ 100 , with multipole moments being the reciprocal of angular scale. However, depending on the value of r the amplitude of these bumps vary. From this Figure, the peak modelled at a multipole of ~ 100 is difficult to measure due to the power spectrum produced by the gravitational lensing component of the B -mode signal. This lensing B -mode component arises from the polarised CMB photons being deflected while they've travelled through the Universe due to gravitational lensing (Hanson et al., 2013), transforming part of the E -modes into B -modes, in what will be called "lensing B -modes". A theoretical model presented in Figure 1.5 identifies the amplitude of the power spectrum produced by this component can be larger in amplitude than the primordial B -mode component at multipoles ≥ 100 depending on the value of r . The values presented in Figure 1.5 are $r=0.03$ and $r=0.01$ both of which produce lower amplitudes at multipoles ≥ 100 when compared to the lensing power spectrum.

Therefore, the total B -mode power spectrum is the combination of primordial B -modes and lensing B -modes. Constraining r from B -mode measurements can discriminate between inflation models (Dodelson et al. (1997), Bhattacharya et al. (2022)) therefore it is important that both components of the B -mode power spectrum are measured to better our understanding of inflation. Lensing B -modes have been measured at small angular scales (large multipoles) (Hanson et al. (2013), Pan et al. (2023), Collaboration et al. (2014)). Measuring the degree-scale (low multipoles) B -mode polarisation emerges as the next step in B -mode searches. This thesis will therefore focus predominately on the primordial B -mode component.

1.2 B -MODE EXPERIMENTS

Over the last 20 years several CMB experiments have been undertaken, the results of which are the measurements obtained from polarisation sensitive CMB experiments and are displayed in Figure 1.5. The results come from a range of balloon-based, ground-based and space-based experiments which span from multipole moments of 2 – 2500.

Balloon-based B -mode experiments launch instruments into the stratosphere at altitudes of ~ 40 km above sea-level and provide flight durations of ~ 2 months (Masi et al., 2019). By flying at stratospheric levels, the balloons are able to access more of the atmospheric window which is otherwise less transmissive at ground levels allowing for higher frequencies (≥ 330 GHz) to be better measured, thereby enabling better measurements of the thermal dust which would otherwise contaminate CMB measurements (Masi et al., 2019).

These types of experiments are excellent precursors for both ground-based and space-based telescopes. The total cost of balloon-based experiments is approximately ten times cheaper than ground-based experiments and approximately hundred times cheaper than space-based experiments. They also allow technologies to be tested and quality assured before being sent

into space. The instruments can be recovered after the flights allowing for maintenance on the instrument to be carried out. However, balloon-based CMB experiments required certain criteria to be met before they are able to fly, such as the time of year and weather conditions. If these are not met by the time of the scheduled launch it can cause long delays, which sometimes result in year long delays. Examples of previous *B-mode* balloon experiments include MAXIPOL (Hanany, Collins, Johnson, Lee & Tran, Hanany et al.), SPIDER (Gualtieri et al., 2018) and EBEX (The EBEX Collaboration et al., 2018).

Ground-based *B-mode* experiments have been deployed primarily to the South Pole, Antarctica or the Atacama Desert, Chile due to the requirements to either observe the same small patch of sky for long periods of time or observing large patches of the sky. As the South Pole's view of the sky changes very little during the year this site is ideal for performing ultra-deep surveys, whereas the Atacama Desert is well suited for collecting data from very large areas of the sky. Ground-based experiments are easier to maintain due to the easier access to the sites allowing for longer experimental runs and typically these experiments have observation runs spanning multiple years. They also provide a good test for new technologies and can have larger optical designs because they are not limited by weight which constrains balloon- and space-based experiments.

A limitation with ground-based experiments is that they are limited by the atmospheric window on Earth. The Earth's atmosphere restricts the radiation at certain frequencies from reaching the Earth's surface. The South Pole and Atacama Desert have similar atmospheric windows, as indicated by Figure 1.6. Windows in the mm-region of the atmospheric transmission are targeted for ground-based CMB experiments to measure its signals. These windows are seen in Figure 1.6 and are selected to miss the frequency regions that are opaque to transmission (where the transmission is zero). Previous ground-based experiments for the *B-mode* searches includes POLARBEAR (Matsuda et al., 2019) and BICEP2/Keck Array (BICEP/Keck Collaboration et al., 2021).

Space-based experiments can map the entire sky resulting in their ability to measure signals at multipole moments of $\ell \geq 2$ and as the instrument observes in space they are not limited by the Earth's atmosphere. However, space-based missions are limited in the size and the weight of their instruments resulting in their designs needing to be stringent and rigorous. Experiments in space are hugely expensive with their costs often totalling around \$1billion (Stahl, 2018). On top of this, once a space-borne experiment is launched maintenance becomes very challenging without resorting to bringing the instrument back to Earth, adding yet more cost to the project.

With the focus on measuring the fainter *B-modes* amplitudes as seen in Figures 1.4 and 1.5 a better understanding of systematic effects arising from the instruments themselves and how to mitigate their effects is currently being undertaken (Duivenvoorden et al. (2021), Giardiello et al. (2022), Monelli et al. (2023)). This understanding comes from modelling and simulations of the instrument's performance and also from laboratory tests and observing how the instruments

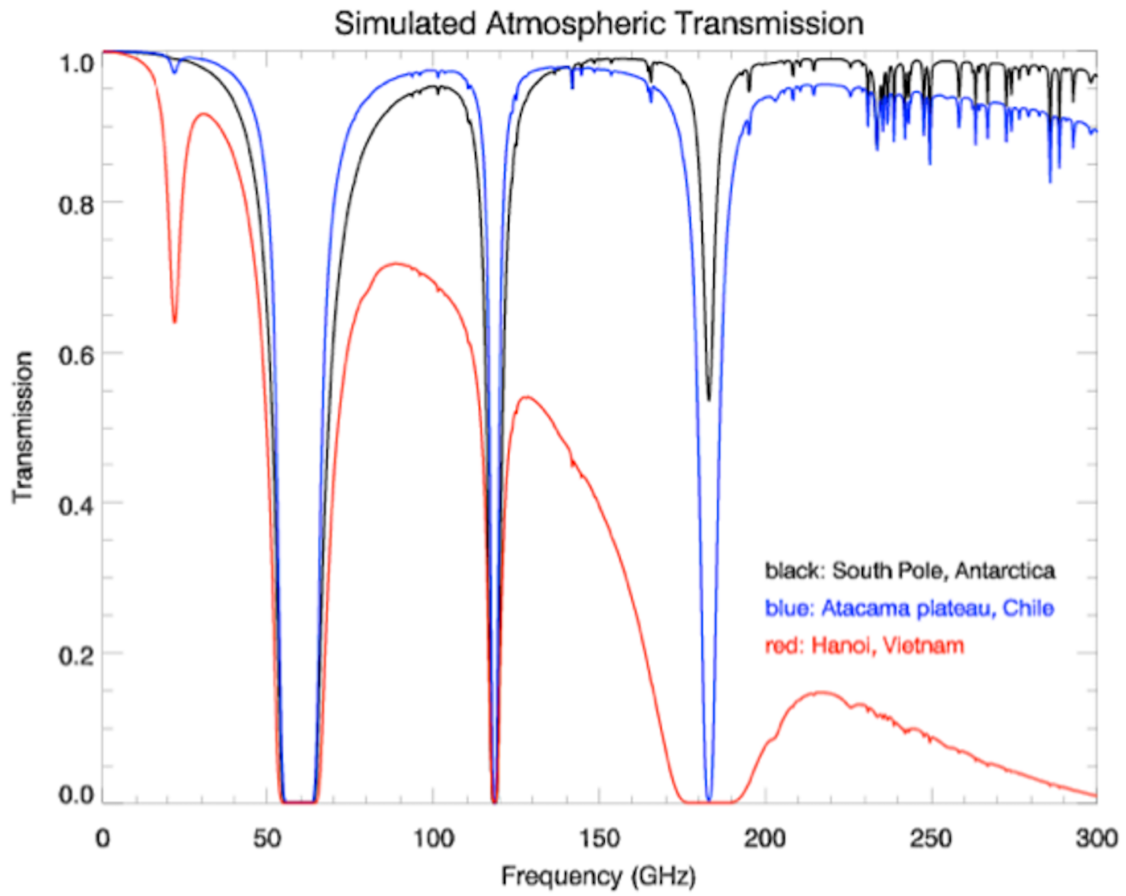


Figure 1.6 – Simulated atmospheric transmission windows for the South Pole (black line), the Atacama plateau (blue line) and Hanoi Vietnam (red line). The least transmission through the atmosphere is simulated at Hanoi which is only 20 m above sea level. Both the Atacama plateau and the South Pole have similar transmission profiles with both being roughly 2500 m above sea level. There are three windows within the blue and black transmission profiles where transmission through the atmosphere is completely blocked. These frequencies can therefore not be measured at these locations (Kovac & Barkats, 2007).

perform in situ. The improvements to instrument design over the years can be seen in Figure 1.5 where the amplitude of the B -mode power spectrum has improved from initial measurements of $\sim 10^0 \mu\text{K}^2$ to $\sim 10^{-3} \mu\text{K}^2$ at $\ell < 10^2$.

The latest results from BICEP2/Keck Array (black dots in Figure 1.5) which targeted the large-scale B -mode signal produced an upper limit of $r < 0.035$ (BICEP/Keck Collaboration et al., 2021). This experiment probes the CMB at large angular scales and is a combination of a 0.26 m telescope and five BICEP2-style receivers in a single telescope mount (five 0.26 m receivers) located in the South Pole, and mainly observes the CMB to measure the primordial B -mode signal.

It is important to note that measurements at small or large angular scales require different telescope designs to be able to access the range in signals. CMB experiments dedicated to small angular scales require large aperture telescopes to be able to have a high enough spatial resolution

to define small angular features present in signals. For example, the South Pole Telescope (SPT) (Carlstrom et al., 2011) is a 10m telescope which was designed to measure the CMB at small angular scales enabling it to measure the lensing B -modes. The SPT is also used to delens the measurements obtained from BICEP2/Keck Array, this is due to the telescope being in the same location and probing the CMB signal at the lensing B -mode scales. This is an important step when measuring for the primordial signals as seen in Figure 1.5 the theoretical model for lensing B -modes peaks at larger values compared to primordial B -modes at larger angular scales. Removing the lensing part enables experiments to probe at smaller amplitudes and target the models shown on Figure 1.5.

To reach the low power levels of the primordial B -mode signal, CMB experiments have utilised a polarisation modulator. Balloon- and ground-based experiments such as EBEX (The EBEX Collaboration et al., 2018) and POLARBEAR (Hill et al., 2020) have used HWPs to modulate the linear polarisation of the CMB to frequencies away from unpolarised signals and $1/f$ noise caused by the atmosphere which would otherwise obscure the faint B -mode signal. This modulation allows experiments to extract the faint primordial B -mode signals to levels such as those seen in Figure 1.5.

Future experiments are expected to improve further on the results seen in Figure 1.5. CMB-S4 (Abazajian et al., 2022), a ground-based experiment, is set to deploy twelve telescopes across both the Atacama Desert and South Pole sites. These telescopes will include nine small aperture telescopes (SATs) and three large aperture telescopes (LATs) allowing the experiment to measure the CMB over a large range of angular scales and deploy hundreds of thousands of detectors to reach greater sensitivities. LiteBIRD (Collaboration et al., 2023) is a space-based telescope that is dedicated to measuring the primordial B -mode signal at large angular scales. It will deploy three polarisation sensitive telescopes installed in the satellite and observe the entire sky for three years across fifteen frequency bands, enabling it to distinguish between CMB signals and Galactic foreground signals. Another ground-based experiment, the Simons Observatory (SO), will deploy three SATs aiming to measure the primordial B -mode signal at large angular scales. All three SATs will be using an HWP to detect this faint signal, and as such the SO is a key experiment to this thesis.

1.3 THE SIMONS OBSERVATORY

The SO is a new ground-based CMB which will achieve first light during 2024 and is already located in the Atacama Desert. It's site in the Atacama Desert, with a dry and clear climate, is at an altitude of 5,200 m above sea level ensuring only low levels of water vapour and cloud impact its measurements.

To achieve the SO's goals a set of telescopes has been built using two distinct designs

(Collaboration et al. (2019), Galitzki et al. (2018)). There will be one 6 m LAT (Xu et al., 2021) and six 0.5 m SATs (Ali et al., 2020) and Figure 1.7 shows the area of the sky each type of telescope will be observing. This LAT will provide high angular resolution to arcminute levels thanks to the size of the first mirror to target a range of scientific goals, such as constraining cosmological models and cataloguing high redshift clusters via the Sunyaev-Zeldovich effect.

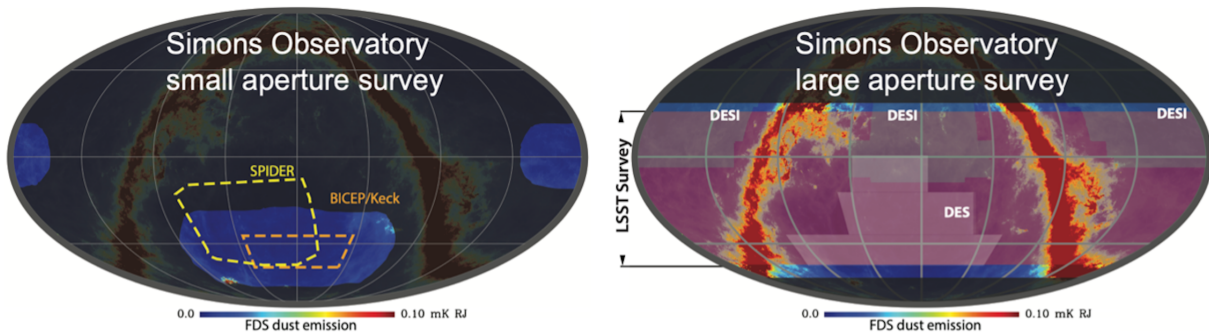


Figure 1.7 – Maps of the proposed sky surveys for both the small aperture telescopes and large aperture telescope being launched by SO. The SATs will observe 10% of the sky whilst the LAT will observe over 40% of the sky. Included are other surveys which probe similar patches in the sky and have similar scientific goals, such as BICEP/Keck and SPIDER whose sky patches overlap the SATs very well and also targeted the primordial B -mode signal (Ade et al., 2019).

Another key goal of the SO programme is to improve the constraints on the amplitude of the hypothesised primordial gravitational waves produced in the early Universe. This will be achieved by making precise measurements of the polarisation signals in the CMB, using many detector arrays for high sensitivity and by employing the set of SATs designed to provide a large FoV.

With this combination of telescopes, they will be able to probe the Universe at both small and large angular scales, providing measurements between 1 arcminute to tens of degrees. They will observe at six frequency bands ranging over 27-285 GHz by dividing the detectors into three dichroic bands; low-frequency (LF), mid-frequency (MF) and ultra-high frequency (UHF). Measuring over a wide range of frequencies will allow the removal of Galactic foregrounds, such as Galactic synchrotron radiation and Galactic thermal dust.

1.3.1 Large Aperture Telescope

The LAT and its receiver (LATR) are currently being deployed in the Atacama Desert with the aim to achieve first light in the early part of 2024. The structure of the LAT presented in Figure 1.8, includes a 6 m primary aperture and two 6 m mirrors. The two-mirror design coupled to the receiver creates a crossed-Dragone telescope. The LATR FoV will be 7.8° .

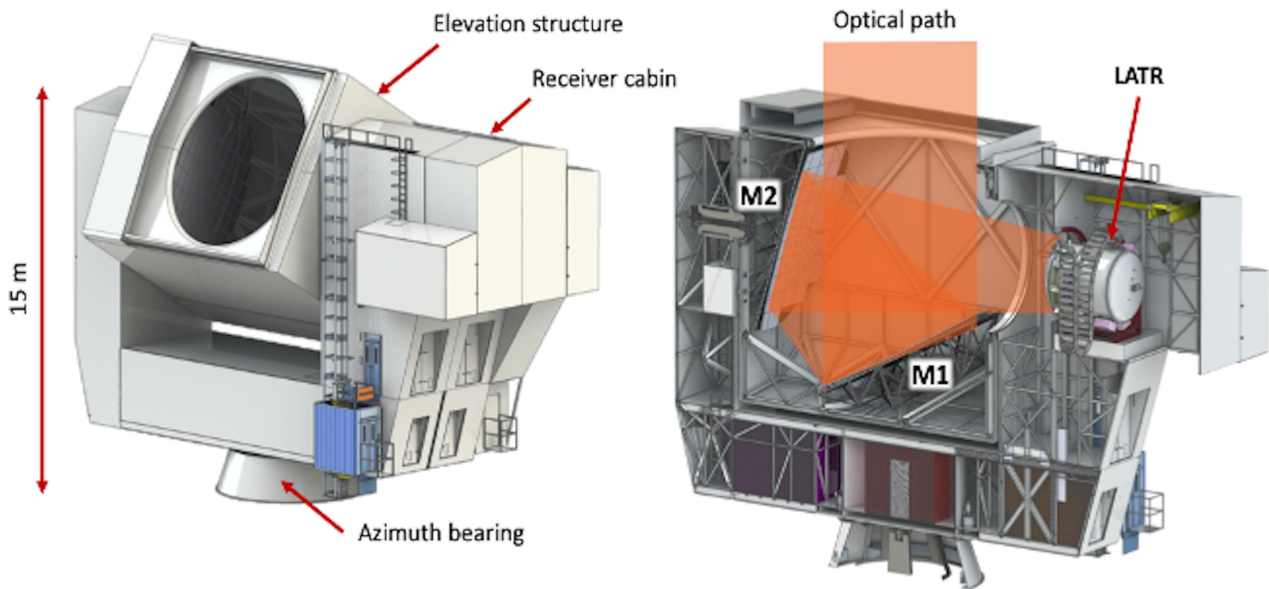


Figure 1.8 – Cross-sectional view of the LAT (Galitzki et al., 2018). Right hand panel shows the first mirror (M1) which will be parabolic and the secondary mirror (M2) which will be a large concave. The first mirror is off-axis meaning the incoming light won't be interfered with by the reflected light off the secondary mirror. The mirrors are also under illuminated and at millimetre and sub-infrared wavelengths this greatly reduces the systematic affects due to diffraction.

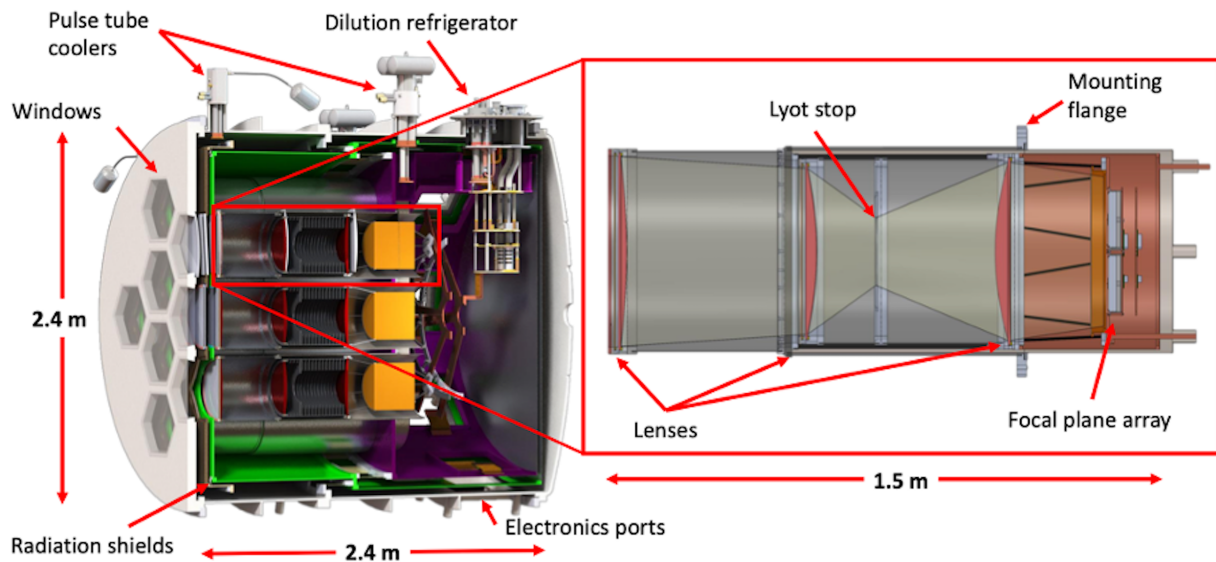


Figure 1.9 – Cross sectional view of the LATR (Galitzki et al., 2018). A more detailed view of an optics tube has also been presented showing the three silicon lens positions which diverge the beam towards the focal plane array.

The LATR will have an overall aperture of 2.4 m with a total of thirteen optics tubes fully operational by the end of 2026. Initially, seven optics tubes will be deployed and operational in 2024. These optics tubes are 40 cm in diameter, comprise of one LF tube centred on 27/39 GHz, four MF tubes centred on 93/145 GHz and two UHF tubes centred on 225/280 GHz (Collaboration et al., 2019). Each optics tube follows the same design (Figure 1.9), which is a refractive system that uses three silicon lenses to condense the desired frequencies towards the focal plane array. Each tube has six temperature stages 300 K, 80 K, 40 K, 4 K, 1 K and 100 mK which is achieved through using both pulse tube coolers (PTC) and Bluefors dilution refrigerators.

The LATR will be able to measure both temperature and polarisation signals within the CMB through the use of its polarised dichroic pixel design. To measure the six frequency bands two types of detector arrays will be deployed. The LF bands will deploy sinuous antennas with lenslets coupled to transition edge sensor (TES) bolometers, this design is based on the one used in POLARBEAR-2 (Westbrook et al., 2018). The second design is used for the MF and UHF optic tubes and is based on the design used for the Atacama Cosmology Telescope (ACT) experiment (Swetz et al., 2011). For this, orthomode transducers fed by monolithic feedhorns are coupled to TES bolometers (Kiuchi et al., 2020). The LF optics tube will have 111 pixels coupled to 444 TESs, the MF and UHF optic tubes will field 1,290 pixels coupled to 5,160 TESs. When all thirteen optic tubes have been deployed, ~60,000 Aluminium-Manganese (AlMn) TES bolometer detectors will be operational, an order of magnitude larger than any telescope previously deployed.

1.3.2 Small Telescope Telescope

SO are currently installing three SATs on site in Chile and aimed to achieve first light in late 2023. Of the SATs being deployed two are MF and one is UHF, with a further three being deployed from 2025, where two will measure the MF bands and one will measure the LF bands. The optical design of each SAT provides a FoV of 35°. The purpose of these telescopes is to focus solely on detecting and measuring the primordial B -mode signal at large angular scales to characterise r to a level of $\sigma(r) \approx 0.002$.

The SATs being deployed are 0.5 m aperture refractive systems and the design of the SATs optics tube (Figure 1.10) follows a similar design to the optics tubes for the LATR. It uses five cryogenic stages; 300 K, 40 K, 4 K, 1 K and 100 mK. At each stage a combination of Cardiff metal-mesh filters (Ade et al. (2006), Pisano et al. (2015)) and/or alumina absorbers are employed to reduce the photon heat-load and sequentially block higher frequency radiation.

Each SAT modulates the CMB polarised signal using a cryogenically rotating HWP located at the 40 K stage. The rotation mechanism is the same design as that deployed in POLARBEAR-2 (Hill et al., 2020). The cold optics assembly is located at the 1 K stage and comprises of a three silicon lens refractive system that focuses the photons towards the focal plane array, located at

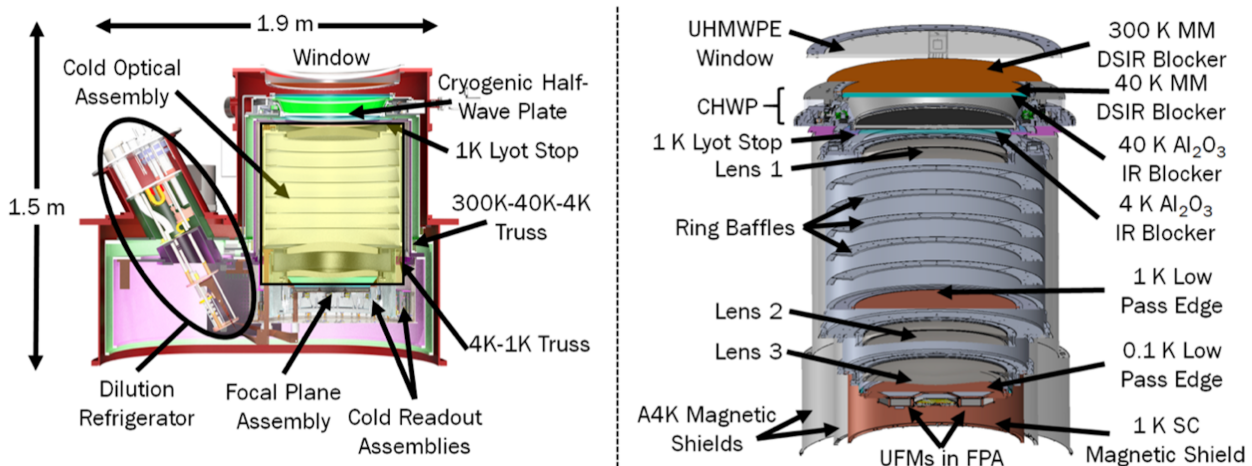


Figure 1.10 – Schematics of the SAT design (Ali et al., 2020). The SAT is a three lens refractive system which focuses the light onto a focal plane array which operates at 100 mK. There are five cryogenic stages in total with the SAT, 300 K, 40 K, 4 K, 1 K and 100 mK. These stages are cooled using a pulse tube cooler and a dilution refrigerator. Each SAT being deployed will also include a continuously rotating HWP which will be held in the 40K stage and acts as a polarisation modulator. This HWP is based on the design deployed in the POLARBEAR-2 instrument (Hill et al., 2020).

the 100 mK stage. The detectors used in both the LATR and SAT are superconducting with a critical temperature of 160 mK the critical temperature being that at which the material becomes superconducting. Being at a 100 mK stage allows them to operate comfortably below their critical temperature and thereby increase their overall functionality.

Each SAT currently being deployed will deploy seven detector modules with the total number of pixels across the two MF SATs being 5,750 pixels, resulting in 23,000 AIMn TES bolometer detectors. Whilst the UHF SAT will deploy 3,000 pixels with 12,000 AIMn TES bolometer detectors (Ali et al., 2020). As with the LATR, the MF and UHF will use orthomode transducers feeding monolithic feedhorns coupled to TES bolometers.

As noted above, two MF and one LF SATs will be deployed in 2025 as part of the SO:UK and SO:Japan projects. The LF SAT will target the synchrotron radiation while the UHF SAT will target the thermal dust emission to distinguish Galactic foregrounds from the polarised CMB signal. As previously discussed, these foregrounds can interfere with observations of the CMB signal. Synchrotron and thermal dust radiation have amplitudes larger than the polarised CMB signal as indicated in Figure 1.11. Characterising these foreground signals over the frequencies where they dominate will enable their removal from the measurements of the CMB polarisation and methods to remove these foregrounds have been established and carried out in previous studies (Nørgaard-Nielsen & Jørgensen (2008), Heurtel-Depeiges et al. (2023), de la Hoz et al. (2023)).

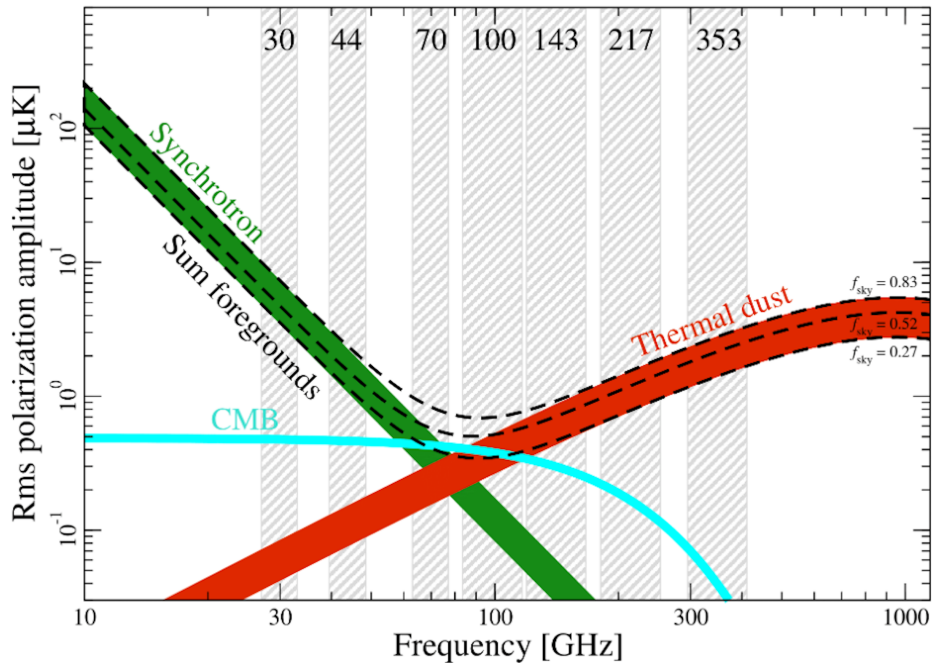


Figure 1.11 – The brightness rms of the Galactic foregrounds, synchrotron (green line) and thermal dust (red line) radiation, along with the polarised CMB radiation (cyan line) as a function of frequency, as observed by Planck (Collaboration et al., 2020).

The work carried out for this thesis focuses on characterisation of HWPs and propagating these results through to r measurements to identify any bias incurred on r arising from these devices.

Half Wave Plate

A wave plate is a device which alters the state of the polarisation traversing through it. For a HWP, as the polarised light wave propagates through the device, a phase difference of half a wave between two components of the polarised light is caused. This phase difference at the output of the device causes a rotation of the polarisation state by 2θ , where θ is the incident polarisation angle with respect to the predefined axes of the device. It is through manipulating this phenomenon that HWPs are used in CMB studies to modulate the linear polarisation to a desired frequency and this is discussed in more detail in Chapter 2.

Three of the SATs deployed at SO will use a HWP with a three plate Pancharatnam design, based on the HWP design developed for the POLARBEAR-2 instrument (Salatino et al. (2017), Hill et al. (2020), Kiuchi et al. (2020)). These HWPs are 0.5 m in diameter and made from sapphire, which is a birefringent material. While the SAT is operational the HWP will continuously rotate on superconducting magnetic bearings and the whole assembly is cooled to 50 K in order to minimise thermal emissions from the plate itself.

As with any optical element deployed in a telescope, it is important to spectrally characterise

the HWP before it is integrated within the telescope. The characterisation is best performed in a laboratory setup where correct optical configurations can be implemented and changes in external conditions, such as humidity, can be monitored.

To characterise a HWP the parameters of its Mueller matrix need to be calculated across the experimental working frequency bands. A Mueller matrix is a 4x4 matrix which describes the polarisation changing properties of the system being measured. The matrix parameters can change depending on the frequency being measured and the incident angle of the polarised light incident on the sample. Therefore, it is important to understand the optical setup the sample is placed in when calculating these parameters. This will be discussed in more detail in Chapters 2 and 3.

The SATs being deployed in 2026 plan to use an embedded metal mesh (EMM) style HWP instead of the Pancharatnam design noted above. The EMM HWPs have been used in sub-mm experiments before ([Pisano et al., 2022](#)) and have shown their capabilities as polarisation modulators. There are many benefits to using this type of HWP, for example, they weigh considerably less than their Pancharatnam counterparts and they do not exhibit as much in-band loss when operated at room temperatures. However, a full comparison between the two types of HWPs has never been performed before.

The focus of this thesis is to present the methods used to characterise HWPs, to fully spectrally characterise a HWP and to discuss the results, with a focus on future requirements for measurements when comparing the two types of HWP SO will use.

Therefore, within this thesis, Chapter 2 discusses the background theory supporting the use of a HWP, two types commonly used in sub-mm studies and how to obtain a Mueller matrix. Chapter 3 provides the method for injecting laboratory data into a full analysis pipeline to generate the measured Mueller matrix of a spectrally measured HWP. Chapters 4 and 5 present the laboratory measurements taken of a HWP on both a Vector Network Analyser (VNA) and Fourier Transform Spectrometer (FTS) respectively. These Chapters also present the Mueller matrix of the HWP measured on both systems, generated by the method described in Chapter 3. Chapter 6 provides a discussion of the results presented in the preceding two Chapters. It also identifies the differences between each system and their specific limitations. Finally, the Chapter discusses the characterisation of the EMM HWP and compares it to the Pancharatnam HWPs currently used in CMB studies.

HALF-WAVE PLATE BACKGROUND THEORY

"It is important to draw wisdom from different places. If you take it from only one place, it becomes rigid and stale."

Iroh, *Avatar: The Last Airbender*

Experiments such as SO which look to probe the polarised radiation of the CMB for the primordial component of the B -mode signal deploy polarisation modulators, such as HWPs, to modulate the signal away from astrophysical sources which would otherwise conceal the faint B -mode component. Current and future CMB experiments will also deploy these devices to enable detection of this elusive signal. However, as with any optical device inserted into the optical chain of an instrument, it can introduce systematics into the detected signal. Therefore, it is important to understand how a HWP operates and how one can characterise its performance to identify how it interacts with polarised signals to optimise detection.

This Chapter explores the background theory behind these devices, presents different types that have been used in experiments previously for example, NIKA2 (Pisano et al., 2022) and POLARBEAR (Hill et al., 2020) and introduces their characterisation parameters.

2.1 HALF WAVE PLATES (HWPS)

Wave plates are devices which alter the polarisation state of the incident light that propagate through them. Polarised light has an overall direction to its electric vector whilst travelling along the direction of propagation. The overall direction of the electric field dictates whether the polarised light is linear, circular or elliptical and a brief summary of each are detailed below.

Linearly polarised light arises when the electric vector is confined to a single plane along the direction of propagation, this could be vertical, horizontal or at $\pm 45^\circ$ to the direction of motion. Circular polarisation arises when the electric vector consists of two linear components with the

same amplitude but that are perpendicular to one another and have a phase difference of 90° (Toh et al., 2003). This is categorised into either left- or right-hand circularly polarised light depending on the rotation direction. Elliptical polarisation arises from the combination of two linear components that have different amplitudes and a phase difference that is not equal to 90° .

With this in mind, a wave plate works by decomposing the incident polarised light into two orthogonal polarisation components. One component propagates at a slower speed compared to its orthogonal component due to the material properties, causing a phase difference to occur. The components are then recombined at the output of the device and depending on the phase difference, the polarisation state of the incident light can change to produce either linear, circular or elliptical polarised light.

Common waveplates used in experiments are known as quarter wave plates (QWPs) and HWPs. These are designed to produce a phase difference of either a quarter or a half wave respectively. QWPs are used in experiments when circular polarised light is required to be measured because the phase difference of a quarter wave causes QWPs to convert linear polarised light into circular polarised light or vice versa enabling the signals to be measured. For a HWP due to their phase difference of half a wave they rotate linear polarised light into another state of linearly polarised light through rotating the incident polarisation angle by twice its value, as previously stated in Chapter 1.

The HWPs being deployed in SO are polarisation modulators and are continuously rotated, this continuous rotation allows the polarised light to be modulated to $4f$, f being the rotational frequency of the HWP. Signals detected at frequencies other than $4f$ will therefore be rejected in the demodulation process (Ade et al., 2009), this includes any systematic effects produced from components in the optical chain after the HWP. For example, intensity-to-polarisation leakage (I-to-P) arising from unpolarised signals being converted to polarised signals from the interactions with optical elements in the instrument.

Prior to being introduced to CMB instruments, HWPs have a history of being deployed in experiments at shorter wavelengths. At sub-mm wavelengths experiments (Pisano et al. (2022), Wilson et al. (2020)) have also been implementing HWPs into their instruments to measure polarisation signals. The main technology used for HWPs in mm-wavelengths is birefringent HWPs designed using the results discovered by Pancharatnam. However, there is an emerging technology used in sub-mm experiments that have shown good performance over the working frequency bands (Pisano et al. (2012), Maffei et al. (2012), Pisano et al. (2022)) known as embedded metal mesh HWPs.

2.1.1 Pancharatnam HWPs

In the 1950s Pancharatnam published a series of papers ([Pancharatnam \(1955a\)](#), [Pancharatnam \(1955b\)](#)) which the progression of polarised light through stacked birefringent materials, and determined the optimal rotated angle each layer needed to be placed at to produce the desired output. It was through varying these angles, the material properties and frequency being observed that the output Stokes vector (discussed later in this Chapter) could be changed by causing a certain phase delay in the polarised light propagating through the material.

These results were utilised to stack birefringent materials, an example shown in Figure 2.1, such as quartz and sapphire and produce an output phase shift of 180° thus creating a Pancharatnam-designed HWP. Having a phase shift of 180° enables linearly polarised light to be rotated by two times the input polarisation angle (relative to the axes of the device itself).

The simplest HWP consists of one birefringent plate. However, these devices only produce the 180° phase delay at a single frequency as a result of the refractive indices and thickness of the material used, see equations (2.1) and (2.2). Pancharatnam's results showed that multiple birefringent plates can be stacked on top of one another to broaden the frequency band a HWP can operate over. These HWPs have been used in previous CMB studies ([Hanany, Collins, Johnson, Lee & Tran \(Hanany et al.\)](#), [Essinger-Hileman et al. \(2016\)](#), [Gualtieri et al. \(2018\)](#), [The EBEX Collaboration et al. \(2018\)](#), [Hill et al. \(2020\)](#)) and have been produced in the configuration of 1, 3 or 5 plate devices as seen in Figure 2.1.

Sapphire has a crystalline structure and is a uniaxial material, see Figure 2.2, which in a 3D cartesian coordinate system (x, y, z) the refractive index varies along one axis. For example, the y -axis, will differ in its refractive index when compared to the x - and z - axes. The x - and y - axes are referred to as either the extraordinary (slow) axis and the ordinary (fast) axis, assuming the radiation is propagating along the z -axis. Typically, the plate is cut so the direction of propagation is perpendicular to the extraordinary axis which is the axis with the larger refractive index.

As an example, if the direction of propagation is taken to be along the z -axis, when a linearly polarised state of light strikes the surface of the plate it can be decomposed into two components along the x and y axes. As the wave traverses the length of the material one component will have a lower velocity to the other component due to the difference in refractive indices between the ordinary and extraordinary axes. The optical path difference (OPD) between the two wave components is given by

$$\Delta = d(n_e - n_o) \quad (2.1)$$

where d is the thickness of the material and n_e and n_o are the refractive indices of the extraordinary and ordinary waves respectively. This in turn produces a phase delay of

$$\delta = \frac{2\pi}{\lambda_0} \Delta \quad (2.2)$$

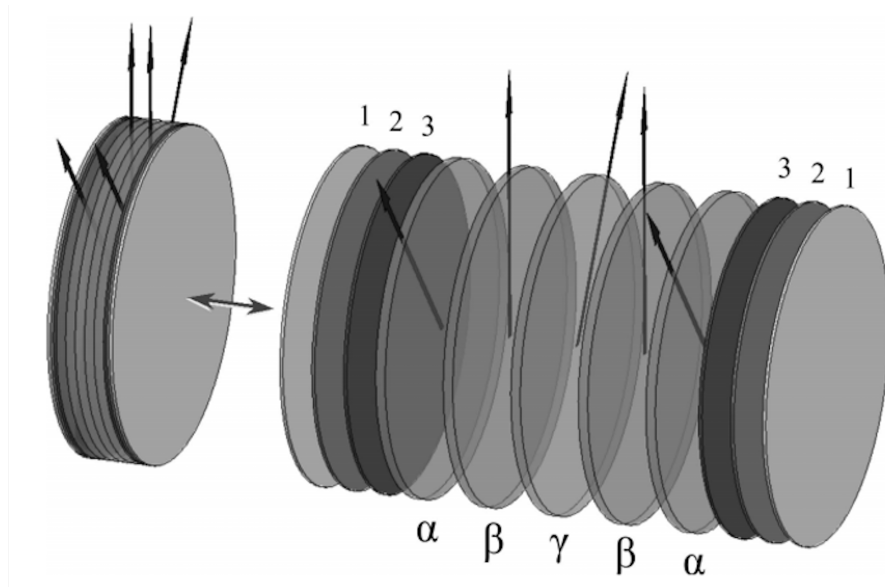


Figure 2.1 – Schematic of the HWP for the QUaD experiment (Savini et al., 2006). This is a 5-plate Pancharatnam-designed HWP (denoted by α , β and γ which represent the angle each plate is rotated by with respect to the extraordinary axis of the previous plate) and has a 3-layer anti-reflection coating (ARC), each layer is represented by the numbers 1, 2 and 3 in the diagram. This ARC was decided on to minimise the reflections caused by the large refractive index of sapphire.

where λ_0 is the vacuum wavelength. This phase delay causes the polarisation state to rotate and the value of phase difference between the two components can be changed by varying three parameters; the difference in the refractive indices for the two axes, the thickness of the plate and the wavelength of the input light. These parameters can be seen in equations (2.1) and (2.2). HWPs are tuned to produce an OPD of half a wavelength, therefore producing a phase delay of 180° (π), which is seen from substituting $\Delta = \lambda_0/2$ into equation (2.2).

Sapphire is a more prominent material for HWPs in the FIR/sub-mm frequency range because of its naturally high level of birefringence. The refractive indices of the extraordinary axis and ordinary axis is 3.39 and 3.06 respectively (Savini et al., 2006). Other crystal materials, such as calcite, typically do not have as large of a difference in refractive indices, with the ordinary and extraordinary refractive indices being 1.66 and 1.49 respectively. From equations (2.1) and (2.2) a larger difference in refractive indices means the thickness of the plates can be smaller to produce a half wave phase difference. However, this larger refractive index creates a strong mismatch with plane waves propagating in free space, resulting in high reflection coefficients and the need for anti-reflection coatings (ARCs).

Therefore, issues facing the use of sapphire HWPs include the size limitations as well as the ease of adding ARCs due to the problem of delamination of the ARC when devices are subjected to repeated cryogenic cooling cycles. It is difficult to obtain sapphire plates with diameters $>0.5\text{m}$

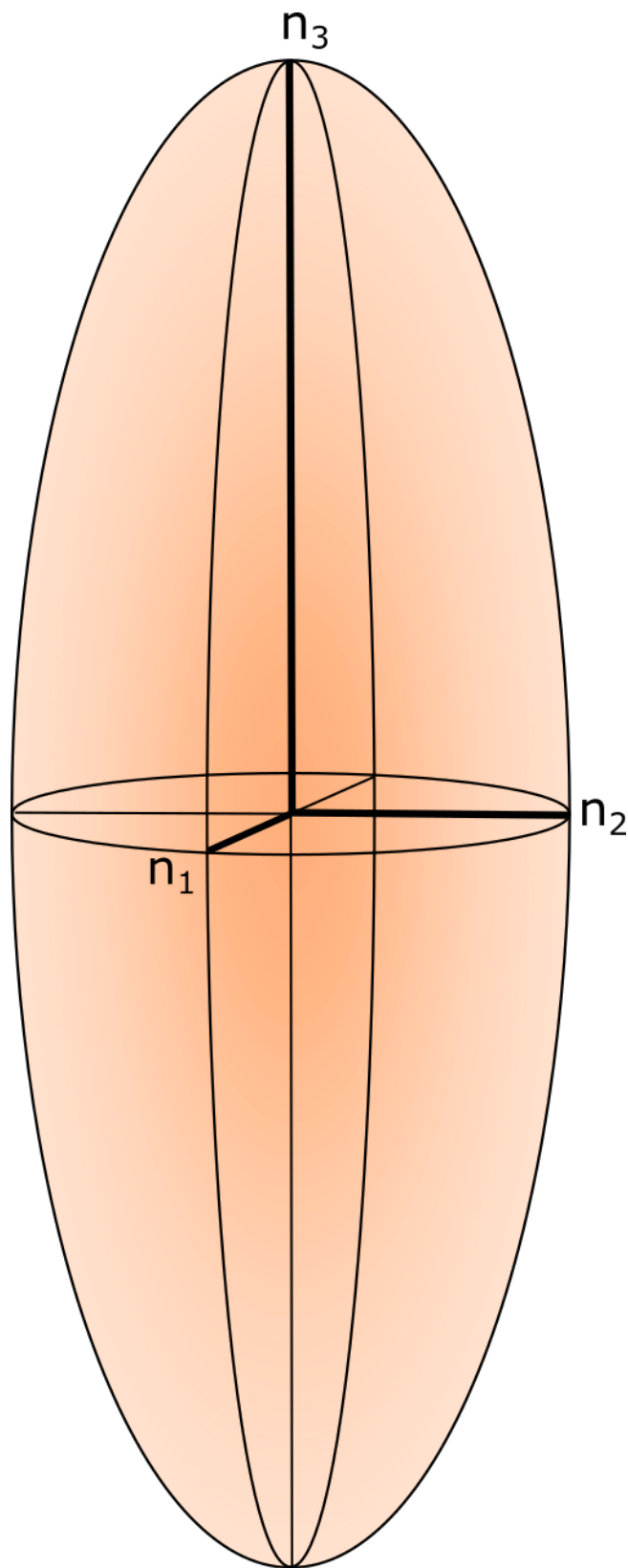


Figure 2.2 – Schematic of a uniaxial material. In a 3D setup, two axes have the same refractive index (denoted by n_1) whilst one axis has a different refractive index (denoted by n_3).

which as the number of detectors increase further, causing focal plane sizes to increase, will prove to be an issue with future experiments. Additionally, stacking multiple plates of sapphire causes the weight of these devices to become heavy and for future space-based CMB experiments this poses a problem.

However, as mentioned above other HWP technologies are coming to the fore as viable replacements for the current sapphire ones in refractive systems.

2.1.2 Embedded Metal Mesh HWPs

Embedded metal mesh (EMM) HWPs have shown, through modelling, simulations ([Pisano et al. \(2012\)](#), [Maffei et al. \(2012\)](#)) and their use in current experiments ([Wilson et al. \(2020\)](#), [Pisano et al. \(2022\)](#)), that they can perform to the same standard as their birefringent crystalline structured counterparts ([Zhang et al., 2011](#)).

An EMM HWP uses metal mesh technologies ([Ade et al., 2006](#)), incorporating capacitive and inductive metal mesh geometries each of which generates a phase shift with an opposite sign to one another. Using the results shown from Lerner ([Lerner, 1965](#)) and Shatrow ([Shatrow et al., 1995](#)), multiple metal mesh layers comprised of two types of patterns are used to tune the phase shift to the desired value which for a HWP is 180° . One pattern is continuous parallel metal lines which is orientated along one polarisation axis, see Figure 2.3. This pattern acts like an ideal inductive load for incident radiation which has its electric field parallel to the direction of the lines. The effective inductance of these wires depends on the width and spacing of the lines, and therefore the effective inductance can be altered through these parameters.

The second pattern is parallel metal lines with periodically spaced gaps. These are aligned along the other polarisation axis, orthogonal to the axis described above, see Figure 2.3. For incident radiation with the electric field parallel to the direction of these lines this pattern acts like a combination of an inductive and a capacitive load in series, of which the inductance and capacitance also depend on the geometry of the design.

These two patterns can also be used as anisotropic mesh filters ([Ade et al., 2006](#)) that interact differently with orthogonal polarisation, see Figures 2.5 and 2.6. One filter is a capacitive low-pass filter (LPF) and another filter is an inductive high-pass filter (HPF). These filters are orientated along orthogonal axes thus interact differently and separately with orthogonal polarisations. The LPF transmits signals at low frequencies whilst reflecting signals at frequencies higher than the cut-off frequency, which is the frequency at which diffraction occurs due to the design of the filter. The HPF transmits signals at high frequencies and reflects signals at frequencies below its cut-off frequency and each filter produces a phase shift in opposite directions to each other such that when combined it equals 180° . These two designs are then combined together to create a bandpass which the HWP operates over.

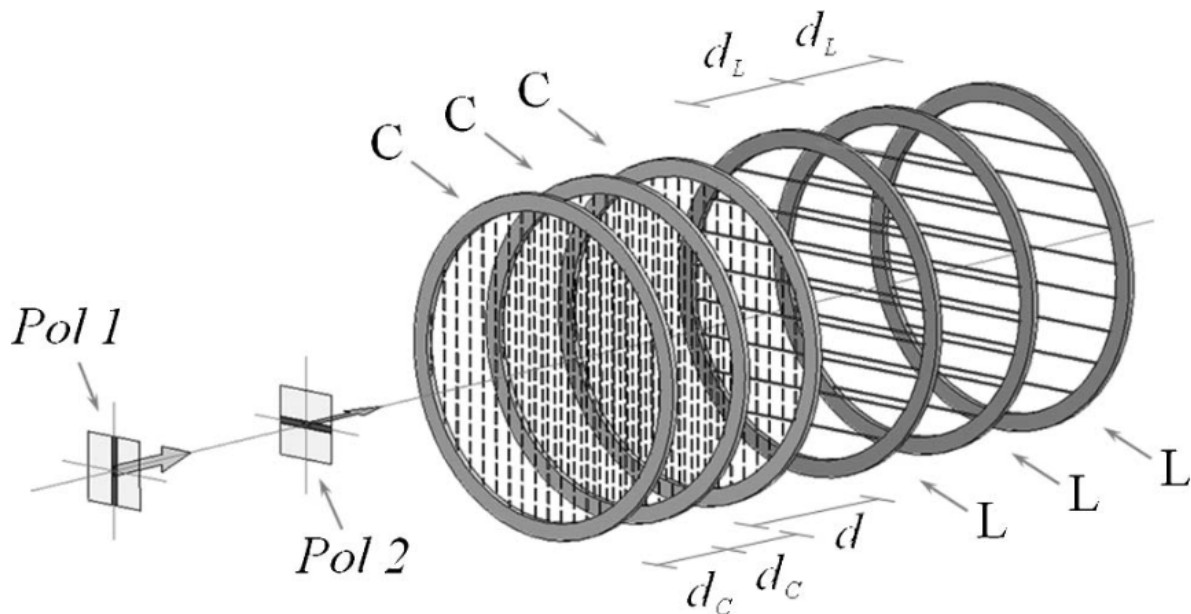


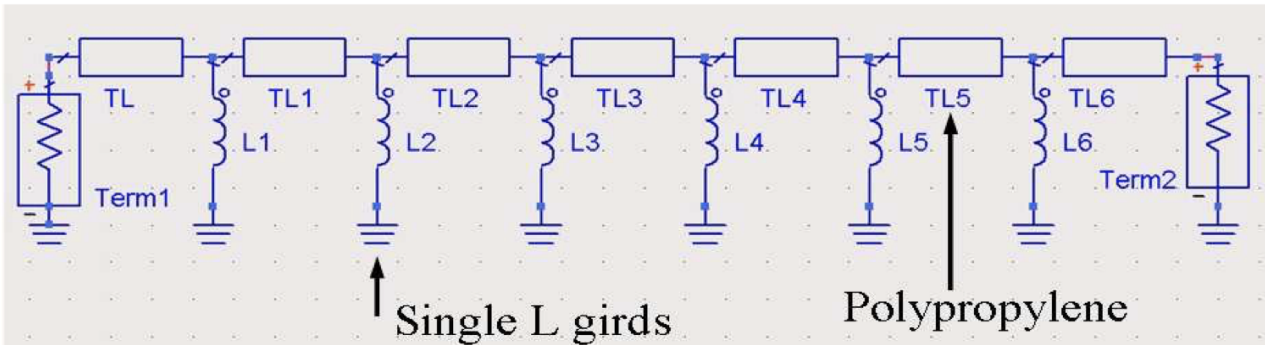
Figure 2.3 – Example of a wave plate with three conductive layers and three inductive layers, denoted by C and L respectively. The distance between the conductive layers and inductive layers is set differently to the distance between the consecutive layers for each mesh design, denoted by d and d_C or d_L . (Pisano et al., 2008).

To compute the phase shift of an EMM HWP softwares are required to model how EM radiation interacts with each element. Typically softwares such as Advanced Design System (ADS) are used to create transmission line models. Through using two transmission line models, one to model inductive grids and one to model the capacitive grids, scattering parameters for orthogonal polarisations can be computed, an example of the two models is see in Figure 2.4. The scattering parameters calculated from both models are combined to determine the phase difference between the orthogonal polarisations. Through varying the parameters of the inductors and capacitors the performance of the mesh HWP can be optimised in order to achieve a near flat phase shift of 180° and high transmission over the working frequency range.

The optimised design parameters obtained through the transmission line models, such as the optimised lumped impedance, allows softwares like High Frequency Structure Simulations (HFSS) to determine the grid geometries needed for the HWP design. It achieves this through modelling the scattering parameters of individual metal patterns allowing it to relate the geometrical parameters to its lumped impedance through solving Maxwell's equations on a cell by cell basis.

Each filter is manufactured with thin copper grids embedded into polypropylene (Ade et al. (2006), Pisano et al. (2012), Pisano & others (2014)). The grids for the inductive filter are parallel lines whilst the grids for the capacitive filter are parallel 'dashed-lines'. Multiple layers of the same filter are stacked together to increase the bandwidth the EMM HWP performs over. This is

6 layer L girds:



6 layer C girds:

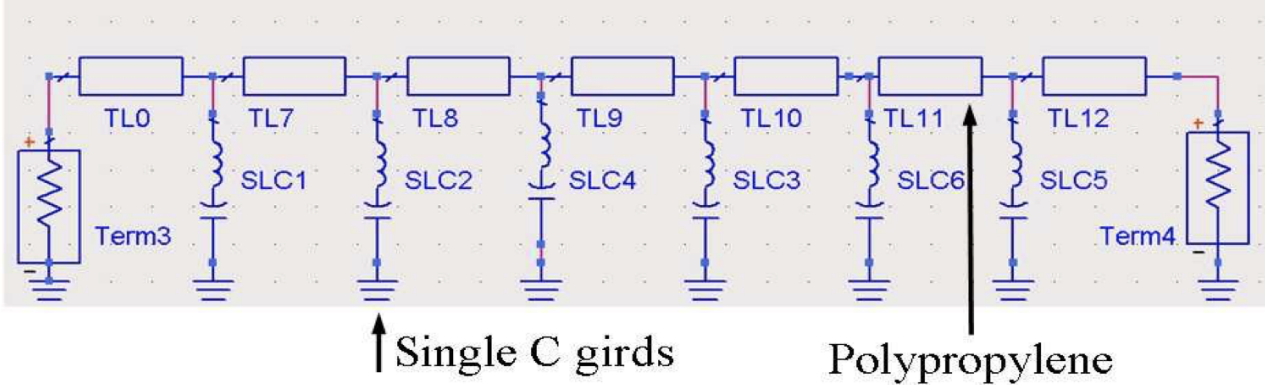


Figure 2.4 – Example of a transmission line model for an EMM HWP. This shows two different transmission line models for six capacitive grids and six inductive grids, which are embedded in polypropylene. To ensure that the thickness of the models were the same as the thickness of each set of six grids and their spacers, additional sections of polypropylene was added which are depicted in the diagram as the rectangle boxes. (Zhang et al., 2011)

observed in Figure 2.5 where there are six layers of each capacitive and inductive filter to broaden the bandwidth. Applied to either side of the plate are ARCs to reduce reflections between free space and the HWP materials. The design of each EMM HWP is achieved through specifically developed propagation matrix code (Pisano et al., 2012), which has not been included in this thesis because it is outside its scope and the design was obtained through private conversation with Prof. Giampaolo Pisano of Sapienza University of Rome.

The EMM HWPs are becoming a promising replacement for current birefringent HWP designs used in CMB experiments because they are more cost effective to manufacture, diameters can currently be manufactured to the same size as sapphire HWPs (50cm) with the possibility to improve upon this with their diameters being created to larger sizes. Additionally, the device’s weight is lower than their Pancharatnam counterparts, whilst still maintaining a good performance (Pisano et al. (2022), Maffei et al. (2012)). However, thorough characterisation’s of these devices

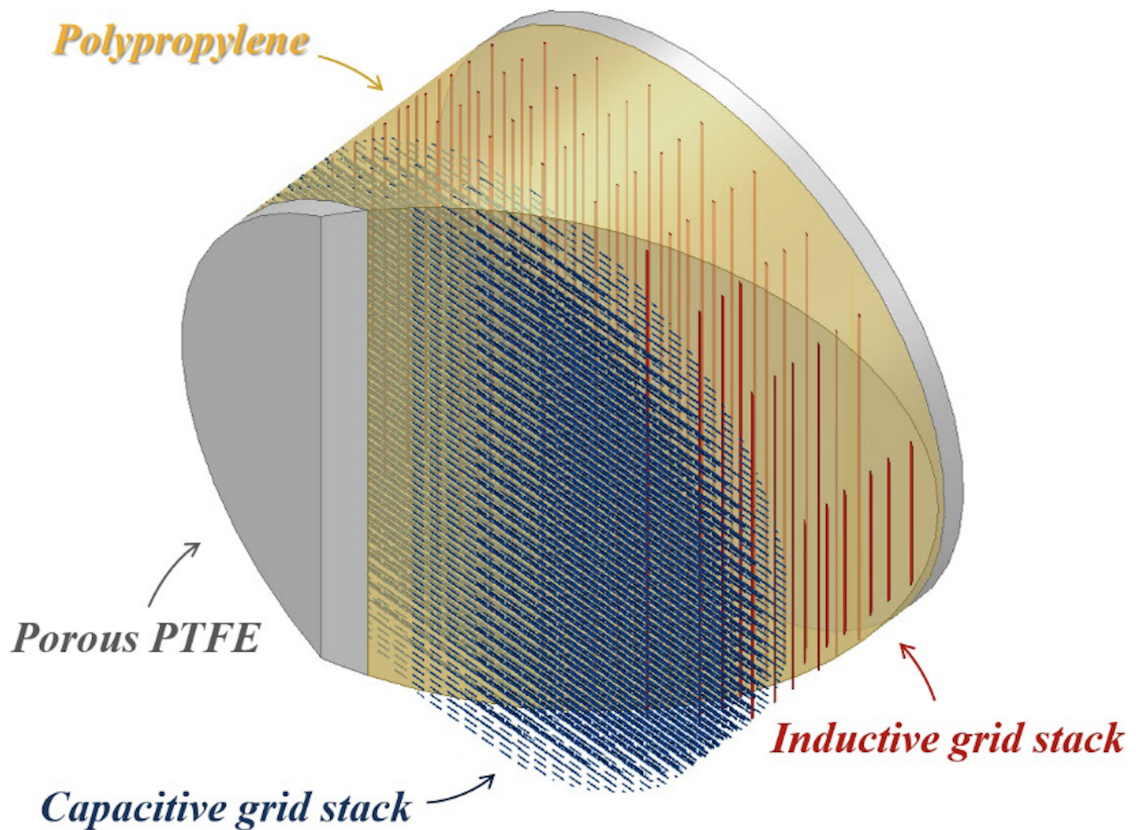


Figure 2.5 – CAD drawing of an embedded metal mesh HWP. The capacitive (blue dashed lines) and inductive (red lines) grids can be observed being embedded in polypropylene layers. An anti-reflecting coating of porous PTFE is applied to reduce the level of reflection as incident light propagates between refractive indices of materials (Pisano et al., 2022).

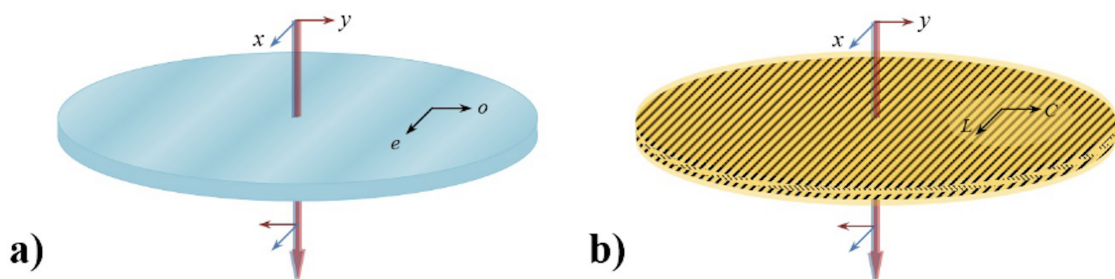


Figure 2.6 – a) A birefringent HWP with its extraordinary and ordinary axes shown, b) an EMM HWP with its inductive and capacitive axes. From these sketches it is shown that the inductive and capacitive axes replace the extraordinary and ordinary axes respectively for an EMM HWP. The optical axis is denoted by the large red and blue arrow, with its x and y axes shown (Pisano et al., 2022).

need to be carried out to truly understand their optical performance and to compare to the Pancharatnam designed HWPs. Characterisation of HWPs is achieved through measuring their Mueller matrix.

2.1.3 Mueller Matrices

HWPs are characterised through their Mueller matrices, which are a 4x4 matrix that describes how polarised signals are affected by propagating through optical devices. Mueller calculus was proposed in 1943 (Schmidt, 2022) using Stokes formalism. Stokes formalism arose in 1852 by George Stokes when he defined a set of parameters (Schmidt, 2022) which would be able to describe the state of polarisation in vector form.

These have been termed the Stokes parameters and comprise real measured values and are described according to equation (2.3)

$$S = \begin{pmatrix} I \\ Q \\ U \\ V \end{pmatrix} = \begin{pmatrix} \langle E_x^2 \rangle + \langle E_y^2 \rangle \\ \langle E_x^2 \rangle - \langle E_y^2 \rangle \\ 2\langle E_x E_y \cos(\Delta\delta) \rangle \\ 2\langle E_x E_y \sin(\Delta\delta) \rangle \end{pmatrix} = \begin{pmatrix} \langle I_0 \rangle + \langle I_{90} \rangle \\ \langle I_0 \rangle - \langle I_{90} \rangle \\ \langle I_{45} \rangle - \langle I_{135} \rangle \\ \langle I_{LC} \rangle - \langle I_{RC} \rangle \end{pmatrix} \quad (2.3)$$

where (I, Q, U, V) describe the Stokes parameters. In equation (2.3), I describes the total intensity of the light, Q describes the linear polarisation in horizontal or vertical directions, U describes linear polarisation in either diagonal direction ($\mp 45^\circ$) and V describes circular polarisation. The terms E_x and E_y are the amplitude of the electric vector along the x and y axes respectively. The term $\Delta\delta$ is the difference in phase along the y -axis to the x -axis. I_0 describes the intensity of the light wave along the 0° rotation (the 0° is determined with respect to the device axes), whilst I_{90} , I_{45} and I_{135} describe the intensity of the wave along the 90° , 45° and 135° rotation axis respectively. Finally, I_{LC} and I_{RC} describes the intensity of the left and right circular polarisation respectively. The chevron brackets denote time-averaged values.

Mueller calculus describes how the Stokes vector may change as it passes through multiple optical devices. It can do this through associating each optical device with an associated 4x4 Mueller matrix which contains information about the devices' polarisation characteristics. Optical devices commonly used in polarisation experiments have pre-defined Mueller matrices. For example, a horizontal linear polariser has a Mueller matrix defined as

$$M_{HLP} = \begin{bmatrix} 1 & 1 & 0 & 0 \\ 1 & 1 & 0 & 0 \\ 0 & 0 & 0 & 0 \\ 0 & 0 & 0 & 0 \end{bmatrix} \quad (2.4)$$

which allows horizontal linearly polarised light to propagate through to detection. Alternatively, a

vertical linear polariser has a Mueller matrix is defined as

$$M_{VLP} = \begin{bmatrix} 1 & -1 & 0 & 0 \\ -1 & 1 & 0 & 0 \\ 0 & 0 & 0 & 0 \\ 0 & 0 & 0 & 0 \end{bmatrix} \quad (2.5)$$

which allows vertical linearly polarised light to propagate through to detection.

Mueller matrices for wave plates can be defined using

$$M_{WP} = \begin{bmatrix} 1 & 0 & 0 & 0 \\ 0 & 1 & 0 & 0 \\ 0 & 0 & \cos(\phi) & \sin(\phi) \\ 0 & 0 & -\sin(\phi) & \cos(\phi) \end{bmatrix} \quad (2.6)$$

where ϕ is the phase shift the wave plate produces, for a HWP this is 180° . The matrices introduced in equations (2.4), (2.5) and (2.6) have assumed that the devices' (x', y') axes are aligned along the (x, y) axes of the optical setup. However, if the devices axes are instead at an angle, θ , to the optical setup's axes the incident Stokes parameters need to be mapped onto the (x', y') axes. This is achieved through a Mueller rotation matrix defined as

$$M_{rotator}(\theta) = \begin{bmatrix} 1 & 0 & 0 & 0 \\ 0 & \cos(2\theta) & \sin(2\theta) & 0 \\ 0 & -\sin(2\theta) & \cos(2\theta) & 0 \\ 0 & 0 & 0 & 0 \end{bmatrix} \quad (2.7)$$

and to rotate it back to the optical setup axes a rotation of $-\theta$ is required, turning equation (2.7) into

$$M_{rotator}(-\theta) = \begin{bmatrix} 1 & 0 & 0 & 0 \\ 0 & \cos(2\theta) & -\sin(2\theta) & 0 \\ 0 & \sin(2\theta) & \cos(2\theta) & 0 \\ 0 & 0 & 0 & 0 \end{bmatrix} \quad (2.8)$$

which is achieved using trigonometric identities. These rotator equations (2.7) and (2.8) are particularly useful when calculating the performance of a HWP because the HWP rotates a linear polarised signal causing the signal to be at an angle to the system axes. Using the equations (2.7) and (2.8) allows us to account for this difference in axes angles.

For experimental setups the output Stokes vector can be calculated by multiplying the input Stokes vector by the Mueller matrices of all optical elements in the setup, this output vector then describes the whole optical system. For example, to calculate the output Stokes vector for an experimental setup that contains a source which propagates a signal initially through a horizontal polariser and then through a vertical polariser, at which the signal then is the output Stokes vector, S_{out} , equation would be

$$S_{out} = M_{VLP}M_{HLP}S_{in} \quad (2.9)$$

where S_{in} is the input Stokes vector.

Using the formalism's described above we can venture to characterise each element in the optical chain of an instrument with Mueller matrices to understand how polarised light propagates through the instrument and is therefore affected by the instrument. This would provide an understanding to the level of systematics present which is required for associating an error on r .

2.1.4 HWP non-idealities

Optical devices used in telescope designs will deviate from their theoretical ideal performance due to a number of reasons, such as material properties, the manufacturing procedure, reflections, absorption, etc.

$$M_{HWP} = \begin{bmatrix} M_{II} & M_{IQ} & M_{IU} & M_{IV} \\ M_{QI} & M_{QQ} & M_{QU} & M_{QV} \\ M_{UI} & M_{UQ} & M_{UU} & M_{UV} \\ M_{VI} & M_{VQ} & M_{VU} & M_{VV} \end{bmatrix} \quad (2.10)$$

To describe a the performance of a HWP Mueller matrices are used and equation (2.10) shows a HWPs, where (I, Q, U, V) are the Stokes parameters, as explained in Section 2.1.3. The deviation from ideal performance, see equation (3.1), is what is known as non-idealities and these can arise in a HWP. Understanding a HWPs non-idealities is crucial in understanding the bias it may cause on measurements of scientific parameters, such as r . There are several areas in a HWPs performance where non-idealities can arise, such as its polarisation efficiency, polarisation leakage and frequency dependent rotation angle, which will be discussed in the next Section.

Polarisation efficiency

The polarisation efficiency for a HWP describes how well the incident linear polarisation propagates through through the device without being affected by it. It is calculated from equation (2.11),

$$\varepsilon = \left(\frac{M_{QQ}}{2} - \frac{M_{UU}}{2} \right) / \eta \quad (2.11)$$

where η is the optical efficiency of the HWP defined by equation (2.12).

$$\eta = M_{II} + \frac{M_{QQ}}{2} + \frac{M_{UU}}{2} \quad (2.12)$$

The polarisation efficiency should be equal to 1 for an ideal HWP, however, reflections off the multiple material layers in a HWPs design will cause the level of polarisation propagated through the device and detected to be reduced. Another way that the efficiency is affected is through rotational instabilities. It has been shown (Azzoni, 2023) that any shift in the HWP angle can cause the M_{QQ} and M_{UU} terms to be altered. This shift is caused by not knowing the correct position of the extraordinary axis of the HWP which in turn means that the sky signal is modified by a polarisation angle rotation of this shifted HWP angle.

Polarisation efficiency less than 1 causes the amplitude of E and B power spectra to decrease in size as shown in (Azzoni, 2023). As a result of a change in their amplitude this then leads to a bias on r , it is therefore imperative that the polarisation efficiency of a HWP is measured and properly understood in order to retrieve the correct amplitude of these power spectra.

Polarisation leakage

It has been shown (Duivenvoorden et al., 2021) that non-idealities which arise in HWPs can cause $E^- \rightarrow B$ -mode leakage which in turn can cause B -mode residuals. Polarisation leakage can occur from a HWP non-idealities in the form of the polarisation rotation. Polarisation rotation affects the M_{QU} and M_{UQ} terms due to the HWP rotating the polarisation such that part of the polarisation signal in one orientation is detected in the orthogonal state. This can be caused by small defects in the material which refract the incident polarisation such to cause the overall rotation of the incident polarisation to change and be detected in the orthogonal state.

Additionally, as previously mentioned for the polarisation efficiency of a HWP, polarisation leakage may also arise when the HWP angle is shifted by a certain amount (Azzoni, 2023). The shift in angle causes the M_{QU} and M_{UQ} terms to be altered consequently giving rise to polarisation leakage which further causes mixing of $E^- \rightarrow B$ -modes, affecting the overall power spectra.

Frequency dependent polarisation angle

In Section 2.1.1 it was shown that the phase shift incurred by a HWP is frequency dependent for a Pancharatnam designed HWP. Stacking multiple plates to increase the frequency bandwidth of the HWP causes the HWPs effective fast axis to have a frequency dependence associated to it. This results in polarisation sensitive experiments having a frequency dependent polarisation angle sensitivity. Due to the frequency dependence it can be difficult to calibrate it out due to sky components, such as Galactic foregrounds, with different frequency characteristics requiring different offset values (Duivenvoorden et al., 2021).

It has also been shown (Duivenvoorden et al., 2021) that error in the calibrated polarisation angle offset can cause $E^- \rightarrow B$ -mode leakage as residual maps trace the shape of the input E -mode spectrum. This is due to the offset angle for dust being different for the offset angle due to the CMB at 95 GHz and 150 GHz respectively. It is then clear that a single HWP offset angle will not effectively reduce B -mode residual caused by HWP non-idealities. Further to this, Pancharatnam HWPs, in particular those that are 3-layered (Duivenvoorden et al., 2021), produce a significant frequency dependent rotation angle offset which acts like a polarisation angle offset, leading to further $E^- \rightarrow B$ -mode leakage if not corrected for.

However, the phase shift produced by EMM HWPs described previously in Section 2.1.2 do not have the same inherent frequency dependence as Pancharatnam HWPs do. Instead the

phase shift is altered through the geometry of the HWP design therefore a frequency dependent polarisation angle is less prevalent for these types of HWPs. This is an advantage to using these in future CMB experiments.

To begin to properly account for the non-idealities which arise in HWPs and to begin to compare Pancharatnam and EMM HWPs, characterisations of their performance are required. To be able to perform characterisations and comparisons of device such as HWPs, experimental data and analysis pipelines to feed the data into are required to produce a HWPs Mueller matrices. Methods to acquire these are discussed in Chapters 3, 4 and 5. It is then through these matrices that analysis on the biases caused by non-idealities can begin.

EXTRACTING HWP PERFORMANCE FROM DATA ANALYSIS

"Started making it. Had a breakdown. Bon appétit."

James Accaster, *The Great Stand Up To Cancer Bake Off*

Through calculating a device's Mueller matrix we are able to calculate the extent to which a device deviates from its ideal performance. An ideal performance describes how the device should perform provided it was theoretically perfect. Deviations from this performance are expected because of various factors such as the manufacturing of the device and the material properties. Therefore, it is important to measure the experimental performance of each optical device used in an instrument to understand how it deviates from this ideal performance because it is from this that we would be able to understand how non-idealities may manifest as systematic effects in instruments.

This Chapter will describe the method required to inject laboratory measurements of a HWP into software to calculate its Mueller matrix. The method described here is based on the method described in the BLASTPol paper ([Moncelsi et al., 2014](#)) where they performed a comprehensive full characterisation of the BLASTPol HWP. BLASTPol was the first experiment to publish literature describing the characterisation of their HWP using its measured spectral transmission. They furthered their analysis by injecting the HWPs Mueller matrix components into a map-making algorithm, allowing analysis to be undertaken into the affects caused by the HWPs non-idealities to be completed.

3.1 MODELLING EXPERIMENTAL DATA FOR FULL CHARACTERISATION OF HWPS

As mentioned in Chapter 2, a Mueller matrix is a 4x4 matrix that provides information about polarisation characteristics of devices. It has diagonal elements that describe the total intensity and polarisation that is transmitted through and off-diagonal terms that describe the mixing between intensity and polarisation states.

For any device there is a mathematical ideal case for its performance. For a HWP this is given by a set of 16 coefficients in its Mueller matrix and its phase shift. For an ideal HWP at a rotation angle (angle of the polarised light incident on the first plate relative to its extraordinary axis) of $\theta = 0^\circ$ the Mueller matrix is given by (Collett, 1993)

$$M_{HWP} = \begin{bmatrix} 1 & 0 & 0 & 0 \\ 0 & 1 & 0 & 0 \\ 0 & 0 & -1 & 0 \\ 0 & 0 & 0 & -1 \end{bmatrix} \quad (3.1)$$

and the output phase difference of the polarised light is $\Delta\delta = 180^\circ$.

Deviations from the ideal coefficients given in equation (3.1) give an insight into the non-idealities of the HWP, therefore it is important to understand how to capture these deviations arising in HWPs. To retrieve the Mueller matrix coefficients the spectral transmission of the HWP at several rotation angles need to be measured in an optical setup and fitted to a model. In the following Section the method required to generate this model is described.

3.1.1 Modelling optical measurements

To generate a Mueller matrix of a HWP experimental setups are required which can measure a polarised output of a device relative to a known polarised input. In particular, for a HWP two different types of experimental polarised measurements are required. These are known as co- and cross-polarisation (from hereon will be referred to as co- and cross-pol). Co-pol measurements detect parallel polarised light to the incoming signal. Cross-pol measurements detect the orthogonal polarised light to the incoming signal. Spectra of the experimental setup in each configuration are measured without the HWP inserted into the setup to obtain the polarised signal produced by the experiment itself, also referred to as background spectra. The HWP would then be inserted into the setup and spectra obtained and ratioed to the background spectra. Measuring spectra data sets as a function of the HWPs rotation angle provides an understanding of the HWPs performance as it can be measured how well the HWP rotates the polarised light. Further detail on this method can be found in Chapters 4 and 5.

Through combining both the co- and cross-pol experimental data sets with separate models

a HWPs Mueller matrix can be generated. Both co- and cross-pol experimental setups can be expressed in matrix format by using Stokes formalism, as seen in Chapter 2. Expressing each element in the optical chain as a Mueller matrix two equations, (3.2) and (3.3), are generated which describe the results of the laboratory measurements, such as those described in Chapters 4 and 5, in the following way

$$S_{out}^{cp} = \vec{D}^T \cdot M_p^h \cdot R(-\theta) \cdot M_{HWP} \cdot R(\theta) \cdot M_p^h \cdot \vec{S}_{in}^h \quad (3.2)$$

$$S_{out}^{xp} = \vec{D}^T \cdot M_p^v \cdot R(-\theta) \cdot M_{HWP} \cdot R(\theta) \cdot M_p^h \cdot \vec{S}_{in}^h \quad (3.3)$$

where \vec{D}^T is the Stokes vector for the intensity detected at the detector, M_p^h and M_p^v are the Mueller matrices for ideal polarisers orientated to transmit horizontal and vertical polarisation respectively, $R(\theta)$ is the Mueller rotation matrix, M_{HWP} is the HWP Mueller matrix and \vec{S}_{in}^h is the input polarisation beam, which for this example is set to be horizontal. The superscripts *cp* and *xp* in equations (3.2) and (3.3) denote co-polarisation and cross-polarisation respectively.

By inserting the matrices in equation (3.2) the following equation is obtained

$$S_{out}^{cp} = \begin{pmatrix} 1 & 0 & 0 & 0 \end{pmatrix} \cdot \begin{pmatrix} 1 & 1 & 0 & 0 \\ 1 & 1 & 0 & 0 \\ 0 & 0 & 0 & 0 \\ 0 & 0 & 0 & 0 \end{pmatrix} \cdot \begin{pmatrix} 1 & 0 & 0 & 0 \\ 0 & \cos(2\theta) & -\sin(2\theta) & 0 \\ 0 & \sin(2\theta) & \cos(2\theta) & 0 \\ 0 & 0 & 0 & 0 \end{pmatrix} \cdot \begin{pmatrix} 1 & 1 & 0 & 0 \\ 1 & 1 & 0 & 0 \\ 0 & 0 & 0 & 0 \\ 0 & 0 & 0 & 0 \end{pmatrix} \cdot \begin{pmatrix} 1 \\ 1 \\ 0 \\ 0 \end{pmatrix} \quad (3.4)$$

where a_{ij} (i and j are values between 0-3) are parameters in the HWP Mueller matrix and computing the matrix multiplications provides the following

$$S_{out}^{cp} = a_{00} + \frac{a_{11}}{2} + \frac{a_{22}}{2} + \frac{1}{2} (a_{11} - a_{22}) \cos(4\theta) + \frac{1}{2} (a_{21} + a_{12}) \sin(4\theta) + (-a_{10} - a_{01}) \cos(2\theta) + (-a_{20} - a_{02}) \sin(2\theta) \quad (3.5)$$

which can be simplified to

$$S_{out}^{cp} = A + B \sin(2\theta) + C \cos(2\theta) + D \sin(4\theta) + E \cos(4\theta) \quad (3.6)$$

where

$$\begin{aligned} A &\equiv a_{00} + \frac{a_{11}}{2} + \frac{a_{22}}{2}, \\ B &\equiv (-a_{20} - a_{02}), \\ C &\equiv (-a_{10} - a_{01}), \\ D &\equiv \frac{1}{2} (a_{21} + a_{12}), \\ E &\equiv \frac{1}{2} (a_{11} - a_{22}). \end{aligned} \quad (3.7)$$

To obtain the similar equation for cross-pol, S_{out}^{xp} , the same matrices are inserted into equation

(3.3), apart from one M_p^h matrix because it is replaced with the vertical linear polariser matrix presented in equation (2.5). Using the same method described above to obtain S_{out}^{cp} the following is obtained for S_{out}^{xp}

$$S_{out}^{xp} = A' + B' \sin(2\theta) + C' \cos(2\theta) + D' \sin(4\theta) + E' \cos(4\theta) \quad (3.8)$$

with,

$$\begin{aligned} A' &\equiv a_{00} - \frac{a_{11}}{2} - \frac{a_{22}}{2}, \\ B' &\equiv (a_{20} - a_{02}), \\ C' &\equiv (a_{10} - a_{01}), \\ D' &\equiv \frac{1}{2}(-a_{21} - a_{12}), \\ E' &\equiv \frac{1}{2}(-a_{11} + a_{22}). \end{aligned} \quad (3.9)$$

By performing linear combinations with equations (3.7) and (3.9) all the individual elements of the Mueller matrix for a generic HWP can be expressed in the following way

$$\begin{aligned} a_{00} &= \frac{1}{2}(A + A'), \\ a_{01} &= -\frac{1}{2}(C + C'), \\ a_{02} &= -\frac{1}{2}(B + B'), \\ a_{10} &= \frac{1}{2}(-C + C'), \\ a_{11} &= \frac{1}{2}(A - A' + E - E'), \\ a_{20} &= \frac{1}{2}(-B + B'), \\ a_{22} &= \frac{1}{2}(A - A' - E + E'), \\ a_{12} &= a_{21} = \frac{1}{2}(D - D'). \end{aligned} \quad (3.10)$$

The Mueller matrix for a HWP contains 16 coefficients, an example shown in equation (3.1), but only 9 coefficients are provided in equation (3.10). This is because the experiments performed in this thesis only measure linear polarisation and therefore coefficients which describe circular polarisation are set to equal zero and excluded from equation (3.10). To provide these coefficients a QWP would be required in the experimental setup, which through its 90° phase shift would produce circular polarisation. However, these types of experiments are past the scope of this thesis and therefore only the 9 coefficients in equation (3.10) shall be discussed in further detail in this work. This is because the level of circular polarisation present in CMB experiments is negligible (Montero-Camacho & Hirata, 2018), therefore the 7 coefficients excluded from this thesis are not as prevalent to the studies presented in this work. However, going forward measurements

should be performed to characterise a HWPs performance with circular polarisation to quantify the systematic errors that may be introduced.

Using equations (3.7) and (3.9) in a fitting routine along with the measured spectral transmission of a HWP will enable the best fit parameters for each matrix coefficient in equation (3.10) to be calculated. The method to facilitate this is described in the following Section.

3.1.2 Estimating the Mueller Matrix coefficient values from laboratory data

To calculate the Mueller matrix coefficients previously described a fitting routine will be used to obtain the best fit parameters for each coefficient. The fitting routine that will be utilised for this work is a Markov Chain Monte Carlo (MCMC) (Speagle, 2020), this will apply the model equations (3.7) and (3.9) to the measured spectral performance of the HWP whilst allowing for the uncertainties on the estimates to be found.

An MCMC is a stochastic method that explores the probability distribution of all model parameters, achieved through implementing several random ‘walkers’ that sample the full multi-dimensional parameter space. These ‘walkers’ are of a number of chains that take steps in each parameter space, slowly converge to a set of parameters which best fit the data. Each step a walker takes is accepted through calculating the likelihood for each sample and then maximising its distribution and through these chains the posterior distribution of each parameter can then be estimated. Prior knowledge on parameters, such as previous experimental results can be incorporated in the process through determining the parameter space the chains walk in.

The MCMC package used for this work was ‘emcee’ (Foreman-Mackey et al., 2013). To estimate the 9 parameters in equation (3.10) in order to characterise a HWP we first need to estimate the parameters in equations (3.7) and (3.9), which are $[A, B, C, D, E]$ and $[A', B', C', D', E']$ respectively. It is these parameter sets which are estimated using a MCMC because of the two independent data sets obtained. The estimated parameters can then be inserted into each Mueller matrix coefficient presented in equation (3.10) and their values calculated.

Using the co-pol datasets MCMCs were generated that initiates 10 chains which probed 5 dimensions to estimate the $[A, B, C, D, E]$ parameters. Within these MCMCs a flat logarithmic prior function was used with the following conditions

$$\ln(Prior) = \begin{cases} 1 & \text{if } -2 < A, B, C, D, E < 2 \\ 0 & \text{otherwise} \end{cases} \quad (3.11)$$

and the same prior is used for the cross-pol MCMCs but the $[A, B, C, D, E]$ parameters are replaced with $[A', B', C', D', E']$. A flat prior was used due to the very limited literature that could inform my simulation without my new data. A flat prior essentially sets the fitting range which describes the parameter space believed is needed to find the best model. A few cases were tried before settling on the ranges presented in equation (3.11). These trials included increasing the

range to be between -10 and 10 for each parameter and setting very specific ranges for each parameter.

The following logarithmic Gaussian likelihood function was used

$$\ln(Likelihood) = -\frac{1}{2} \sum_n \left[\frac{(O_n - M_n)^2}{\sigma_n^2} \right] \quad (3.12)$$

where O_n is the observable data, M_n is the modelled data and σ_n^2 is the standard deviation in the data. The statistical error on the background spectra measured is used as the standard deviation of the data. Equations (3.11) and (3.12) are the logarithmic versions of the prior and likelihoods and are used to estimate the posterior probability function which is calculated using

$$Posterior \propto Likelihood \times Prior \quad (3.13)$$

but with the log-likelihood and log-prior equations (3.11) and (3.12), equation (3.13) turns into

$$\ln(Posterior) \propto \ln(Likelihood) + \ln(Prior). \quad (3.14)$$

Initial conditions are required to provide the chains with initial positions, for which $[1, 0, 0, 0, 1]$ was used as initial conditions for the co-pol MCMC. Initial tests were performed with a 1000 steps for each chain to identify the initial conditions for the fit. This ensured that the initial conditions chosen were correct and the fit was working properly, after this check the step size was increased to 5000 and the first 1500 steps were removed from the chain as a “burn-in” stage. A burn-in stage is used to give the chains time to reach their equilibrium distribution which can be particularly useful if the initial starting points for each chain is not in a high probability area. Therefore, this stage will remove these points leaving the chain with samples in higher probability areas and calculating the mean and standard deviation for each parameter from these values.

This method is repeated to generate a MCMC using the cross-pol data sets with initial positions of $[1, 0, 0, 0, -1]$ to estimate the $[A', B', C', D', E']$. The estimated parameters can then be used in equation (3.10) to calculate the Mueller matrix coefficients along with their associated errors. This method to create MCMCs to enable characterisation of HWPs using experimental data was used in Chapters 4 and 5 where their results are also presented.

SPECTRAL CHARACTERISATION OF A HALF WAVE PLATE, USING A VECTOR NETWORK ANALYSER

"Failure is only the opportunity to try again, only more wisely this time."

Iroh, *Avatar: The Last Air Bender*

In an ideal scenario HWPs would demonstrate perfect behaviour; show a 100% polarised transmission along one axis with 100% rejection along the other and operate over a broad wavelength band. However, irrespective of the construction method used, this will never be the case and spectral structure will be present in the HWP measurements. In the case of the metal mesh HWPs described in Chapter 2 the material used in its construction will cause absorption loss, and the inductive and capacitive grids will be designed to work at certain wavelengths. These systematic imperfections must be accounted for and the aim of this work is to quantify the degree to which their performance affects the data extraction of the CMB polarisation signals, in particular the *B*-mode power spectrum. To do this, I must spectrally characterise the HWP in orthogonal polarisations as a function of its angle of rotation and about its full rotation.

Despite HWPs having been used on CMB experiments since MAXIPOL ([Johnson et al., 2007](#)) in 2003, most HWPs have only been measured at 0°, 45°, 90° axis rotations. The first full characterisation of a HWP performance was for the BLASTPol instrument ([Moncelsi et al., 2014](#)), where the Pancharatnam plates were assembled and tested at Cardiff. Within this Chapter I have reviewed, replicated, and developed this process to characterise a metal mesh type HWP, with a plan to directly compare Pancharatnam and metal mesh HWP devices in future.

The BLASTPol paper ([Moncelsi et al., 2014](#)) used a polarising Martin-Puplett Fourier Transform Spectrometer (FTS), running between 20 – 60 cm⁻¹ (600 – 1800 GHz), and set up with additional

polarisers at the exit of the interferometer to ensure linear polarisation throughout. The HWP was placed in a rotator and spectra were measured at 5° intervals in co- and cross-pol configurations with 2° steps taken close to the maximum and minimum spectra. Chapter 5 describes the detailed equivalent set-up used in this work, which has been optimised for a longer wavelength operation (see Table 4.1) to cover the NIKA2 bands.

In addition, I have taken equivalent data sets, over the same angular rotation steps and the same wavelength range (Table 4.1) using a more commonly used vector network analyser (VNA) and is detailed in Section 4.1. This has allowed for a comparison between the techniques used (see Chapter 6), to assess the better method (with all things considered) and to discuss limitations, as well as to track both data sets through pipeline software to understand the way that systematic effects and errors will ultimately affect data analyses.

4.1 SPECTRAL CHARACTERISATION USING A VECTOR NETWORK ANALYSER

A VNA is a form of a radio frequency (RF) network analyser widely used for RF design applications, which can measure both amplitude and phase properties of a device under test (DUT). It measures the so-called scattering parameters (S-parameters) of a transmission line, or in this case its optical equivalent, allowing reflected and transmitted responses to be measured (Figure 4.1). The Rohde and Schwarz ZVA 67 VNA (KG, 2023) used here is a 4-port device, but only 2 ports have been used in this thesis, as presented in the simple schematic in Figure 4.1.

S-parameters describe how a DUT modifies a signal. This signal can be either transmitted or reflected in a forward or reverse direction. Figure 4.1 shows an example of a 2-port system and its corresponding S-parameters. A scattering matrix, as depicted in equation (4.1) allows the incident signal (a_1 and a_2) to be connected to the output signal (b_1 and b_2).

$$\begin{bmatrix} b_1 \\ b_2 \end{bmatrix} = \begin{bmatrix} S_{11} & S_{12} \\ S_{21} & S_{22} \end{bmatrix} \begin{bmatrix} a_1 \\ a_2 \end{bmatrix} \quad (4.1)$$

From equation (4.1) and using linear equations, if I define the wave direction by their absolute direction and consider the incident wave at port 1, it could exit from either port 1 or port 2. However, if port 2 is terminated in a load identical to the system impedance then b_2 will be totally absorbed making $a_2 = 0$. Likewise if port 1 is terminated in the system impedance then $a_1 = 0$. Therefore, each S-parameter can be extracted and expressed in its own equation, presented in equations (4.2) to (4.5)

$$S_{11} = \frac{b_1}{a_1} \quad (4.2)$$

$$S_{12} = \frac{b_1}{a_2} \quad (4.3)$$

$$S_{21} = \frac{b_2}{a_1} \quad (4.4)$$

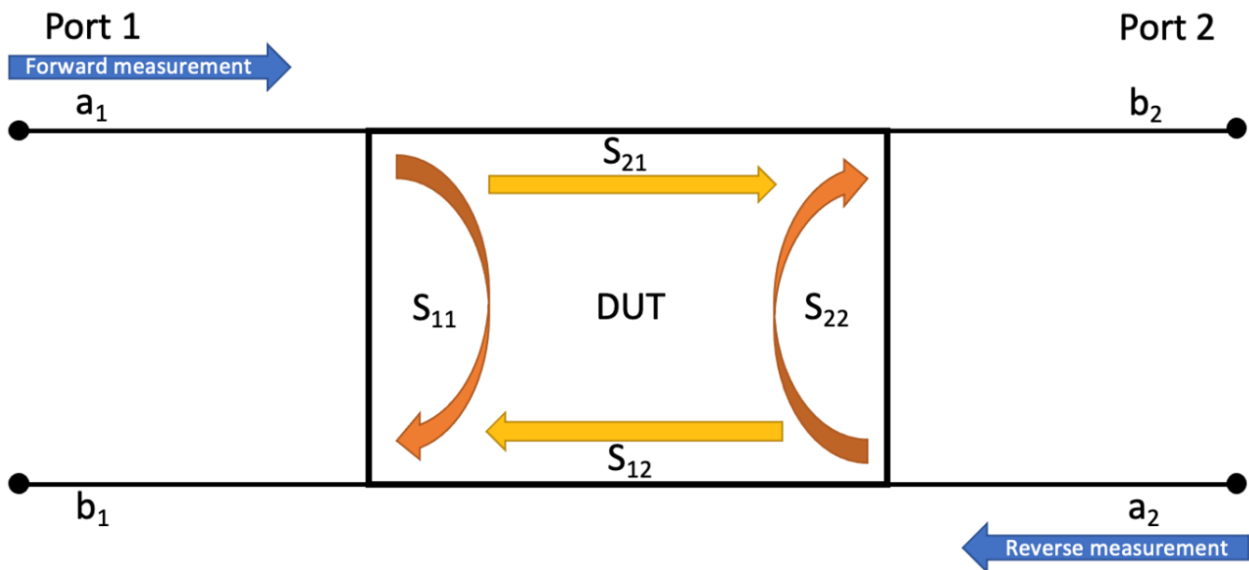


Figure 4.1 – Schematic diagram of a 2-port VNA system, the terms a and b denote the input and output respectively in the system. A device under test (DUT) modifies a signal that is transmitted or reflected in the forward or reverse direction. The S_{ij} , where i and j are either numbers 1 or 2, denote the S-parameters of the system and their arrows correspond to the direction in which they refer to.

$$S_{22} = \frac{b_2}{a_2} \quad (4.5)$$

by taking the ratio of the output signal to the input signal the input reflection coefficient, S_{11} , the forward transmission coefficient, S_{12} , the reverse transmission coefficient, S_{21} , and the output reflection coefficient, S_{22} can be calculated. The data sets discussed in this Chapter only recorded S_{21} , effectively measuring only the transmission of the device.

4.1.1 Setting up the VNA optical bench

Using a VNA gives the advantage of extracting both the amplitude and phase information over a large dynamic range, in what appears to be a simple arrangement of a receiver and a transmitter head. However great care must be, and was, taken to limit the affect on the quality of data caused by standing waves and poor experimental practice. Several examples are given in the following Sections to outline steps taken to mitigate the affect on the quality of data.

Rotation between polarisation states

Different antenna headsets, devices used to transmit and receive RF signals which are connected to the VNA, are used to cover the full frequency range required (see Table 4.2 for details) and great care must be taken to maintain alignment to the optical axis during the change from one

head set to another. Additionally, the receiver head needed to be rotated by 90° with respect to the transmitter to perform cross-pol measurements, so again, great care must be taken to maintain the optical axis during this rotation.

Optical element checks for each frequency band

When switching the frequency bands being measured over by changing the heads, checks need to be carried out before optical measurements are performed. These checks should consider, but not limited to, the focal length of the lenses (as explained in Section 4.1.3), the alignment of the system, the sources of standing waves, the beam size and apertures. I assessed these alignment issues whilst monitoring the signal strength at the receiver and kept track of the consistency of these power levels. This set-up process is detailed within Section 4.1.4.

Background measurements

To account for any potential electronic drifts in the VNA system, backgrounds must be taken every four measurements to observe any variation in power due to the time taken to perform four measurements taking roughly thirty minutes. These background measurements allow us to monitor the drifts. These subsequent backgrounds may be used to ratio against measurement spectra if there are any significant differences between background sets. An average of the background taken for each head is presented in Section 4.1.2 in Figure 4.5.

The backgrounds provide the spectral envelope of the VNA system and through ratioing the data by the background measurements I extracted out the transmission spectra for the HWP. The sample must be removed from the optical path when taking background measurements and care must be taken to not knock optical elements in the setup resulting in potential misalignments. Placing the sample back into the optical path needs to occur at the same position it was removed from because a variation in performance could occur across the surface of the sample or when the sample is placed at slight angles with respect to the optical axis.

Standing waves

In order to remove standing wave issues, I placed both mounting stages and consequently each antenna head, on moveable stages. A standing wave is created from waves travelling in opposite directions being superimposed and the resulting wave appeared to vary in amplitude but not spatially. Each moveable stage is moved by predetermined steps to average out standing waves present at each frequency. The receiver and transmitter are moved by different increments which ensured that I could measure the standing waves completely because if they moved by the same amount then each harmonic of the standing waves would not be able to be measured and averaged out.

Rotation mechanism error

A rotation mechanism is used to measure the transmission response of samples at various rotation angles. The device is positioned in the centre of the test bench (see Figure 4.4) and is difficult to reach, thus when I repositioned the rotation angle I ensured that I had rotated to the correct angle by reading the value from the top of the device, not from the front. Reading the angle position straight on causes a parallax error of $\sim 0.5^\circ$ on the angle due to the position being determined by a sharp wooden point.

I have highlighted in the Sections above areas in the optical setup and methodology that require particular care and attention when performing optical characterisation measurements. In the following Sections I present the results of what happens when the optical setup is misaligned and the method required to correct the issues with the results from the realignments.

4.1.2 Optical configuration

The previous optical setup used for the characterisation of a HWP (Moncelsi et al., 2014) was created for a Fourier Transform Spectrometer (FTS). A 'cold finger', a structure which enables an optical device to be cryogenically cooled whilst held in the optical path, was used to cryogenically cool the Pancharactnam HWP to 120K because the material used (sapphire) has a large amount of absorption at room temperatures (Loewenstein et al., 1973). Therefore, that optical setup needed to also consider the need to cryogenically cool the device.

However, for the purposes of this experiment the metal mesh HWP being characterised has less stringent requirements to be cryogenically cooled due to the absorption properties of polypropylene (Patti et al., 2019) being lower, allowing it to perform very well at room temperatures. Additionally, the NIKA2 HWP is positioned as one of the first optical elements in the instruments optical chain and is held outside of the cryogenic stages. This further reduces the requirement to cryogenically cool it for this experiment.

In addition, the ultimate size of the HWP required for SO is too large to test cryogenically or optically on the current Cardiff testbed. Therefore, whilst I took inspiration from the setup used in the BLASTPol HWP (Moncelsi et al., 2014) I varied it slightly to account for conditions unique to a VNA setup which can be seen in Figures 4.2, 4.3 and 4.4.

To cover the frequency range required for the NIKA2 HWP, the optical configuration will need to account for switching multiple horns and frequency extender units, while maintaining optical alignment accuracy. The NIKA2 frequency bands are identified in Table 4.1 which will be used to define the HWP spectral requirements.

A single VNA receiver/transmitter combination will have a finite useable bandwidth and therefore a series of heads was required to cover the full NIKA2 range. The antenna heads

Central frequency [GHz]	Bandwidth [GHz]
150	82
260	107

Table 4.1 – NIKA2 band definitions and corresponding bandwidths (Pisano et al., 2022).

Configuration	VNA Horn/Extender	Central frequency [GHz]	Device	Measurements
Transmission	Flann standard gain 110-170 GHz horn 29240 R&S WR-6 Extender	150	NIKA2 HWP	HWP in Co-Pol orientation HWP in Cross-Pol orientation
Transmission	Q-Par standard gain 160-260 GHz horn VDI WR-4.5 Extender	150 and 260	NIKA2 HWP	HWP in Co-Pol orientation HWP in Cross-Pol orientation
Transmission	Flann standard gain 220-330GHz horn 32240– R&S WR-3 Extender	260	NIKA2 HWP	HWP in Co-Pol orientation HWP in Cross-Pol orientation

Table 4.2 – VNA measurements and the horn extenders required. See Table 4.3 for clarification on co-polarisation and cross-polarisation measurements.

and extenders to be used are shown in Table 4.2 along with identifying the VNA measurements required to fully characterise the spectral response of the HWP.

With the Cardiff setup, the VNA had a dynamic range of 75 dB and there were systematic measurement errors associated with the setup that will be discussed later in this Section. It is important to note that the frequencies shown in Tables 4.1 and 4.2 are for reference only, full sweeps over the frequency bands were performed.

The optical testbed used at Cardiff (Figures 4.3 and 4.4) used two off-axis parabolic mirrors and two planar-convex lenses in its configuration. This provided a Gaussian telescope beam (GBT) at the HWP position. The antenna horns were mounted on moving linear stages and positioned at pre-programmed positions using the LabVIEW interface. Both the transmitter and receiver linear stages were positioned at 20 mm whilst the third linear stage was positioned at 60 mm. This third linear stage is mounted to the test bench and was not used during this experiment, however, to ensure the lenses did not strike this stage when scanning I positioned it at 60 mm along the linear stage.

Each transitional stage had pre-determined positional steps to move through, which was stored in a motor configuration file. This file can be modified but the steps are determined by the frequency range of the horns and the requirement to move through at least ten wavelengths. Each motor file was read into LabVIEW which configured all stages before a measurement commenced. The VNA bench has been designed with repeatability in mind, therefore each component had a set position on the bench.

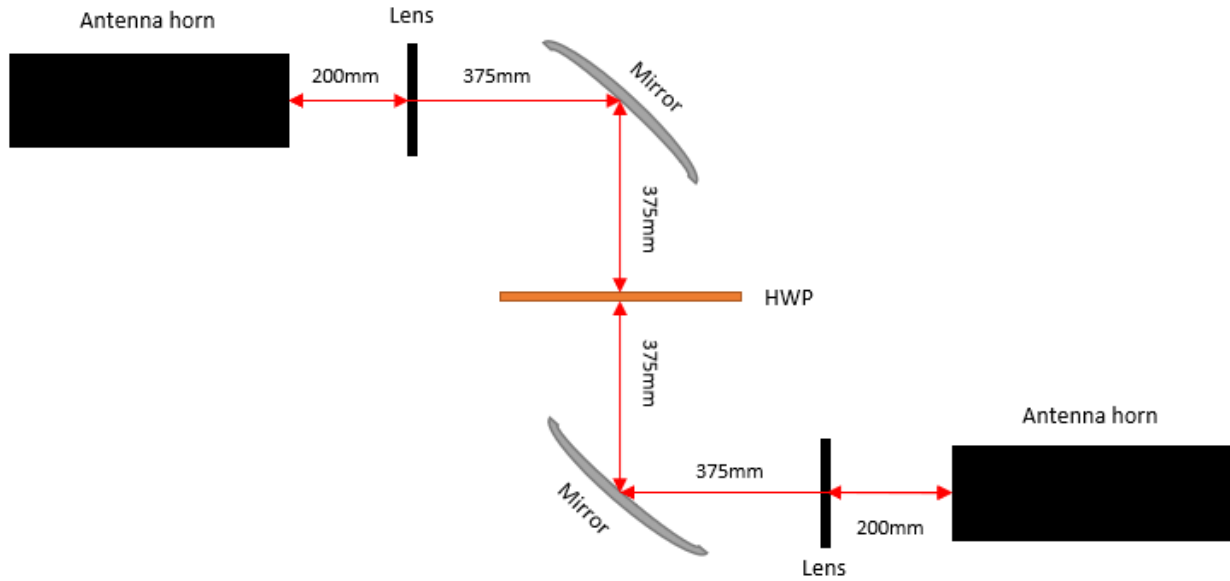


Figure 4.2 – Schematic diagram of the optical test bench for transmission measurements for the NIKA2 HWP. An antenna horn set is used (one transmitter and one receiver) where one antenna horn transmits a signal towards a planar-convex lens (located at its focal length, which for this experiment was 200 mm), the signal is reflected off a mirror, through the HWP mounted in a rotator. Once it has been transmitted through the HWP the beam is reflected off another mirror, through a planar-convex lens (again located at its focal length) where it is then detected by the receiver.

To fully characterise a HWP, two types of measurements were carried out; co- and cross-pol, Table 4.3 shows the orientation of each head needed to obtain each of these measurements. The cross-pol measurements are complimentary results to the co-pol; as one measures a maximum signal the other measures a minimum signal. Therefore, both types of measurements were needed for a full characterisation of the HWP because it allows analysis of the modulation efficiency, to identify if polarisation states are mixing (i.e., how well the HWP returns linear polarisation) and the amount of power reaching the detector. The modulation efficiency of the HWP is calculated through

$$\text{modulation efficiency} = \frac{T_{cp}^{0^\circ} - T_{xp}^{0^\circ}}{T_{cp}^{0^\circ} + T_{xp}^{0^\circ}} \quad (4.6)$$

where $T_{cp}^{0^\circ}$ and $T_{xp}^{0^\circ}$ are the transmission values of the co- and cross-pol data sets when the HWP is at the 0° angle.

It is important to note here that any deviation from the optical path for any of the optical elements will cause a change in the power received. This is because if any misalignment is present the beam will not be centred on the antenna waveguide causing a fraction of the power to be detected. If this is the case, then the characterisation of a device can also be incorrect and understanding its performance will be masked by the inaccuracies of the setup.

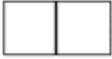








Measurement	Transmitter extender horn	HWP	Receiver extender horn
Co-pol at 0°			
Co-pol at 90°			
Cross-pol at 0°			

Table 4.3 – Orientation of antenna horns for co-pol and cross-pol measurements at given rotation angles for the HWP, as well as the HWP rotation position.

Setting the VNA bench into a co-pol configuration with each head orientated for vertical polarisation, the configuration seen in Figure 4.3 and 4.4, the first data set taken needs to account for the spectral response of the antenna horns and optics of the system. This will be referred to as the background spectrum and is obtained through scanning the VNA without the presence of the HWP. It was used as a reference spectrum and was what all subsequent spectra were ratioed against. It contains information on the systematics of the instrument being used to measure the devices under test.

All available background scans acquired over the multiple days of measurements were averaged for each frequency band. Their statistical dispersion (see Figure 4.5) was calculated and was used as an estimate for the uncertainty associated with the spectra collected. Using this method for the uncertainties associated with the measurements allows for the account of any drifts in the electrical response of the horns and other potential systematic effects in the system, such as thermodynamic condition changes and environmental effects. Figure 4.5 includes a 10σ standard deviation in each spectra to be able to observe the error associated with each frequency.

The HWP was then inserted into the system, position shown in Figure 4.4 and spectra were obtained every 5° interval, reduced to 2° around the maxima and minima, as a function of frequency resulting in a data cube. Each spectrum was measured at a given rotational angle and was obtained from the average of eighty-two scans with the receiver and transmitter moving

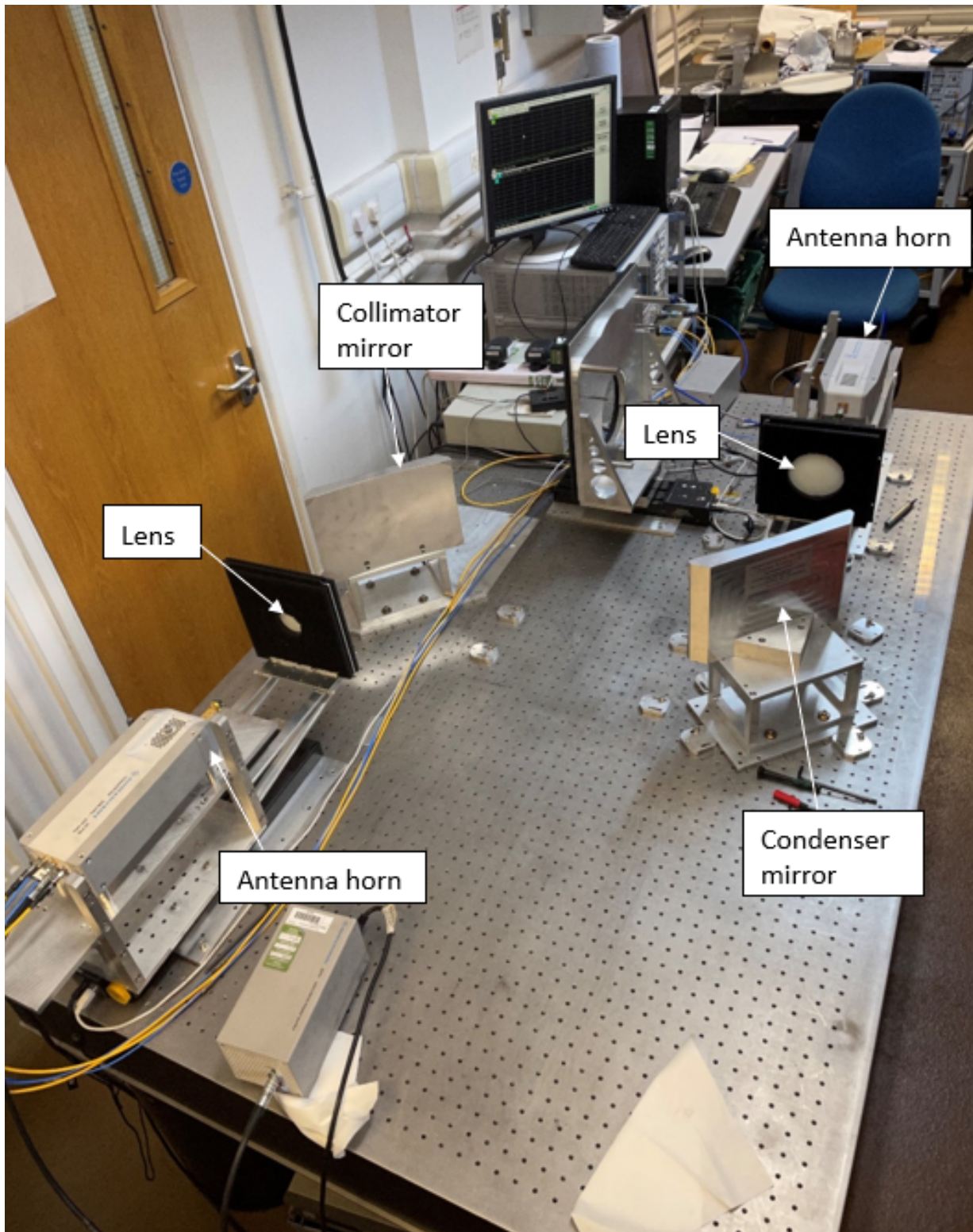


Figure 4.3 – VNA optical bench setup in vertical polarisation orientation and co-pol setup. This setup generates a Gaussian beam and, in this configuration, would generate a vertical polarisation background for co-pol. This photo is complimentary to the schematic given in Figure 4.2.

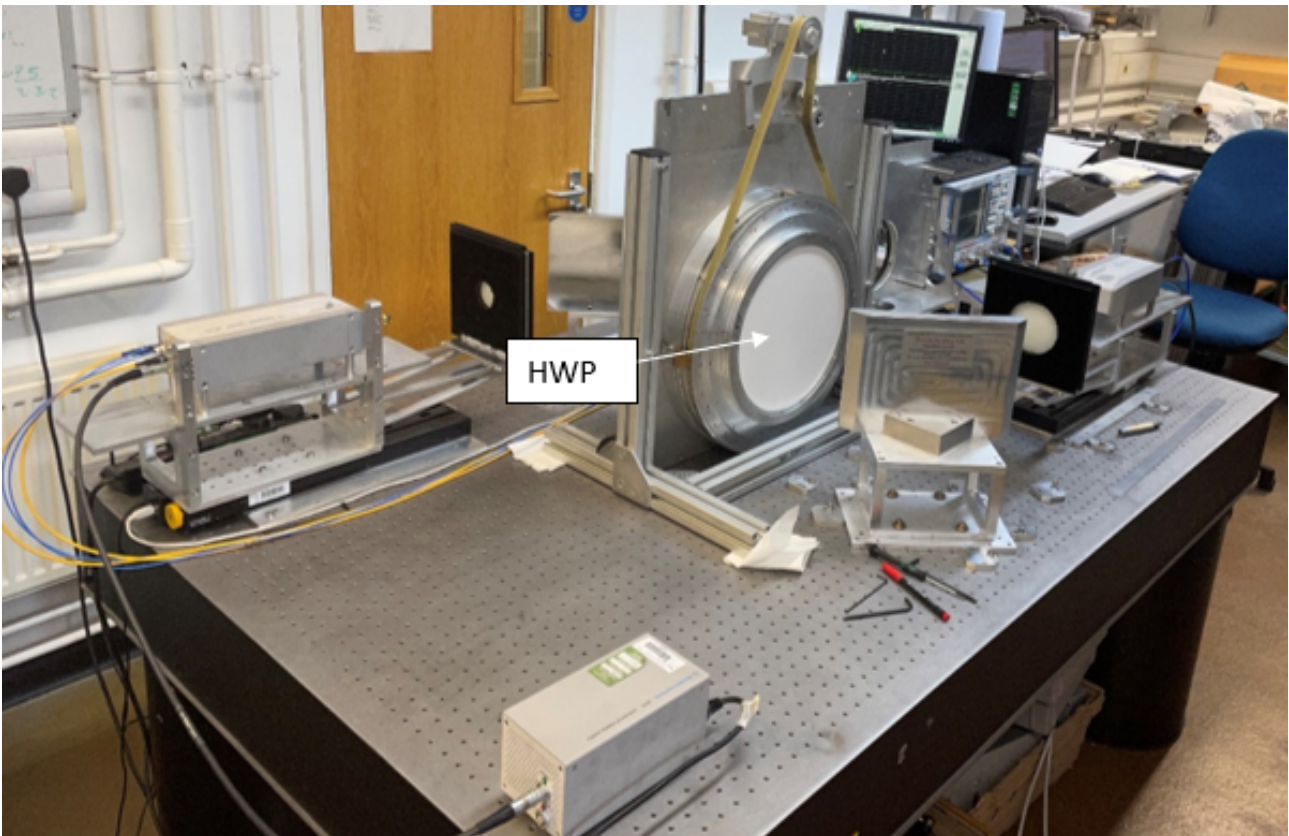


Figure 4.4 – VNA optical bench setup in vertical polarisation orientation with the NIKA2 HWP placed in the beam path. The HWP position is marked to ensure repeat placement. This photo is complimentary to the schematic given in Figure 4.2.

forward at different increments to account for standing waves. The spectra were then divided by the background data sets, obtaining the transmission spectra of the HWP as a function of frequency.

To obtain the cross-pol data cubes the receiver was rotated by 90° and mounted onto the Y plane (see Figure 4.13) to be fixed into position. This rotation allowed vertical polarisation to be measured. The same method above was applied to obtain the spectra over the rotational angles.

Over the course of two weeks data cubes were obtained for both co-pol and cross-pol transmissions, shown in Figures 4.6 and 4.7. These show the full data sets including the intermediate angles where the data was taken roughly every 5° between 0° and 360° . Figures 4.8 and 4.9 show the data sets of angles close to the maxima and minima angles to for clarity.

The cross-pol data cube in Figure 4.7 is very spikey when compared to the co-pol data cube in Figure 4.6 which can be attributed to the fewer rotational angles being plotted. The cross-pol dataset has only eight sets of spectra compared to the eighty-seven spectra taken for co-pol. If there were the complete eight-seven sets of spectra the spikes would be less defined, however, the overall values shown would not change very much which indicate a much lower transmission

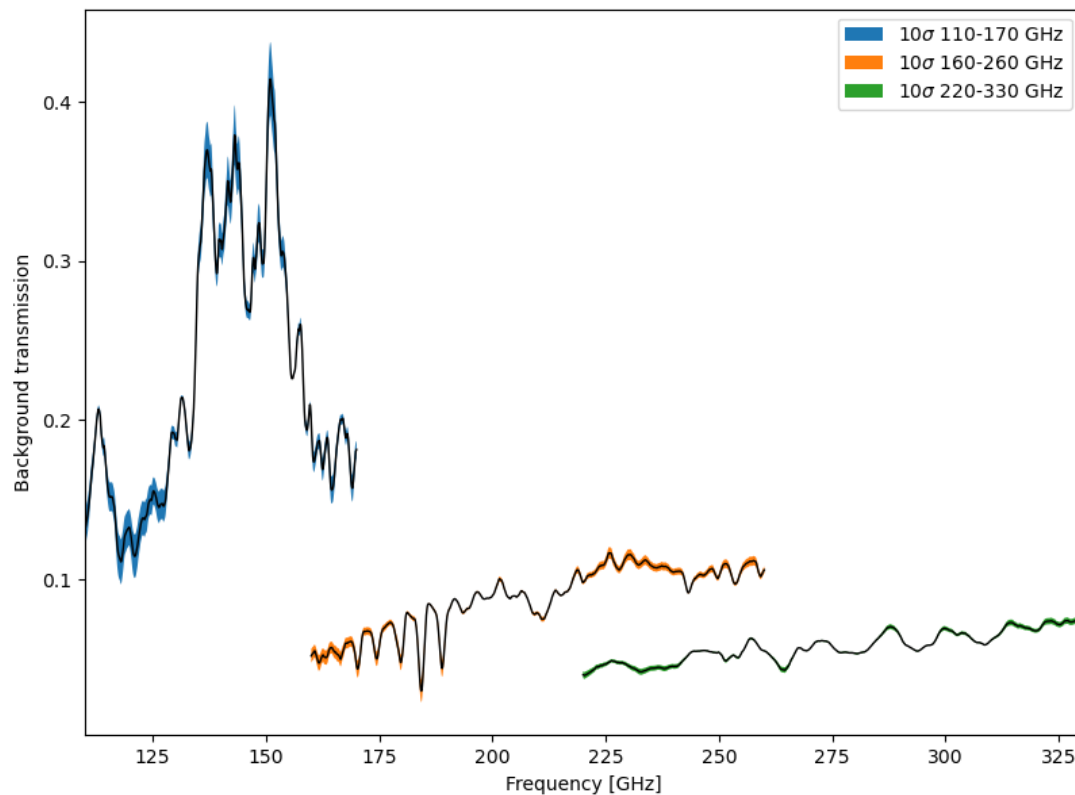


Figure 4.5 – Mean background spectra (black lines) as a function of frequency. These were calculated by averaging all the background spectrum measured during the experiment. The error bars, denoted by the blue, orange and green coloured regions, are quantified as the statistical error on the mean and to be able to observe the error it has been multiplied by 10.

across the frequency bands (approximately 50%) compared to the co-pol transmission.

A HWP rotates linear polarisation by 2θ , with θ as the incident polarisation angle, therefore through 360° rotation measurements there are four maxima and four minima. The angles assigned to the spectra in Figures 4.8 and 4.9 do not coincide with the maxima and minima angles typically noted in literature (Moncelsi et al., 2014). This is because the HWP is arbitrarily placed into the rotator, and thus, the angles are for reference only and correspond to the angles marked on the rotator. The rotation step size changed from 5° to 2° near the maxima and minima angles, allowing us to identify if the HWP was passing through those angles and what the level of transmission was.

If I were to take slices along the frequency axis in Figures 4.6 and 4.7 I would measure the modulation function. This is because these slices show how well the HWP, at each frequency, rotates the linear polarisation. Through the combination of these slices from both the co- and

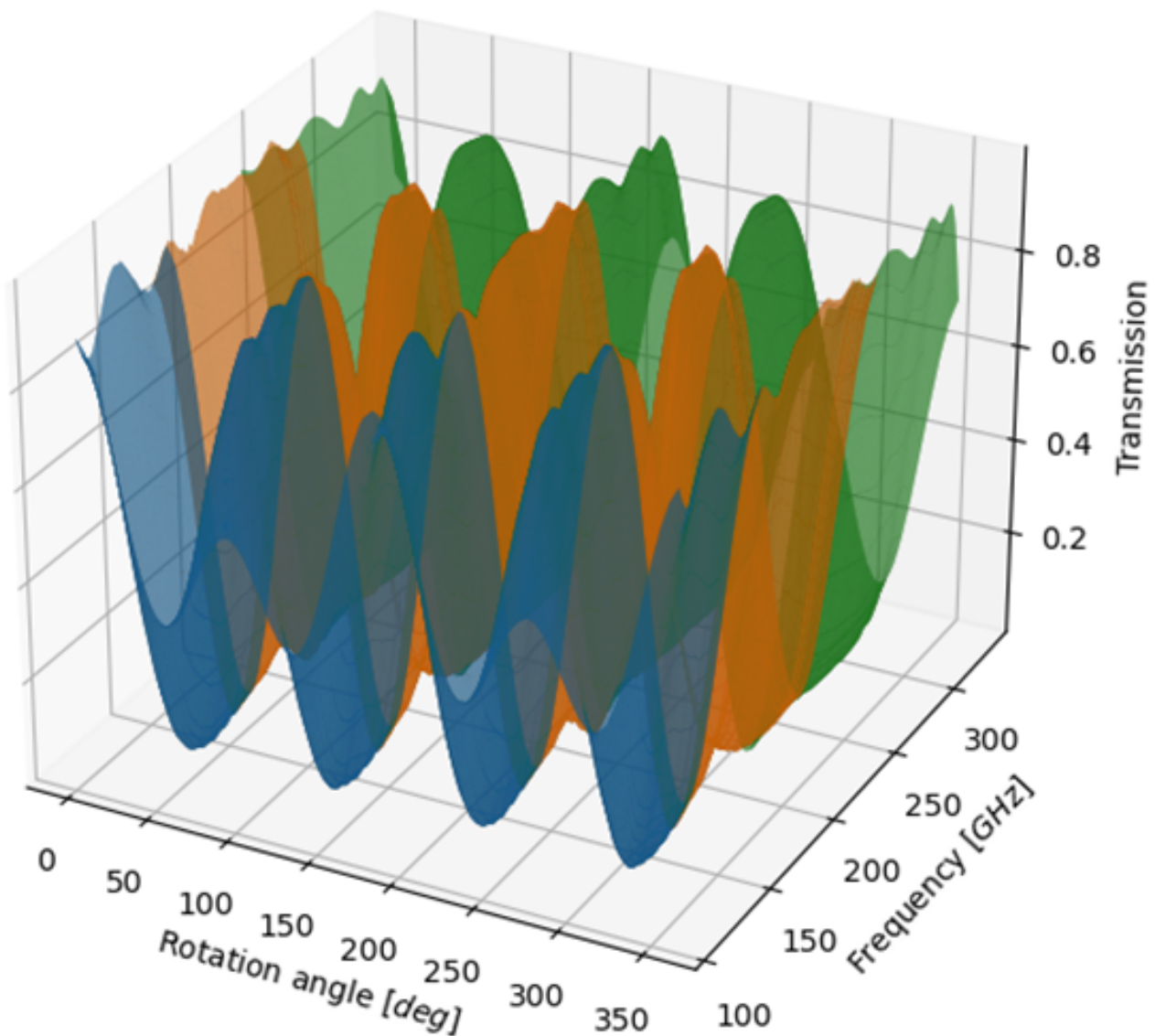


Figure 4.6 – Co-polarisation data cube showing all three frequency ranges (blue is 110-170 GHz, orange is 160-260 GHz and green is 220-330 GHz) and how the HWP performance varies over them. Plotted are the spectra as a function of rotation angle and frequency. In this plot all 87 spectra measured in the co-polarisation configuration are presented.

cross-pol data cubes I can start to fit models to them and compute the Mueller matrix parameters needed to characterise the HWP (as seen in Chapters 2 and 3).

If instead I took slices along the rotation angle axis I measure the transmission spectrum of the HWP at each angle. Several of these slices are shown in Figures 4.8 and 4.9 where structure present from the experiment can be observed. For example, the undulations observed from the 110-170 GHz band can be attributed to a phenomenon known as Fabry-Perot fringes and is a result of reflections between the surface of materials in the setup, i.e., the HWP. These fringes

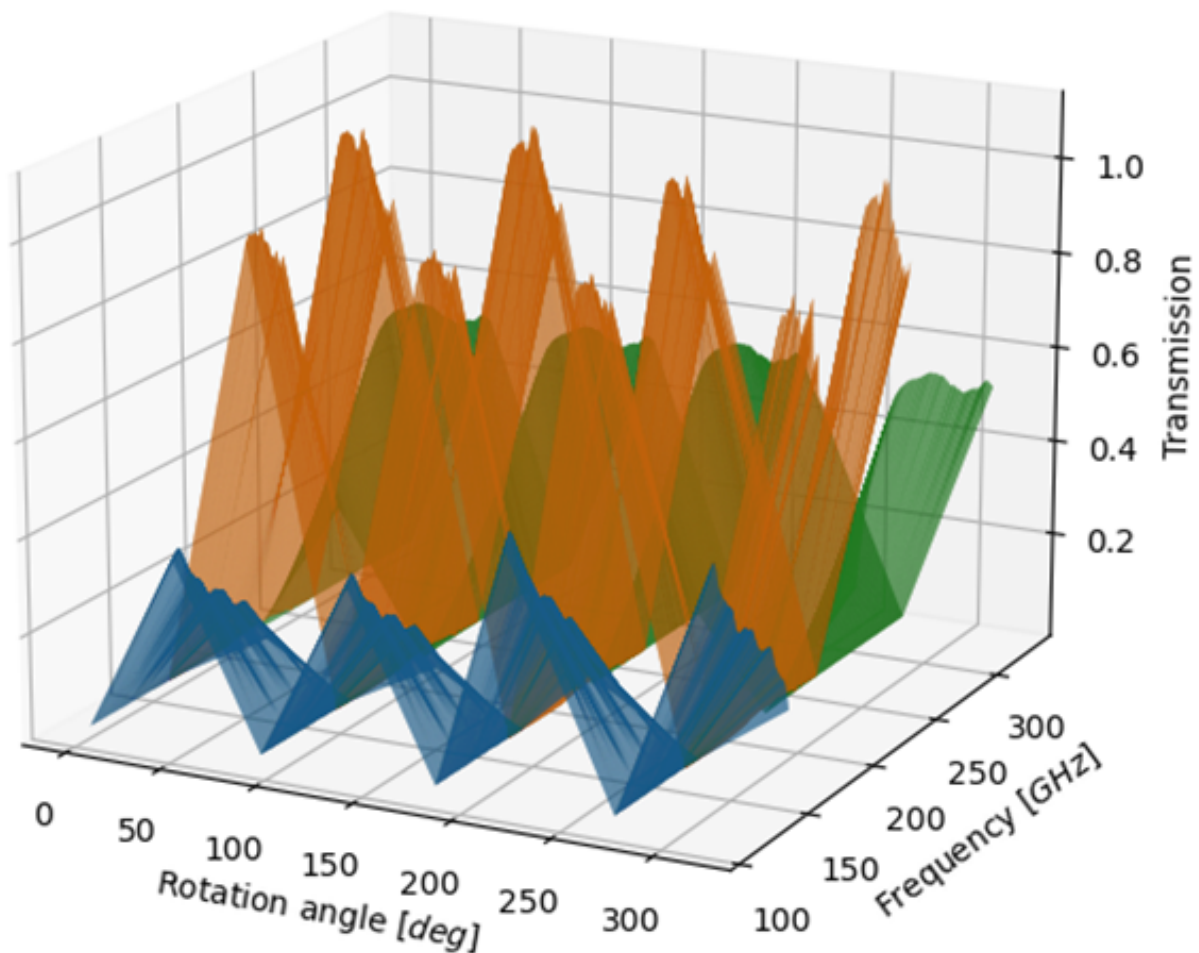


Figure 4.7 – Cross-polarisation data cube showing all three frequency ranges (blue is 110-170 GHz, orange is 160-260 GHz and green is 220-330 GHz) which presents how the HWP performance varies over them. Plotted are the spectra as a function of rotation angle and frequency. In this plot only 8 spectra in the cross-polarisation configuration are presented, these being the angles around the maximum and minimum plots in the HWPs rotation. Through plotting these values the limits of the HWPs performance can be observed as it rotates through 360°.

have been greatly reduced by applying an ARC to both sides of the HWP. The transmission across the 150 GHz and 260 GHz bands was measured to be ~ 0.92 and ~ 0.96 for the co-pol maxima spectra whilst the transmission across the NIKA2 150 GHz and 260 GHz bands was measured to be ~ 0.77 and ~ 0.62 respectively for the cross-pol maxima spectra. For the maxima transmission these values should equal 1, indicating that there is a loss in transmission from the HWP especially during the cross-pol measurements with the transmission down $\sim 30\%$.

In both Figures 4.8 and 4.9 a dip in transmission was observed at 200 GHz. This dip is caused by the design of the HWP. As NIKA2 operates over two separate frequency bands (refer to Table 4.1) the HWP is required to perform optimally over both bands. To enable this the HWP design

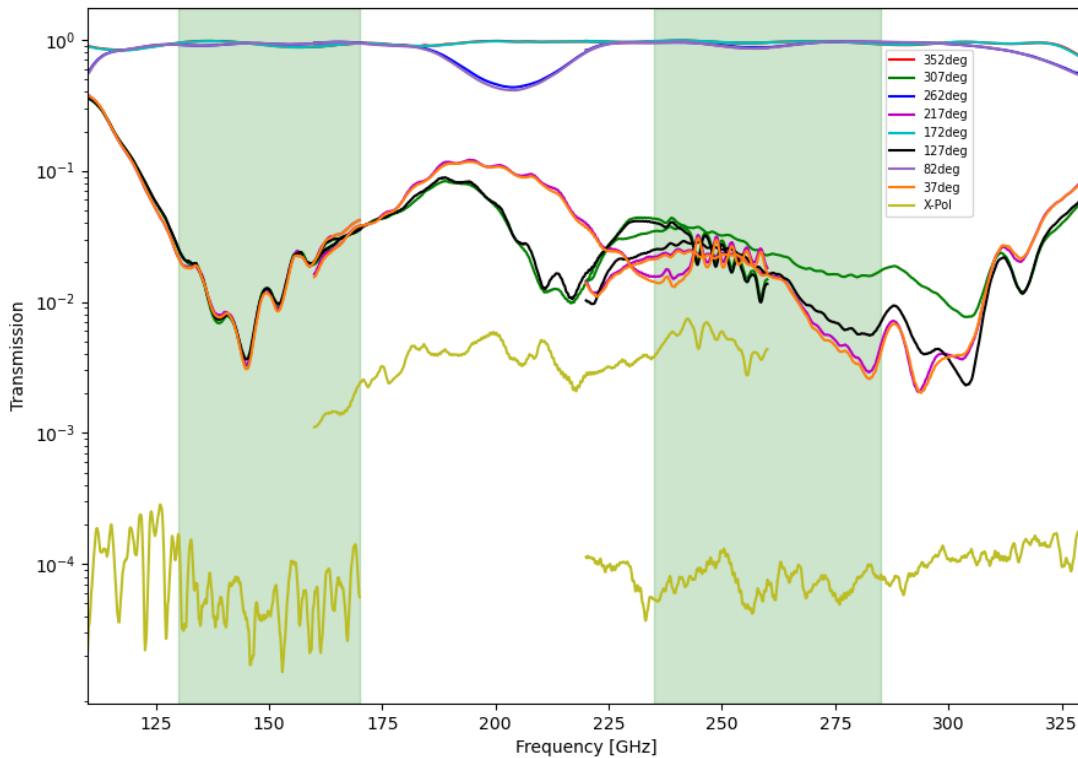


Figure 4.8 – Co-pol maximum and minimum transmission spectra, which represent the HWP rotation positions where the maximum and minimum signals were detected. The yellow curves denote the background x-pol measurement, which is the signal detected with polarisers P1 and P2 orthogonal to each other and the HWP not in the optical path.

parameters were chosen which saw that an effective phase shift of 180° is maintained over both bands but this results in a reduction in transmission between bands.

From Figure 4.9 it can be observed that there was poor continuity across the three frequency bands, with roughly a 2.5 dB difference in the maxima values. Due to the nature of cross-pol measurements (one horn required a rotation of 90° about the optical axis) it was believed that the difference observed was a result of a combination of misalignments in the optical setup and/or uncorrected inherent drifts in the VNA.

A source for misalignment in this setup would arise from the antenna horns not rotating about the optical axis as the optical configuration changes from co- to cross-pol. If this were the case, a loss in power would be seen because the signal would not be received in the centre of the antenna horn extender, instead a fraction of power would be striking the edge of the antenna extender. A full exploration of the misalignment is discussed in Section 4.1.3 along with methods used to correct for them.

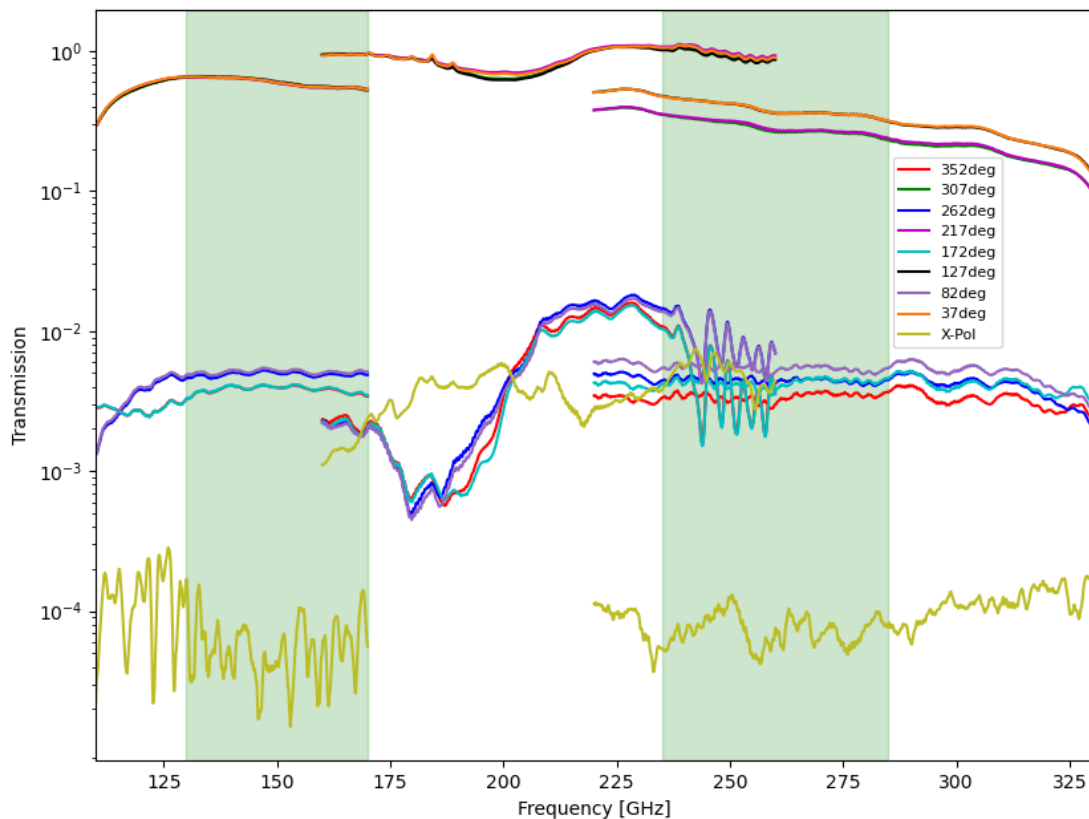


Figure 4.9 – Maximum and minimum transmission spectra produced by the NIKA2 HWP in the cross-pol configuration using a VNA test bench. The x-pol levels are presented as the yellow curves. From this Figure a disconnect across the frequency bands is noted in the maximum spectra with approximately a 2.5 dB difference in their amplitude. This is believed to be due to misalignment in the optical setup.

Using the spectra presented in Figures 4.8 and 4.9 in equation (4.6) the modulation efficiency was measured and plotted (seen in Figure 4.10) and was found to be ~ 0.993 and ~ 0.991 across the 150 GHz and 260 GHz working bands respectively, with its expected value to be 1, producing a small deviation from its expected value. In particular, the 160-260 GHz section loses 4% of modulation efficiency from the HWP not being designed to create the perfect 180° phase difference in this frequency region. However, as the cross-pol configuration was expected to have a misalignment to its optical system I have also plotted the modulation efficiency of the HWP using the data obtain at a rotation angle of " 45° " because this will use the maximum transmission spectrum from the cross-pol data set. The modulation efficiencies calculated from this was ~ 0.812 and ~ 0.618 for the 150 GHz and 260 GHz bands respectively, a much lower modulation efficiency than previously calculated.

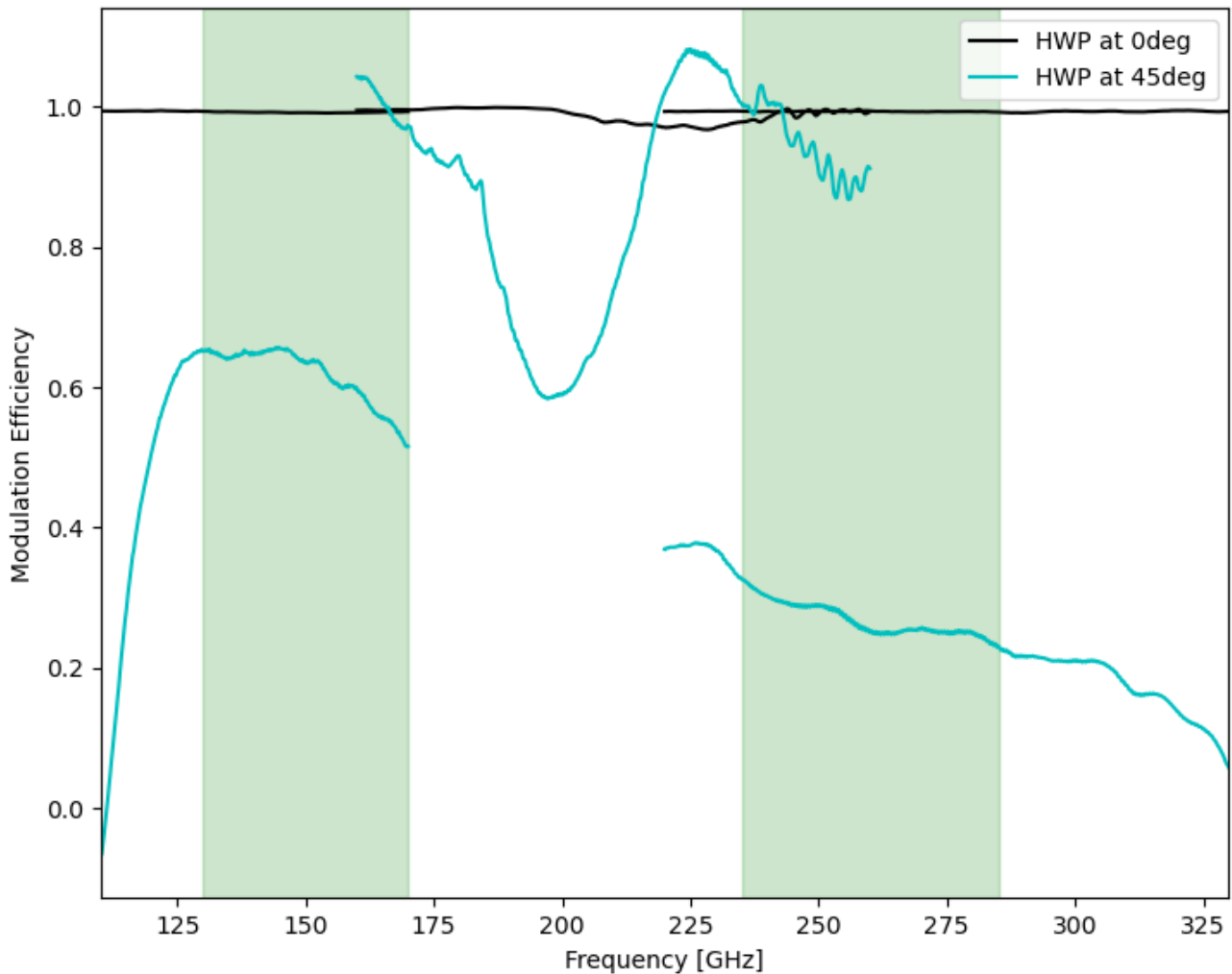


Figure 4.10 – Modulation efficiency of the NIKA2 HWP as measured on the VNA system at Cardiff University. It is important to note here that it has been obtained using the results seen in Figures 4.8 and 4.9. Using equation (4.6) produces the black curve producing an average modulation efficiency of 0.993 and 0.991 over the 150 GHz and 260 GHz bands respectively. However, this is calculated from a maximum spectrum from the co-pol data set and a minimum spectrum from the cross-pol dataset. As it was assumed that the cross-pol configuration was misaligned I have included the modulation efficiency measured at the "45°" rotation angle which is presented as the cyan curve in this Figure. The modulation efficiency measured using these spectra is 0.812 and 0.618 for the 150 GHz and 260 GHz bands respectively, indicating a much worse efficiency than previously expected. The shaded green areas indicate the working bands of the NIKA2 experiment.

The Mueller parameters in Figure 4.11 were obtained by injecting the data cubes from Figures 4.6 and 4.7 into the Mueller matrix pipeline described in Chapter 3 where they were compared against a model and sets of parameters were fit to both the data and model. A larger spread in the off-diagonal parameter values is noted across the 110-170 GHz and 220-330 GHz frequency ranges caused by lower transmission across the frequencies seen in the cross-pol measurements.

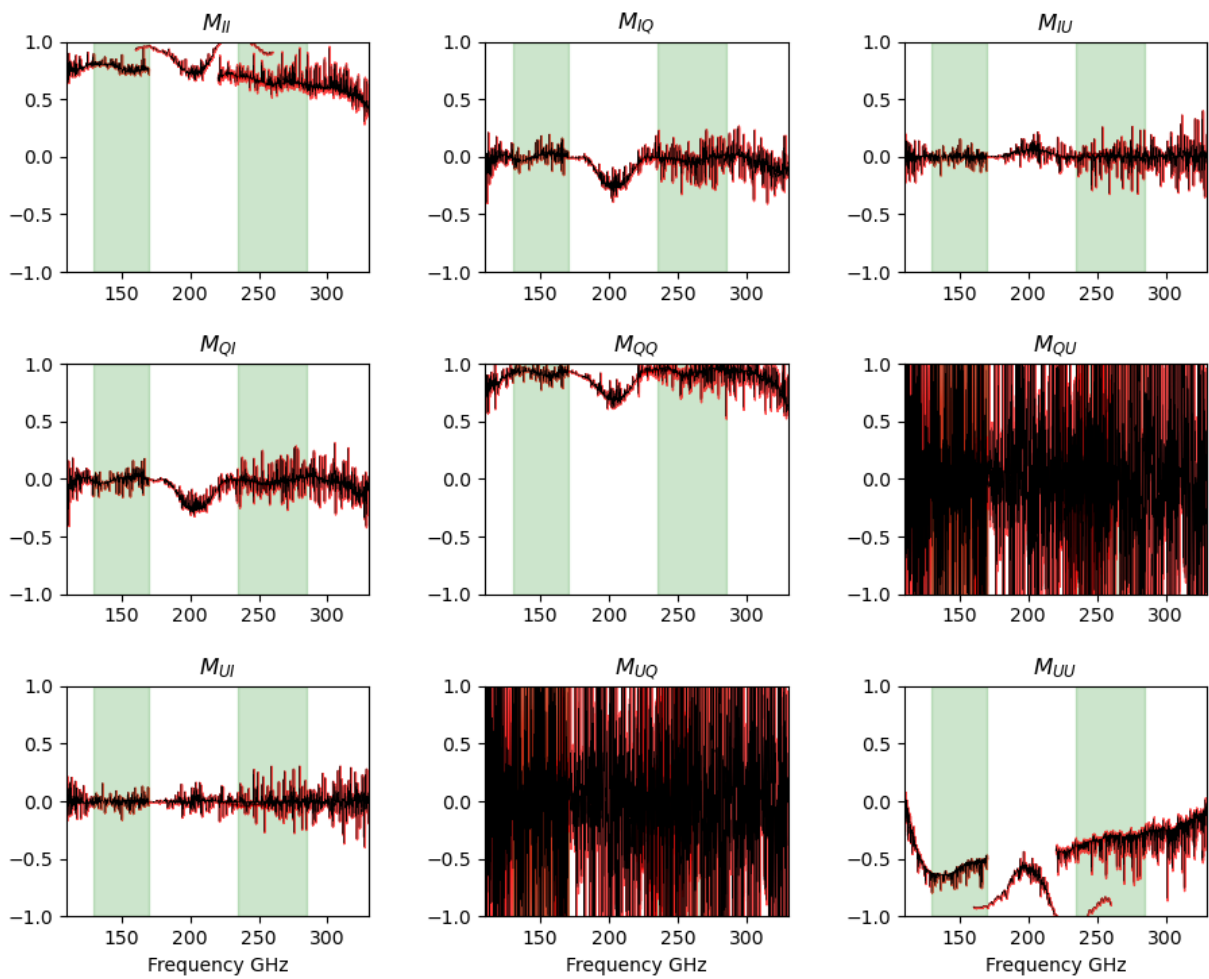


Figure 4.11 – Mueller matrix coefficients (black line) for a given angle (θ°) generated using the MCMC pipeline developed from the method described in Chapter 3 and injecting 'misaligned' cross-pol data. This only uses the maximum and minimum spectra from both the co-pol and cross-pol data sets. The error bars are shown in red and are the standard deviation in the calculated Mueller matrix coefficients. The working bands of the HWP have been included as the green shaded regions.

A large variation is observed in the M_{QU} and M_{UQ} parameters. These parameters describe the polarisation rotation arising if leakage from one polarisation to another was occurring. The values observed in Figure 4.11 indicate that the HWP was mixing the linear polarisation states and the receiver was therefore not measuring lower transmission signals. However, this could be arising from the optical system itself not being correctly aligned therefore causing the transmitted polarisation signal to be rotated. The large spread in these parameters were also attributed to the number of rotation angles fitted by the MCMC. For the coefficients in Figure 4.11 only eight transmission spectra measured at different angles were injected into the MCMC pipeline, this was seemingly too few points to constrain the model to the data sets.

The diagonal parameters M_{II} and M_{UU} describe the transmission of linear polarisation of vertical (horizontal) and -45° ($+45^\circ$) states respectively. Due to the nature of the Mueller matrix, M_{UU} also showcases how well the phase difference of the HWP was performing to its expected value of 180° by how close it is to the value of -1 . Both M_{II} and M_{UU} were seen to have discontinuity between the frequency bands due to the discontinuity between the cross-pol measurements seen in Figure 4.9. From the alignment checks the discontinuities will be corrected for and no longer seen in the Mueller matrix graphs. The results seen in the 160-260 GHz band in Figure 4.11 indicate that if corrections were made to the predicted alignment issues the HWP would produce Mueller matrix parameters close to the ideal parameters; diagonal values will be close to 1 or -1 and off diagonal terms would be near 0 for the working bands.

From generating the Mueller matrix parameters, other parameters that help understand the performance of a HWP can be calculated and they are the optical efficiency, η , and the polarisation efficiency, ε . The optical efficiency describes how efficient the HWP is at transmitting the radiation through and is calculated from equation (2.12).

For the values provided in Figure 4.11 the optical efficiency of the HWP across the frequencies measured is seen in Figure 4.12 and calculated to be 0.953 and 0.964 across the 150 and 260 GHz bands respectively. These values indicate a high percentage of light was transmitted through the HWP over these frequency bands. While the polarisation efficiency described how well the HWP transmitted and rotated the linear polarisation signal and can be obtained through implementing equation (2.11).

From the results provided in Figure 4.11 I calculated the polarisation efficiency of the NIKA2 HWP, averaged over each frequency band, to be 0.884 and 0.821 for the 150 and 260 GHz bands respectively. These values appear larger than the data in Figure 4.12 would suggest for these frequency bands as the polarisation efficiency (magenta line) appears to have an amplitude of approximately 0.7 in the 260 GHz band, however, the 160-260 GHz data provides polarisation efficiencies greater than 0.9 which were accounted for in the calculation of the polarisation efficiency.

From the initial results presented in this Section it was clear that there were issues with the optical setup of this experiment. In the following Sections, methods performed to check the alignment and correct for any issues found are described.

4.1.3 Performing realignment of test bench

As previously discussed when setting up an optical bench there is a call for great care and attention in handling and placing each element in the optical chain. This is because small deviations in the correct alignment can cause the beam to deviate from the optical path and reduce the power being detected. For this experiment as the HWP needs to be measured using three

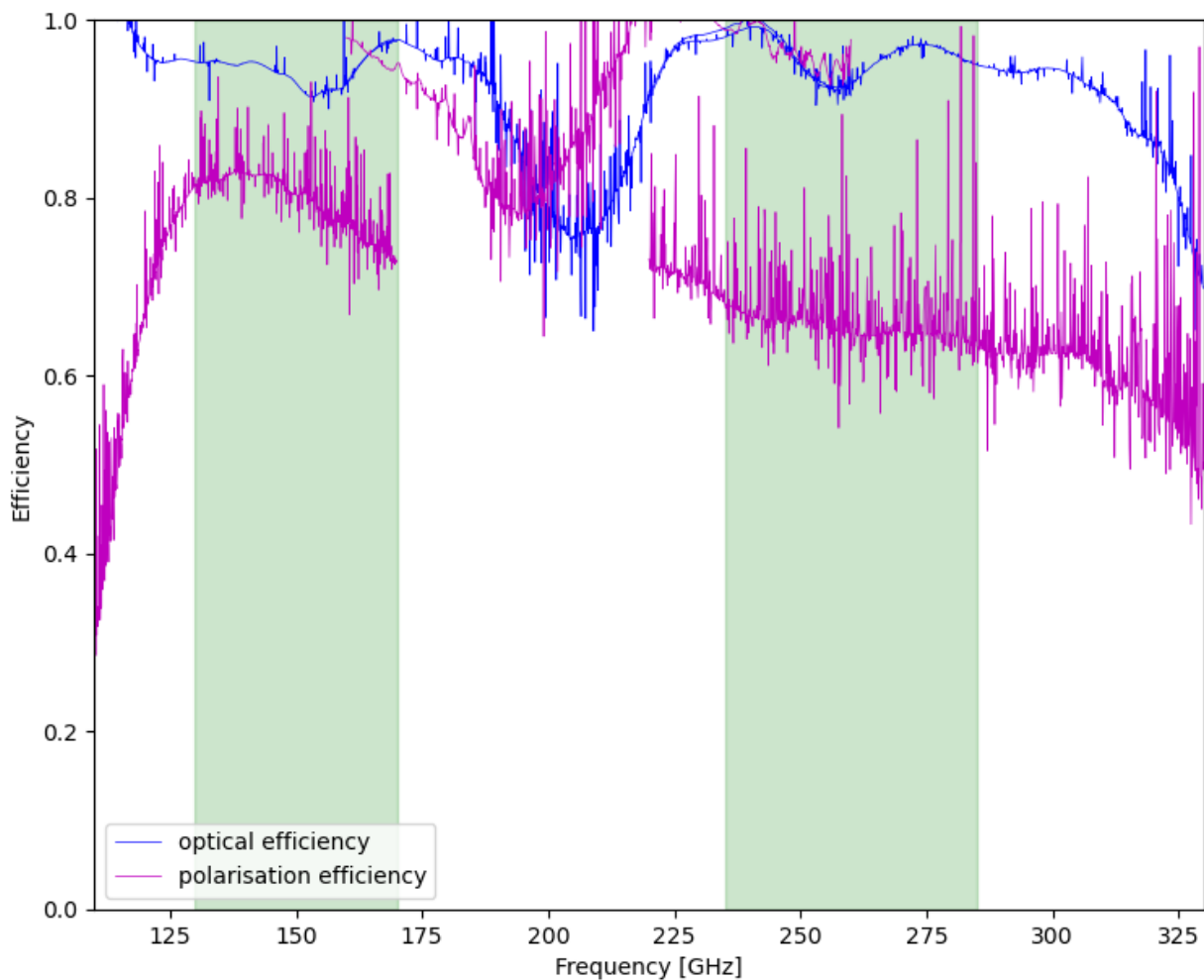


Figure 4.12 – Optical (blue curve) and polarisation (magenta curve) efficiency of the NIKA2 HWP as measured on the VNA system at Cardiff University. It is important to note here that this has been obtained using the results seen in Figures 4.8 and 4.9. The shaded green areas indicate the working bands of the NIKA2 experiment. The average optical efficiency across the two bands was calculated to be 0.953 and 0.964 for 150 GHz and 260 GHz respectively. The average polarisation efficiency across the two bands was 0.884 and 0.821 for 150 GHz and 260 GHz respectively.

different VNA antenna heads (see Table 4.2) there was an even greater need to ensure that the nature of the optical test bench was known to greater detail.

Analysing the results seen in Figures 4.6 to 4.9, we confirmed that there are alignment issues in this setup. This was concluded from the difference seen between the co- and cross-pol measurements. If the difference seen between the frequency bands were due to the HWP device itself then the difference would also be present in the co-pol measurements, however, they were not. Therefore, checks were required to be carried out to locate the alignment problem.

The VNA test bench comprised of a few optical components, each of which could have contributed to the differences seen in Figures 4.6 to 4.9. Therefore, optical alignment checks on

the following components were performed to verify and adjust each optical device according to the procedure described in Sections 4.1.3 to 4.1.3. The optical elements checked were; transmitter lens, receiver lens, collimating mirror, condensing mirror, each antenna horn and extender being used, transmitting mounting stage and receiver mounting stage.

Height measurements of the antenna horns to the optical axis

Each antenna head sat on a mounting stage. This stage allowed the head to be secured into place in both the X and Y planes (see Figure 4.13). When the head rotated from one plane to the other it was paramount that it rotated about the same point on the optical axis. This ensured that the heads stayed aligned to the optical axis.

To confirm if each antenna head rotated around the optical axis an initial measurement of the height of each antenna head with respect to the optical bench was performed. Ideally this measurement would be equal to the optical axis height, however, this may not be the case. Through measuring the height, changes to each head's feet can be made to either increase or decrease the height to bring the heads back to the optical axis height, which for this optical test bench was 237.5 mm.

To identify if changes were needed, the height of the optical bench to the centre of the horn was measured. This was done in both X and Y planes and the difference between the recorded heights and optical axis height was calculated and included in Table 4.4 and was repeated for each antenna head. This procedure was done for an extra antenna horn which was not included in Table 4.2 and was carried out and recorded for completeness but will not be used in further work discussed here.

To bring the antenna horns to the same height as the optical axis, the feet for each antenna head were adjusted in both position and height. Changing the height of the antenna head in the Y plane translates to a lateral change in position for the heads in the X plane. Therefore, the holes originally drilled into each mounting plate were made rectangular. The rectangular holes were made long enough to be able to account for the largest change in height needed for the Y plane. For the X plane, the feet were simply changed to account for a reduction or increase in the height as seen fit from the results in Table 4.4.

Along with measuring the antenna horn heights, the height from the centre of each mirror to the optical bench was measured. The results are shown in Table 4.5 and compared to the optical axis height.

The collimator refers to the mirror closest to the transmitter and the condenser refers to the mirror closest to the receiver, which was the antenna horn on the right in Figure 4.3 for this setup. The results from mirror height measurements were consistent with the optical axis height and therefore no changes were made.

Model of antenna horn	Transmitter (TX) or receiver (RX) horn	Height measurement in S-Pol position (mm)	Difference between optical axis height (mm)	Height measurement in P-Pol position (mm)	Difference between optical axis height (mm)
Q-Par standard gain 70-110 GHz horn – R&S WR-10 Extender	RX	237.82	+0.32	239.04	+1.54
Q-Par standard gain 70-110 GHz horn – R&S WR-10 Extender	TX	237.36	-0.14	238.005	+0.505
Flann standard gain 110-170 GHz horn 29240 R&S WR-6 Extender	RX	236.58	-0.92	240.35	+2.85
Flann standard gain 110-170 GHz horn 29240 R&S WR-6 Extender	TX	237.13	-0.37	240.25	+2.75
Q-Par standard gain 160-260 GHz horn VDI WR-4.5 Extender	RX	236.85	-0.65	237.75	+0.25
Q-Par standard gain 160-260 GHz horn VDI WR-4.5 Extender	TX	236.84	-0.66	236.67	-0.83
Flann standard gain 220-330 GHz horn 32240 – R&S WR-3 Extender	RX	236.93	-0.57	240.13	+2.63
Flann standard gain 220-330 GHz horn 32240 – R&S WR-3 Extender	TX	236.88	-0.62	239.95	+2.45

Table 4.4 – Height measurements of each antenna horn from the top of the optical bench to the centre of the waveguide. This is done in both vertical and horizontal positions and the difference between the optical axis is calculated.

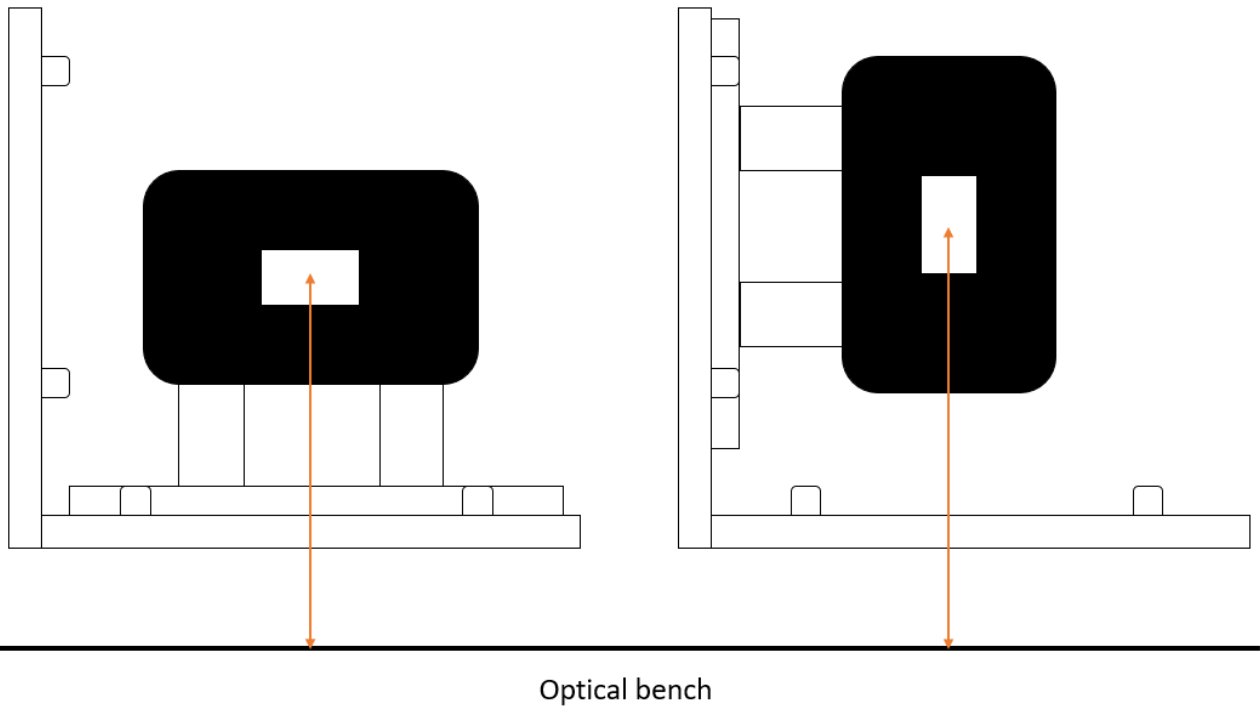


Figure 4.13 – Measuring the optical height from the centre of the horn to the top of the optical bench in left) X-axis and right) Y-axis planes. It is important to note that the structure shown is held on mounting stages and therefore is further from the bench than denoted in the diagram.

Mirror	Centre (mm)	Optical axis height (mm)	Difference (mm)
Collimator	237.44	237.50	-0.06
Condenser	237.55	237.50	+0.05

Table 4.5 – Height measurements for the collimator (closest to the transmitter) and condenser (closest to the receiver) mirror centres and compared to the height of the optical axis.

Rotating about the optical axis

A crucial aspect of any experimental setup is that all optical elements in the chain align to the optical axis. The optical axis is defined as the axis to which light propagates down. If any element is not central on this axis reductions in power arise. For cross-pol measurements this is even more prevalent because of the added complexity of the receiver rotating about the optical axis. If this rotation causes the centre position of the antenna head to be different when in the X or Y plane, the receiver will not detect the full power of the system.

To find the centre point in each plane, the distance between the centre of each dowel pin on the mounting stage and marked the halfway point in both X and Y plane were measured first (seen in Figure 4.14). The centre point between the dowel pins is found because the dowel pins are used to secure the antenna plates to the mounting stage meaning the centre point aligns with the

centre of the antenna horn.

Next, the distance between the found centre point to the corner of the mounting structure (as shown in Figure 4.14 (righthand side image)) is measured for both X and Y planes and recorded in Table 4.6. Ideally this value in both planes should be the same.

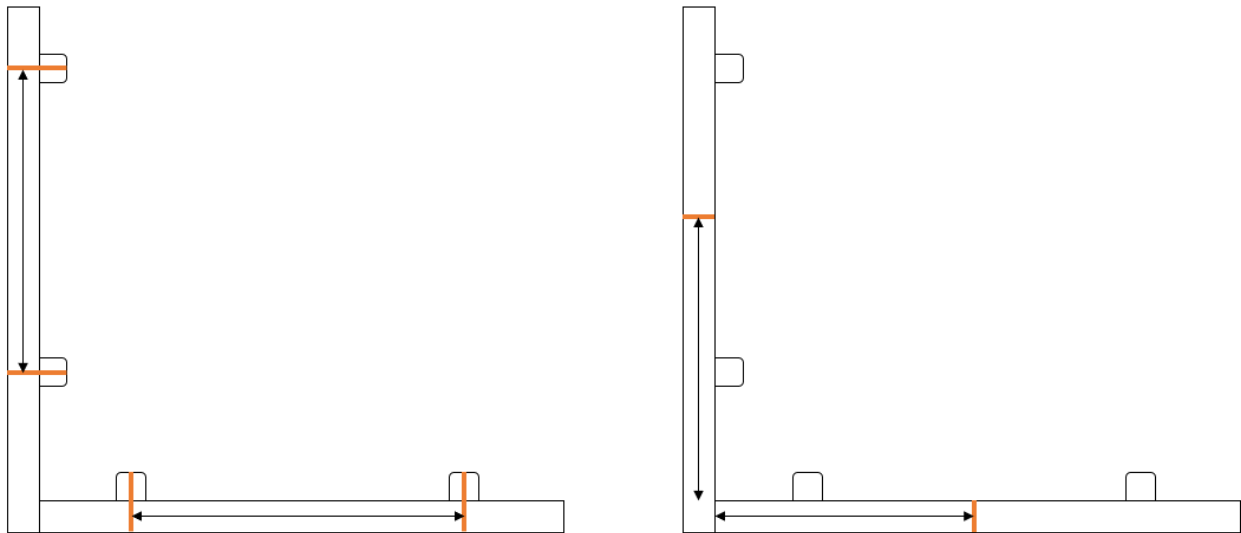


Figure 4.14 – Schematic of the measurements performed to find the position of the centre of rotation the antenna horns should be rotating about when moving from a co-pol configuration to a cross-pol configuration. Left) Finding the centre point between the dowel pins in both X (horizontal) and Y (vertical) planes. Right) Measuring the distance from the centre point, found in the left image, of the X and Y plane to the edge of the mounting plate.

Mounting structure	Centre of X axis (mm)	Centre of Y axis (mm)	Distance from edge to centre X axis (mm)	Distance from edge to centre Y axis (mm)
TX	47	47	69.5	72.5
RX	47	47	70	72

Table 4.6 – Measurements of the centre point between the dowel pins for both X and Y plane on the mounting stage and distance between corner of mounting stage to each centre point.

The distance from the corner to each centre point should be identical, therefore, a 2 mm shim was added to the X plane, indicated in Figure 4.15. Marks were added to the mount structures to use as reference points for alignment procedures discussed in Section 4.1.3.

Aligning the centre of the feedhorn to the optical axis in both X and Y orientations

Each antenna head had a feedhorn attached to it and this was used to guide the power to be detected towards the receiver. To detect the maximum amount of power in the system the feedhorn

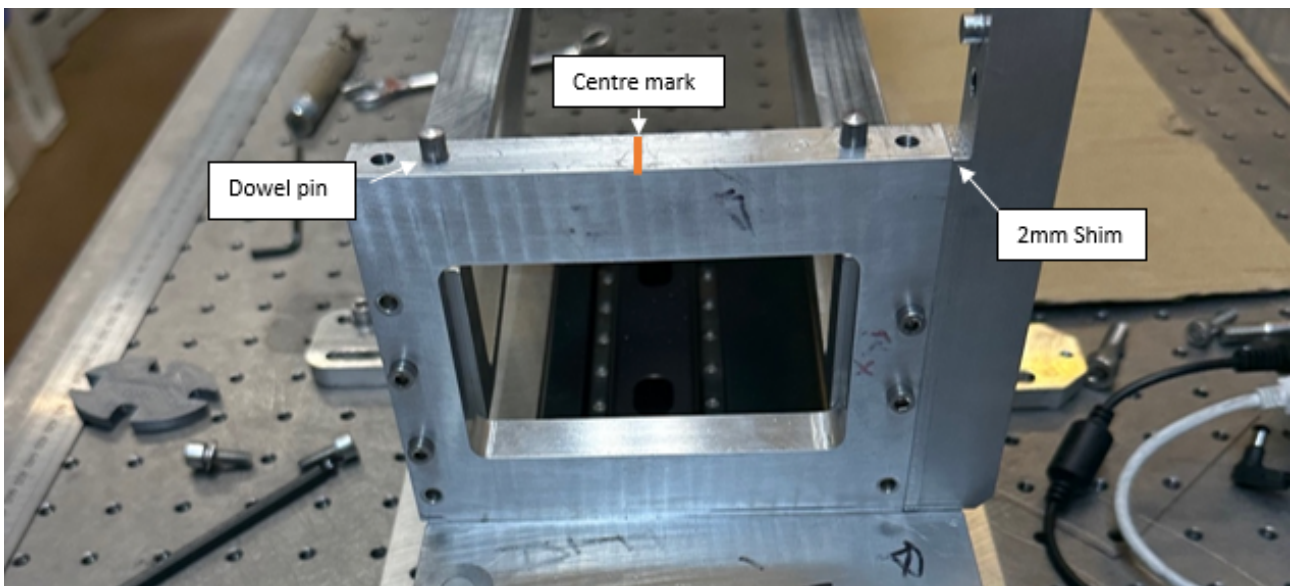


Figure 4.15 – Antenna mounting structure with a 2 mm shim added to the X-axis to correct the centre of rotation position. A centre mark for the X-plane has also been marked.

needed to be fully aligned to the optical axis. The feedhorns used in this experiment vary in size depending on the frequency ranges measured due to the size of the wavelength associated with them. For example, the feedhorn attached to the 110-170 GHz antenna heads were much larger than the feedhorns attached to the 220-330 GHz antenna heads. Therefore, the alignment checks were even more important for the 220-330 GHz antenna heads because even the smallest misalignment in the system can cause a reduction in power detected.

To align the centre of each antenna horn extender, a laser with a cross hair was placed on a jack set at the optical axis height at one end of the bench and pointed towards the antenna mounting structure. The laser was aligned to the centre marks shown in Figures 4.15 and 4.16 and a target was added at the other end of the bench where the centre of the cross hair fell. To place this target, both height and lateral adjustments were carried out to the laser to enable the laser cross hairs to fall on each central mark made on the front and back of the mounting structure. By rotating the laser by very small amounts this allowed the laser to be brought onto centre in the X plane. An aperture was then placed between the laser and mounting structure and aligned such that the laser went through the centre of the aperture. The aperture and target (see Figure 4.17) were not moved until the alignments for all horns were finished because these acted as reference points.

The laser settings were changed to produce a dot and was aligned to the optical axis using the two markers on the bench, the aperture and the target. An antenna horn (see Table 4.4 for list of antennas being aligned) was placed on the mounting structure and the feedhorn was removed to expose the waveguide aperture (see Figure 4.18) in order to observe where the laser fell in

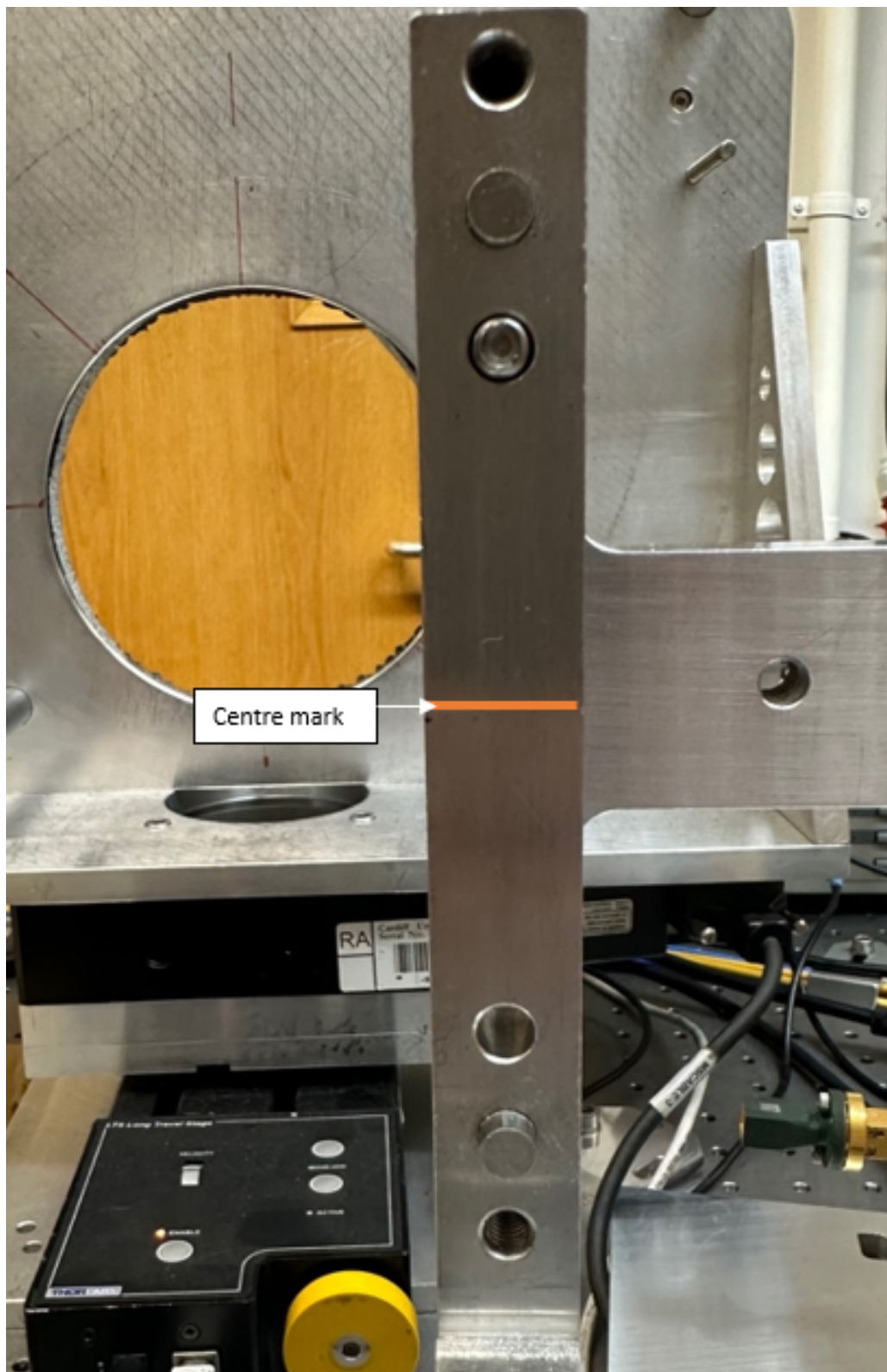


Figure 4.16 – Antenna mounting structure in the Y-axis with the centre mark visible.

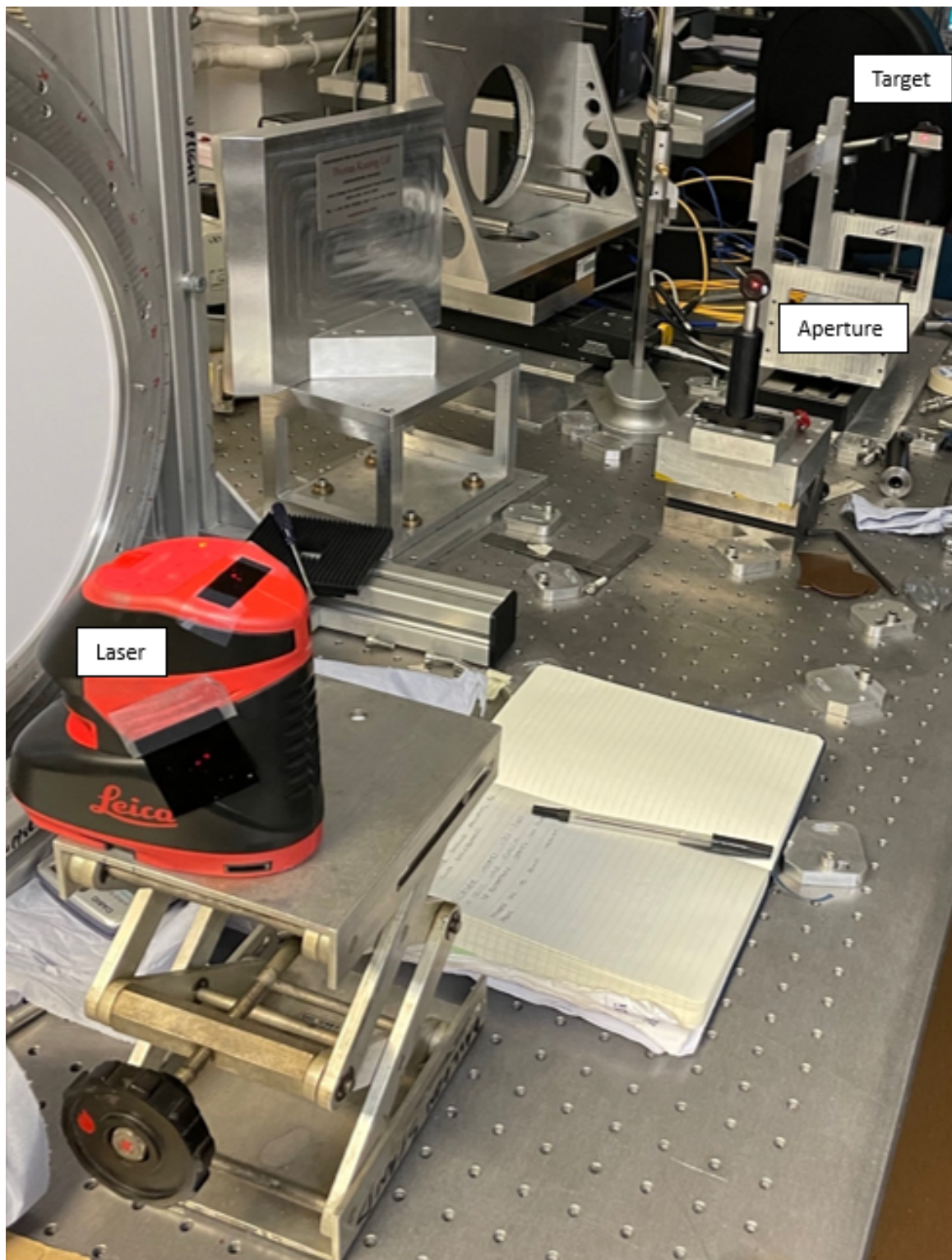


Figure 4.17 – Aligning the laser to the optical axis of the system using the centre marks on the mounting structure and from this target was added at the end of the bench and an aperture between the laser and target. The target and aperture remained on the bench whilst the alignment of each horn was carried out.

relation to it, identifying if any adjustments needed to be made to the position of the head.

To align the centre of the waveguide-aperture to the laser, the bolts holding the antenna to the mounting plate were undone slightly to allow for lateral movements in the X plane. As there were four bolts holding the head to the mounting plate, small rotations of the antenna can be carried out by holding the front of the head down whilst performing lateral movements to the back two bolts. The head was moved in such a way to bring the rectangle aperture of the extender into the centre of the laser. Once the centre of the aperture was aligned, a reflective surface was fixed to the waveguide to reflect the laser back towards itself.

The reflective surface used was not perfect and did not reflect the laser perfectly because as the reflective surface was rotated by 180° the reflected laser point was in a new position to its 180° counterpart. Therefore, the antenna head was realigned in such a way that the middle point between the two reflections fell on the centre of the testbed aperture.

After, the reflective surface was removed and the laser position was checked to see if it was aligned to the centre of the waveguide aperture. If it was not, the above steps were repeated to bring the waveguide aperture back to centre. The reflective surface was then fixed onto the waveguide and the same procedure to reflect the laser back through the centre of the testbed aperture was carried out. These steps were repeated until the waveguide aperture was aligned with the laser dot after the reflection corrections. This procedure had an error associated with the alignment of 0.33° .

Once the head was aligned to the X plane it was rotated by 90° and fixed to the mount in the Y plane. The reflective surface was fixed onto the waveguide and the two reflections were checked. If the centre of the testbed aperture did not align with the centre of the two reflections, the head was rotated back to the X plane and the position moved accordingly. The rotation back to the X plane must be performed before any changes are made because if the bolts were loosened whilst the antenna head was held in the Y plane the head would slip and all previous adjustments would become redundant, so care is needed in this step.

If the waveguide aperture was higher than the laser dot in the Y plane it required the antenna head to be moved from left to right (when looking at the antenna head face on) in the X plane. The alternative is true if the aperture was below the laser dot in the Y plane. However, it was important that the laser dot remained central on the waveguide aperture in the X plane. Therefore, whilst small changes were made to account for the Y plane position, the laser dot was still central on the waveguide aperture in the X plane. Once the changes were made, the reflective surface was fixed onto the waveguide once more and the reflection measurements repeated to ensure the reflection fell on the centre of the testbed aperture in the X plane.

The bolts were then tightened to hold the antenna head in place and the head was rotated 90° and fixed into position in the Y plane. All steps were then repeated until the laser dot fell on the centre of the waveguide aperture in both planes. This was repeated for all heads described in

Table 4.4.

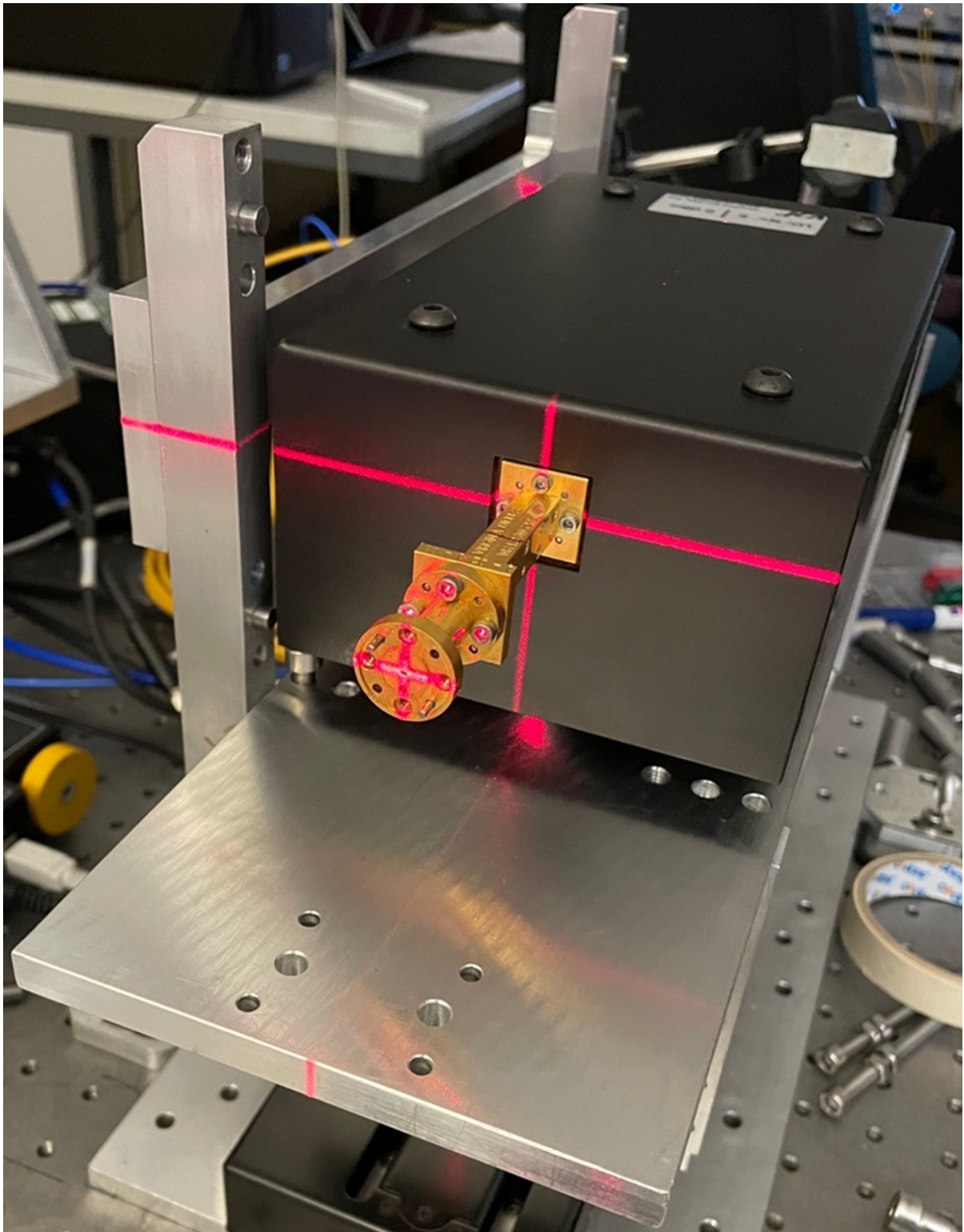


Figure 4.18 – Cross hair laser checking the adjustments to VNA antenna head were centred on the rotation point in the vertical polarisation orientation (X-axis).

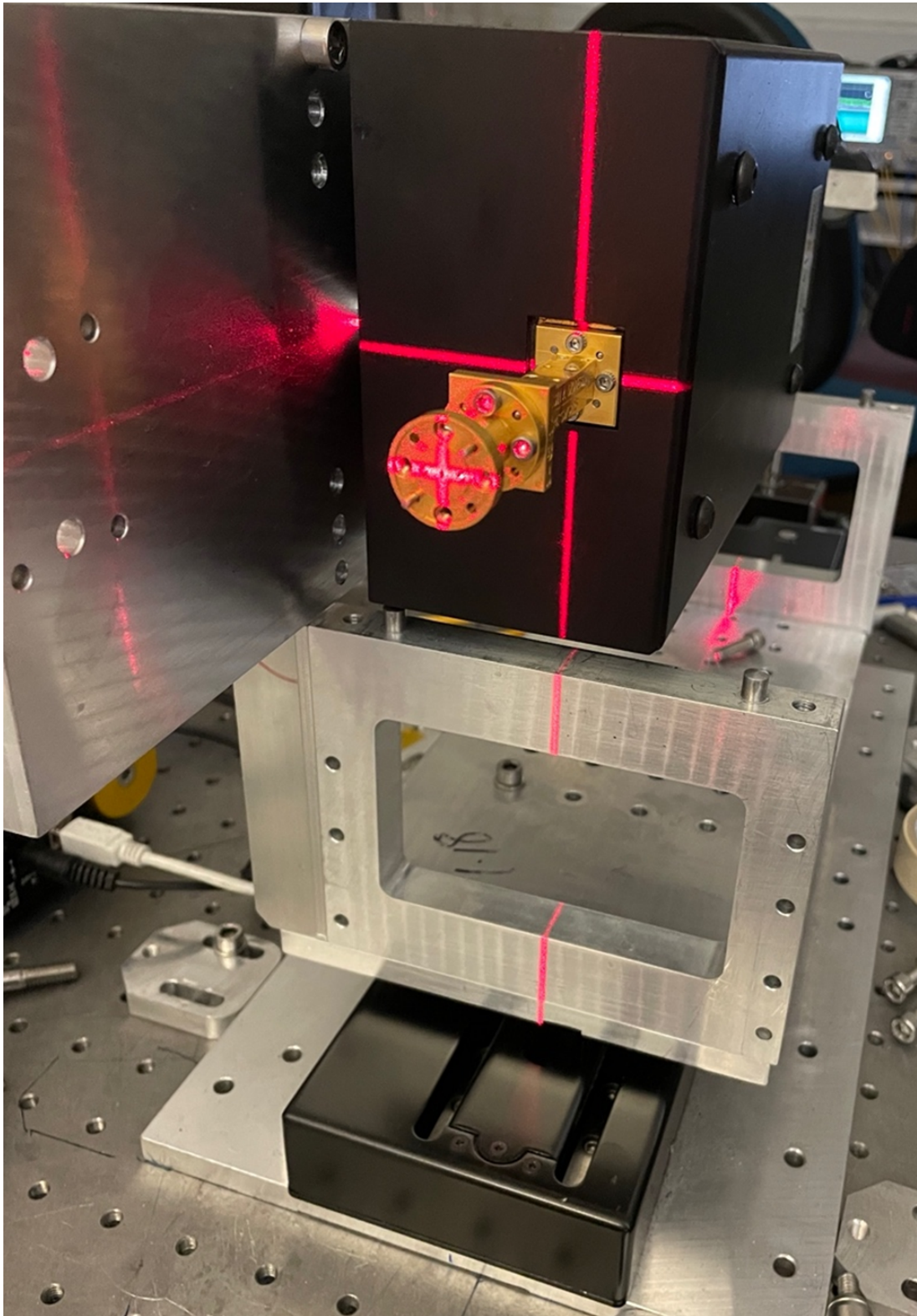


Figure 4.19 – Cross hair laser checking the adjustments to VNA antenna head were centred on the rotation point in the horizontal polarisation orientation (Y-axis).

Correctly positioning the lenses

It was also important to check the optical alignment of the lenses. In this setup a planar-convex lens placed in front of the transmitter to refract the diverging waves produced by the transmitter to produce a collimated beam. A second planar-convex lens, placed in front of the receiver, refracted the collimated beam to converge the light rays onto the receiver to be detected. If the centre of the lens did not sit on the optical axis by even a couple of millimetres, then the beam will not be refracted exactly towards the centre of the receiver and power would be lost.

To check if the lenses were centred on the optical axis the location of the centre of the lens was compared to the laser dot location. To do this the same setup as the antenna horn alignment was used and then align the laser dot with the two markers on the optical bench (testbed aperture and target). The lens was placed flushed at the end of the lens mounting arm, as seen Figures 4.20 and 4.21. The difference in height between the laser dot and the centre of the lens which had been previously indicated by a red marker pen dot on the lens itself was measured. This was repeated by placing the lens at the back of the lens mounting arm (see Figure 4.21). All steps were repeated for the second lens and recorded in Table 4.7.

Lens	Height of lens centre (mm)	Height of laser dot on lens (mm)
TX lens	235.11	237.46
RX lens	235.12	237.43

Table 4.7 – Measurements of the height of the centre of each lens and the height of the laser dot on each lens.

Comparing the results in Table 4.7 there was a difference of roughly 2 mm in height between the optical axis and the centre of each lens. A 2 mm shim was added to the joint between the aluminium base and the Eccosorb on both the TX and RX lenses to bring the centre of the lenses back onto the optical axis. Whilst the recorded difference between the optical axis and the height of the centre of each lens was greater than 2 mm, I only used a 2 mm shim in each case due to the difficulty to manufacture a shim to the exact specification desired. Additionally, the measurements had errors associated with them from parallax error when measuring the height, i.e., how well did I correctly position the callipers to the centre of each object before recording the values. Therefore, this is used as an initial correction. In Section 4.1.3, I performed a full optical system check to ensure these changes to the lenses performed well and observed whether further changes were needed.

Each lens in this system was able to be moved laterally and translated forwards and backwards on the lens mounting arm. Therefore, it was required to observe if the height of the centre of each lens changed when the lens was moved laterally as well as translated along the arm. There are a few reasons why changes in height may occur when the lens is translated along the arm. Firstly,



Figure 4.20 – Laser aligned to aperture and target with lens inserted to measure position of laser dot with respect to the centre of the lens. On the lens the centre is marked by a black dot. The lens is at the front of the lens mounting structure here.

there may be a change in the height on one side of the lens arm to the other. This could come about due to a sanding issue or just purely how the structure was made but if this is the case then

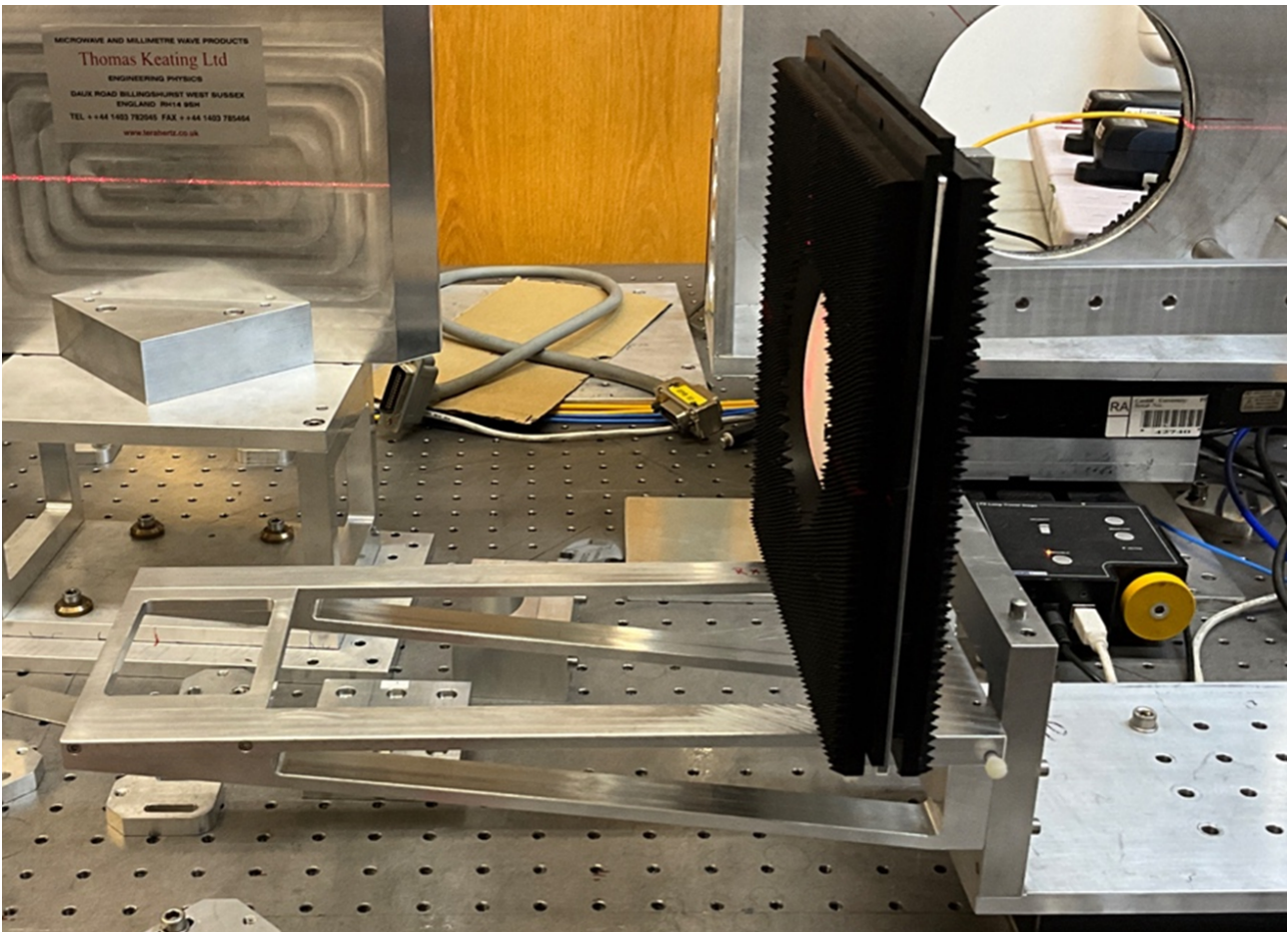


Figure 4.21 – Lens moved to the back of the lens mounting structure. Measurements of laser dot position is repeated and any change in its position denotes lateral changes as the lens moves from the front of the structure to the back.

the lens when in position at one end might be different to the other because the centre has dipped slightly.

Secondly, height might vary across the length due to how the lens is held in place. The arm might just naturally dip on one side therefore when the lens translates across the lens arm a change in signal could be observed. Also, the lenses used in this setup have a small allowance for lateral movement. Therefore, the lateral position is found for each lens that allows for the centre of each lens to be aligned to the optical axis.

To check and correct for this, the full receiver mounting structure is assembled. This includes the antenna head and lens structures (see Figure 4.21). Placing the receiver lens (RX) at the front of the lens arm and laterally moving it to be flush against one side of the arm (seen in Figure 4.20), the laser dot's height and position on the lens were measured and repeated after moving the lens laterally to be flushed against the other side of the arm. After the lens was position at the back of the lens arm (see Figure 4.21) and the above procedure was repeated and the results recorded in

Table 4.8. The results from Table 4.8 indicated that receiver lens needed to be lifted by ~1 mm. The length of both lens arms was 310 mm and the length connecting the lens arms to the antenna mounting structure was 50 mm, therefore to lift the arm up by 1 mm a shim of 0.15 mm was added between the lens arm and mounting structure.

Lens	Height of laser dot on lens at front left of arm (mm)	Height of laser dot on lens at front right of arm (mm)	Height of laser dot on lens at back left of arm (mm)	Height of laser dot on lens at back right of arm (mm)
RX	130.92	131.03	131.18	131.35
TX	130.89	131.07	130.74	131.42

Table 4.8 – Measurements of the height of the laser dot on each lens at the front and back of the lens arm. Left and right positions denote the lens being flush to that side of the lens arm as you look at the antenna mounting structure head on.

The receiver structure was dismantled, and the transmission structure assembled. The full lateral and translational procedure check was repeated on the transmission lens (TX) and the results are shown in Table 4.8. It was observed that the lens needed to be lifted by ~1 mm on the righthand side of the structure which was achieved through placing a small shim of 0.1 mm between the lens arm and mounting structure.

Finally, to get the correct lateral position at each lenses' focal length (200 mm), the laser was removed from the system, an antenna head was mounted to the mounting structure in the X plane and the corresponding lens was placed on the lens arm. The VNA was turned on and was set to measure S21 in dB in a continuous sweep mode. A trace marker was placed in the middle of the sweep. The value of the trace marker was recorded, and the lens was moved laterally until the S21 value measured was closest to 0 dB because this indicated the system was at a position that produced a maximum amount of power being detected. Once this position was found, the lens was tightened to that position. It is important to note here that through tightening the lens into position there was a resulting small change to the lateral position due to the screws pushing against the structure. This in turn changed the power detected, with roughly a decrease of 0.1 dB to the detected signal, in some cases it was observed to be a 0.2 dB decrease.

To confirm that the optimal position had been found, the lens was moved left and right slightly. Through moving the lens either side, I observed a similar decrease in the signal detected, which indicated that this position was the optimum lateral position for each lens.

Checking alignment corrections

When changes to optical elements on an optical bench have occurred, it is important to assemble the complete optical chain and run a full check on the system. This check is to ensure all changes

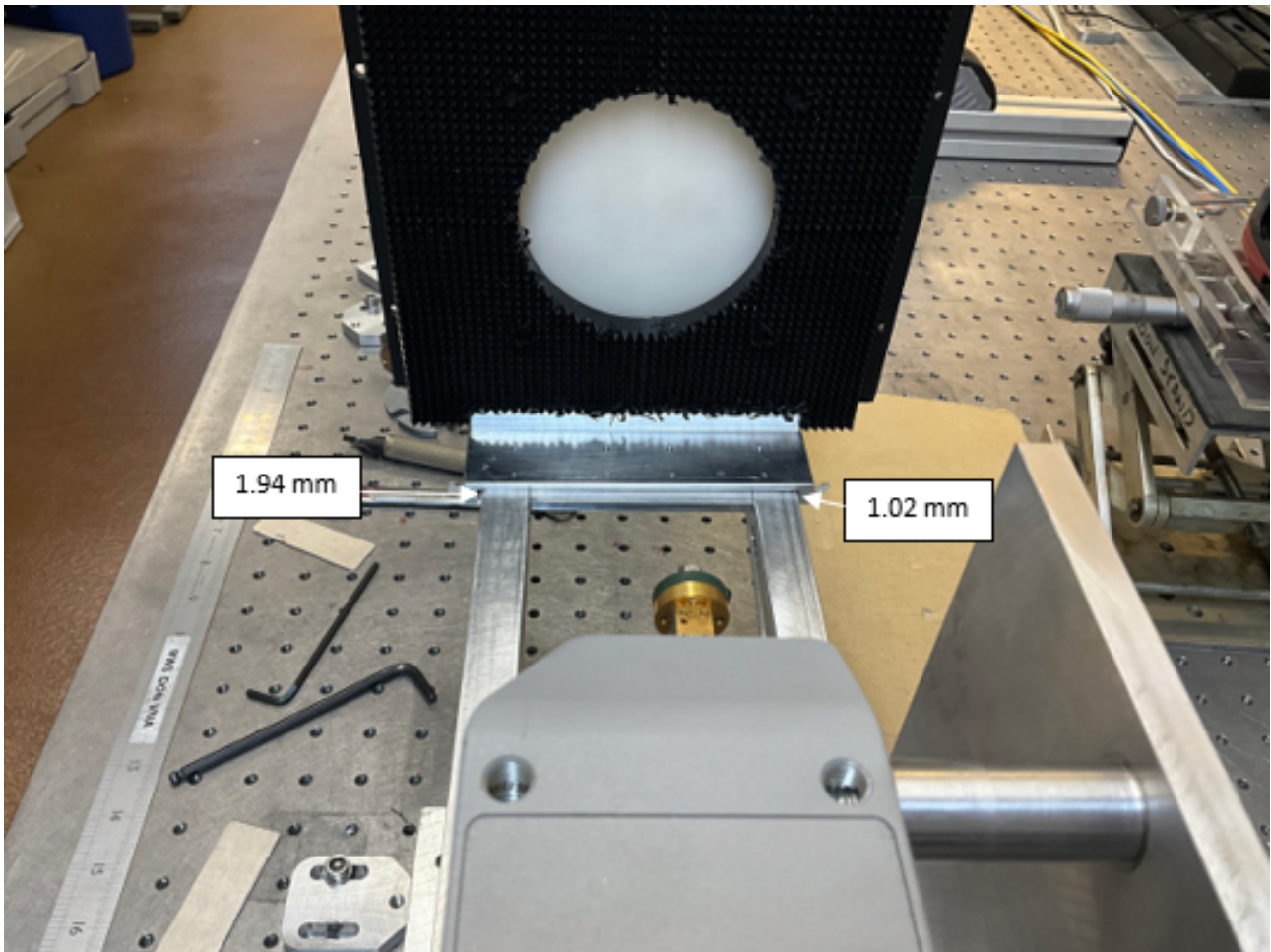


Figure 4.22 – Position of receiver lens on the structure.

enable the full, available power in the system to be detected.

The optical test bench was reconstructed with all elements, minus the lenses, as shown in Figure 4.3, and a laser dot placed in the HWP position, see Figure 4.4. The laser dot was aligned to the centre of each mirror (denoted by a marker dot on their surface), and it was observed how the laser hit the wave guide of the TX and RX horns. Due to the laser seeing the lenses as opaque, if I had kept the lenses in the optical system, I would have not been able to observe where the laser landed on each waveguide aperture.

Small changes to the antenna head positions were needed to correct for small misalignments still present in the system. This was shown through the laser dot not being perfectly centred with each waveguide aperture. Setting the antenna heads in the X plane orientation and carrying out the procedure described in Section 4.1.3, corrections to the small misalignments were carried out to bring the waveguide apertures on centre in both planes.

Placing the lenses back onto the optical test bench, position shown in Figures 4.22 and 4.23, the VNA was turned on and the detected signal was checked to ensure the maximum signal

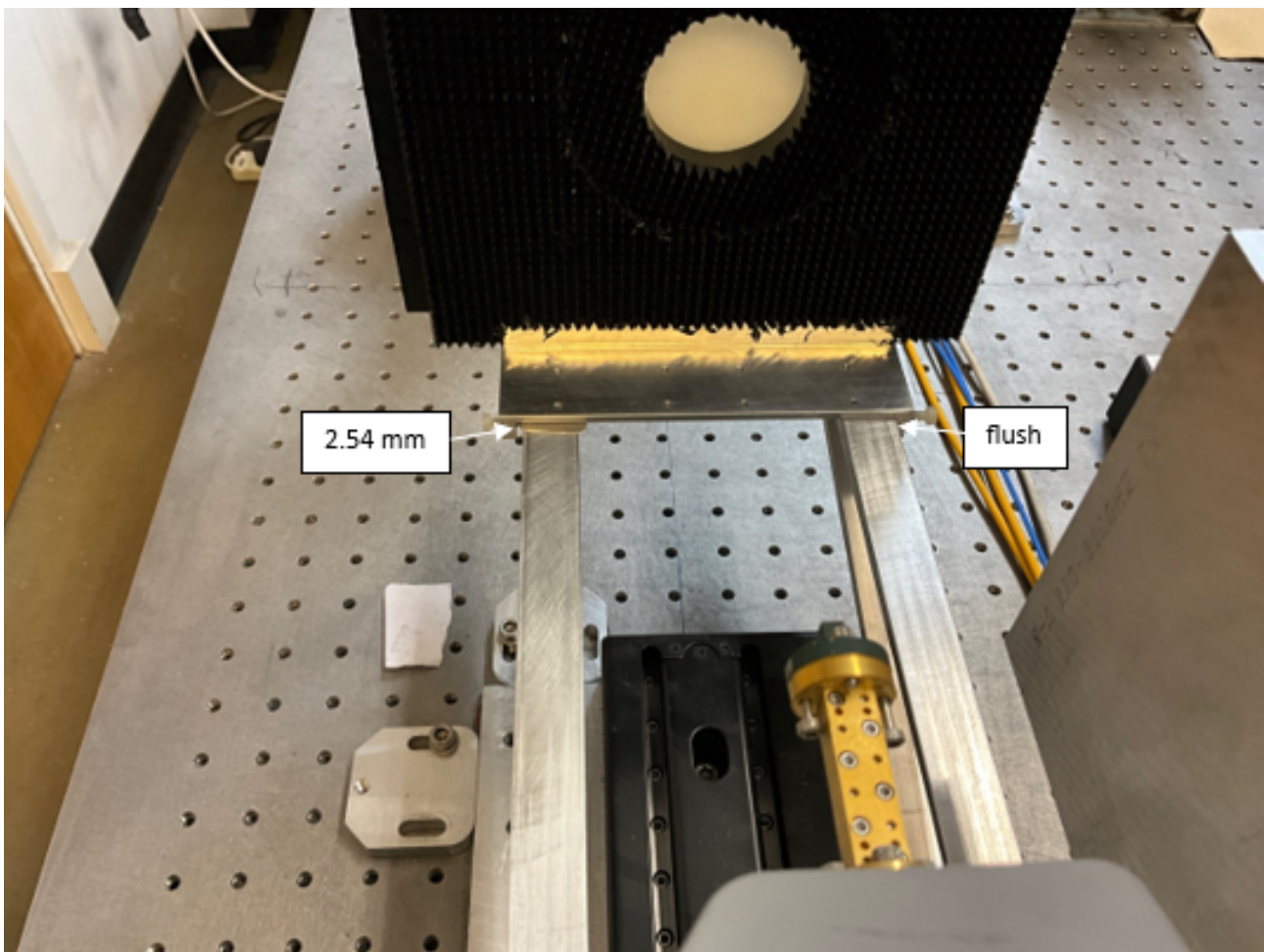


Figure 4.23 – Position of the transmitter lens on the structure. The lens has a 70 mm aperture in it to reduce the size of the beam.

available was being achieved across all bands. This was done through moving each optical element slightly in both lateral and translational movements to check that the signal decreased each time. The decrease in signal was expected because, if the system was completely aligned it would be at maximum power and slight movements either side any optical element position would move it out of alignment thus decreasing the overall power. Once this check was complete, the lenses were secured in place.

4.1.4 Results from VNA optical bench realignment

I have described various techniques used to align optical devices to the optical axis in this Chapter. The procedures showed how crucial it is to ensure the optical setup is fully aligned when characterising devices because small changes to positions, both vertically and laterally, of any optical component can affect the power being received by a detector.

I follow the same method as described in Section 4.1.2 to obtain a new cross-pol data cube

to observe any improvements in the spectral transmission from the realignments. The new data cube is shown in Figure 4.24. An initial observation of Figure 4.24 shows that the continuation between frequency bands is smoother with transmission in the 110-170 and 220-330 GHz bands measuring higher levels of transmission across the whole band.

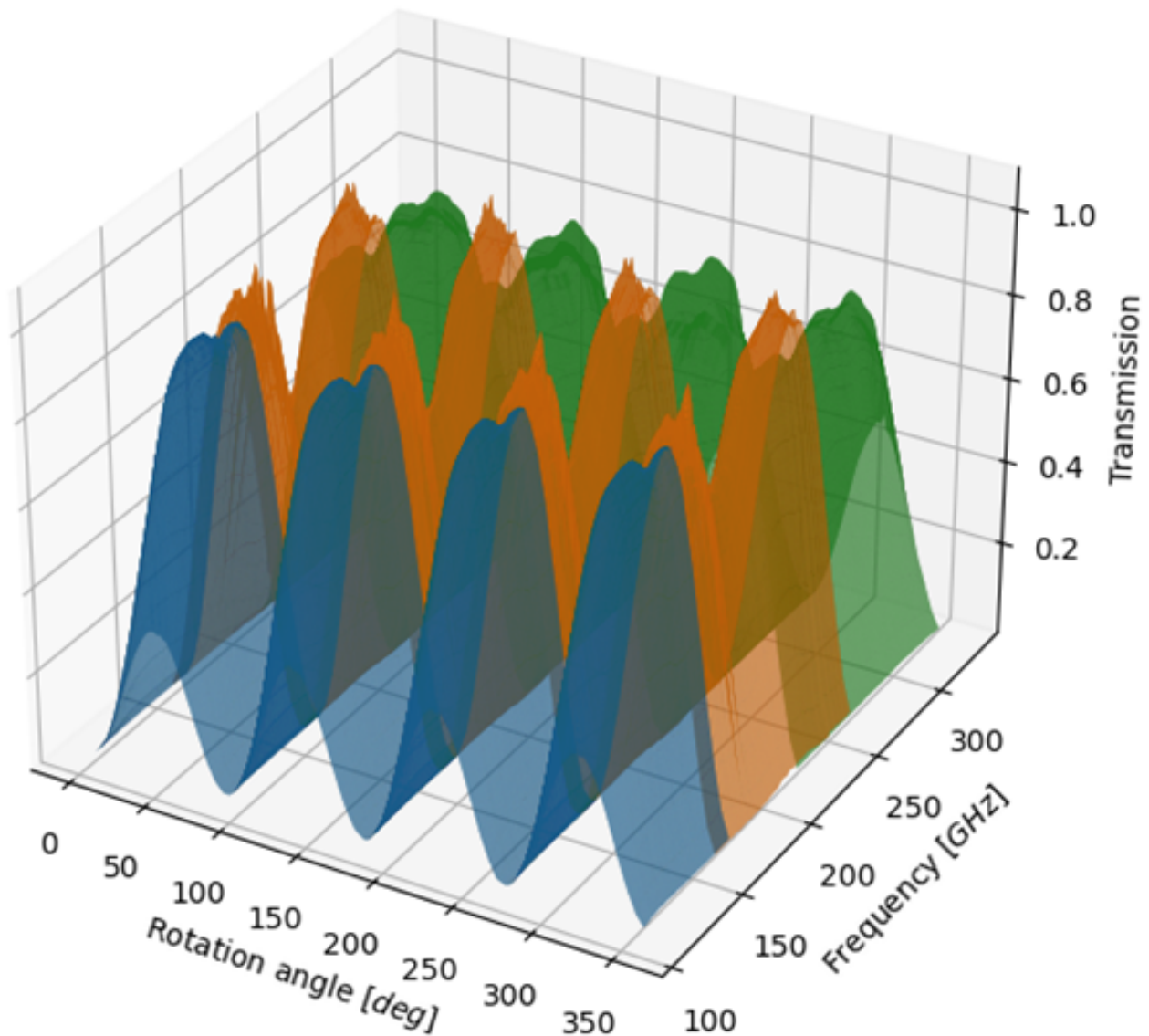


Figure 4.24 – Cross-polarisation data cube showing all three frequency ranges (blue is 110-170 GHz, orange is 160-260 GHz and green is 220-330 GHz) which presents how the HWP performance varies over the ranges with the corrected optical alignment. Plotted are the spectra as a function of rotation angle and frequency. In this plot all 87 spectra in the cross-polarisation configuration are presented, through plotting these values the limits of the HWPs performance can be observed as it rotates through 360°.

The transmission spectra at the HWPs maxima and minima angles are shown in Figure 4.25. As previously stated in Section 4.1.2, the angles in Figure 4.25 are purely arbitrary which

correspond to angles on the displayed on the rotation device and are used for reference if repeat measurements are required.

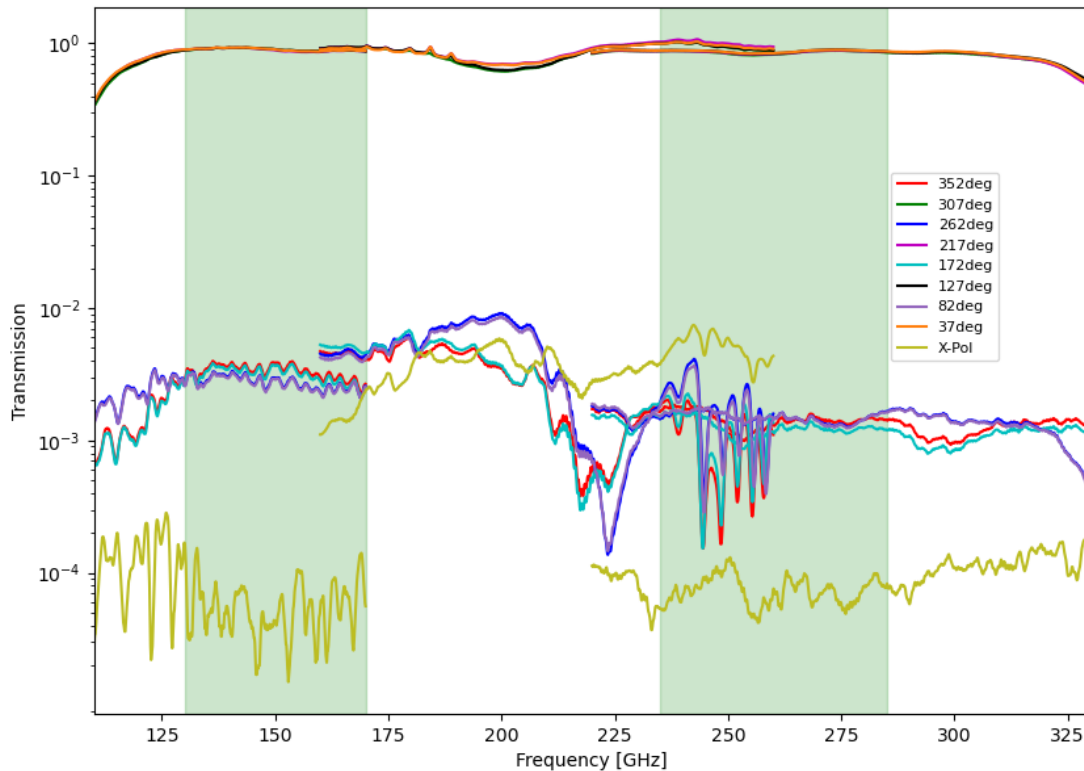


Figure 4.25 – The new maxima and minima cross-pol measurements for the cross-pol measurements of the NIKA2 HWP using the VNA optical setup. The maxima spectra sit above 10^{-1} across the frequencies, whilst the minima spectra all sit below 10^{-1} across the frequencies. However, this excludes the yellow line which is background x-pol, the signal detected when the polarisers P1 and P2 are orthogonal to each other and the HWP is not present in the optical path. The shaded green areas denote the working bands of the NIKA2 experiment.

Comparing the cross-pol results obtained in Figure 4.9 to Figure 4.25 there is an improvement in the overlap between the frequency bands due to the realignment work carried out with the total transmission recorded over the bandwidths is now 0.92 and 0.91 for 150 GHz and 260 GHz respectively, showing an increase of $\sim 30\%$ across the bands. From the transmission spectra measured, I verify the experimental setup is symmetric with respect to the HWP rotation due to the overlap with spectra measured with rotation angles 180° apart (expected to have the same results at angles 180° apart).

The increase in spectral transmission also corresponded to an increase in the calculated modulation efficiency across the measured frequencies which was calculated to be ~ 0.992 and

~0.997 across the 150 GHz and 260 GHz bands respectively. Comparing Figures 4.10 and 4.26 it is shown that the values are much closer to 1 across all frequencies and that the structure (ripples) in the 220-330 GHz range as greatly improved. The dip in efficiency observed in Figure 4.10 has also improved across the 160-260 GHz band, with levels being measured at ~0.993. Additionally, when calculating the modulation efficiency when the HWP was rotated by "45°" the calculated modulation efficiency is now 0.95 and 0.94 across the 150 GHz and 260 GHz bands respectively, an increase of 0.14 and 0.33 respectively.

Initial measurements of cross-pol (Figure 4.9) indicated a disconnect in transmission between frequency bands which, when injected into the Mueller matrix pipeline (from Chapter 3), produced Mueller matrix parameters shown as the black lines in Figure 4.27. The matrix parameters suffered greatly from a difference in power across each band, especially in the diagonal terms. In the off-diagonal parameters I saw a large spread in values across all bands, indicating leakage across the polarisations and the parameters not constrained. The diagonal parameters in Figure 4.27 shows the discontinuity across the bands that is indicated and discussed in Figure 4.9.

However, the cyan lines in Figure 4.27 shows the Mueller matrix parameters produced from injecting the new maxima and minima spectra into the pipeline. From these results I can observe that there is variation across each parameter over all bands. This indicates that mixing between polarisation states was arising from the miss alignment of the optical setup.

The off-diagonal terms M_{QU} and M_{UQ} in the new Mueller matrix plot still produce a larger variation in coefficient values across the measured frequencies when compared to the other seven coefficients. Due to the values for these coefficients not equalling zero it indicates the HWP causing the linear polarised signal to rotate such that it mixes into other linear polarised states. However, comparing the black lines to the cyan lines in Figure 4.27 overall all parameters have vastly improved from the realignment procedures carried out and are closer to the ideal Mueller matrix for a HWP of $[1, 1, -1]$ for the diagonal terms and 0 in the off-diagonal terms.

The full data cube, Figure 4.24, was then injected into the Mueller matrix pipeline along with the co-pol data cube, Figure 4.6, to generate the Mueller matrix parameters which are shown in Figure 4.28. The full data cubes (all eighty-seven spectra) were used instead of just the maxima and minima spectra to constrain the model to the data more effectively, Figure 4.27 presents the Mueller matrix parameters generated by the maxima and minima spectra pre-realignment and after the realignment. The introduction of all the spectra is shown to reduce the variation in the M_{QU} and M_{UQ} terms significantly.

The Mueller matrix parameters in Figure 4.28 have small disconnects over the frequencies measured particularly seen in M_{II} and M_{UU} , this is a result of the use of multiple antenna horns to enable to characterisation of the NIKA2 HWP over its operational frequencies. Whilst most parameters show great continuity across the bands there is to be expected small variations due to the measurements not being continuous because each antenna horn has its own systematic

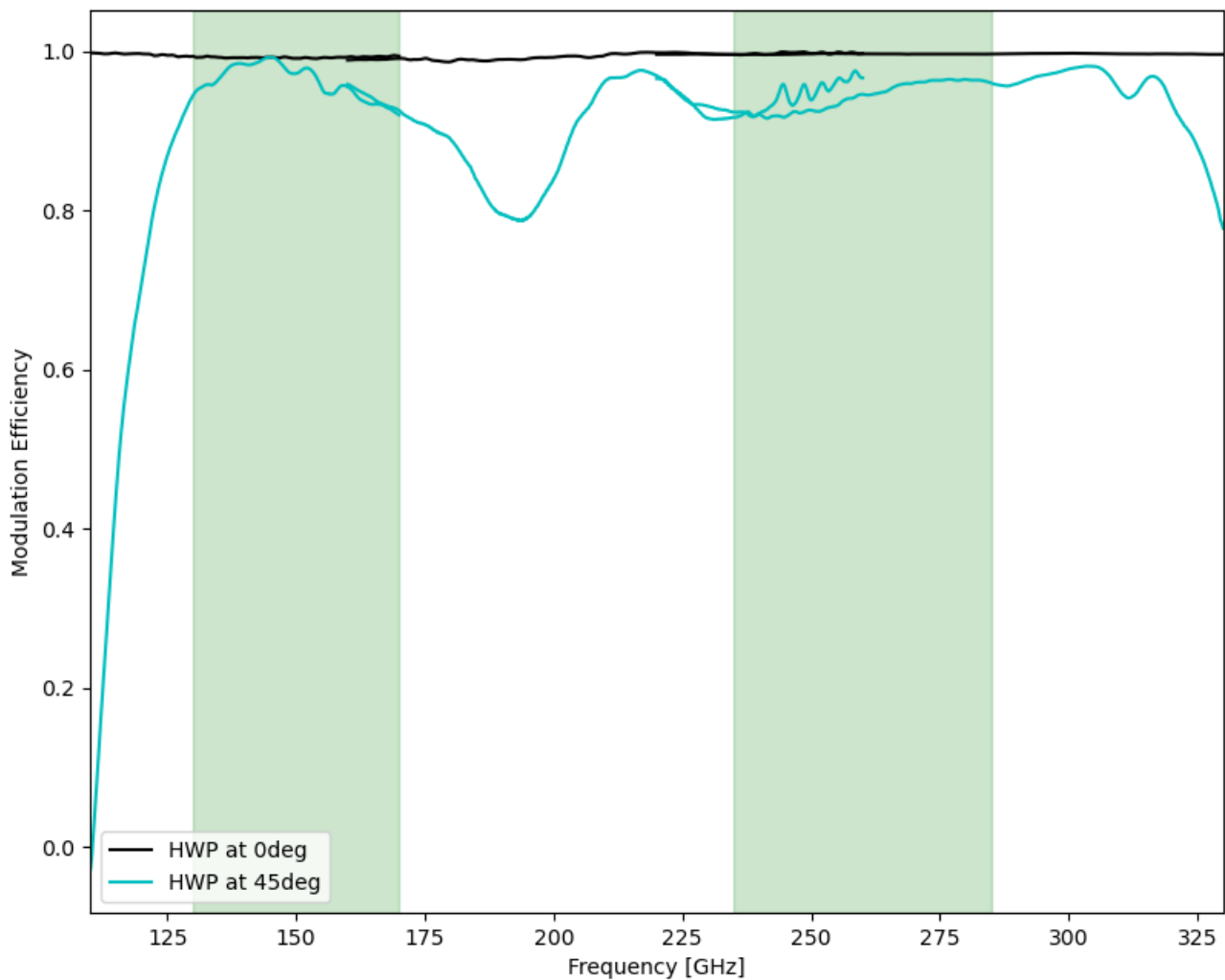


Figure 4.26 – Modulation efficiency of the NIKA2 HWP obtained using equation (4.6) and the data cubes from the VNA experiment. In particular, this modulation efficiency arises from injecting the cross-pol measured after the realignment of the system. Included in this Figure are the modulation efficiencies calculated with the HWP rotation to "0°" and "45°", both of which should produce values equal to 1. When the HWP is at "0°" the calculated efficiency was 0.992 and 0.997 for the 150 GHz and 260 GHz bands respectively, "45°" the values calculated were 0.95 and 0.94 for the 150 GHz and 260 GHz bands respectively. While the "45°" values are 3-4% lower than when the HWP is rotated to "0°" when compared to Figure 4.10 it is shown that after the realignment these "45°" values have increased by 0.14 and 0.33 respectively. The shaded green areas correspond to the bandwidths of the NIKA2 experiment.

uncertainties associated with it. These disconnects are also present in the spectra, as seen in Figure 4.25, inferring that the features present in spectra are carried through to the pipeline.

Across both Figures 4.27 and 4.28 when observing at ~200 GHz more spread in the Mueller matrix parameters is observed. This spread is attributed to the dip that is seen at ~200 GHz in the maxima spectra in Figure 4.25. This dip occurs over frequencies outside of the working bands of the NIKA2 experiment and is therefore caused by the design of the HWP. Due to the design, along

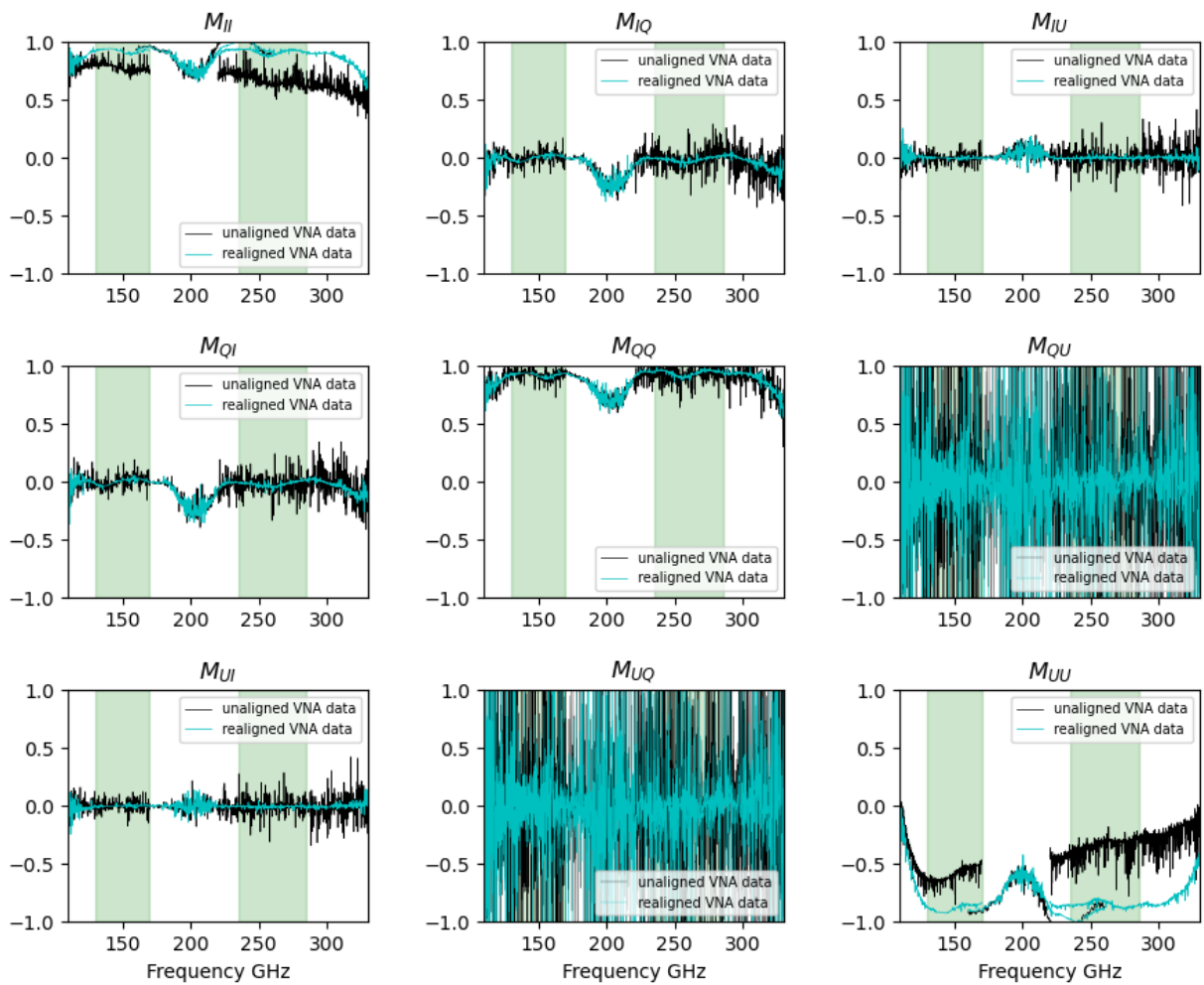


Figure 4.27 – Mueller matrices of the NIKA2 HWP produced using eight transmission spectra measured before (black lines) and after (cyan lines) the realignment procedure described earlier in this Chapter. Before the realignment of the optical system the three frequency ranges measured on the VNA do not overlap with each other in the M_{II} and M_{UU} terms. The amplitude of the M_{UU} term in the 110-170 and 220-330 GHz ranges were measured at ~ -0.5 or higher, in particular at the higher frequencies the amplitudes were calculated to be closer to 0. All other matrix parameters calculated overlap with each other, but the realignment data shows less spread between values over the frequency ranges. The data sets used to generate this plot are presented in Figures 4.8, 4.9 and 4.25. The shaded green areas correspond to the working bands of the NIKA2 experiment. Errors for each Muller matrix parameter value has been excluded from this plot to ensure viewing the values was easier.

one of the axes of the HWP (where the inductive wires were aligned with the polarisation vector) the transmission decreases quite a bit over the out of band frequencies. Therefore, this difference at these angles causes the model to not converge as well due to the difference in the expected intensity.

The mean average of each Mueller matrix parameter shown in Figure 4.28 is provided in Table

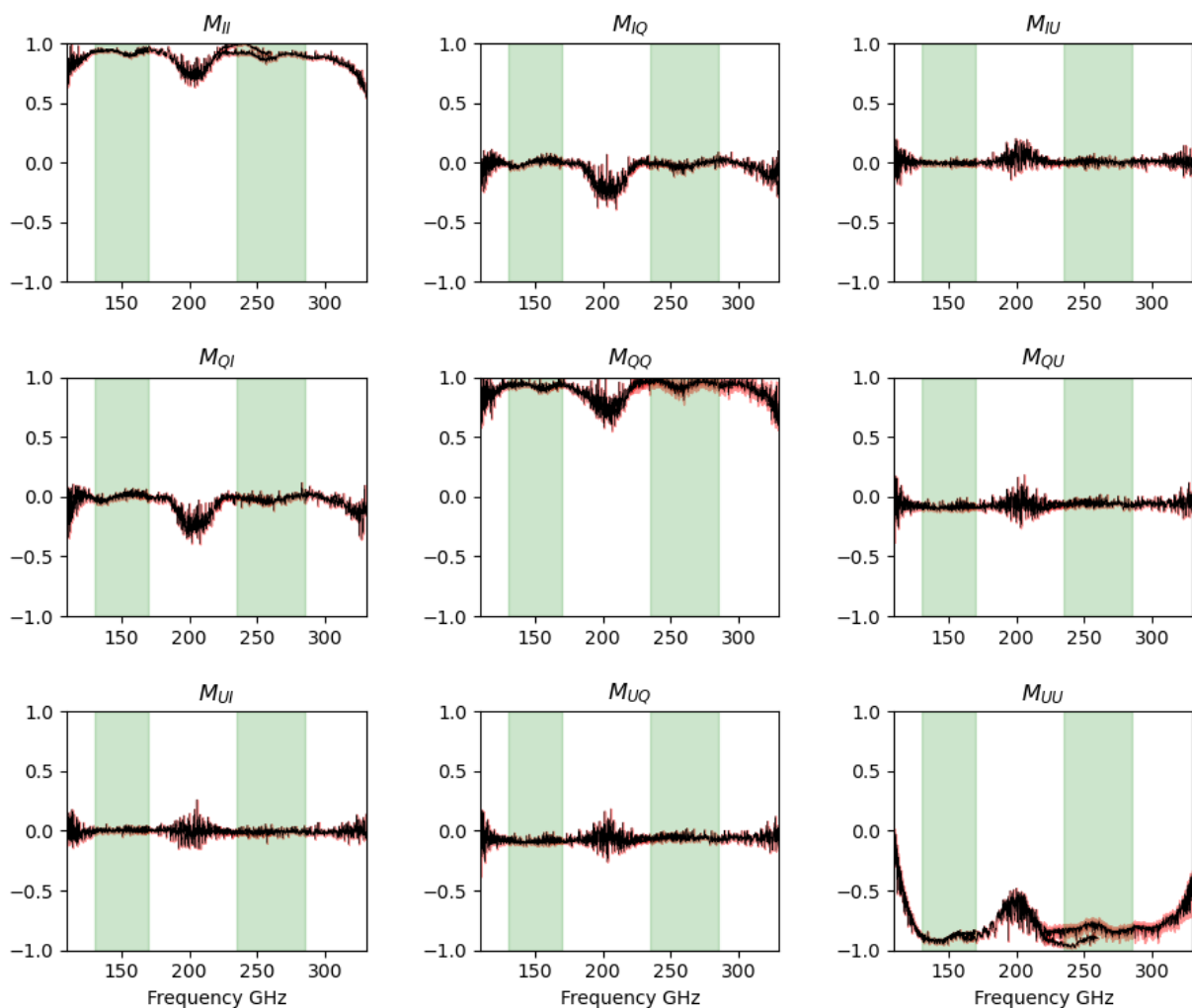


Figure 4.28 – Mueller matrix of the NIKA2 HWP (at a given angle of $\theta = 0^\circ$) measured using the VNA setup at Cardiff University. Errors are included in red and represent the standard deviation in the parameter values. The green shaded regions represent the NIKA2 bandwidths and show the frequencies over which the HWP should be performing over.

4.9, along with their errors and theoretical values. These values indicate that there is a deviation from the theoretical value expected which arises due to the systematic errors of the HWP.

Using the parameters calculated in Figure 4.29 and injecting them into equation (2.12) it is shown that the optical efficiency was 0.95 and 0.96 for the 150 GHz and 260 GHz bands respectively. Injecting the parameters into equation (2.11) yielded the polarisation efficiencies of 0.96 and 0.95 for the 150 GHz and 260 GHz bands respectively. These values indicate that the HWP is transmitting nearly all the incident radiation in the system and rotating it by 2θ .

From performing the optical realignment methods described in this Chapter an overall improvement was seen in the calculated performance of the HWP, especially in its working bands. This showcases the importance of optical alignment of a system when characterising

Mueller matrix parameter	150 GHz band average	260 GHz band average	Error in value for 150 GHz	Error in value for 260 GHz	Theoretical value
M_{II}	0.93	0.93	0.0006	0.0004	1
M_{IQ}	0.008	-0.018	0.0021	0.0008	0
M_{IU}	-0.004	0.009	0.0019	0.0005	0
M_{QI}	0.008	-0.019	0.0021	0.0008	0
M_{QQ}	0.93	0.95	0.0015	0.0158	1
M_{QU}	-0.088	-0.057	0.0037	0.0023	0
M_{UI}	0.004	-0.012	0.0019	0.0005	0
M_{UQ}	-0.088	-0.057	0.0037	0.0023	0
M_{UU}	-0.89	-0.88	0.0015	0.0158	-1

Table 4.9 – Mean values for the Mueller matrix parameters generated using the VNA co- and cross-pol data cubes shown in Figures 4.6 and 4.24. Also included are the errors associated with these means and the theoretical values each parameter should be.

an optical device because it can affect the understanding of how a device performs. In the next Chapter the same experiment will be performed as described here but using a FTS optical setup allowing the comparison between those results and the results presented in this Chapter. This comparison will therefore enable a discussion on how each setup performs and if there are other issues which are present in one setup to the other.

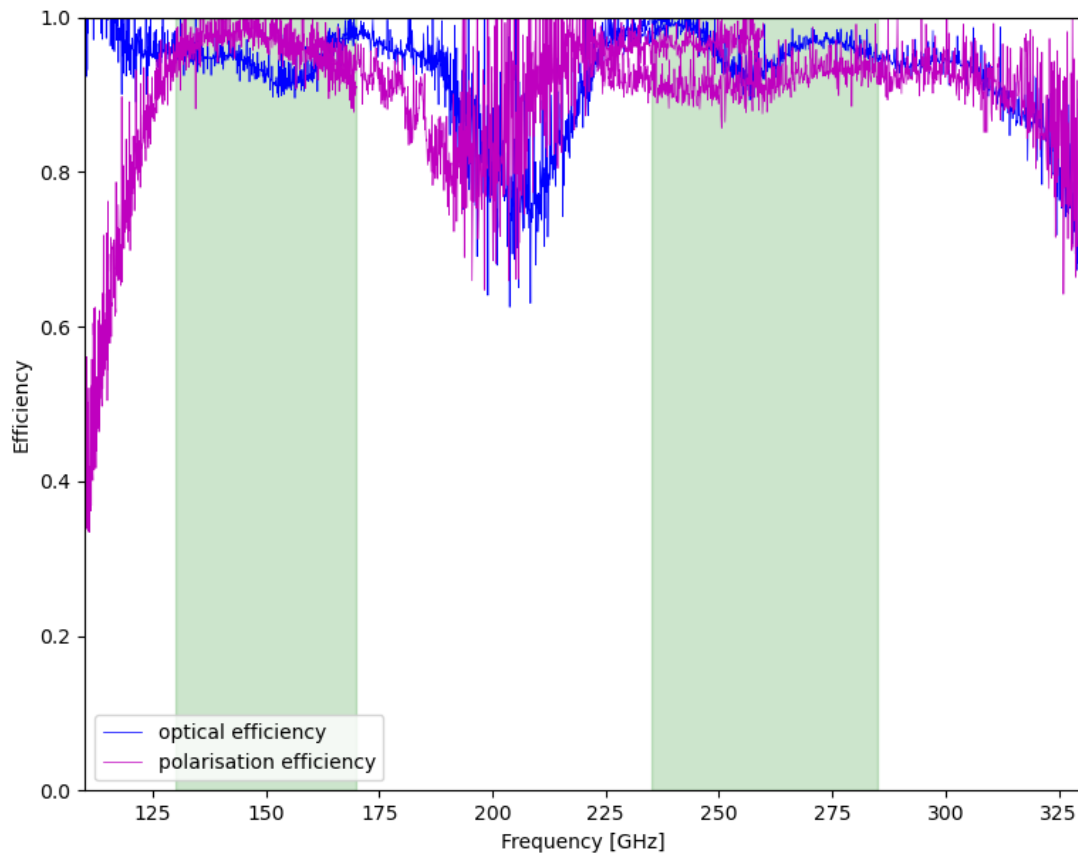


Figure 4.29 – The optical (blue line) and polarisation (magenta line) efficiencies measured from using the Mueller matrix parameters calculated in Figure 4.28 for the NIKA2 HWP. The polarisation efficiency has a disconnect between the 160-260 GHz and 220-330 GHz ranges which follows from the spectral transmission data presented earlier. The dip at 200 GHz has more spread across the values and is due to the spread in transmission observed in the VNA transmission spectra. The shaded green areas represent the bandwidths of the NIKA2 experiment.

SPECTRAL CHARACTERISATION OF A HALF WAVE PLATE, USING A FOURIER TRANSFORM SPECTROMETER

"If I wasn't meant to recover from mistakes, why on earth would I make so many of them?"

Northernlion, *Youtube*

Chapter 4 described the method used to characterise a HWP designed for the NIKA2 experiment using a VNA. In this Chapter a similar method to measure the performance of the NIKA2 HWP is performed, but instead using a polarising Fourier Transform Spectrometer (pFTS). As was explained in Chapter 4, I have used the method explained in the BLASTPol paper ([Monceli et al., 2014](#)) but adapted it for this setup to obtain data sets to enable a full characterisation of the HWP.

Equivalent data sets to those obtained in Chapter 4 have been taken over the same rotation steps and wavelength range needed to characterise the NIKA2 HWP (see Table 4.1). Characterising the same HWP on two independent optical setups gives validation to the data and allows for a comparison of the techniques being used, which is done in Chapter 6.

5.1 THE POLARISING MARTIN-PUPLETT FTS

The pFTS system discussed in this Section is based on a Martin-Puplett interferometer ([Martin, 1982](#)). This type of FTS works by polarising the emission of a radiation source, thus allowing splitting of the radiation into the two arms of the interferometer via a polarising beamsplitter. With reference to Figure 5.1 an emission source is located in a module at the exit of which is a linear

polariser. The linearly polarised light then enters the interferometer module, where it is divided at a beamsplitter, half is reflected at 90° and half is transmitted. At the end of each arm, roof-top mirrors then reflect the incident radiation effectively rotating the E-vector by 90° . Thus, changing the phase of the waves and allowing what was previously reflected to be transmitted and vice versa. The two light paths emerging from the beamsplitter then interfere and it is this interfering pattern that is measured at the detector as a time-stream. If the path length travelled by the light in each arm is the same, we have constructive interference and a sinusoidal signal of twice the amplitude of the individual light path. However, one of the mirrors is movable and through moving it in pre-determined intervals an interferogram is measured, which is a signal measured as a function of optical path length. Through Fourier transforming this signal a spectrum of transmission against wavenumber is generated. As a note to the reader, who may not be a spectroscopist and familiar with wavenumber units, we can easily convert from wavenumber to frequency in GHz by multiplying by 30.

The pFTS used in this experiment utilises a mercury arc lamp as its source which emits incoherent radiation. The system uses an input polypropylene polariser, a wire grid beamsplitter, and an output polariser. The pFTS is encased and held under vacuum; the output from the FTS passes through a polypropylene window and feeds to a detector which can be positioned directly at the output or set back from it but along the optical axis.

The detector used in these measurements was a Helium-4 cryopumped Germanium bolometer running at 1.5 K. The bolometer is feedhorn-coupled and is designed for measurements up to 40 cm^{-1} by deployment of suitable filtering placed in the cryostat. For this experiment, I additionally placed a 12 cm^{-1} low pass edge (LPE) filter directly in front of the detector, in order to limit excess radiation and to optimise measurements to the band of operation of the HWP device.

5.1.1 Optical configuration

In the optical setup for the HWP experiment two planar-convex lenses were aligned to the optical beam, creating a Gaussian beam configuration. In this configuration two wire grid polarisers were placed in the beam path, denoted as P1 and P2 in Figure 5.3. For reference, when going between polarisation states required for the co- and cross-pol measurements, P1 and P2 were the only polarisers to be rotated. They were not placed parallel to the optical path, but at slight angles (seen in Figure 5.2) to minimise standing waves created from reflections in the system. Finally, a low-pass filter was placed just before the detector window to filter wavenumbers larger than 12 cm^{-1} (360 GHz) from entering the detector system.

The pFTS body itself is evacuated, which is beneficial as it minimises the scattering of the emitted light off of particles and environmental fluctuations. However, the optical setup of this experiment is exposed to air which at the frequencies being measured mean there are noticeable

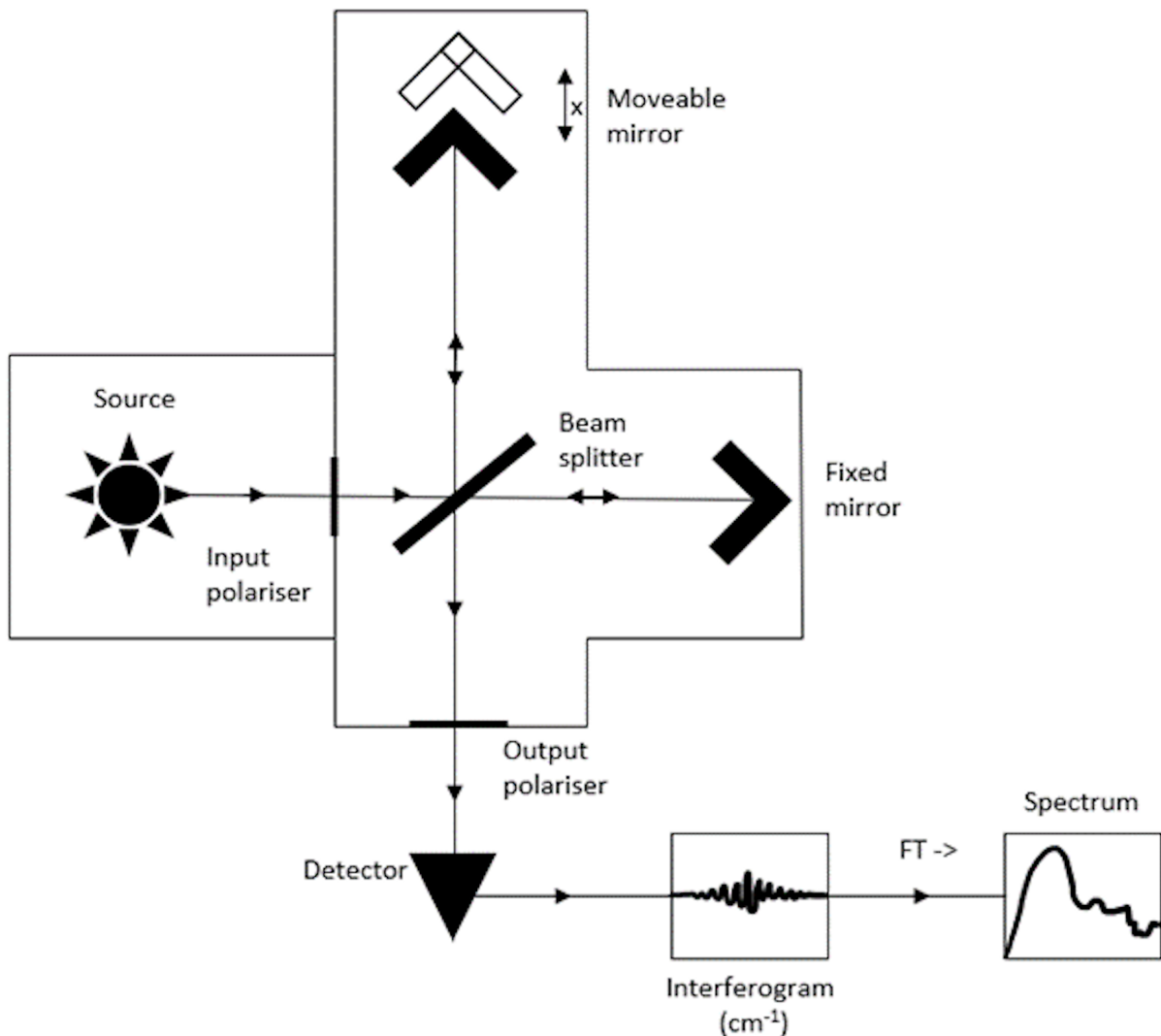


Figure 5.1 – Schematic of a Martin-Puplett interferometer showing the path the light takes within the module towards the detector. A source emits radiation which is subsequently polarised by a polariser. This polarised light is split at a beamsplitter (held at 45°), half is reflected down one arm and half is transmitted down the other arm. A rooftop mirror is located at the end of each arm where the polarised light's electric vector is rotated by 90°, changing the phase of the waves. The two waves interfere at the output of beamsplitter and it is this signal which is detected. One rooftop mirror is moveable and through moving it in increments the interference signals detected create an interferogram which is Fourier transformed (FT) to obtain the system's transmission spectrum.

water lines (at 3 and 6 cm⁻¹), which can be monitored, thus I was not too hampered by having the device open to air. Therefore, whilst the pFTS itself is evacuated, it feeds into a Gaussian beam optical setup in which the HWP experiment is placed, the output of which is then fed to the detector. This also means that I was quantifying the device in a near-parallel beam. However, care was taken to take regular background (normalising) spectra and to match those backgrounds in

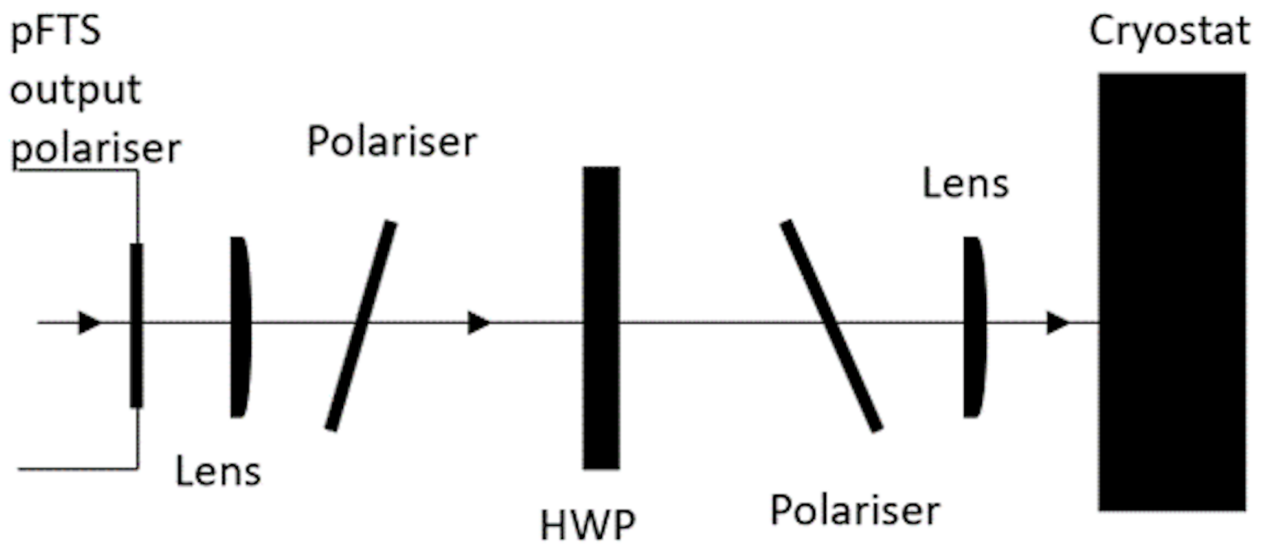


Figure 5.2 – A schematic of the open air optical configuration section of the FTS used for the NIKA2 HWP characterisation. The pFTS produces diverging waves which traverse through a planar-convex lens which refracts the waves into a collimated beam. The second planar-convex lens is placed such to converge the collimated beam towards the detector. Two wire grid polarisers are placed in the collimated beam to ensure polarisation is maintained throughout the system and each is placed at slight angles to minimise standing waves which would occur. The HWP is placed in a rotator between the two polarisers on a platform which is fixed to the bench. The detector in the system is a bolometer which runs at 1.5 K.

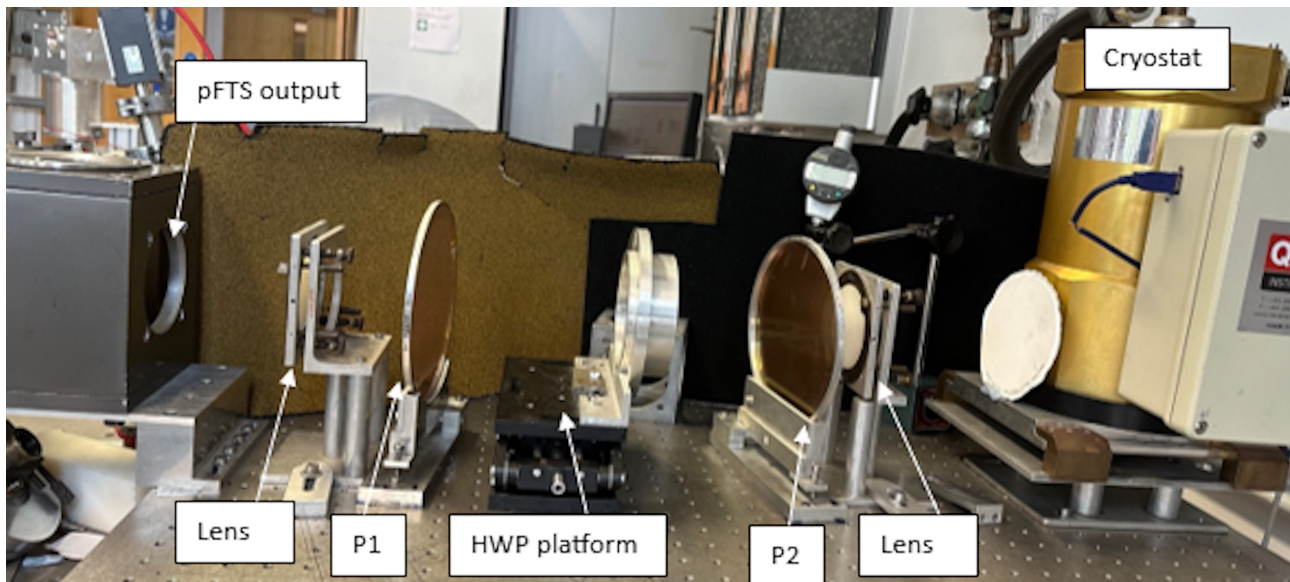


Figure 5.3 – Optical setup outside of the pFTS module. The setup includes two wire grid polarisers (P1 and P2), two planar-convex polyethylene lenses and a HWP platform which the rotator holding the HWP will be placed on. The white disc in front of the cryostat window is the 12 cm^{-1} LPE which prevents frequencies of 360GHz and higher from entering the cryostat and subsequently being detected.

time, as well as ensuring that laboratory traffic was minimised.

Figure 5.2 shows the Gaussian beam section of the experiment, with the pFTS output on the left hand side (LHS) and the detector input on the right hand side (RHS). Care has been taken to minimise systematics by positioning Eccosorb on both sides to shield the experiment. Ideally, blackening would be used around each metal surface in the beam path to reduce the reflections that might occur and any chance of standing waves.

When changing the optical configuration in Figure 5.3 it is important to ensure that after the rotation of the polariser (P2 in Figure 5.3) it is firmly secured in place, ensuring the wire lines are exactly orthogonal to the first polariser (P1 in Figure 5.3). This establishes the ability for the optical system to completely transmit the orthogonal polarisation signal to that of the co-pol optical configuration. Additionally, it is also important to ensure that the polarisers are not placed parallel to the optical axis but at slight angles to reduce the standing waves caused by the reflections off their surfaces.

Care and attention is needed when extracting the HWP out of the optical system to measure the background spectrum as to not strike other optical elements in the system such to cause misalignments, but in such to not damage the HWP which would affect its performance. Furthermore, to ensure repeatability the position the HWP is placed back into the optical beam at the same position to maintain consistent measurements of the device. Before placing the HWP into the system it is best to mark the centre position on the rotation device and platform to be able to reposition to the same place and ensure repeatability.

The rotator which housed the HWP in Chapter 4 (see Figure 4.4) was too large to fit on the optical bench for the FTS experiment. Instead, a rotator with an outer diameter of 120 mm was used instead. The NIKA2 HWP, which had a 300 mm diameter, was cut to 110 mm and placed in the rotating device and placed on the HWP platform. To ensure repeatability, the centre of the HWP rotator was marked and aligned with the centre of the HWP platform each time measurements were taken.

The rotator was rotated automatically through the LabVIEW software. This was utilised in the measurement strategy by programming the “0°” angle of the rotator to be the first maxima position found from the VNA measurements in Section 4.1.2 which was the 352° position on the rotator. To achieve this, I removed the HWP directly from the VNA rotation mechanism and marked the position of the maxima angles on the HWP itself. This allowed us to align the HWP to the corresponding angles in the FTS rotation mechanism to allow repeatable measurements between setups. The polarisers were initially aligned with respect to each other, with the wires in the vertical position with reference to the optical bench, thus producing horizontal polarisation.

A small cryostat houses a feedhorn-coupled bolometer cooled to 1.5 K through pumping on a liquid helium cooled bath. The spectral coverage of this instrument was therefore defined by the low pass filters, 40 cm^{-1} , held in the cryostat to minimise photon noise. The rapid scan system

recorded interferograms every $16 \mu\text{m}$ sampling interval over a 10cm optical path difference at a scan speed of 0.7 cm^{-1} and a spectral resolution of 0.05 cm^{-1} . The HWP was sampled over the aperture of the rotator mechanism which was 80 mm and the signal measured at the detector was the integrated response over that area.

5.1.2 Measurement strategy and resulting spectra

As with the VNA measurements to characterise the NIKA2 HWP, described in Section 4.1.2, the FTS measurements for the NIKA2 HWP characterisation followed a similar method to the BLASTPol HWP characterisation method (Moncelsi et al., 2014). Differences in the setup arise due to the working bands NIKA2 performs over (see Table 4.1) and subsequently the frequency bands that the HWP performs over, therefore a different pFTS was used. The BLASTPol HWP experiment utilised a pFTS that was held completely under vacuum, including its optical setup that held the HWP device. Whereas the NIKA2 HWP experiment used an evacuated pFTS module while the optical setup, where the HWP was placed, was in open air conditions resulting in different steps being taken to perform the two measurement types for the characterisation. The method taken to characterise the HWP is described in this Section.

Following the conventions described in Table 4.3, P1 and P2 were both held with their wires vertically for co-pol measurements. While for cross-pol measurements P1 was fixed and P2 was rotated and held with its wires horizontally.

A background (normalising) spectrum was the first data set to be obtained by scanning the system without the presence of the HWP. This data set defined the FTS reference spectral envelope and subsequent spectra measured with the HWP placed back into the beam path were normalised by this background spectrum to account for spectral signature of the system. A raw interferogram consisted of fifteen average forward scans and fifteen averaged backwards scans, these are separately Fourier transformed and these two are then averaged. This process is then repeated and that average also taken. In this way the statistical uncertainty associated with the average on a single data set was found to be negligible. If I averaged together all of the background interferograms taken over the course of the data measurements (approximately two weeks for each configuration), I can take their statistical dispersion as an estimation of the uncertainty associated with all the spectra taken over the course of those weeks. Through this procedure I was able to account for the changes in the external environment and the drifts in the bolometer responsivity. I report the mean background spectra and the associated error for the co-pol and cross-pol measurements in Figure 5.4. The errors were used to estimate the uncertainties on the HWP Mueller matrix parameters.

To obtain the final data sets, the HWP spectra were normalised to the background spectra allowing the instrumental envelope to be taken out of the HWP measurements providing the

transmission of the anti-reflection coated HWP alone as a function of frequency and rotation angle.

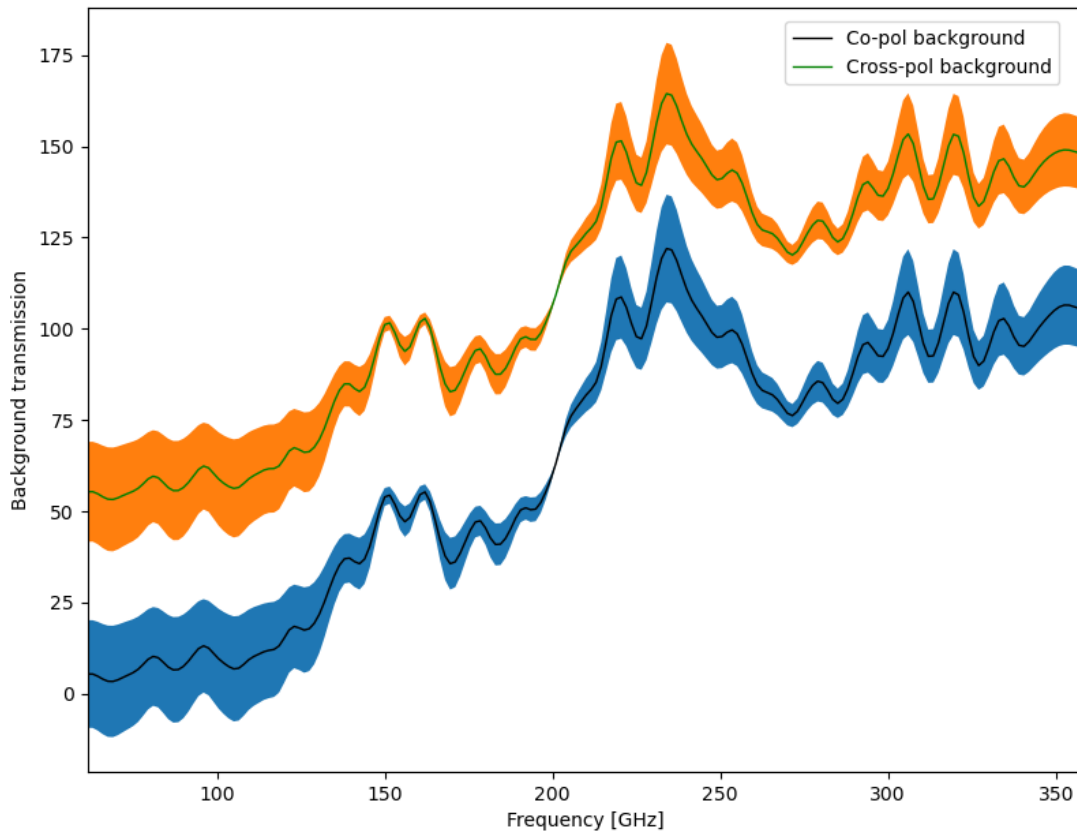


Figure 5.4 – Background spectra for co-pol (black curve) and cross-pol (green curve) with their respective errors associated (blue and orange regions). The blue and orange regions represent ten times the standard error for the background spectra measured in order for the values to be visible. The cross-pol background (green curve) has been moved by an arbitrary constant as these backgrounds overlap with the co-pol backgrounds otherwise.

A central mark had been added to the rotator mechanism to denote the centre of the aperture. The HWP mounted in its rotator, was then placed on the HWP mounting stage, as depicted in Figure 5.3, and the central mark was aligned to the central mark on the mounting stage, ensuring the HWP sat centrally and parallel in the optical path. Spectra were obtained at intervals of 5° with steps decreasing to 2° around both maxima and minima angles. This change in rotation step was to accurately ensure that I resolved the performance around the two axes of the HWP.

Over the course of a month, measurements were obtained and data cubes acquired for both co-pol and cross-pol transmissions. Figures 5.5 and 5.6 respectively show the spectra of rotation angles near the HWP maxima and minima for visual clarity in log format to clearly show the

x-pol level. A plot of the maxima and minima for the co-pol in linear format is provided in Figure 5.10 which shows the fringing present in the maxima spectra in clearer detail. The full data sets with intermediate rotation angles taken approximately every 5° are shown in Figures 5.8 and 5.9 which amounts to eighty-seven individual data sets of sixty scans at one hundred and ninety two frequency points.

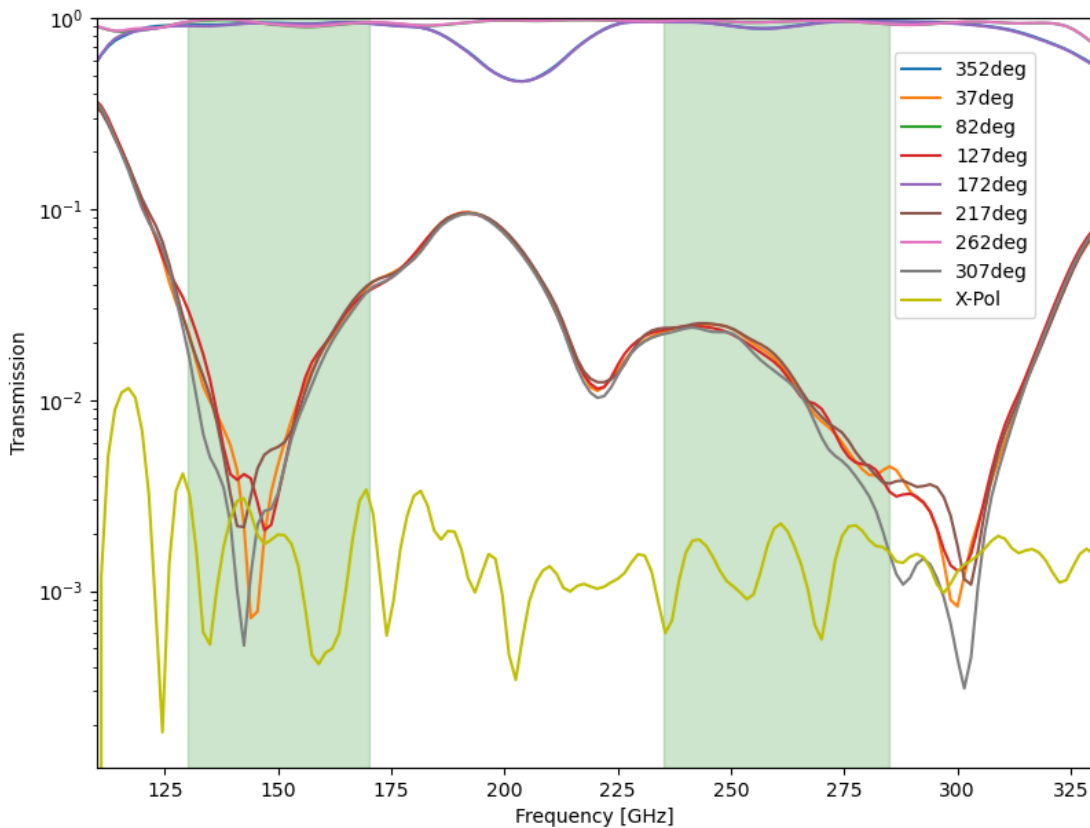


Figure 5.5 – Measured co-pol transmission spectra of a NIKA2 anti-reflection coated embedded metal mesh HWP. Spectra shown are at rotation angles close to the expected maxima and minima, the intermediate angles are omitted here but are shown in Figure 5.8. The angles denoted in the legend are arbitrary values used to reference the angle on the rotation mechanism used to rotate the HWP, allowing for repeat measurements to occur. The ‘zero’ values also might not occur exactly at the zero angle which is why transmission spectra are taken around the expected value. The x-pol spectrum is included as the yellow curve and the shaded green regions denote the NIKA2 frequency bands.

Another useful parameter to calculate using the co- and cross-pol spectra is known as the modulation efficiency which is calculated from equation (4.6) and describes how well the HWP rotates the polarisation by 2θ . From the FTS experiment the modulation efficiency was obtained

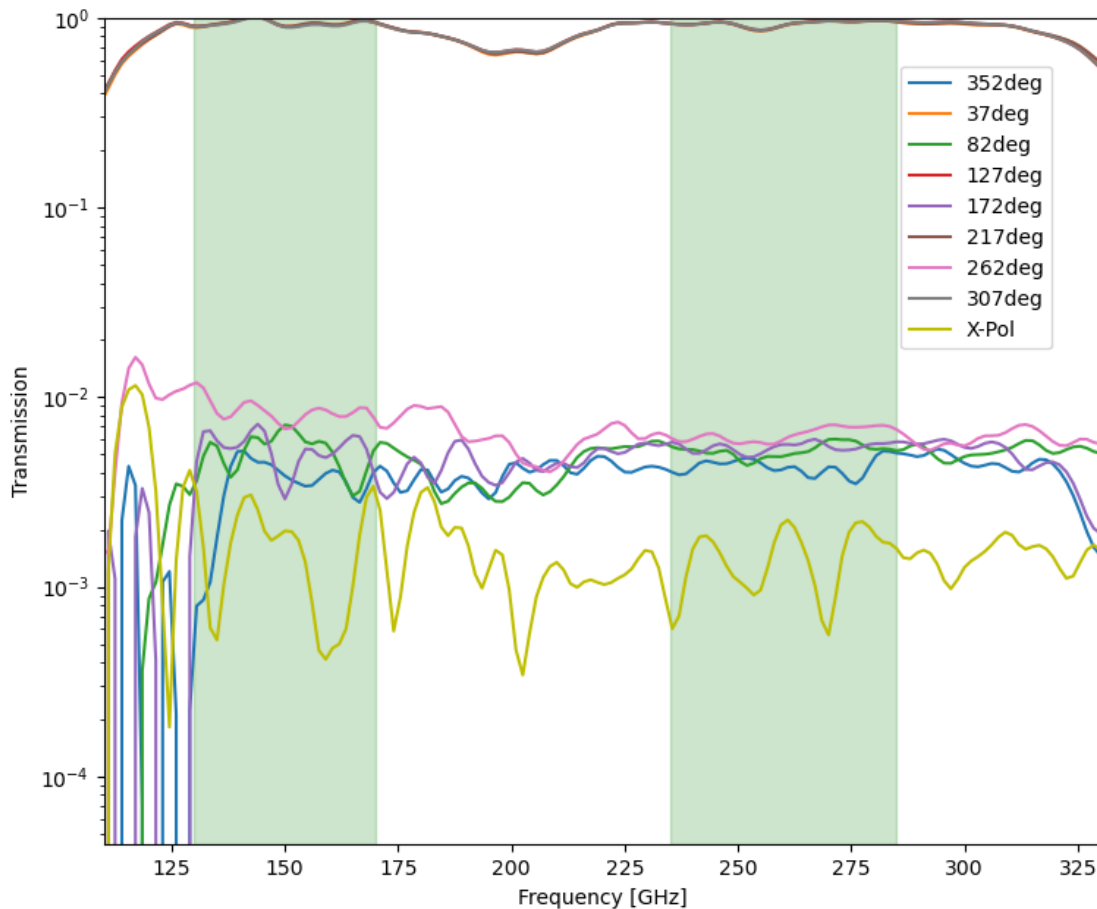


Figure 5.6 – Measured cross-pol transmission spectra of the NIKA2 anti-reflection coated embedded metal mesh HWP. Spectra shown are at rotation angles close to the expected maxima and minima, the intermediate angles are omitted but are shown in Figure 5.9. The angles denoted here are arbitrary and are used to reference the angles on the rotation mechanism. The x-pol spectrum is included as the yellow curve and the shaded green regions denote the NIKA2 frequency bands.

and shown in Figure 5.7 which measured the modulation efficiency to be ~ 0.992 and ~ 0.996 across the 150 GHz and 260 GHz bands respectively. The ideal value for the modulation efficiency is 1 therefore the results calculated from this experiment indicate that a small percentage of the incident polarised signal was not being modulated by the HWP at the "0°" rotation angle, in this example when the co-pol produces a maximum signal and the cross-pol configuration produces a minimum signal. When the HWP was rotated to "45°" the modulation efficiency was calculated to be ~ 0.973 and ~ 0.969 for the 150 GHz and 260 GHz bands respectively, indicating the HWP was not modulating the incident polarisation as well, with it losing about 3% efficiency over the

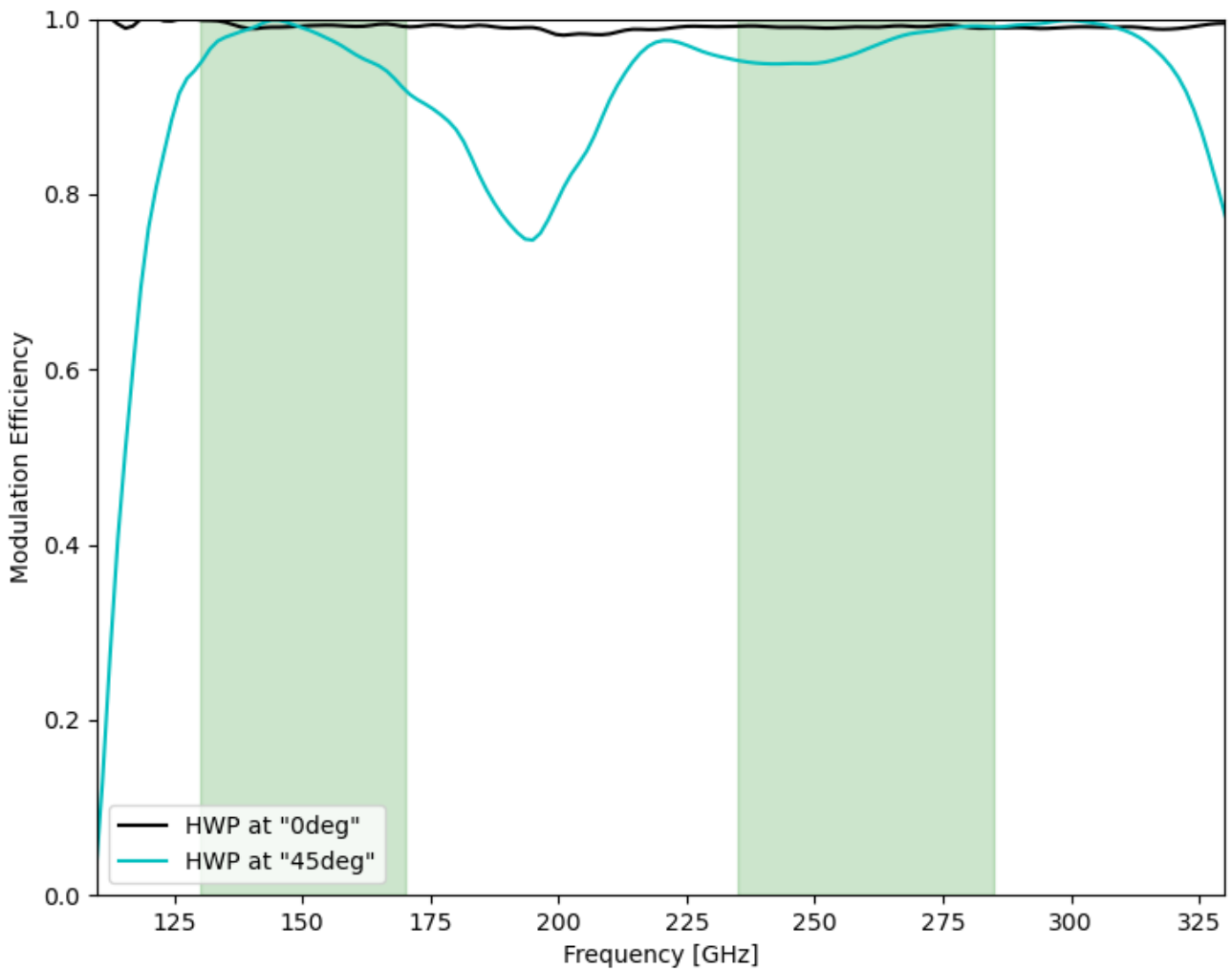


Figure 5.7 – Modulation efficiency of the NIKA2 HWP from the FTS experiment and was calculated using spectra in Figures 5.5 and 5.6 in equation (4.6). The modulation efficiency of the NIKA2 HWP was calculated to be greater than 0.98 across all frequencies, with its value approximating to 0.992 across the 150GHz band and 0.996 across the 260GHz band when the HWP was rotating to "0°". When the HWP was at a rotation of "45°" the modulation efficiency calculated was 0.973 and 0.969 for the 150GHz and 260GHz bands respectively. The shaded green areas represent the working bands of the NIKA2 experiment.

frequencies. From the equation (4.6) the modulation efficiency is expected to be 1 if this was an ideal HWP, i.e., it perfectly modulated the incident polarisation signal.

At the end of each co-pol and cross-pol measurement run, further measurements were taken to characterise the instrumental x-pol of the setup. To measure the x-pol, the polarisers were orientated to the cross-pol configuration i.e., P2 is set with its wires horizontal to the optical bench, the HWP was removed from the system and measurements were taken in this configuration. This measurement shows the noise floor of the FTS system and the baseline to which I could expect to measure. This measurement allows us to observe the level of polarisation mixing within the optical

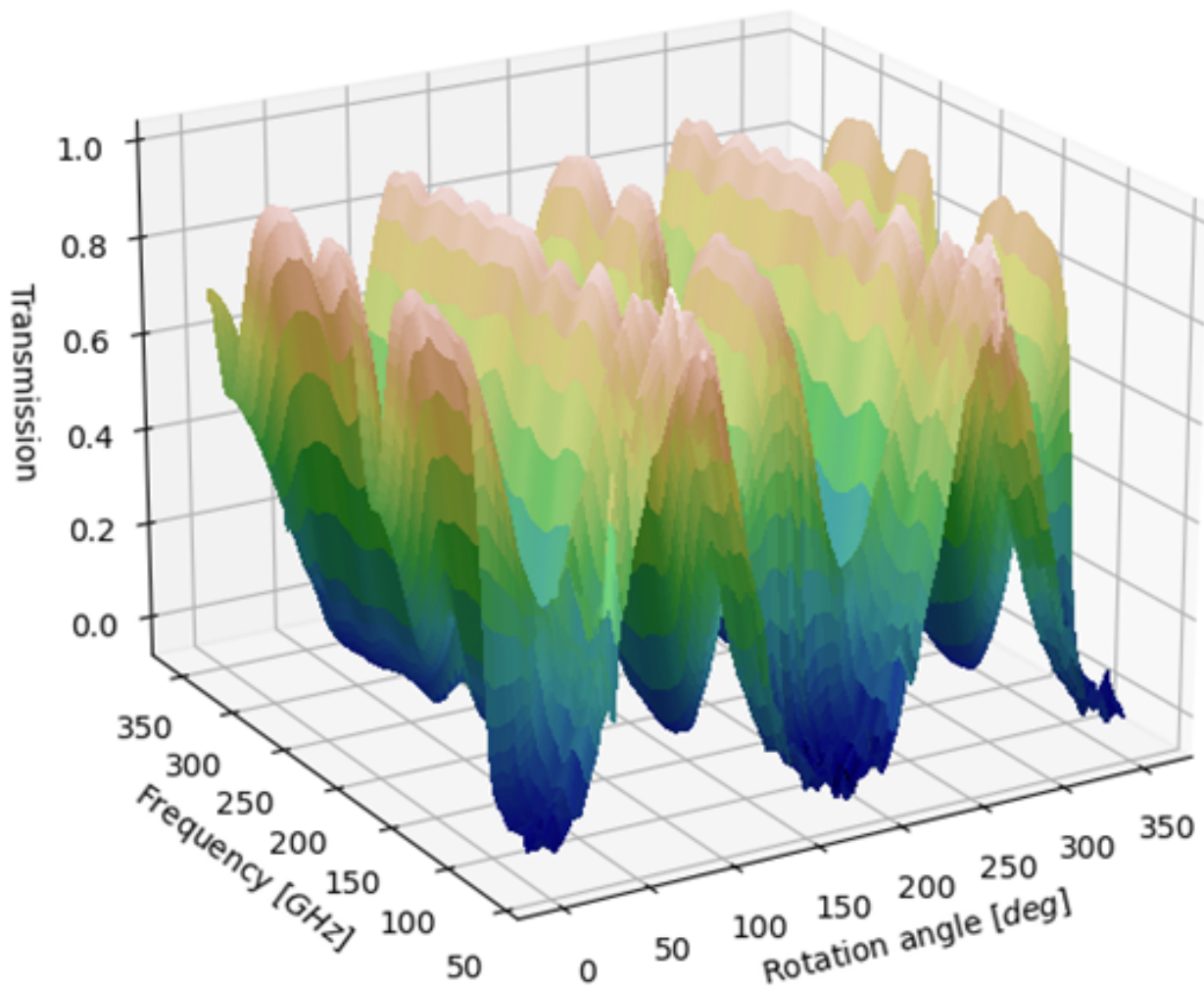


Figure 5.8 – Data cube for the co-pol spectral transmissions of the HWP at rotation angles between 0° and 359° . Measurements of the spectral transmission were taken every 5° and the increments were changed to 2° close to maxima and minima angles.

setup itself. Ideally, this would be zero across the full frequency range, however, due to deviations from perfect performance for the elements in this system this data set will deviate from zero.

Two spectra were acquired in this configuration, averaged, and then normalised against co-pol background spectra. Across the working bands for this HWP I recorded a x-pol level of less than 0.5%. The resulting spectra is included in Figure 5.5 and 5.6.

Features that are visible in Figures 5.10 and 5.11 are spectral fringes caused by small reflections between dielectric substrates in the optical path (such as the polarisers) which cause standing waves. The HWP itself, as an embedded metal mesh type, has multiple layers of polypropylene which enhances the amplitude of the fringes by introducing small amounts of absorption at every internal reflection.

From the spectra produced in Figures 5.10 and 5.11 it can be observed that the HWP is

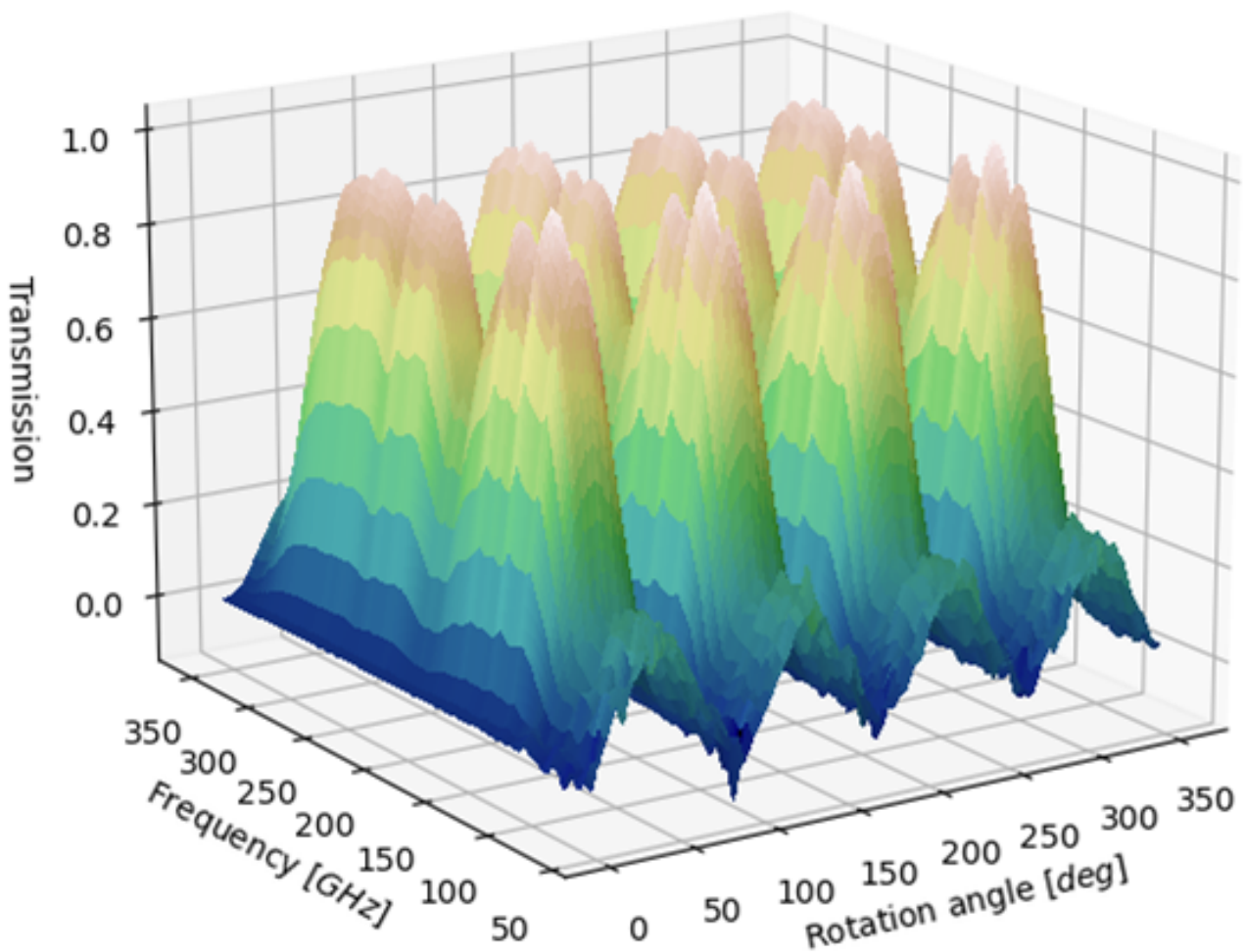


Figure 5.9 – Data cube for cross-pol spectral transmissions of the HWP at different rotation angles. Measurements of the spectral transmission were taken every 5° and the increments were changed to 2° close to maxima and minima angles. Comparing to Figure 5.8 it is shown that these results are in counterphase to each other.

successfully tuned to the operational bands of the NIKA2 experiment due to the transmitted signal being ~ 0.94 and ~ 0.93 for the 150 GHz and 260 GHz bands respectively with the transmission values dropping outside of those bands. For the cross-pol transmission spectra the average transmission across the two bands was ~ 0.94 and ~ 0.93 for 150 GHz and 260 GHz respectively.

5.2 RESULTS

The Mueller parameters in Figure 5.12 were obtained by injecting the data cubes from Figures 5.8 and 5.9 into the Mueller matrix pipeline described in Chapter 3. Across the HWPs working bands each matrix parameter produced values close to the theoretical values given in equation 3.1 with small deviations observed. The average values for each matrix parameter are provided in Table 5.1.

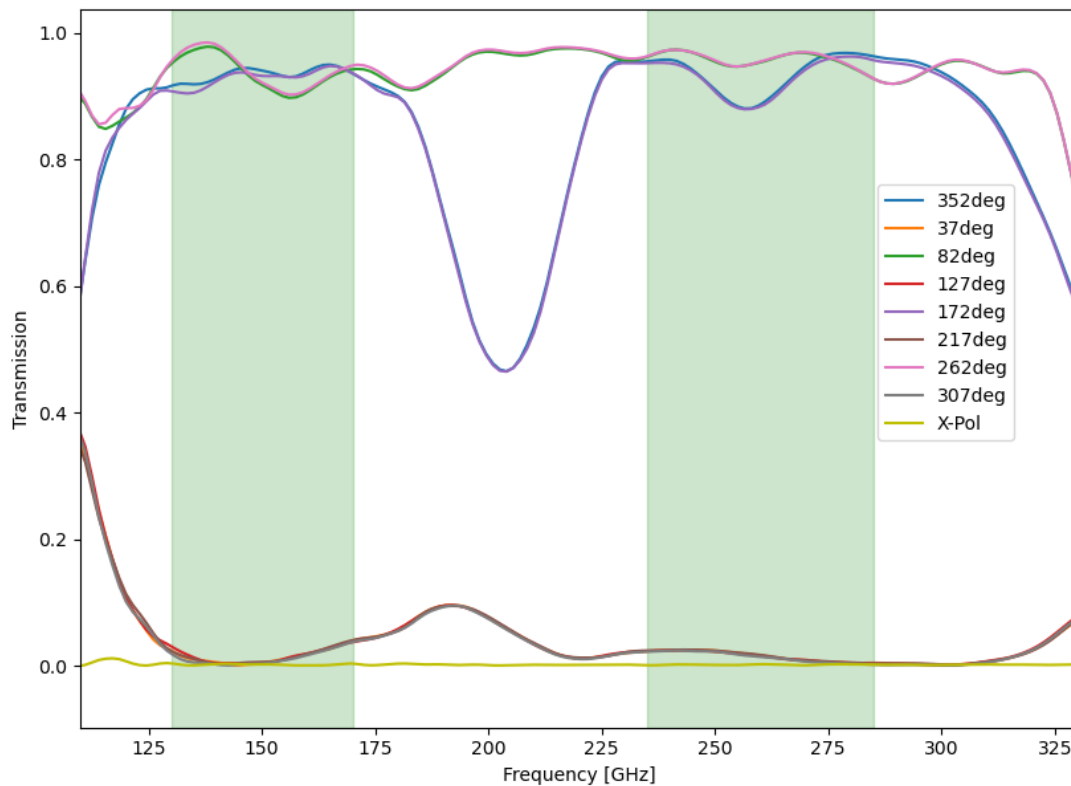


Figure 5.10 – Measured co-polarisation transmission spectra of a NIKA2 anti-coated embedded metal mesh HWP presented in Figure 5.5 but in linear format. The angles denoted in the legend are arbitrary values used to reference the angle on the rotation mechanism used to rotate the HWP, allowing for repeat measurements to occur and are just for reference for repeat measurements in the setup. The ‘zero’ values also might not occur exactly at the zero angle which is why transmission spectra are taken around the expected value.

The diagonal terms M_{II} , M_{QQ} and M_{UU} describe the total intensity and linear polarisation measured from the HWP. Each has a theoretical value of 1, 1 and -1 respectively, i.e., there should be 100% transmission of the signal produced by the FTS. The negative sign which arises for the M_{UU} component is due to the rotation of the polarisation angle which the HWP causes, described in Chapter 2. The measured values as presented in Table 5.1 indicate deviations from these expected values, with the largest difference being 0.09 across both frequency bands with the M_{UU} parameter. This is caused by the phase difference created between the HWPs axes not equalling 180° exactly across the measured frequencies.

The off-diagonal parameters M_{IQ} , M_{QI} , M_{UI} and M_{IU} describe intensity to polarisation leakage. These terms theoretically should equal 0, but from these results it is observed that they have an amplitude between 0.0002 - 0.016, across the two working bands, indicating there is a

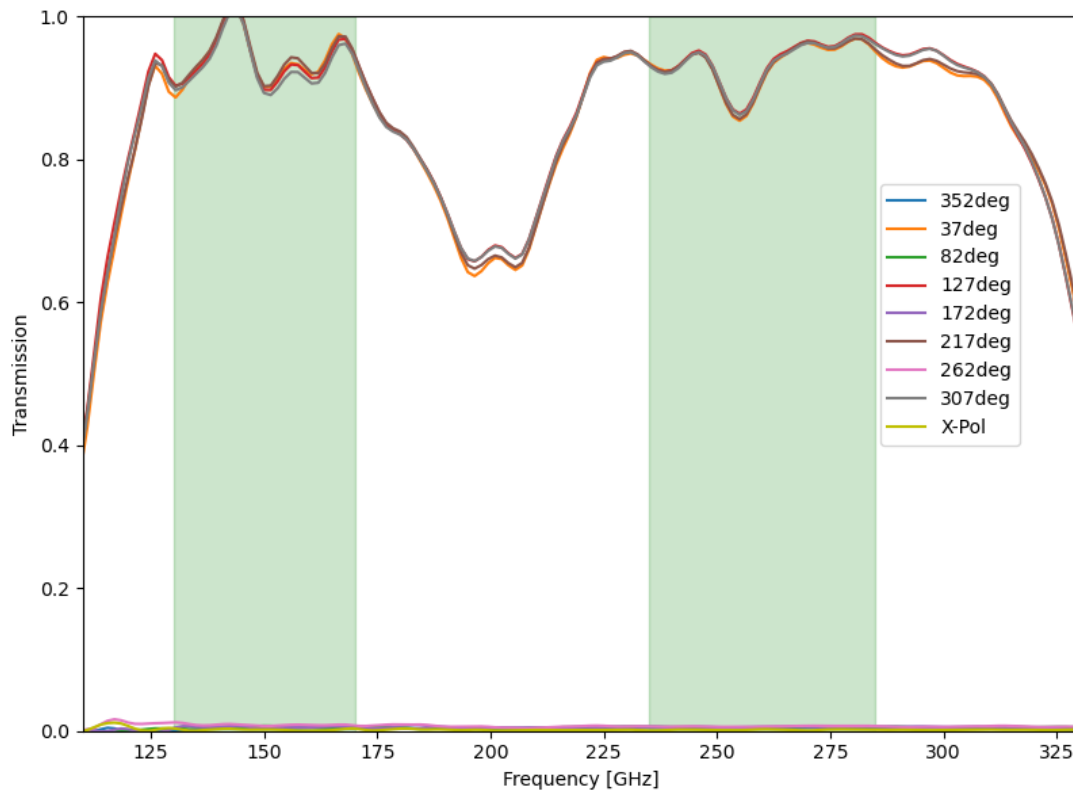


Figure 5.11 – Measured cross-polarisation transmission spectra of a NIKA2 anti-coated embedded metal mesh HWP presented in Figure 5.6 but in linear format. The angles denoted in the legend are arbitrary values used to reference the angle on the rotation mechanism used to rotate the HWP, allowing for repeat measurements to occur and are just for reference for repeat measurements in the setup. The ‘zero’ values also might not occur exactly at the zero angle which is why transmission spectra are taken around the expected value.

low level of leakage ($\sim 1\%$) caused by the HWP from intensity to polarisation.

The M_{QU} and M_{UQ} parameters describe polarisation leakage, i.e., if there is any leakage from one polarisation to another. The theoretical ideal values for these parameters are 0 but from the results provided in Table 5.1 from the pFTS experiment it shows that these parameters produce amplitudes of 0.078 and 0.07 across the two bands. This is a significantly high level of polarisation leakage and indicates a substantial amount of linear polarisation is being rotated to elliptical polarisation as a result of the phase difference of the HWP not equally 180° over the bands causing the modulation to deviate from the ideal case.

The Mueller matrix parameters can be observed to taper off at the lower (120 GHz) and higher (310 GHz) frequencies measured. This is due to the HWP being designed to work over the NIKA2 instruments bandwidths of which these frequencies lie outside of. Outside of the working bands

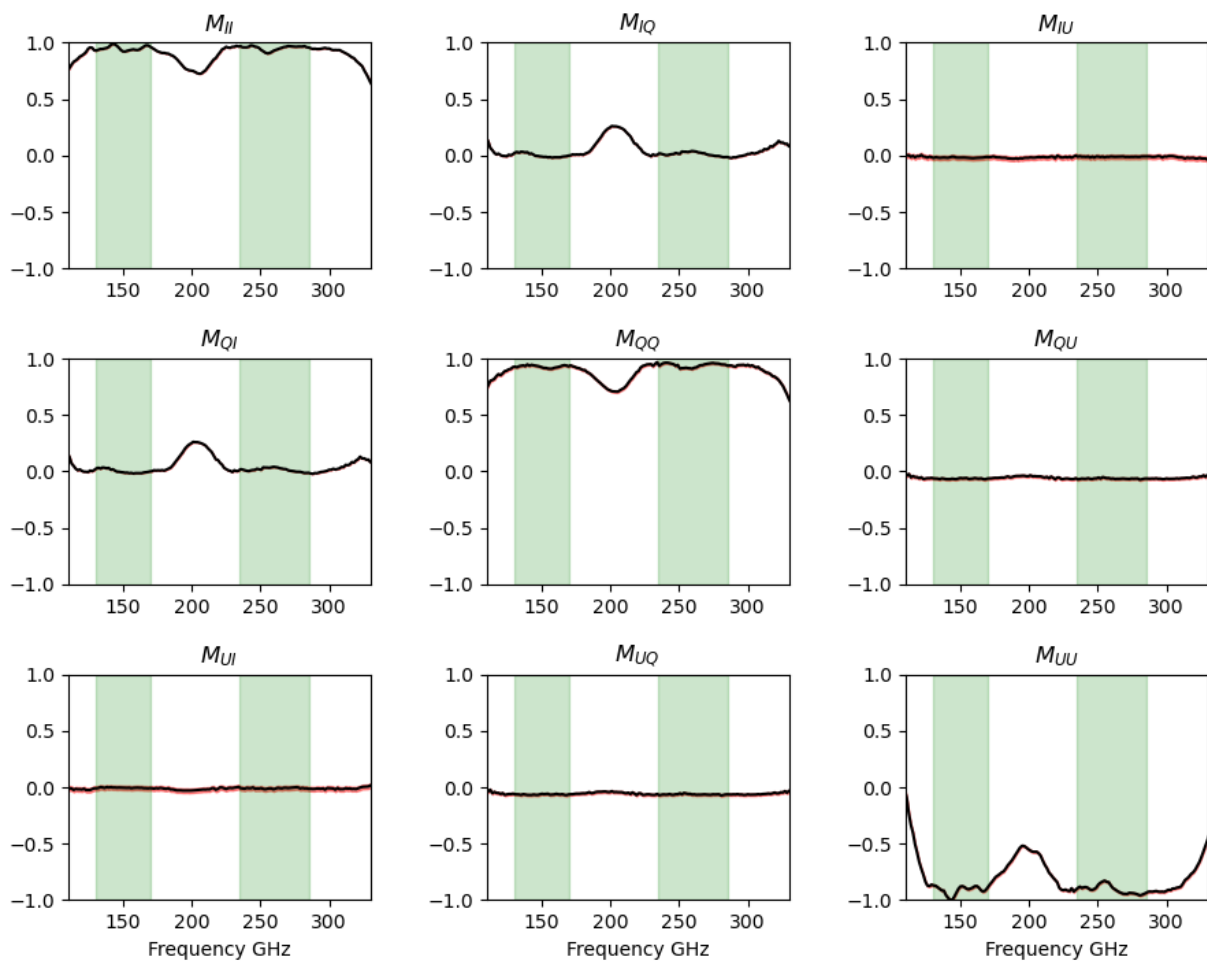


Figure 5.12 – Mueller matrix of the NIKA2 HWP (at a given angle of $\theta = 0^\circ$) using a pFTS at Cardiff University with errors (1σ , red shaded area) and working bands (shaded green area) included.

of the NIKA2 experiment the HWP is designed to produce phase differences not equal to 180° resulting in the linear polarisation being rotated to elliptical states. Therefore, the performance of the HWP will be worse and the parameters will deviate from the ideal values more. Further to this, in the parameters M_{II} , M_{IQ} , M_{QI} , M_{QQ} and M_{UU} a dip is present at ~ 200 GHz and is caused by the requirement of the HWP performing equally well over two frequency bands and which caused the design to include a reduction in values to enable this. The smaller bump in the dip at ~ 200 GHz is caused by the feature seen in the spectra at ~ 200 GHz in Figure 5.11.

Injecting the parameter values presented in Figure 5.12 into equations (2.12) and (2.11) the optical efficiencies of the NIKA2 HWP was calculated to be 0.96 and 0.97 for the 150 GHz and 260 GHz band respectively. The polarisation efficiencies were calculated to be 0.96 and 0.95 for the 150 GHz and 260 GHz band respectively. These values were expected to be equal to 1 for each frequency band if the HWP was performing as the theoretically ideal device as this

Mueller matrix parameter	150 GHz band average	260 GHz band average	Error in value for 150 GHz	Error in value for 260 GHz	Theoretical value
M_{II}	0.95	0.95	0.000572	0.000416	1
M_{IQ}	-0.003	-0.016	0.002106	0.000799	0
M_{IU}	0.016	0.009	0.001941	0.000471	0
M_{QI}	0.0002	-0.012	0.002106	0.000799	0
M_{QQ}	0.93	0.94	0.001480	0.015841	1
M_{QU}	0.078	0.07	0.003657	0.002323	0
M_{UI}	-0.005	-0.008	0.001941	0.000471	0
M_{UQ}	0.078	0.07	0.003657	0.002323	0
M_{UU}	-0.91	-0.91	0.001480	0.015841	-1

Table 5.1 – Band averaged matrix parameters for the NIKA2 HWP measured using a pFTS with their associated errors and expected theoretical values.

would indicate that the HWP is transmitting all incident radiation and rotating the linear polarisation perfectly. However, the small deviation from 1 for each of these efficiencies indicates that the HWP was rotating some of the polarisation by values which caused the linear polarisation to become elliptical polarisation and also the HWP was reflecting some of the radiation as not all of it was transmitted.

This Chapter has presented the results obtained from measuring the spectral transmission of the NIKA2 HWP using a FTS and generated the HWPs Mueller matrix components. Within the next Chapter I compare these results with the results presented in Chapter 4 and discuss future work to be performed.

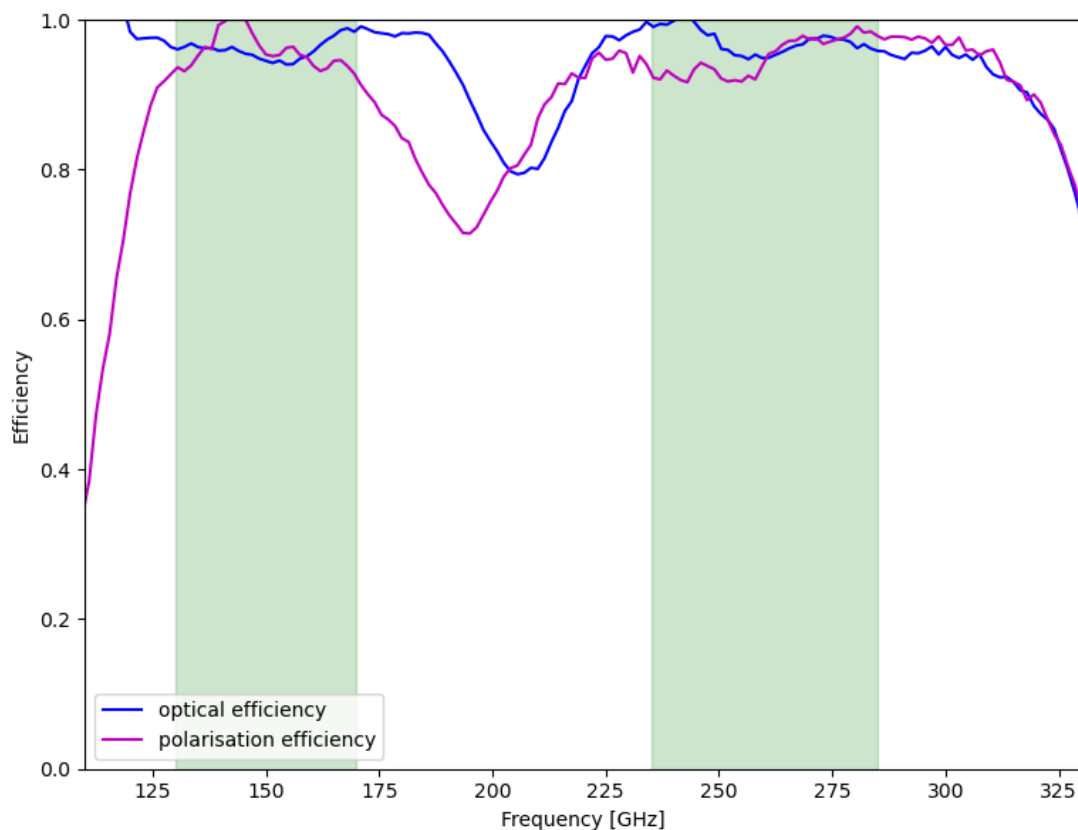


Figure 5.13 – The optical (blue line) and polarisation (magenta line) efficiency measured by using the Mueller matrix parameters calculated in Figure 5.12 for the NIKA2 HWP. The average optical efficiency was 0.96 and 0.97 for the 150 GHz and 260 GHz bands respectively. The average polarisation efficiency was calculated to be 0.96 and 0.95 for the 150 GHz and 260 GHz bands respectively. The shaded green areas represent the bandwidths of the NIKA2 experiment and indicate the frequencies the HWP should be performing perfectly over.

DISCUSSION

"And here, poor fool! With all my lore, I stand no wiser than before."

Goethe, *Faust*

This thesis has presented two different types of HWPs commonly used in sub-mm experiments, the theory behind how they work, why future CMB polarisation experiments are considering to use them and the method to generate their Mueller matrices in order to characterise their performance. This method was used to generate the Mueller matrices of an embedded metal mesh HWP design, calculated from two different laboratory setups.

In this Chapter I will compare the results presented in Chapters 4 and 5 to conclude which system is preferred for HWP characterisation measurements, the FTS or VNA.

6.1 COMPARISON OF THE VNA AND FTS SYSTEMS

The VNA and FTS used in Chapters 4 and 5 respectively used a different optical setup to characterise the NIKA2 HWP. In this Chapter I review those differences and the advantages and disadvantages of each.

6.1.1 Dynamic range

While the two optical setups described in Chapters 4 and 5 measured the same device, they produced different results due to the properties of each instrument used. One difference was the dynamic range of the two instruments which describes the difference between the output power and the noise floor of the system. The VNA had a dynamic range of 75 dB, whilst the FTS only had a dynamic range of 30 dB, indicating that the VNA was better suited to detect low power

signals, which for the characterisation of HWPs is very useful for the minima measurements as these values are expected to be equal to zero.

The x-pol of the FTS was measured to be ~ 0.002 whilst the VNA recorded an x-pol of ~ 0.003 across the two bandwidths of the NIKA2 experiment. X-pol refers to the mixing of polarisation states caused by the measuring system itself. This level is important to measure because it can highlight how much signal might be lost from the rotation of the polarisation states. However, if the full frequency range was measured and taken into account the VNA x-pol would be considerably higher due to the 160-260 GHz antenna heads used. These provided a substantial level of polarisation mixing into the system.

6.1.2 Spectral resolution and scan time

The spectral resolution describes the separation between the frequencies a signal is measured at and the spectral resolution for the VNA and FTS systems described in this thesis were different, see Table 6.1. The higher spectral resolution of the VNA means the system allows for more spectral detail to be measured that the FTS system may not be able to measure. However, the spectral resolution of the VNA and FTS can be set by the user because it is determined by the size of the frequency steps.

Spectral System	Spectral resolution [GHz]
FTS	1.5
VNA 110-170 GHz	0.06
VNA 160-260 GHz	0.1
VNA 220-330 GHz	0.11

Table 6.1 – The spectral resolution of the FTS and VNA systems used in Chapters 4 and 5 presented in GHz units. The spectral resolution of each antenna head set used in the VNA system is provided in this Table, with the 110-170 GHz range having the highest spectral resolution of the entire set. The spectral resolution of the FTS was set by the optical path difference used in the experiment which was 10 cm^{-1} .

For the VNA system the spectral resolution is determined by the number of sweep points, for this work it was 1001, and the measurement bandwidth of the VNA system, i.e., 110-170 GHz would have a 60 GHz bandwidth.

Alternatively, the spectral resolution of a FTS depends on the maximum optical path difference (OPD), which describes the furthest distance the moveable mirror travels from the stationary mirror in the FTS system. The spectral resolution is inversely proportional to the maximum OPD therefore increasing this distance would provide a higher spectral resolution. However, this can be limited by the available space in the laboratory depending on the distance.

When deciding on the spectral resolution to use the time taken to generate the spectral data sets needs to be considered because a higher spectral resolution results in narrower frequency bandwidths, thus meaning more data points between the frequency range being measured. This increase in the number of data points will cause the time taken measuring the device under test to greatly increase, therefore, if there are time constraints on using the spectral system a lower spectral resolution could be considered to account for this.

For example, the spectral resolution of the VNA system produced 1001 spectral transmission data points for each antenna head set used (Table 6.1). The time taken for each spectra was approximately 10 minutes and the total time to obtain the data cubes presented in Figures 4.6 and 4.24 was two weeks. While the FTS system had 192 spectral transmission data points over a frequency range of 90-330 GHz for each spectra presented in Chapter 5. Each scan took approximately 20 minutes to finish resulting in the data cubes presented in Figures 5.8 and 5.9 taking four weeks to complete. The time spent measuring the NIKA2 HWP using the FTS system took twice as long to take the same set of spectral data as was performed on the VNA system.

Computationally though the larger data sets produced from the VNA method results in the pipeline generated in Chapter 3 to take approximately 6 hours to run, while the data sets produced using the FTS method only took approximately 30 minutes to run in order to generate the Mueller matrix of the NIKA2 HWP. The VNA therefore uses a substantial amount of power to compute the HWPs Mueller matrix components over the measured frequency range compared to the FTS, which if this pipeline is being used on a laptop can affect the laptop's performance over time.

6.1.3 Test benches and alignments

When assembling any optical test bench there are many factors that require careful attention. An essential criterion to any test is ensuring all optical elements are aligned to the optical axis. From initial measurements performed on the VNA test bench I found realignment was required for many of the optical elements because they were not centred along the optical axis. Chapter 4 details all the methods required to centre each optical device along the optical axis. Performing these methods corrected the spectra produced by each antenna head and allowed for the HWP to be correctly characterised.

However, this alignment issue signifies the VNA optical setup was not an intuitive instrument to use when carrying out HWP characterisations. Small lateral movements in the lens mount positions could cause the signal detected to change by 0.2-0.5 dB. To centre each antenna head required lateral, rotational and vertical changes none of which were trivial procedures. This therefore identifies the need for users to comprehensively understand optical alignments before using the instrument.

The FTS optical setup in comparison is more straight forward and easier to understand, and

therefore useful for users who need to measure optical devices, such as HWPs. For example, for cross-pol and x-pol measurements the receiver was required to rotate about a point by 90° which if the point is not along the optical axis can cause a reduction in the received signal, as seen in Chapter 4. However, the FTS setup described in Chapter 5 rotates a polariser, P2, by 90° instead to measure the cross-pol and x-pol spectra.

Performing measurements on devices which have diameters larger than 30 cm was an issue on the FTS system because of the design of the workbench and the space available in the optical setup. The polarised signal could not be transmitted through the centre of the device but rather the edge of it. While it is good to check the device for uniformity, the centre is where the majority of the desired signal will propagate, thus initial measurements should be performed in this location. To overcome this the FTS would need to be raised or the workbench would need to have a cut out added to it where large devices could sit and rotate so that the centre is aligned to the optical axis. To perform the measurements on the NIKA2 HWP on the FTS system the HWP was cut down to a 100 mm diameter size.

6.1.4 HWP rotating mechanism

For the measurements using the VNA system, moving the HWP in and out of the beam was very strenuous due to the size and weight of the rotating structure, and the requirement to ensure optical devices in the optical chain were not struck in the process. The rotator, with the HWP held in place, weighed approximately 5 kg and was tilted at 45° angles twice every four measurements which put a strain on my shoulders and arms. Additionally, it was important to ensure that the HWP rotation structure did not scratch the bench and so cardboard was placed under the edges of the rotating mechanism to allow it to slide along the bench without scratches. Ensuring the integrity of the bench was important as scratches would cause the bench to no longer be entirely flat with the potential to affect measurements.

Moving the HWP rotating structure is required every four transmission measurements because of the need to monitor the drift in the signal caused by the antenna heads used in the VNA setup. This drift happens over time and to account for it in the measurements I ratioed all four measurements against the two background measurements either side of the transmission measurements to account for it. I also ratioed the backgrounds together to observe if any significant drift occurred over the time period between the background measurements.

For future measurements a pulley system should be applied to bring the rotation mechanism in and out of the beam to ensure repeat positioning but also to ensure the physical well-being of the user due to the measurements from Chapter 4 taking a physical toll on the user.

For the FTS system the rotating mechanism had an outer diameter of 120 mm and weighed approximately 1 kg with the HWP held in place. With the setup of the optical bench for this setup

the rotator could be lifted with ease out of the beam.

6.1.5 Frequency range required for characterisation

The NIKA2 experiment operates over the frequency bands stated in Table 6.2, therefore, the VNA and FTS were required to operate over these frequencies in order to characterise the NIKA2 HWP's performance. The frequency range therefore measured in this thesis was fairly large.

Central frequency [GHz]	Bandwidth [GHz]
150	82
260	107

Table 6.2 – NIKA2 band definitions and corresponding bandwidths (Pisano et al., 2022).

The VNA system described in Chapter 4 covered the frequency range required to fully characterise the performance of the NIKA2 HWP, however, three antenna head sets were required in order to achieve this. Initial measurements shown in Section 4.1.2 with Figure 4.9 indicated misalignments within the optical test bench across all three antenna sets and from Figure 4.28 provided in Section 4.1.4 it was shown that after the realignment of the optics in the system a mismatch between antenna sets was still observed between the 160-260GHz and 220-330GHz sets. Furthermore, replacing each antenna head to measure the full range required small adjustments to the optical setup, such as moving the lenses to place them at their focal lengths due to each antenna set being located at different positions along the optical axis resulting in different distances from the lenses. As discussed in Section 4.1.3 this was done to ensure the maximum amount of signal was detected from the system.

Additionally, introducing more devices into a system introduces different systematic errors to the measurements which was seen from the results in Section 4.1.4 (Figure 4.28) in which a large spread is observed in matrix parameters at approximately 200 GHz. This was found to be due to the antenna heads themselves and they were subsequently sent for repairs.

Alternatively, the FTS system used in this thesis could measure spectral transmission between 90-1200GHz but a LPE was placed in front of the cryostat window resulting in the FTS measuring between 90-330 GHz. The benefit to this is the FTS could measure the entire frequency range in a single run, only introducing the systematics of the system once. However, CMB experiments also measure signals at frequencies lower than 90 GHz, therefore requiring that devices deployed in their instruments be able to perform over these frequencies. However, the FTS system at frequencies below 90 GHz had a low signal to noise ratio causing the measured spectral transmission to not be representative of the device under test due to its signal being engulfed by the noise of the system. Therefore, to measure devices at frequencies below 90 GHz an alternative spectral instrument would be required.

6.2 COMPARISON OF THE MEASURED HWP PERFORMANCE

In Chapter 3 a pipeline was explained in which one could use experimental datasets to generate a HWPs Mueller matrix. Using this pipeline two Mueller matrices were generated using two different experimental setups, and their results described in Chapters 4 and 5. As both experiments used the same HWP, designed for the NIKA2 experiment, Mueller matrices for both setups should be identical. However, there are small variations in the performance measured between each setup, seen in particular at the higher frequencies.

6.2.1 Transmission spectra of the NIKA2 HWP

Both optical setups described in Chapters 4 and 5 recorded co-pol and cross-pol spectra as a function of rotation angle and frequency. The resulting co-pol maxima and minima for both VNA and FTS are shown in Figures 6.1 and 6.2 respectively, both Figures closely follow the same data apart from a couple of differences. One such difference being the small peak in the minima curves measured by the VNA (magenta, orange, green and brown curves seen in Figure 6.1) present in the frequency range 160-260 GHz do not overlap with one another, whereas the minima curves produced from using the FTS do overlap very well. The cause of this was later found to be due to the antenna head set used for the 160-260 GHz range as it was found to have substantial drift throughout later measurements and was sent for repair.

Another difference between the spectra produced by the VNA and FTS setups is the structure present in the 110-170 GHz range in Figure 6.1. Fabry-Perot fringing can be observed from the small bumps present in the minima spectra which arise from reflections in the optical setup. This is the conclusion drawn because the fringing was not observed in the FTS spectra in Figure 6.2 and if they were produced due to the HWP itself it would be seen in both sets.

The x-pol measured for the VNA and FTS defines the level of polarisation mixing inherent to each setup and was measured in the VNA setup to be ~ 0.0008 and ~ 0.003 for the 150 GHz and 260 GHz bands respectively. For the FTS setup the x-pol was measured to be ~ 0.002 and ~ 0.001 for the 150 GHz and 260 GHz respectively. However, whilst the x-pol spectrum measured over 110-170 GHz and 220-330 GHz and were at levels of 10^{-4} the measured values over the 160-260 GHz range were nearly two magnitudes higher and were shown to be at the same level as the co- and cross-pol spectral transmission measurements (seen in Figure 4.8).

To characterise the HWP on the VNA system three different antenna heads were used. From Figure 4.25 it was seen that the 160-260 GHz and 220-330 GHz curves do not overlap exactly due to the alignment of the 220-330 GHz antenna head. The aperture of the antenna horn was smaller compared to the other two antenna sets used because of the frequency range they measured over. This difference in size caused the margin of error for optical alignment to be smaller due to

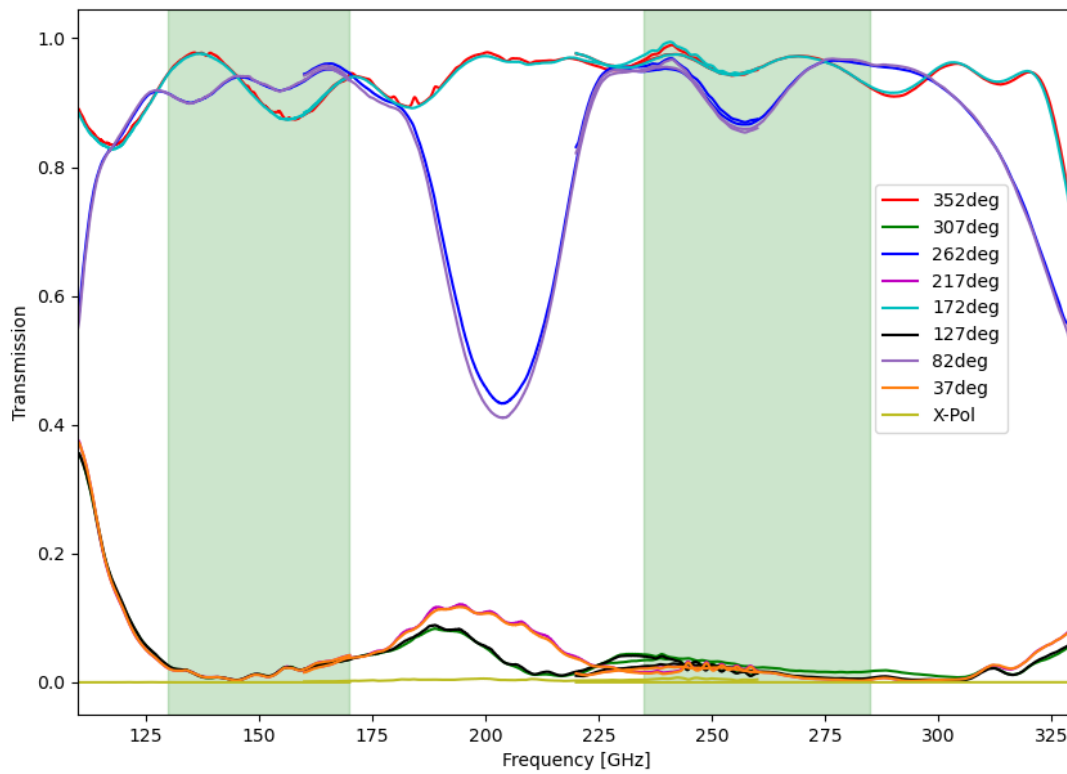


Figure 6.1 – Maxima and minima spectra from co-polarisation measurements using the VNA, plotted in a linear format. Structure in the system can be observed in the 160-260 GHz range by the ripples in the minima spectra. The x-pol measured level of the VNA system is plotted as the yellow curve. The angles denoted in the legend as arbitrary to the system and are noted for repeatability. Shaded green areas correspond to the working bands of the NIKA2 experiment.

the smaller collecting size. Any small deviations in optical alignment will affect the signal detected at these frequencies due to this.

When comparing the maxima spectra in Figures 6.1 and 6.2 (angles 352° , 82° , 172° and 262°) to the modelled and experimental performance of the NIKA2 HWP design (depicted in Figure 6.3) both the VNA and FTS experiments generate similar profiles to its modelled performance. The overall performance of the HWP across the measured frequency range aligns well with the model in both the VNA and FTS setups and verifies the HWP transmits the polarised signal as expected over the designed frequency bands.

The overall transmission of the HWP in both co-pol and cross-pol is good with over 90% transmission being measured across the working bands. This is consistent with what is required from the HWP and the measured transmission along either the capacitive (C) or inductive (L) axis is ≥ 0.9 (Pisano et al., 2022).

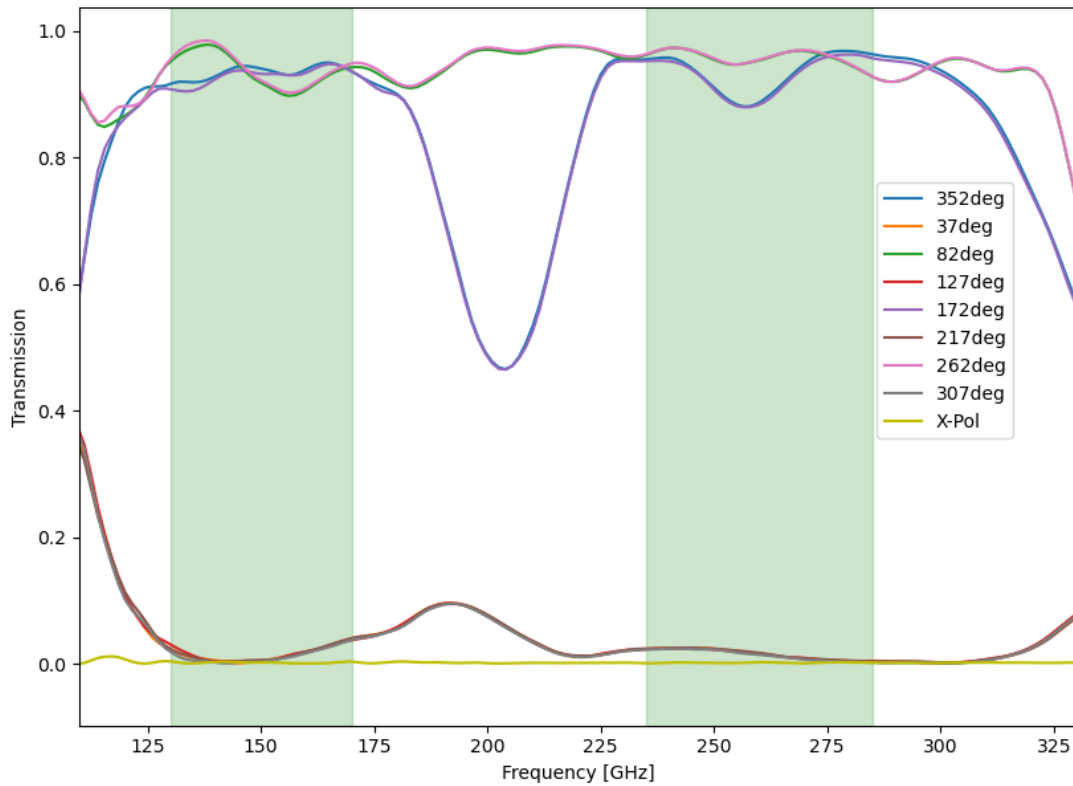


Figure 6.2 – Maxima and minima spectra produced from the co-polarisation measurements using the FTS setup, plotting in a linear format. The maxima data sets (blue, green, purple and pink curves) overlap well with each other and therefore agree well. The minima data sets (orange, red, brown and grey curves) overlap each other and therefore the measurements agree with each other. Shaded green areas correspond to the working bands of the NIKA2 experiment and the yellow curve denoted the x-pol of the FTS system which describes the polarisation mixing caused by the FTS instrument itself.

6.2.2 Mueller matrices of the NIKA2 HWP

The Mueller matrix parameters obtained from the VNA and FTS experiments, blue and black curves respectively in Figure 6.4, show from first observations most parameters appear to agree with one another with a few noticeable differences. For example, the $[M_{IQ}, M_{QI}, M_{QU}, M_{UQ}]$ values are different between optical instruments in that their values have opposite signs and therefore appear to be mirrors along $y = 0$.

For the M_{IQ} and M_{QI} terms, the VNA calculated the average values to be ~ 0.008 and ~ 0.008 at 150 GHz and ~ -0.018 and ~ -0.019 at 260 GHz respectively. This change in sign was found to be caused by one of the polariser Mueller matrices used to generate the FTS's model equations

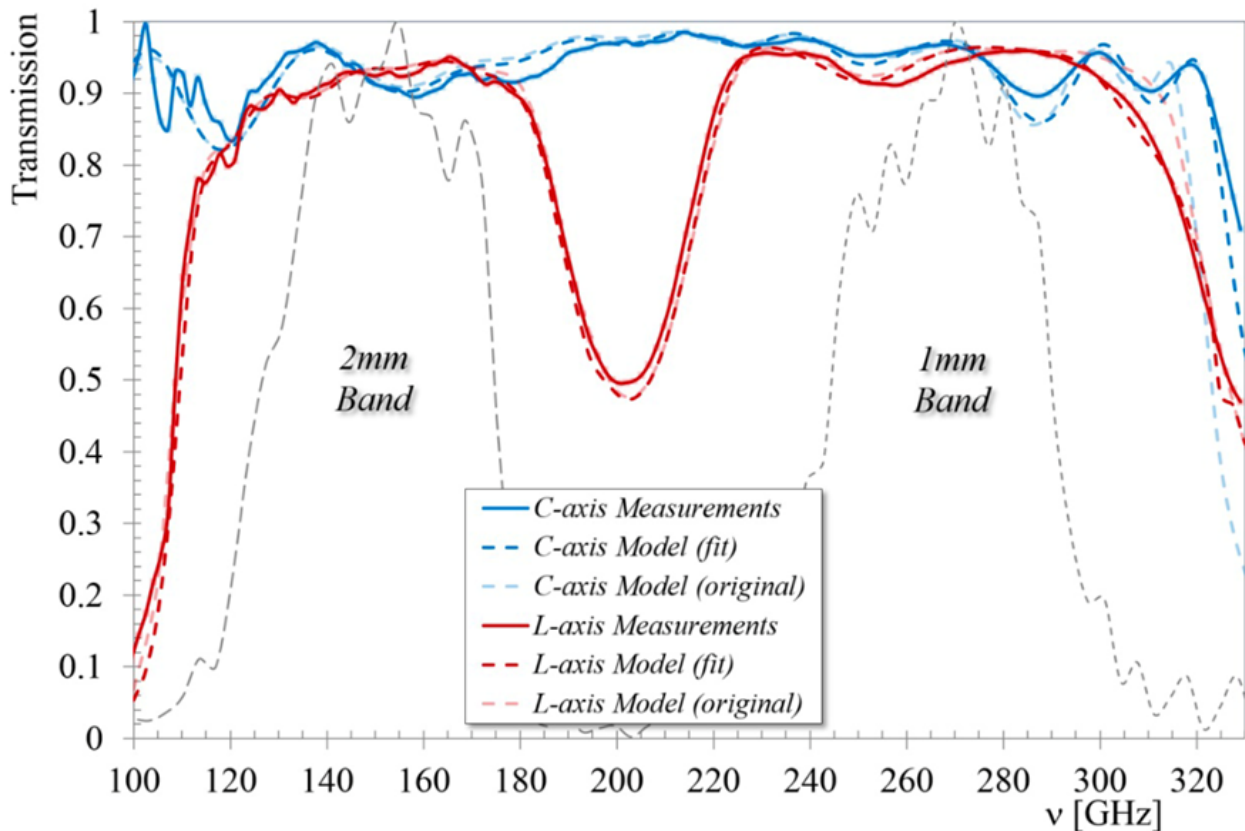


Figure 6.3 – Modelling behaviour of the NIKA2 HWP and measurements that were taken of it in 2015 at Cardiff using an FTS. The black dashed lines indicate the bandpass of the NIKA2 experiment. The labels of C-axis and L-axis indicate the orientation of the axes of the HWP, these means that the C-axis or L-axis was parallel with the optical axis (Pisano et al., 2022).

Mueller matrix parameter	150 GHz FTS	150 GHz VNA	260 GHz FTS	260 GHz VNA	Theoretical value
M_{II}	0.95	0.93	0.95	0.93	1
M_{IQ}	-0.003	0.008	-0.016	-0.018	0
M_{IU}	0.0016	-0.004	0.009	0.009	0
M_{QI}	0.0002	0.008	-0.012	-0.019	0
M_{QQ}	0.93	0.93	0.94	0.95	1
M_{QU}	0.078	-0.088	0.07	-0.057	0
M_{UI}	-0.005	0.004	-0.008	-0.012	0
M_{UQ}	0.078	-0.088	0.07	-0.057	0
M_{UU}	-0.91	-0.89	-0.91	-0.88	-1

Table 6.3 – Mean values for the Mueller matrix parameters generated using the VNA co- and cross-pol data cubes shown in Figures 4.6 and 4.24. Also included are the errors associated with these means and the theoretical values each parameter should be.

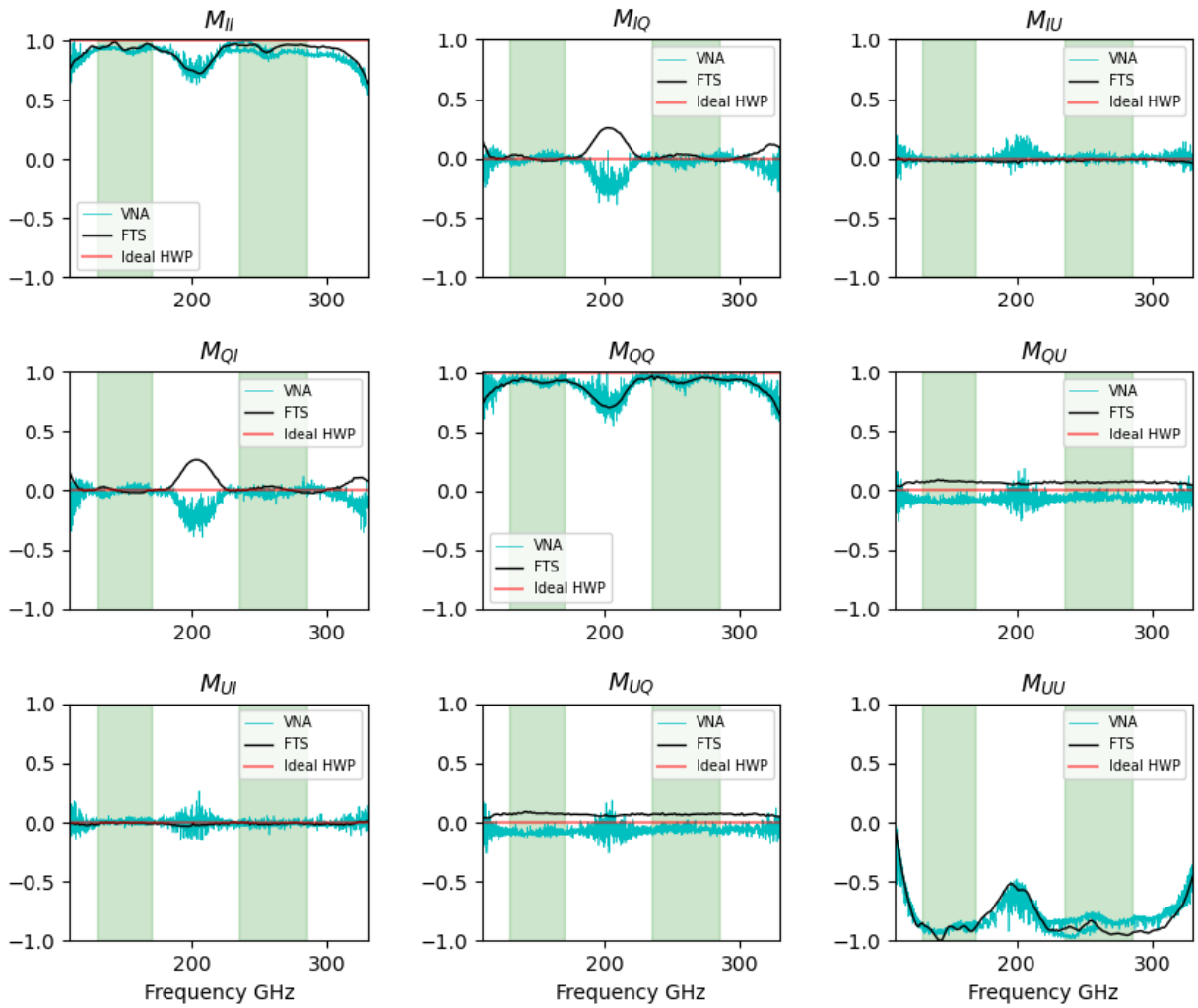


Figure 6.4 – Overlaying the Mueller matrix components calculated from both the FTS (black curves) and VNA (blue curves) first presented in Chapters 5 and 4 respectively. The working bands are shown at the green shaded regions centred on 150 GHz and 260 GHz. The ideal matrix parameter values are also plotted at a red shaded area. Error bars have been excluded from this plot to avoid confusion with overlapping values, the errors can be seen in Figures 4.28 and 5.12 for the VNA and FTS results respectively.

from Chapter 3. For the experimental setup described in Chapter 5 the input polariser matrix used should have been a horizontal polariser matrix, as described in equation (2.4), however, a vertical polariser matrix was used instead. As is shown in equations (2.4) and (2.5) the difference between the Muller matrices for each polariser are negative signs in two of the off-diagonal terms. These two terms when added to the matrix produces the change seen in signs. The model equations were corrected, and the results are shown in Figure 6.5.

For the M_{QU} and M_{UQ} terms in Figure 6.5 there is still a difference in results determined from the VNA and FTS setups. The VNA produced average values of ~ -0.088 and ~ -0.057 at 150

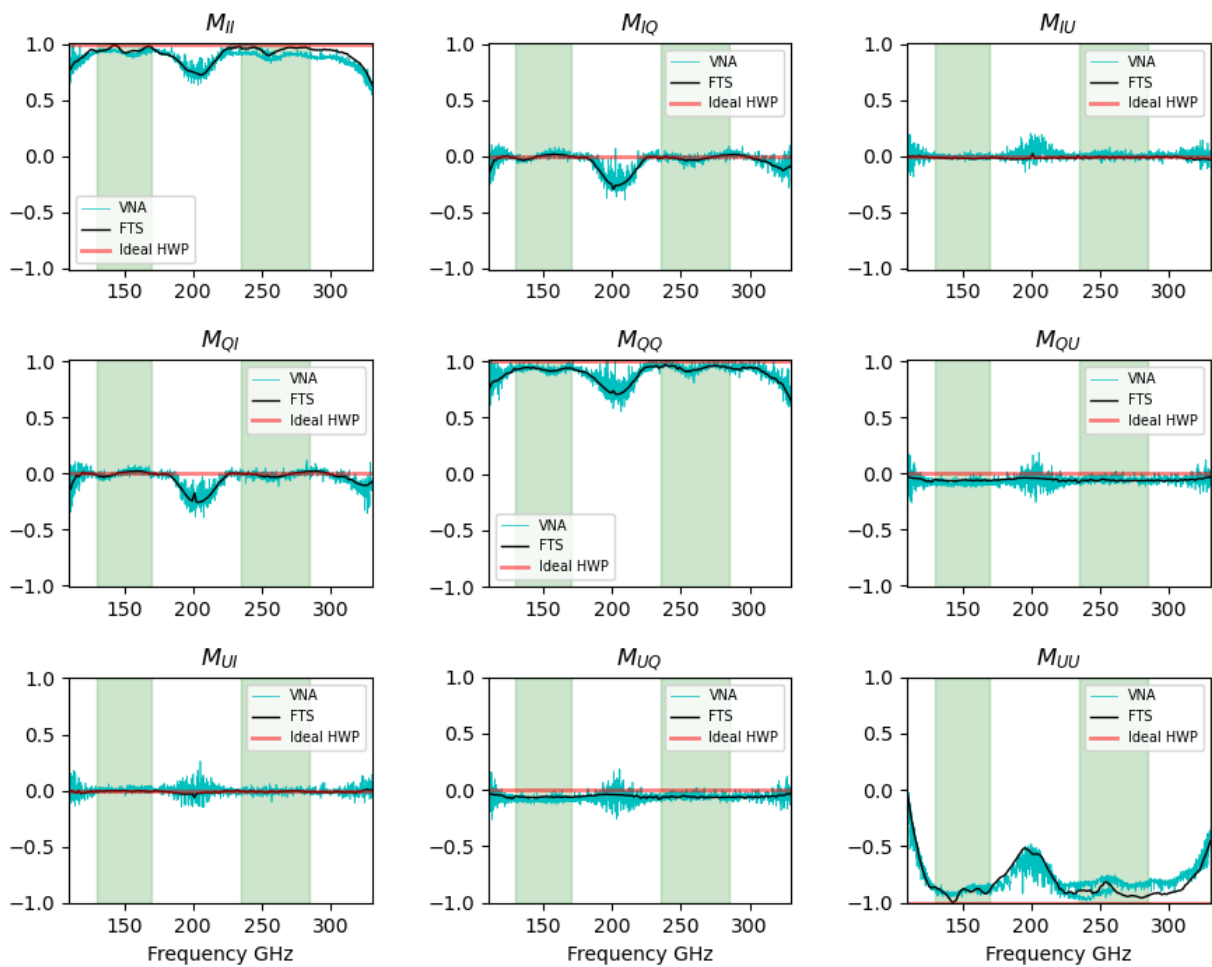


Figure 6.5 – Mueller matrix parameters produced from the VNA (blue line) and FTS (black line) spectra with the corrected matrix parameter equations to account for the FTS polarisation orientation. Matrix parameter values for an ideal HWP is included (red lines) in the plot. The working bands for NIKA2 is included as the shaded green areas to indicate the frequencies the HWP has been designed to work for. Error bars have been excluded from the Figure but are seen in Figures 4.28 and 5.12 for the VNA and FTS respectively.

GHz and 260 GHz respectively. The VNA produced $\sim 3\%$ difference across the frequency bands indicating that at the lower frequencies there is a higher level of polarisation mixing occurring within the HWP. Whereas the FTS produced average values of ~ 0.078 and ~ -0.069 at 150 GHz and 260 GHz respectively. The FTS measurements indicate there was a 1% difference in polarisation mixing occurring from the HWP which is substantially lower than that recorded by the VNA. Overall however, between the VNA and FTS the 150 GHz band produces a lower average than the VNA and vice versa for the 260 GHz band. These terms are still producing a difference in sign between the VNA and FTS setup which I believe is arising due to the misplaced negative sign in my pipeline, work is currently being carried out to check for this. If this is not the reason for the difference in sign further work will need to be done to understand the source of the problem.

Both experiments indicate that a substantial amount of polarisation mixing is occurring across the frequency range being measured with a level of $\sim 7\%$ of transmitted polarised light being mixed to other polarisation states. This mixing is caused by the polarisation state being rotated to a different state typically caused by the material of the device which causes a change to the phase difference. This level is fairly constant across all frequencies measured but further analysis is required to understand how this HWP is mixing the polarised light constantly over the frequencies measured.

For the diagonal terms $[M_{II}, M_{QQ}, M_{UU}]$ the VNA experiment provided averages of ~ 0.93 , ~ 0.93 and ~ -0.89 at the 150 GHz band and ~ 0.93 , ~ 0.95 , ~ -0.88 at the 260 GHz band respectively, while the FTS results provided averages of ~ 0.95 , ~ 0.93 , ~ -0.91 at the 150 GHz band and ~ 0.95 , ~ 0.94 , ~ -0.91 at the 260 GHz band. For both the VNA and FTS averages there is little change across the frequency bands with the largest difference being 2% between the M_{QQ} term in the VNA results. It was expected from the results that there would be very little change in matrix terms across the frequency bands because the HWP was designed to perform equally across both bands. Across both bands, the FTS produced diagonal parameters with roughly 2% higher values than the VNA system indicating that the HWP was performing better at transmitting the polarised signal across the rotation angles and frequencies.

For the off-diagonal terms $[M_{IU}, M_{UI}]$, the VNA experiment produced averages across each working band of ~ -0.004 and ~ 0.004 at the 150 GHz band and ~ 0.009 and ~ -0.012 at the 260 GHz band respectively, whereas the FTS experiment produced average values of ~ -0.003 and ~ 0.0002 at the 150 GHz band and ~ -0.016 and ~ -0.012 at the 260 GHz band. These matrix parameters indicate that mixing from intensity to polarisation is occurring from the HWP at levels of $\sim 1\%$ across the frequencies measured and indicate that HWP is also causing polarisation mixing.

For a theoretically ideal HWP the terms $[M_{II}, M_{QQ}, M_{UU}]$ are expected to produce values 1, 1 and -1 respectively whilst $[M_{IQ}, M_{IU}, M_{QI}, M_{QU}, M_{UI}, M_{UQ}]$ are all expected to equal 0 (expected values shown as red lines in Figure 6.5). The results presented in Chapters 4 and 5 and in Figure 6.5 deviate from these expected values due to the realistic performance of the HWP. The phase difference produced between axes will not be exactly 180° over the frequency band due to the necessity of compromising between performance and covering two frequency bands, as well as material properties.

Further to this, the experimental setup itself can cause structure within the measured spectra and affect the calculated performance of the HWP as shown within Chapter 4. The fluctuations in the VNA Mueller matrix components seen at 200 GHz is attributed to the 160-260 GHz antenna heads used in the experimental setup and as previously discussed above, the variance in measured spectra across these frequencies cause the fluctuations seen here.

Whilst the 110-170 GHz and 160-260 GHz matrix parameters from the VNA generate very similar profiles to the the matrix parameters generated from the FTS, the matrix parameters

M_{II} and M_{UU} in Figure 6.5 indicate that the measured results in the 220-330 GHz range are different for the VNA and FTS. This indicates the 220-330 GHz antenna heads still have a small misalignment that is causing them to see a reduction in signal being measured. These heads are the most difficult to align due to the smaller size in antenna used as a result of the wavelength being measured. If these heads are rotated or translationally off the optical axis the beam is less likely to be captured by the antenna horns.

6.2.3 Modulation, optical and polarisation efficiencies

Other parameters that were calculated to characterise the performance of the NIKA2 HWP in this thesis were the modulation, optical and polarisation efficiencies. These were calculated using equations (4.6), (2.12) and (2.11) and the results measured in Chapters 4 and 5 for the VNA and FTS setups respectively.

Spectral System	Modulation efficiency 150 GHz	Optical efficiency 150 GHz	Polarisation efficiency 150 GHz	Modulation efficiency 260 GHz	Optical efficiency across 260 GHz	Polarisation efficiency 260 GHz
VNA	0.992	0.953	0.957	0.997	0.964	0.946
FTS	0.992	0.961	0.959	0.996	0.970	0.952

Table 6.4 – The modulation, optical and polarisation efficiencies for the NIKA2 HWP calculated from the results produced using the FTS and VNA systems. From these results it is observed that each system calculates approximately the same values for each parameter. The modulation efficiency which is calculated using equation (4.6) uses the spectral transmission measured at the same rotation angles from the co-pol and cross-pol data sets, the result describes how well the HWP rotates the polarised signals and therefore how well it modulates the linear polarised light. Whilst the optical and polarisation efficiencies were calculated using equations (2.12) and (2.11) respectively using the Mueller matrix values presented in Figure 6.5 and describes the HWPs ability to transmit the total light and the total polarised light. For all of these values it is expected that they would be equal to 1.

The modulation, optical and polarisation efficiencies for NIKA2 HWP as measured using either the VNA or FTS systems are presented in Table 6.4. The values calculated show very small differences between each system indicating good validation of results. Additionally, these values indicate that of the detected signal transmitted through the HWP a large proportion of that signal is polarised and modulated, therefore, indicating that the HWP is performing very close to the ideal case.

6.3 SUMMARY OF THE COMPARISON BETWEEN THE SPECTRAL SYSTEMS

From reviewing the spectral characterisation of the NIKA2 HWP produced by both the VNA and FTS systems I have concluded that both systems should be used when performing a full characterisation of a HWP. This is due to the complimentary nature each provides to the measurements. The VNA system provides measurements at low frequency ranges (<90 GHz) and higher spectral resolution, while the FTS provides the ability to measure over larger frequency ranges in one scan reducing the errors in the stitching needed between the multiple receiver/transmitter headsets used in the VNA setup.

6.4 INJECTING MUELLER MATRIX COEFFICIENTS INTO ANALYSIS PIPELINES TO GENERATE SCIENTIFIC RESULTS

Propagating the Mueller matrix parameters of the HWP through to measurements of r in order to calculate any bias arising from the HWP are important to identify the level of systematic error devices introduce to instruments. To inject the measured Mueller matrix parameters into CMB measurements analysis pipelines dedicated to understanding instrumental systematic affects are required.

One such pipeline is *s4cmb* (Fabbian & Peloton, 2021), which studies the impact of systematics on the scientific results for CMB experiments through using the input sky, scanning strategy and input telescope (i.e., the design of the telescope being used) and simulates time-ordered data (TOD) for that setup, seen in Figure 6.6. TODs refer to data being arranged according to when it was received. From the TODs it can then create output sky maps, see Figure 6.7.

During this thesis I edited the “Input Telescope” section of the pipeline, seen in Figure 6.6, to store the calculated Mueller matrix parameters presented in Figure 6.5 in order to call them in other sections of the pipeline. To do this I created a function which reads in each Mueller matrix parameter and averaged them over the telescopes bandwidths to be stored as their parameter names. These were then injected into the TOD pipeline, in the function ‘map2tod’ which takes the scanned input sky maps and converts them into a TOD. Inputting the coefficients here enables the HWP performance to be included in the TODs, incorporating the HWPs systematics into the output sky maps.

Following the method described in (Giardiello et al., 2022) I built the initial infrastructure which incorporates the HWPs non-idealities measured from experimental data sets to generate output sky maps, see Figures 6.7 and 6.8 which present the output maps produced when incorporating an ideal or non-ideal HWP respectively. The matrix parameters presented in equation (3.1) were injected into *s4cmb* to retrieve the maps shown in Figure 6.7. The averaged Mueller matrix parameters retrieved from the FTS experiment over the 150 GHz band for the NIKA2 HWP

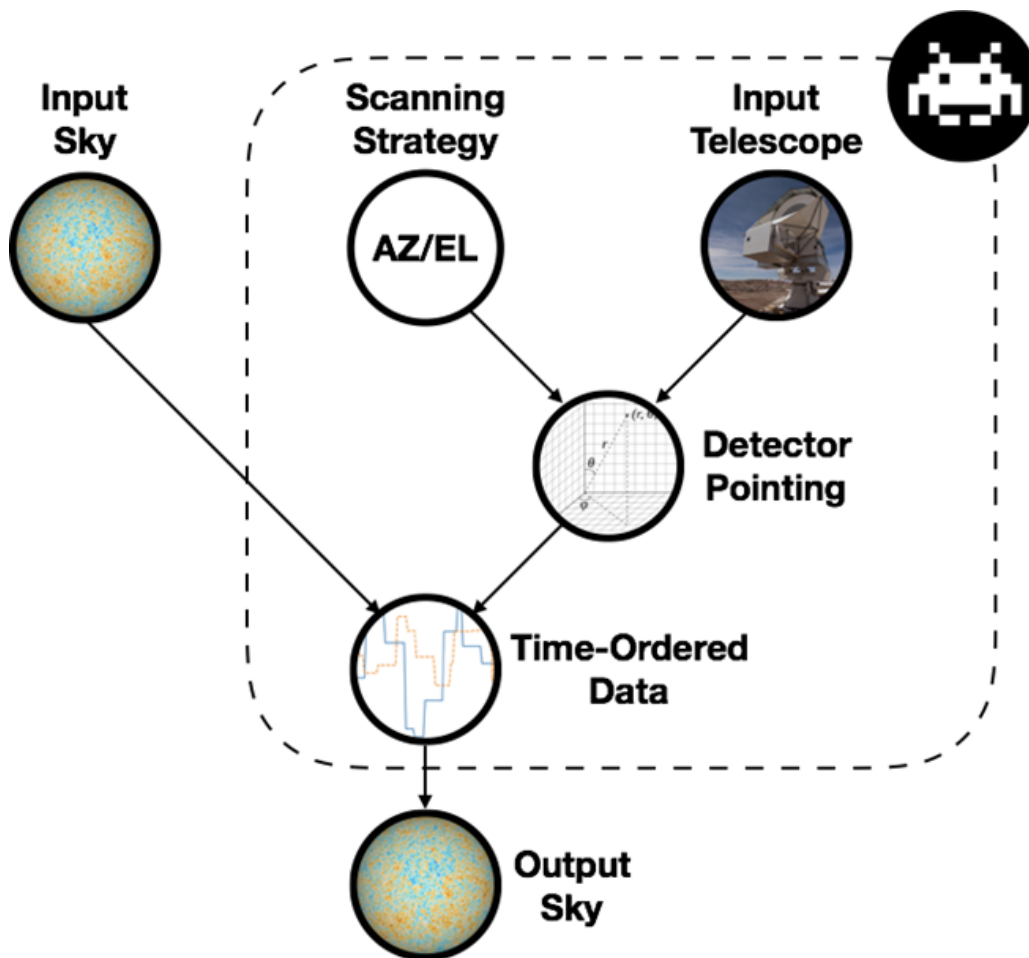


Figure 6.6 – Flow diagram to visualise the structure for the ‘*s4cmb*’ analysis pipeline (Fabbian & Peloton, 2021). The dashed box represents the analysis pipeline of *s4cmb* that can be edited. This pipeline inputs data generated from CMB experiments scanning the sky and injects instrumental systematic effects into the timestream to generate real data and inform future designs for CMB experiments. The Mueller matrix coefficients were stored in the Input Telescope section of the pipeline to then be called in the TOD section within its map making module ‘map2tod’ where the matrix coefficients are injected into the TODs.

were injected into *s4cmb* which produced the maps seen in Figure 6.8 after demodulation. The difference between the input sky and the demodulated sky maps are shown in the right hand columns and indicate that the non-ideal HWP performance causes differences to be seen in the I , Q and U maps. I did not include any other sources of systematics in the map making progress.

The difference observed in the I map in Figure 6.8 is of ~ 15 mK which when compared to the input values is not a large difference, which is to be expected given the measured performance of the HWP. The difference seen in Figure 6.8 between the Q and U input maps to their respective output maps is ~ 1 mK with this mainly contributed from the deviation from ideal seen in the M_{QQ} , M_{UU} , M_{QU} and M_{UQ} matrix parameters. As was discussed in Section 2.1.4 the polarisation efficiency and polarisation rotation caused by the HWP is observed in these parameters and there

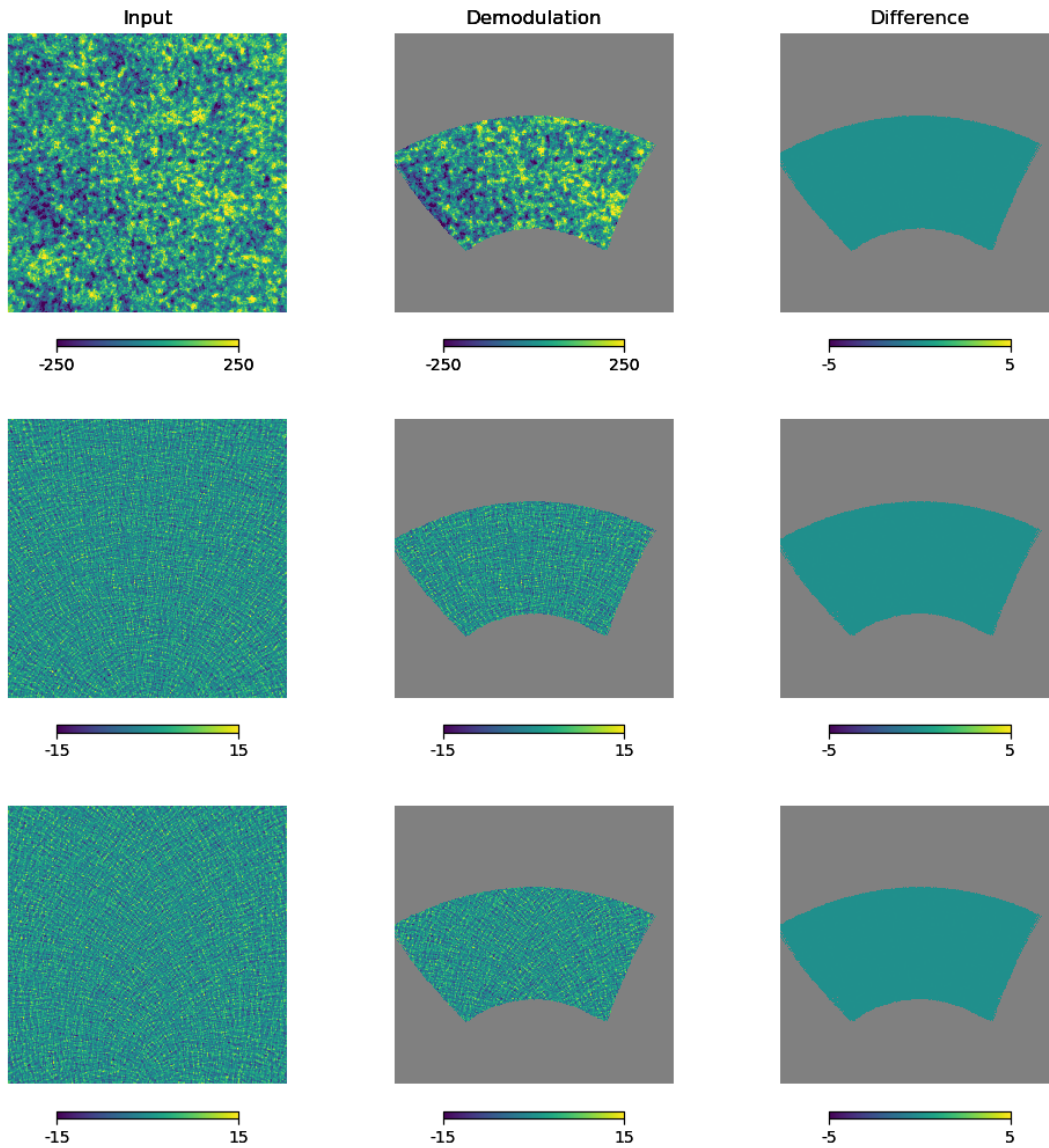


Figure 6.7 – Sky patch maps generated using the ‘*s4cmb*’ pipeline. Left column shows the input sky maps in the I (top), Q (middle) and U (bottom) parameters. The middle column shows the maps after demodulation and the right column shows the difference between the left and middle columns. For this particular plot the Mueller matrix for an ideal HWP was injected into the TOD timestream, see equation (3.1). All difference maps, I , Q and U , produce no variation between the ‘Input’ and ‘Demodulation’ plots because the ideal HWP Mueller matrix is injected, incorporating no systematics into the system and therefore not altering the input maps.

affects are then translated through to the maps and further onto the power spectrum calculations. It is through generating these maps that calculating the bias on r caused by the implementation of a HWP can be achieved.

To generate the systematic value of r associated with HWP non-idealities I took the sky maps generated in Figures 6.7 and 6.8 and injected them into the ‘*NaMaster*’ pipeline (Alonso et al.,

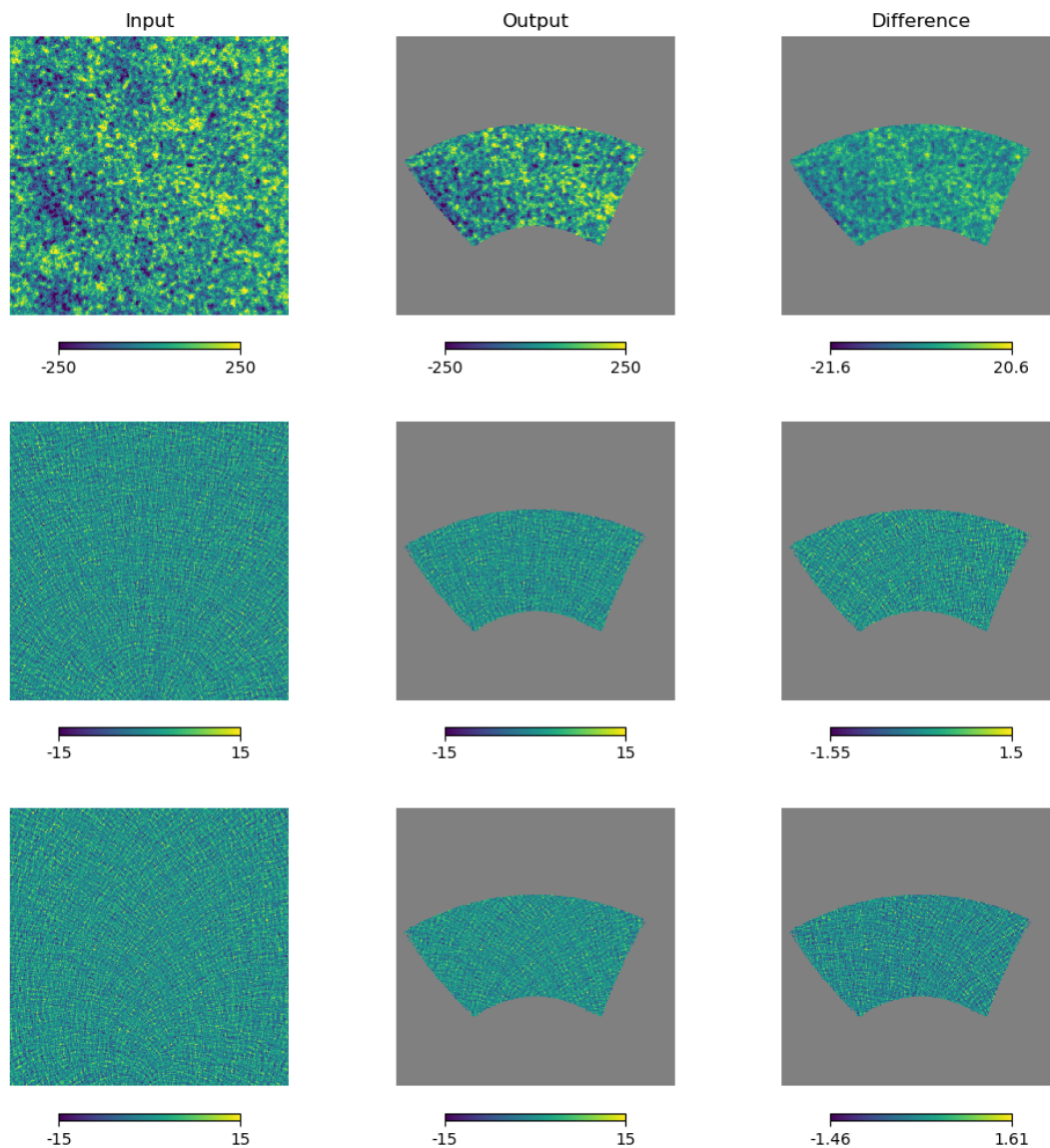


Figure 6.8 – Sky patch maps generated using the ‘*s4cmb*’ pipeline. Left column shows the input sky maps in the I (top), Q (middle) and U (bottom) parameters. The middle column shows the maps after demodulation and the right column shows the difference between the left and middle columns. For this particular plot the Mueller matrix for a non-ideal HWP was injected into the TOD timestream. The 150 GHz averaged Mueller matrix parameters obtained from the FTS experiment, provided in Table 6.3, were used to produce these output sky maps. The difference maps for I , Q and U produce variation between the ‘Input’ and ‘Demodulation’ plots due to the HWP systematics caused by the non-ideal parameters injected.

2019). This pipeline enables the user to input their measured sky maps in order to calculate the TT , EE , BB , TE and EB power spectra generated from their instrument. Therefore, taking the results from Figures 6.7 and 6.8 as well as their masks and the instrumental beam defined in the *s4cmb* pipeline, I computed the power spectra for both the ideal and non-ideal HWP cases. As the

focus of this thesis was on primordial B -mode measurements I report the BB power spectrum measured from both the ideal and non-ideal HWP cases in Figure 6.9.

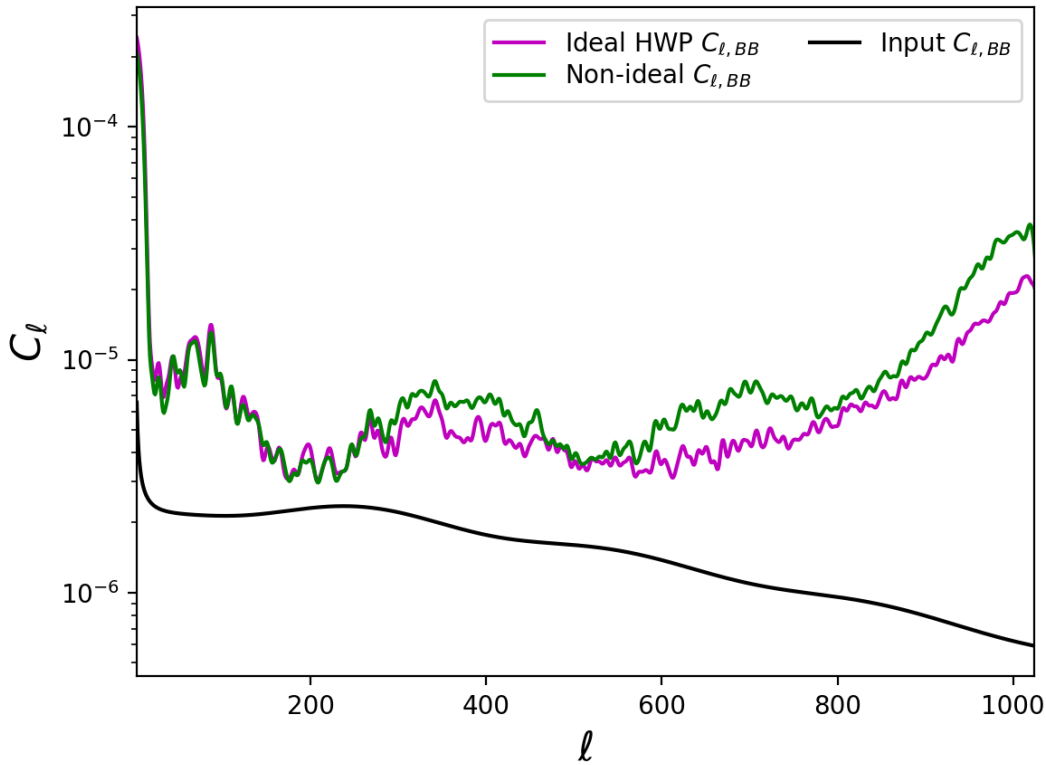


Figure 6.9 – BB power spectra for both the ideal (magenta curve) and non-ideal (green curve) HWP cases. Included in the plot is the input BB power spectrum (black curve) used in *s4cmb*. Comparing the two BB power spectra it is clear that the non-ideal HWP case affects the power spectrum at multipoles >250 by changing the amplitude of the spectrum.

Subtracting the $C_{\ell,ideal}$ and $C_{\ell,non-ideal}$ power spectrum from one another the corresponding residual signal was fitted to a tensor-only CMB power spectrum which had a free amplitude. Through varying this amplitude between 0 and 10 with total number of steps of 10,000 I calculated the systematic value of r to be $\delta r = 0.008 \pm 0.002$ which indicates that the systematics induced by this type of HWP at 150 GHz would be above the required threshold for instrumental systematics in CMB B -mode experiments which for LiteBIRD is $\delta r \sim 10^{-4}$ (Azzoni, 2023).

However, this difference might be accounted for in the contamination of E -modes in the B -mode component which is caused by a partial sky coverage, i.e. not full sky. This is believed to be the case due to the ideal HWP power spectrum returning a curve that is not similar to the input power spectrum used and due to the ideal case not including any instrumental systematics in it the input power spectrum should theoretically not be altered. But if the contamination of E -modes in the B -mode component remains in the maps the amplitude of the power spectrum will

be increased due to the larger amplitude of the E -mode component. *NaMaster* does provide the user with the ability to apply B -mode purification, which enables the removal of the contamination for E -modes in the B -mode component at map level, however, when I applied this to the calculation of the power spectra it returned a result which contained no values.

The cause for this is uncertain at present times and further optimisation of my codes are needed to analyse in more depth these effects. Additionally, other pipelines will be used to calculate δr to identify if there is any variance in the values produced, such as those discussed in (Duivenvoorden et al., 2021). In addition, my power spectra considered a CMB only scenario, work will be done to extend this analysis to include other scenarios, such as lensing, to determine how non-idealities in the HWP might translate to a bias on r with these included.

6.5 EMBEDDED METAL MESH VS. SAPPHIRE

The initial aim for this thesis was to compare the performance of an embedded metal mesh (EMM) HWP to a sapphire Pancharactnam-designed HWP, but due to Covid-19 and time constraints this work could not be performed.

As CMB experiments push for better sensitivity levels which in turn results in deploying a larger number of detectors, the requirement for larger optical devices is becoming more prevalent due to the increase in focal plane sizes. However, sapphire plates can currently only be manufactured to diameters of ~ 50 cm which sets a limit to how large the sapphire HWPs can be manufactured to. Plus, due the sapphire HWP design requires stacking of multiple plates in order to broaden the bandwidths the HWP performs over it causes the weight of the device to increase, with the current weight for the SO MF sapphire HWP being >20 kg. For space-based B -mode experiments such as LiteBIRD this added weight is not ideal when looking to launch an instrument into space. The refractive indices of sapphire are ~ 3.4 and ~ 3.06 and therefore there is a significant requirement for an ARC to be applied to the front and back of the device in order to reduce the amplitude of reflection that would otherwise occur, however, previous studies (Hill, 2020) have shown how difficult it can be to apply ARCs to sapphire plates.

Sapphire also has a large absorption coefficient (Loewenstein et al. (1973), Savini et al. (2006)) cause the optical performance of a sapphire HWP to have a strong dependence on the temperature of the system. Therefore, it is crucial to measure the transmission of a sapphire HWP at the temperature of operation. Previous literature (Loewenstein et al. (1973), Savini et al. (2006)) provide data which describes the change in refractive indices of sapphire due to temperature. These data sets were used in the BLASTPol HWP experiment (Moncelsi et al., 2014) to extrapolate the spectral transmission of their sapphire HWP to cryogenic temperatures of 4 K, allowing its performance to be determined.

Comparatively, an EMM HWP has a lower absorption coefficient, less temperature dependence

and the weight of these devices is $<1\text{kg}$. The diameter of these devices is limited by the laboratory capabilities of the current fabrication facility and the limits on polypropylene availabilities. Currently, EMM HWPs are being made to 320 mm maximum outer diameters and have been shown to perform as well as their sapphire counterparts ([Monceli et al. \(2014\)](#), [Pisano et al. \(2022\)](#)). However, with SO:UK requiring an EMM HWP with a diameter of $\sim 50\text{ cm}$, the maximum diameter of these EMM HWP will need to be increased. A detailed comparison between the performances of sapphire and EMM HWPs will continue at Cardiff.

This work will be performed in the next six months as three 100 mm diameter sapphire plates have been acquired by Cardiff University and are designed to perform over bandwidths centred on 93 GHz and 150 GHz. I am currently carrying out work to determine the refractive indices of the ordinary and extraordinary axes in each plate. Once these measurements have been performed and the axes determined, assembling them to form a three plate Pancharatnam HWP will be carried out using a recipe provided from Prof. Giorgio Savini of UCL ([Savini, 2022](#)). This sapphire HWP will be compared to an equivalent EMM HWP design which is currently being finalised and a prototype is set to be manufactured in the coming months. This EMM will be designed to perform over bandwidths centred on 93 and 150 GHz and be 200 mm in diameter.

Both of these HWP types will be characterised using the method that has been described in this thesis and their Mueller matrix components will be propagated to measure r as described above. Comparing these types of HWPs will inform on the benefits and disadvantages each might bring to an experiment as well as their effects on scientific goals.

Overall, I have found that the EMM HWPs performance to be very comparable to the sapphire Pancharatnam HWPs currently used in CMB experiments and have a number of advantages to their use in CMB studies. Therefore, they are very promising devices to use in future CMB experiments.

CONCLUSION

"To the stars who listen, and the dreams that are answered."

Sarah J Maas, *A Court of Mist and Fury*

As explored in Chapter 1, current and future CMB experiments are pushing to constrain and measure the primordial B-mode signal, known as the 'smoking-gun' for cosmic inflation, which has eluded detection so far. Due to its small amplitude, as seen in Figure 1.4, CMB experiments are increasing their sensitivities by deploying more detectors than ever before, from a few hundred detectors to an order of magnitude of 10^4 . However, there is also a requirement to understand the level of systematic errors arising from devices within the instrument design prior to its deployment. In particular, CMB experiments targeting the primordial *B*-mode component typically deploy a HWP to modulate the linear polarised signal of the CMB. Therefore, it is crucial to understand how the HWP performs over the experiments bandwidths and measure the bias level it introduces to the scientific goals. This thesis explores the method required to characterise the performance of a HWP to calculate the bias they introduce to measurements of r .

HWPs are devices which rotate linear polarised light to other linear polarised states while allowing unpolarised signals to traverse freely through the device. Sapphire HWPs, designed using the results obtained by Pancharatnam in the 1950s, have been deployed in CMB *B*-mode experiments over the last 20 years with current experiments, such as SO, continuing to deploy them within their instruments. However, future CMB experiments such as SO:UK and LiteBIRD plan to implement EMM HWPs, a different type of HWP, as their polarisation modulator. The principle theory for HWPs is presented in Chapter 2, along with the differences between EMM and Pancharatnam HWPs and how Mueller matrices characterise a HWPs performance.

A Mueller matrix is a 4x4 matrix which describes how the polarisation states of a light beam change after propagating through a device. These matrices were derived by Mueller through using Stokes formalism, which is expanded on in Chapter 2. These matrices can be used to

describe a full range of optical devices of which can be multiplied together to produce a matrix which describes an entire setup in order to calculate the Stokes output of the system. Combining measured spectral transmission of a HWP an optical setup can be used to generate the Mueller matrix of a HWP, such an analysis was performed and presented in the BLASTPol paper (Moncelsi et al., 2014). Here they use MCMCs to estimate model parameters from fitting experimental models to experimental data sets in order to calculate the HWPs Mueller matrix parameters.

Previous characterisations of HWPs include BLASTPol which saw a five plate sapphire HWP spectrally characterised using a polarising FTS at Cardiff University. Those characterisations reported on the Mueller matrix components measured over the frequency bandwidths of the BLASTPol experiment and propagated their findings through to map making algorithms to include the non-idealities arising from the HWP.

However, the diameter of the BLASTPol HWP was ~90 mm and could therefore be measured comfortably on the FTS test bench at Cardiff University. But the size of the NIKA2 HWP was ~300 mm in diameter, resulting in being too large for the centre of the HWP to sit in the optical beam of the FTS system. To characterise this HWP it was decided to use the VNA system instead to spectrally characterise the HWP. Initial measurements of the cross-pol data, provided in Figure 4.9, indicated issues with the alignment of the system over all three frequency bands measured were arising because the average spectral transmission of a maxima spectrum measured in the cross-pol configuration was 0.77 and 0.62 for the 150 GHz and 260 GHz band respectively. Comparatively, the simulated maxima transmission values for the NIKA2 HWP were >0.9 and the corresponding spectral transmission values measured from the co-pol data sets were 0.92 and 0.96 for 150 GHz and 260 GHz respectively, indicating the cross-pol configuration was losing ~30% of the transmitted power. A full realignment of the system was performed and the methods used to correct for the misalignment between optical elements in the system, such as the lenses, the mirrors and the antenna horns, is discussed in depth in Chapter 4.

The realignment caused the spectral transmission values to increase for the cross-pol measurements, with the average values recorded at 0.92 and 0.91 for the 150 GHz and 260 GHz band respectively and is presented in Figure 4.25. Injecting the spectra in Figures 4.6 and 4.24 into the Mueller matrix analysis pipeline generated from using the method provided in Chapter 3, the Mueller matrix for the NIKA2 EMM HWP was estimated using a MCMC and the results are presented in Figure 4.28. Their average values across the 150 GHz and 260 GHz bands are recorded in Table 4.9. The diagonal terms in the Mueller matrix, M_{II} , M_{QQ} and M_{UU} , were estimated to be 0.93, 0.93 and -0.89 for 150 GHz and 0.93, 0.95 and -0.88 for 260 GHz, while the off-diagonal terms were estimated to be close to 0.

To validate the characterisation results obtained using the VNA system, the same procedure to characterise the performance of the NIKA2 HWP from spectral transmission measurements was also performed using a polarising FTS system, described in Chapter 5. Due to the limitations of

the optical test bench used for this system the HWP was cut to a diameter of 110mm and inserted into a mechanical rotator and placed in the beam seen in Figure 5.3. The FTS system did not require any realignment to the optics and produced an average transmission of 0.94 and 0.93 across the 150 GHz and 260 GHz band respectively for both the co- and cross-pol transmission. For the Mueller matrix components, the diagonal terms were calculated to be 0.95, 0.93 and -0.91 for 150 GHz and 0.95, 0.94 and -0.91 for 260 GHz, with the off-diagonal terms also producing values close to 0.

Both techniques produced very similar results for the spectral transmission and Mueller matrix components of the NIKA2 HWP with difference of approximately 0.02 between the diagonal terms. This difference most likely arises from the difference in spectral transmission measured from each system because the spectral transmission calculated for each band varied by 0.02. Additionally, both the VNA and FTS Mueller matrices produced values for the M_{QU} and M_{UQ} terms which indicated a $\sim 7\%$ level of polarisation mixing. This large level in polarisation mixing indicates the phase difference generated between the two axes of the HWP does not equal 180° causing the linear polarisation to become elliptical slightly. Further work is being carried out to examine and identify where this level is arising from.

The advantages to using a FTS system to spectrally characterise a HWP include the ease in access to optical components in the system, reducing the chance of injury, the systems ability to measure over large frequency ranges with very little change to its small fluctuations in its signal over time. Whilst the VNA system requires multiple antenna heads to cover large frequency ranges such as those used by CMB experiments and the NIKA2 experiment. However, a VNA system provides a higher spectral resolution to the spectral measurements and enables measurements at frequencies below 90 GHz where the FTS begins to have a low signal to noise ratio therefore can not accurately measure the spectral transmission of the HWP. The VNA's dynamic range was 80dB whilst the FTS provided a dynamic range of 30 dB allowing for the VNA to have a higher sensitivity.

Due to Covid-19 plans to propagate the Mueller matrix components through to measurements of r could not be finished within the time frame of this project, however, this will be finished within the following months. This will be achieved through using the method described in Chapter 6 by generating the sky maps shown in Figure 6.7 to propagate through to measurements r using current analysis pipelines. In addition, spectral characterise both an EMM and Pancharatnam HWP could not be finished within the time constraints of this thesis. Current work is being performed to begin building a three plate sapphire Pancharatnam HWP, designed to operate over the SO MF range, spectrally characterise it using the methods described in this thesis and compare its performance to an EMM HWP, built to the same specifications. Both of their Mueller matrix components will be propagated through to measurements of r to measure the level of systematic errors each introduces in the system.

To conclude, this thesis has identified that when spectrally characterising a HWP both a FTS and VNA should be used, especially when measurements are required at frequencies below 90 GHz due to the FTS' poor signal to noise ratio and a VNAs capabilities in this range. I have also concluded that a EMM HWP is a useable device over its designed frequencies and performs as simulated and demonstrated it has a number of advantages over the Pancharatnam HWP, such as the devices weight and size limitations. The embedded metal mesh HWP is very promising device for future CMB experiments.

Bibliography

- Abazajian K., et al., 2022, Snowmass 2021 CMB-S4 White Paper, <http://arxiv.org/abs/2203.08024>
- Ade P. A. R., Pisano G., Tucker C., Weaver S., 2006. Orlando, Florida , USA, p. 62750U, [doi:10.1117/12.673162](https://doi.org/10.1117/12.673162), <http://proceedings.spiedigitallibrary.org/proceeding.aspx?doi=10.1117/12.673162>
- Ade P. A. R., et al., 2009, [Journal of Physics: Conference Series](#), 155, 012006
- Ade P., et al., 2014, [Physical Review Letters](#), 112, 241101
- Ade P., et al., 2019, [Journal of Cosmology and Astroparticle Physics](#), 2019, 056
- Ali A. M., et al., 2020, [Journal of Low Temperature Physics](#), 200, 461
- Alonso D., Sanchez J., Slosar A., 2019, [Monthly Notices of the Royal Astronomical Society](#), 484, 4127
- Alpher R. A., Herman R., 1948, [Nature](#), 162, 774
- Alpher R. A., Herman R. C., 1949, [Physical Review](#), 75, 1089
- Azzoni S., 2023
- BICEP/Keck Collaboration et al., 2021, [Physical Review Letters](#), 127, 151301
- Bahr-Kalus B., Parkinson D., Easter R., 2023, [Monthly Notices of the Royal Astronomical Society](#), 520, 2405
- Bhattacharya R., Debnath A., Sajjanhar E., Sardeshpande S., HernÃ P. T., 2022
- Bonga B., Gupt B., Yokomizo N., 2017, [Journal of Cosmology and Astroparticle Physics](#), 2017, 021

BIBLIOGRAPHY

- Burbidge G., 2001, Quasi-Steady State Cosmology, <http://arxiv.org/abs/astro-ph/0108051>
- Calabrese E., 2020
- Carlstrom J. E., et al., 2011, [Publications of the Astronomical Society of the Pacific](#), 123, 568
- Clesse S., 2015, An introduction to inflation after Planck: from theory to observations, <http://arxiv.org/abs/1501.00460>
- Coil A. L., 2013, pp 387–421, [doi:10.1007/978-94-007-5609-0_8](https://doi.org/10.1007/978-94-007-5609-0_8), <http://arxiv.org/abs/1202.6633>
- Collaboration T. P., et al., 2014, [The Astrophysical Journal](#), 794, 171
- Collaboration T. S. O., et al., 2019, The Simons Observatory: Astro2020 Decadal Project Whitepaper, <http://arxiv.org/abs/1907.08284>
- Collaboration P., et al., 2020, [Astronomy & Astrophysics](#), 641, A1
- Collaboration L., et al., 2023, [Progress of Theoretical and Experimental Physics](#), 2023, 042F01
- Collett E., 1993, Polarized light: fundamentals and applications. Optical engineering (Marcel Dekker, Inc.), v. 36, 36, Marcel Dekker, New York, 1993
- Dodelson S., Kinney W. H., Kolb E. W., 1997, [Physical Review D](#), 56, 3207
- Duivendoorn A. J., Adler A. E., Billi M., Dachlythra N., Gudmundsson J. E., 2021, [Monthly Notices of the Royal Astronomical Society](#), 502, 4526
- Durrer R., 2015, [Classical and Quantum Gravity](#), 32, 124007
- Essinger-Hileman T., et al., 2016, [Review of Scientific Instruments](#), 87, 094503
- Fabbian G., Peloton J., 2021, [Journal of Open Source Software](#), 6, 3022
- Fixsen D. J., Cheng E. S., Gales J. M., Mather J. C., Shafer R. A., Wright E. L., 1996, [The Astrophysical Journal](#), 473, 576
- Foreman-Mackey D., Hogg D. W., Lang D., Goodman J., 2013, [Publications of the Astronomical Society of the Pacific](#), 125, 306
- Fraknoi A., et al., 2017, in , Astronomy. OpenStax, <https://pressbooks.online.ucf.edu/astronomybc/chapter/29-3-the-beginning-of-the-universe/>

- Galitzki N., et al., 2018, [Millimeter, Submillimeter, and Far-Infrared Detectors and Instrumentation for Astronomy IX](#), p. 3
- Gamow G., 1948, [Nature](#), 162, 680
- Giardiello S., et al., 2022, [Astronomy & Astrophysics](#), 658, A15
- Gualtieri R., et al., 2018, [Journal of Low Temperature Physics](#), 193, 1112
- Hadzhiyska B., Spergel D. N., 2019, [Physical Review D](#), 99, 043537
- Hanany S., Collins J., Johnson B. R., Lee A. T., Tran H. T., , p. 8
- Hanson D., et al., 2013, [Physical Review Letters](#), 111, 141301
- Hervías-Caimapo C., Bonaldi A., Brown M. L., Huffenberger K. M., 2022, [The Astrophysical Journal](#), 924, 11
- Heurtel-Depeiges D., Burkhart B., Ohana R., Blancard B. R.-S., 2023, Removing Dust from CMB Observations with Diffusion Models, <http://arxiv.org/abs/2310.16285>
- Hill C. A., 2020, PhD thesis, UC Berkeley, <https://escholarship.org/uc/item/7vk6t7hb>
- Hill C. A., et al., 2020, [Review of Scientific Instruments](#), 91, 124503
- Hinshaw G., et al., 2009, [The Astrophysical Journal Supplement Series](#), 180, 225
- Hu W., Dodelson S., 2002, [Annual Review of Astronomy and Astrophysics](#), 40, 171
- Incardona F., 2020, [arXiv:2009.01100 \[astro-ph, physics:physics\]](#) 10.13130/incardona-federico_phd2020 – 01 – 17
- Jepsen K., 2013, The early universe | symmetry magazine, https://www.symmetrymagazine.org/article/november-2013/the-early-universe?language_content_entity=und
- Johnson B. R., et al., 2007, [The Astrophysical Journal](#), 665, 42
- Joseph A., 2017, in , Investigating Seafloors and Oceans. Elsevier, pp 257–305, doi:10.1016/B978-0-12-809357-3.00005-9, <https://linkinghub.elsevier.com/retrieve/pii/B9780128093573000059>
- KG R. . S. G. . C., 2023, R&S@ZVA vector network analyzer, https://www.rohde-schwarz.com/uk/products/test-and-measurement/network-analyzers/rs-zva-vector-network-analyzer_63493-9660.html

BIBLIOGRAPHY

- Kiuchi K., et al., 2020, in *Ground-based and Airborne Telescopes VIII*. p. 162, [doi:10.1117/12.2562016](https://doi.org/10.1117/12.2562016), <http://arxiv.org/abs/2101.11917>
- Kogut A., Lineweaver C., Smoot G. F., Bennett C. L., Banday A., 1993, *The Astrophysical Journal*, 419, 1
- Kovac J. M., Barkats D., 2007, *CMB from the South Pole: Past, Present, and Future*, <http://arxiv.org/abs/0707.1075>
- La Porta L., Burigana C., Reich W., Reich P., 2008, *Astronomy & Astrophysics*, 479, 641
- Lerner D., 1965, *IEEE Transactions on Antennas and Propagation*, 13, 3
- Loewenstein E. V., Smith D. R., Morgan R. L., 1973, *Applied Optics*, 12, 398
- Luminet J.-P., 2015, *Lemaitre's Big Bang*, <http://arxiv.org/abs/1503.08304>
- Maffei B., Pisano G., Ng M. W., Haynes V. C., 2012. Amsterdam, Netherlands, p. 84520K, [doi:10.1117/12.926683](https://doi.org/10.1117/12.926683), <http://proceedings.spiedigitallibrary.org/proceeding.aspx?doi=10.1117/12.926683>
- Martin D., 1982, Academic, New York, 6, 65
- Masi S., et al., 2019, *EPJ Web of Conferences*, 209, 01046
- Mather J. C., 2010, *Physics Today*, 63, 47
- Matsuda F., et al., 2019, *Review of Scientific Instruments*, 90, 115115
- Moncelsi L., et al., 2014, *Monthly Notices of the Royal Astronomical Society*, 437, 2772
- Monelli M., Komatsu E., Ghigna T., Matsumura T., Pisano G., Takaku R., 2023, Impact of half-wave plate systematics on the measurement of CMB B -mode polarization, <https://arxiv.org/abs/2311.07999>
- Montero-Camacho P., Hirata C. M., 2018, *Journal of Cosmology and Astroparticle Physics*, 2018, 040
- Nørgaard-Nielsen H. U., Jørgensen H. E., 2008, *Astrophysics and Space Science*, 318, 195
- O'Raiheartaigh C., McCann B., Nahm W., Mitton S., 2014, *The European Physical Journal H*, 39, 353

- Ogburn Iv R. W., et al., 2010. San Diego, California, USA, p. 77411G, [doi:10.1117/12.857864](https://doi.org/10.1117/12.857864), <http://proceedings.spiedigitallibrary.org/proceeding.aspx?doi=10.1117/12.857864>
- Pan Z., et al., 2023, A Measurement of Gravitational Lensing of the Cosmic Microwave Background Using SPT-3G 2018 Data, [doi:10.48550/arXiv.2308.11608](https://doi.org/10.48550/arXiv.2308.11608), <http://arxiv.org/abs/2308.11608>
- Pancharatnam S., 1955a, pp 130–136
- Pancharatnam S., 1955b, [Proceedings of the Indian Academy of Sciences - Section A](#), 41, 137
- Patti A., Acierno D., Patti A., Acierno D., 2019, in , Polypropylene - Polymerization and Characterization of Mechanical and Thermal Properties. IntechOpen, [doi:10.5772/intechopen.84477](https://doi.org/10.5772/intechopen.84477), <https://www.intechopen.com/chapters/65584>
- Penzias A. A., Wilson R. W., 1965, [The Astrophysical Journal](#), 142, 419
- Pisano G., others 2014, [Proc. SPIE Int. Soc. Opt. Eng.](#), 9153, 915317
- Pisano G., Savini G., Ade P. A. R., Haynes V., 2008, [Applied Optics](#), 47, 6251
- Pisano G., Ng M. W., Haynes V., Maffei B., 2012, [Progress In Electromagnetics Research M](#), 25, 101
- Pisano G., Tucker C., Ade P. A. R., Moseley P., Ng M. W., 2015, in 2015 8th UK, Europe, China Millimeter Waves and THz Technology Workshop (UCMMT). pp 1–4, [doi:10.1109/UCMMT.2015.7460631](https://doi.org/10.1109/UCMMT.2015.7460631)
- Pisano G., et al., 2022, [Astronomy & Astrophysics](#), 658, A24
- Qu F. J., et al., 2023, The Atacama Cosmology Telescope: A Measurement of the DR6 CMB Lensing Power Spectrum and its Implications for Structure Growth, [doi:10.48550/arXiv.2304.05202](https://doi.org/10.48550/arXiv.2304.05202), <http://arxiv.org/abs/2304.05202>
- Remmen G. N., Carroll S. M., 2014, [Physical Review D](#), 90, 063517
- Salatino M., de Bernardis P., Masi S., 2017, [Journal of Infrared, Millimeter, and Terahertz Waves](#), 38, 215
- Savini G., 2022, Private correspondence: 3-plate Sapphire Pancharatnam design
- Savini G., Pisano G., Ade P. A. R., 2006, [Applied Optics](#), 45, 8907

BIBLIOGRAPHY

Schmidt N., 2022

Seshadri T. R., 1999, *Pramana*, 53, 963

Shatrow A., Chuprin A., Sivov A., 1995, *IEEE Transactions on Antennas and Propagation*, 43, 109

Sheere C., van Engelen A., Meerburg P. D., Meyers J., 2017, *Physical Review D*, 96, 063508

Speagle J. S., 2020, A Conceptual Introduction to Markov Chain Monte Carlo Methods, <http://arxiv.org/abs/1909.12313>

Stahl P., 2018, Multivariable Parametric Cost Model for Ground AND Space Telescope, <https://nasasitebuilder.nasawestprime.com/wp-content/uploads/sites/42/2019/11/22-NASA-Multivariable-Cost-Model-for-Ground-and-Space-Telescopes.pdf>

Stuart C., 2022, What is the flatness problem in cosmology?, <https://www.colinstuart.net/what-is-the-flatness-problem-in-cosmology/>

Swetz D. S., et al., 2011, *The Astrophysical Journal Supplement Series*, 194, 41

The EBEX Collaboration et al., 2018, *The Astrophysical Journal Supplement Series*, 239, 7

Toh B., Cahill R., Fusco V., 2003, *IEEE Transactions on Education*, 46, 313

Tristram M., et al., 2022, *Physical Review D*, 105, 083524

Westbrook B., et al., 2018, *Journal of Low Temperature Physics*, 193, 758

Wilson G. W., et al., 2020, in Zmuidzinas J., Gao J.-R., eds, Millimeter, Submillimeter, and Far-Infrared Detectors and Instrumentation for Astronomy X. SPIE, Online Only, United States, p. 1, [doi:10.1117/12.2562331](https://www.spiedigitallibrary.org/conference-proceedings-of-spie/11453/2562331/The-TolTEC-camera--an-overview-of-the-instrument-and/10.1117/12.2562331.full), <https://www.spiedigitallibrary.org/conference-proceedings-of-spie/11453/2562331/full>

Xu Z., et al., 2021, *Research Notes of the AAS*, 5, 100

Zaroubi S., 2013, pp 45–101, [doi:10.1007/978-3-642-32362-1_2](https://arxiv.org/abs/1206.0267), <http://arxiv.org/abs/1206.0267>

Zhang J., Ade P., Mauskopf P., Savini G., Moncelsi L., Whitehouse N., 2011, *Applied Optics*, 50, 3750

de la Hoz E., et al., 2023, *Monthly Notices of the Royal Astronomical Society*, 519, 3504